Fermilab

FERMILAB-THESIS-2001-25

ANALYSIS OF THE VECTOR BOSON SELF INTERACTION AND THE SEARCH FOR ANOMALOUS COUPLINGS AT $\sqrt{s} = 1.8$ TeV $p\bar{p}$ COLLISIONS

BY

LEONARD STEVEN CHRISTOFEK

B.S., Virginia Polytechnic Institute and State University, 1992
M.S., University of Illinois at Urbana-Champaign, 1995

THESIS

Submitted in partial fulfillment of the requirements
for the degree of Doctor of Philosophy in Physics
in the Graduate College of the
University of Illinois at Urbana-Champaign, 2001

Urbana, Illinois

ANALYSIS OF THE VECTOR BOSON SELF INTERACTION
AND THE SEARCH FOR ANOMALOUS COUPLINGS AT
$\sqrt{s} = 1.8$ TeV $p\bar{p}$ COLLISIONS

Leonard Steven Christofek, Ph.D.
Department of Physics
University of Illinois at Urbana-Champaign, 2001
Professor Steven Errede, Advisor

The production cross section times decay branching ratios for $W + \gamma$ and $Z/DY + \gamma$ have been measured in $\sqrt{s} = 1.8$ TeV $\bar{p}p$ collisions using muon and electron data samples obtained during the 1992-1993 and 1994-1995 collider runs at the Fermilab Tevatron with the CDF detector corresponding to a total integrated luminosity of 110 pb^{-1}. For photons with transverse energy $E_T^{\gamma} > 7.0$ GeV, pseudorapidity in the central or plug region ($\mid \eta_l \mid < 2.4$) and a lepton-photon angular separation $\Delta R_{l\gamma} > 0.7$, we observed 122(213) muon(electron) $W\gamma$ candidates and 36(43) muon(electron) $Z/DY\gamma$ candidates. We observe a total of 335 muon plus electron $W + \gamma$ and 79 muon plus electron $Z/DY + \gamma$ candidates, whereas the standard model expectation is 264.6 ± 18.2 $W + \gamma$ events and 74.2 ± 4.2 $Z/DY + \gamma$ events. The combined electron plus muon channel results correspond to $\sigma \cdot B(W + \gamma) = 19.8 \pm 1.7$ pb and $\sigma \cdot B(Z/DY + \gamma) = 5.5 \pm 0.8$ pb. The next-to-leading-order standard model predictions are $\sigma \cdot B(W + \gamma) = 14.8$ pb and $\sigma \cdot B(Z/DY + \gamma) = 5.8$ pb. For $W + \gamma$, this corresponds to a $\sim 35\%$ excess relative to the standard model prediction.

Acknowledgements

I would like to thank Lee Holloway for accepting me as a research assistant. Lee allowed me complete freedom to pursue whatever I found interesting. Also, I want to thank Steve (my thesis advisor). Steve started my interest into the possible composite nature of the massive gauge bosons. I would also like to thank other members of the CDF $V + \gamma$ group (Doug Benjamin, Debbie Errede, Mike Lindgren, Dirk Neuberger and Bob Wagner). Without their help, this project would never have reached completion.

A special thanks to Randy Keup, Christopher Cawlfield, John Strologas, Dave Lesny, Tom Shaw, Shirley Rothermel and Donna Guzy. I had many helpful physics and CDF discussions with Randy and John. Chris knew everything about computers and applications that I ever needed to know. Dave kept the high energy computers operational. Tom, Shirley, and Donna kept the department running and money flowing, not to mention they provided many stimulating conversations.

I dedicate this work to my Mother, Marlene Christofek, whose support and love was given without reservation. She survived three major surgeries and my childhood to see the successful completion of this thesis. I cannot forget my brother, Richard, and my sister, Christine. Finally, I thank - with an apology - and love Renae. She listened to me when no one else would have while completing this project. She understands the apology.

This thesis was supported in part by the United States Department of Energy under grant `DE-FG02-91ER-40677`.

Contents

List of Tables

List of Figures

Chapter 1

Introduction

1.1 The Standard Model

Physicists have identified four fundamental forces in nature: the strong, the weak, the electromagnetic and the gravitational.[1] The standard model mathematically describes the first three of these four forces.[2] Each of the four forces are mediated by gauge bosons or force carriers. The strong force is mediated by gluons, the weak force is mediated by "weak" bosons, the electromagnetic force is mediated by the photon and the gravitational force is mediated by the graviton. These mediators interact with a set of particles called quarks and leptons. Quarks interact with all three of the force carriers, but the leptons interact only with the weak bosons and the photon.

The standard model integrates two separate theories: quantum chromodynamics (QCD) and the Glashow-Weingberg-Salam (GWS) theory, which unifies the weak and electromagnetic interactions. QCD describes the interaction of quarks with gluons. It is responsible for binding the quarks into tightly packed objects, call hadrons, and for providing stability to protons and neutrons. GWS unifies the interactions of the W and Z bosons, which are responsible for the decay of atomic nuclei and particles, and quantum electrodynamics (QED), which describes interactions between electrons and photons.

[1] We basically follow and summarize the excellent outline in [1].

[2] Gravity is the weakest of these four forces and it presently lacks a consistent mathematical and experimentally verified description. Also, we will ignore the graviton for the discussion that follows.

$$\begin{pmatrix} \nu_e \\ e \end{pmatrix} \begin{pmatrix} \nu_\mu \\ \mu \end{pmatrix} \begin{pmatrix} \nu_\tau \\ \tau \end{pmatrix}$$

Table 1.1: The division of leptons into generations or families. The left grouping is the electron family, the middle grouping is the muon family and the right grouping is the tauon family.

1.1.1 Leptons

There are a total of six leptons that have been experimentally measured. These leptons consist of the electron, the muon and the tauon and their corresponding neutrinos. The electron, the muon, and the tauon are massive and have an electric charge of minus one. The three neutrinos are massless[3] and have no electric charge. Also, every lepton has a half integer spin and a corresponding antiparticle. These leptons are divided into three generations or "families" with one member being charged and the other neutral. This is shown in Table 1.1.

The first generation or electron family consists of the electron (e) and the electron neutrino (ν_e). The electron is the lightest charged lepton and therefore stable because there is nothing for it to decay into and carry its charge away. The electron neutrino has no charge, so it interacts only weakly - like all neutrinos. The second generation or muon family consists of the muon (μ) and the muon neutrino (ν_μ). The muon is identical to the electron, but it is 207 times more massive. Also, the muon is not stable but decays into an electron, antielectron neutrino ($\overline{\nu}_e$) and muon neutrino. This decay conserves not only electric charge but a property called electron and muon number. Finally, the tauon family consists of the tauon (τ) and the tauon neutrino (ν_τ). The tauon is 3,487 times more massive than the electron. The tauon is also unstable and decays similiar to the muon while conserving tauon number. This family conservation is generically known as lepton conservation. We summarize the lepton

[3]Recent experimental evidence indirectly supports neutrinos having mass, but it is not relevant to this discussion.

Lepton	Mass	Charge	Spin
e	0.511 MeV/c^2	-1	1/2
μ	105.66 MeV/c^2	-1	1/2
τ	1777.03 MeV/c^2	-1	1/2
ν_e	< 3 eV/c^2	0	1/2
ν_μ	< 0.19 MeV/c^2	0	1/2
ν_τ	< 18.2 MeV/c^2	0	1/2

Table 1.2: Basic properties of the leptons. These numbers and limits are from the 2000 European Physical Journal C [2]. The electric charges are given in units of proton charge and the spins are given in units of $\hbar$.

properties in Table 1.2.

1.1.2 Quarks

Unlike leptons, quarks are not found isolated in nature. They exist bound together with other quarks in objects called hadrons. It is remarkable that all presently known hadrons can be constructed from only six quarks. The quarks also have half integer spin and can be divided into families, but unlike leptons they have fractional electric charge. The six quarks are: the up quark (u), the down quark (d), the charm quark (c), the strange quark (s), the top quark (t) and the bottom quark (b). Each quark has a corresponding antiquark denoted by placing a bar over its symbol (e.g. $\overline{c}$ is the anticharm quark or c-bar). All the quarks have mass, but because they are always bound together these masses are theoretical in nature[4] and based on certain experimental properties. The up quark is the lightest, with a mass of 2 times the electron, and the bottom quark is 8 times as massive as the electron. The top quark is the most massive with a mass a 348,000 times that of the electron. The quark family structure is shown in Table 1.3.

The quarks can be combined into baryons, hadrons with half integer spin, or

[4]Actually, the masses of the quarks change as a function of the square of the momentum transfer.

$$\begin{pmatrix} u \\ d \end{pmatrix} \begin{pmatrix} c \\ s \end{pmatrix} \begin{pmatrix} t \\ b \end{pmatrix}$$

Table 1.3: The division of quarks into generations or families. The left grouping is the first generation, the middle grouping is the second generation and the right grouping is the third generation.

mesons, hadrons with integer spin. Similiarly, antibaryons and antimesons are constructed from antiquarks. For example, the proton and neutron are baryons, which are composed of three quarks. The proton is made up from the three quarks $p \sim uud$ while the neutron is made up from the three quarks $n \sim udd$. Analogously, the antiproton is constructed from the three antiquarks $\overline{p} \sim \overline{u}\,\overline{u}\,\overline{d}$ while the antineutron is constructed from the three antiquarks $\overline{n} \sim \overline{u}\,\overline{d}\,\overline{d}$. Mesons are generally composed of a quark and an antiquark. The positive charged pi meson is constructed from the two quarks $\pi^+ \sim u\overline{d}$. The properties of the quarks are listed in Table 1.4.

1.1.3 Gauge Bosons

The four forces found in nature are more properly called interactions. The strong interaction is mediated by eight "colored" gluons (g), the weak interaction is mediated by three "weak" bosons ($W^{\pm}$ and Z^0), the electromagnetic interaction is mediated by the photon (γ) and the gravitational interaction by the graviton (G). Each interaction gives rise to its respective force.

All particles in the standard model are represented as fields which are described by quantum field theory. In quantum field theory, one can perform transformations on these fields (e.g. translations, rotations, internal rotations, etc.). These transformations can be classified into two types: global and local. A global transformation acts that same on every point in space. A local transformation varies from point to point. For local transformations, in order to prevent the total energy of the field from changing, it is necessary to introduce additional fields which restore the total energy

Quark	Mass	Charge	Spin
u	1-5 MeV/c^2	2/3	1/2
d	3-9 MeV/c^2	-1/3	1/2
c	1.15-1.35 GeV/c^2	2/3	1/2
s	75-170 MeV/c^2	-1/3	1/2
t	174.3±5.1 GeV/c^2	2/3	1/2
b	4.0-4.4 GeV/c^2	-1/3	1/2

Table 1.4: Basic properties of the quarks. These numbers and limits are from the 2000 European Physical Journal C [2]. The electric charges are given in units of proton charge and the spins are given in units of $\hbar$.

of the field. These additional fields are the gauge bosons.

In the standard model, the gauge bosons are fundamental particles - like the leptons and quarks - which means they are pointlike and have no internal structure. We summarize the gauge boson properties in Table 1.5.

1.1.4 QCD and the Electroweak Model

Each quark in the standard model can have three colors: red, blue, or green.[5] The quarks are not really colored, but the use of color is a convenient way to conceptualize the idea of generalized charges for quarks. QCD describes the interactions between colored quarks. The characteristic feature of this color force is that it increases linearly with distance. For example, as a quark is pulled out of a hadron, the force of the gluons between it and the remaining quarks increases until enough energy is available to create a quark-antiquark pair from the vacuum. The new quarks then pair off with the original quarks to create new hadrons.

Therefore, it is impossible to isolate a single quark because nature creates more quarks to make new hadrons. This property of QCD is called confinement. On the other hand, pushing quarks together in a hadron decreases the force between them.

[5]These colors are arbitrary and actually stand for three different strong charges.

Boson	Mass (GeV/c^2)	Charge	Spin
g	0	0	1
$W^{\pm}$	80.419±0.056	±1	1
Z	91.188±0.002	0	1
γ	0	0	1
G	0	0	2

Table 1.5: Basic properties of the gauge bosons. These numbers and limits are from the 2000 European Physical Journal C [2]. The electric charges are given in units of proton charge and the spins are given in units of $\hbar$.

Eventually, as the quarks keep getting closer together, the coupling goes to zero and the quarks start to behave as free particles. This is called asymptotic freedom.

This color property also explains the way quarks combine to form hadrons, which are strongly interacting particles with no net strong charge. For example, if we were to combine red, blue, and green, we would produce a neutral color. It appears that all hadrons are color neutral or colorless states. Therefore, all baryons must have one red, one blue and one green quark. Antiquarks have anticolor. So mesons have one colored quark and one anticolored quark which produces a colorless state as well.

In any strong interaction, the number and type - up, down, charm, etc. - of quarks must be the same before and after the interaction. This law is known as baryon conservation. It is this conservation law in hadron interactions that is responsible for the stability of the proton. Experimentally, the proton is the lightest baryon because it cannot decay into anything that carries away its baryonic charge.

The Electroweak theory combines the interactions of the γ, $W^{\pm}$ and Z^0 into a unified interaction. The photon couples to the electric charge of particles and the force it produces between particles decreases with distance. Therefore, it has the capability to produce long range or macroscopic forces. As opposed to this, the weak interactions are short range and can only be detected on nuclear distance scales through the decay of particles. The role of the charged weak bosons is to transmute

quarks into other quarks and leptons into other leptons.

The reason for the short range interactions of the W and Z bosons is that they are massive unlike other gauge bosons. The difference in masses between the photon and the weak bosons comes about through the mechanism of spontaneous symmetry breaking. The original electroweak symmetry puts the four components or gauge fields on equal footing (e.g. all the fields have the same mass). It then introduces a spin zero massive particle called the Higgs boson or Higgs field.

This field with its stable solutions interacts with the other fields which produce solutions in which the symmetry is broken. It is this symmetry breaking mechanism that provides masses to the W and Z but keeps the photon massless. So although the underlying theory is symmetrical, its manifestation in the real world does not preserve the symmetry. Currently, the Higgs boson has not been experimentally detected.

1.2 Thesis Overview

The outline of this thesis is as follows. Chapter 2 discusses the theoretical framework for $W\gamma$ and $Z\gamma$ production. Chapter 3 discusses the Tevatron Collider and the B0 detector at Fermilab. Chapter 4 discusses the muon data set, selection and background. Chapter 5 discusses the electron data set, selection and background. Chapter 6 discusses the $V + \gamma$ data sets, selections and backgrounds. Chapter 7 discusses the detector efficiencies and acceptances. Chapter 8 discusses the analysis of the cross sections and cross section ratios. Chapter 9 discusses the conclusions and future prospects.

Chapter 2

Theory of $V + \gamma$ Production

2.1 Introduction

As discussed in Chapter 1, the standard model γ, W and Z gauge bosons are fundamental particles having no internal structure.[1] The gauge symmetry which generated the W and Z bosons severely constrains their couplings to each other.[2] Measuring processes that are sensitive to these couplings provides a test of the gauge theory. The processes that have been proposed are [3, 7]

$$p + \bar{p} \to W^{\pm} + \gamma + X \qquad W^{\pm} \to l^{\pm} + \nu_l \tag{2.1}$$

where X stands for any generic final state and the similiar process

$$p + \bar{p} \to W^{\pm} + X \qquad W^{\pm} \to l^{\pm} + \nu_l + \gamma \tag{2.2}$$

for the charged vector bosons and

$$p + \bar{p} \to Z + X \qquad Z \to l + \bar{l} + \gamma \tag{2.3}$$

for the neutral vector boson. Any deviation from the standard model predictions could signal the possibility that the W and Z are composite particles, or the possibility of new and unknown couplings. These processes are considered below.

[1] In this chapter, we take $\hbar = c = 1$.

[2] The gauge symmetry for W and Z bosons is non-Abelian. For example, $\vec{A} \times \vec{B} \neq \vec{B} \times \vec{A}$. This non-Abelian nature of the gauge bosons is the reason for the severe contraints.

2.2 W γ Production

At a $p\overline{p}$ collider, several processes can produce a W and γ in the final state. The tree-level Feynman diagrams for $W\gamma$ production are shown in Figure 2.1. The first two diagrams, Figures 2.1(a)-(b), are the u-channel and t-channel, respectively, and are associated with initial-state radiation from one of the incoming quarks. Figure 2.1(c) represents the s-channel decay and is the most interesting because it contains the trilinear gauge coupling or vector boson self-interaction. Figure 2.1(d) represents final state or inner bremsstrahlung and is known as radiative W decay.

The vertex function for $q\bar{q}^{'} \rightarrow W^{\pm}\gamma$ production is given by [4]

$$\begin{aligned} , ^{\alpha\beta\mu}(q_1, q_2, P) &= f_1(q_1 - q_2)^{\mu} g^{\alpha\beta} - \frac{f_2}{M_W^2}(q_1 - q_2)^{\mu} P^{\alpha} P^{\beta} \\ &+ f_3(P^{\alpha} g^{\mu\beta} - P^{\beta} g^{\mu\alpha}) + i f_4(P^{\alpha} g^{\mu\beta} + P^{\beta} g^{\mu\alpha}) \\ &+ i f_5 \epsilon^{\mu\alpha\beta\rho}(q_1 - q_2)_{\rho} - f_6 \epsilon^{\mu\alpha\beta\rho} P_{\rho} \\ &- \frac{f_7}{M_W^2}(q_1 - q_2)^{\mu} \epsilon^{\alpha\beta\rho\sigma} P_{\rho}(q_1 - q_2)_{\sigma} \end{aligned} \tag{2.4}$$

where q_1 and q_2 are the momenta of the outgoing W boson and γ (Lorentz indicies α and β, respectively), P is the momentum of the incoming W boson (Lorentz index μ), M_W is the mass of the W boson and the f_i are form factors which are invariant and dimensionless functions of q_1^2, q_2^2 and P^2.

Another, more convenient description, can be given by the effective Lagrangian.[3] The most general effective Lagrangian, with anomalous couplings, that preserves Lorentz and electromagnetic gauge invariance is given by [6]

$$\begin{aligned} \mathcal{L}_{WW\gamma} &= -ie\Bigg[W_{\mu\nu}^{\dagger} W^{\mu} A^{\nu} - W_{\mu}^{\dagger} A_{\nu} W^{\mu\nu} + \kappa\, W_{\mu}^{\dagger} W_{\nu} F^{\mu\nu} + \frac{\lambda}{M_W^2} W_{\lambda\mu}^{\dagger} W_{\nu}^{\mu} F^{\prime\nu\lambda} \\ &\quad + \tilde{\kappa}\, W_{\mu}^{\dagger} W_{\nu} F^{\prime\mu\nu} + \frac{\tilde{\lambda}}{M_W^2} W_{\lambda\mu}^{\dagger} W_{\nu}^{\mu} F^{\prime\nu\lambda}\Bigg] \end{aligned} \tag{2.5}$$

[3] One reason for this is that the Feynman rules are directly read from the effective Lagrangian as opposed to taking functional derivatives of the vertex function with respect to the fields to obtain them.

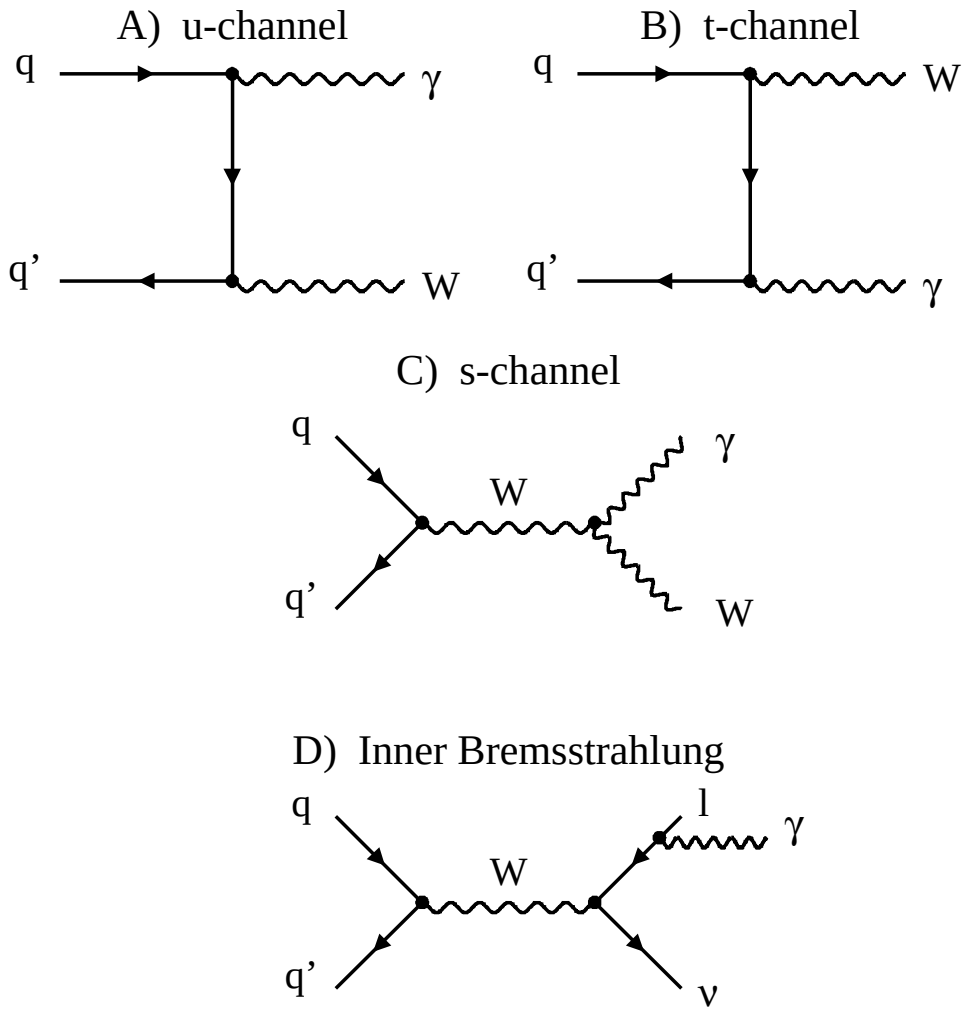

Figure 2.1: Tree-level diagrams for $W\gamma$ production. Diagrams (A)-(B) represent initial-state radiation from the incoming quarks. Diagram (C) represents direct $W+\gamma$ production and contains the vector boson self-interaction. Diagram (D) represents final state radiation or inner bremsstrahlung from the lepton and is known as radiative W decay.

where A^μ and W^μ are the photon and W^- fields, respectively, e is the charge of the proton, $W_{\mu\nu} = \partial_\mu W_\nu - \partial_\nu W_\mu$, $F_{\mu\nu} = \partial_\mu A_\nu - \partial_\nu A_\mu$ and $F'_{\mu\nu} = \frac{1}{2}\epsilon_{\mu\nu\rho\sigma}F^{\rho\sigma}$ where $F_{\mu\nu}$ is the electromagnetic field tensor. The photon is taken to be on-shell and both the virtual and on-shell W couple to essentially massless fermions allowing $\partial_\mu W^\mu = 0$.

The variables $\Delta\kappa = \kappa - 1$, λ, $\tilde{\kappa}$ and $\tilde{\lambda}$ are dimensionless form factors[4] generically written as a_f, where f is a label corresponding to the four anomalous couplings. These momentum dependent variables can be written as [6]

$$a_f(P^2 = \hat{s}, q_1^2 = M_W^2, q_2^2 = 0) = \frac{a_0}{(1 + \hat{s}/\Lambda_W^2)^n} \tag{2.6}$$

where a_0 is a dimensionless constant (e.g. $\kappa_0 - 1, \lambda_0, \tilde{\kappa}_0$ and $\tilde{\lambda}_0$), $\hat{s}$ is the center of mass energy and Λ_W is the scale of energy where new physics becomes important in the weak boson sector due to a composite structure of the W boson. The tree-level standard model predictions for the values of the momentum dependent form factors are $\Delta\kappa = \kappa - 1 = \lambda = \tilde{\kappa} = \tilde{\lambda} = 0$. The behavior of these generalized dipole form factors is shown in Figure 2.2 as a function of Λ_W for different values of the exponent $(n = 1, 2, 3, 4)$ and a center of mass energy of $\hat{s} = M_W = 80.2$ GeV.

Because the incoming W boson has an angular momentum $J = 1$, only four parameters are necessary to describe the $W\gamma$ anomalous vertex due to conservation of angular momentum. The four helicity[5] combinations of the outgoing bosons allowed are $(\beta_\gamma, \beta_W) = (-1, 1), (1, -1), (-1, 0)$ and $(1, 0)$. The two states $(-1, -1)$ and $(1, 1)$ are not allowed because they give a value of $J = 2$ to the incoming W boson. The above helicity combinations are shown graphically in Figure 2.3.

In the static limit, where the photon energy goes to zero, the anomalous couplings can be related to classical electromagnetic multipole moments of the W boson by [6]

$$\mu_W = \frac{e}{2M_W}(2 + \Delta\kappa + \lambda) \tag{2.7}$$

$$Q_W^e = -\frac{e}{M_W^2}(1 + \Delta\kappa - \lambda) \tag{2.8}$$

[4]Strictly speaking, the form factors in the effective Lagrangian are the low energy expansions of the full form factors in the vertex function[5].

[5]The definition of helicity for a particle is $\beta = (\mathbf{J} \cdot \mathbf{p})/ \mid \mathbf{p} \mid$.

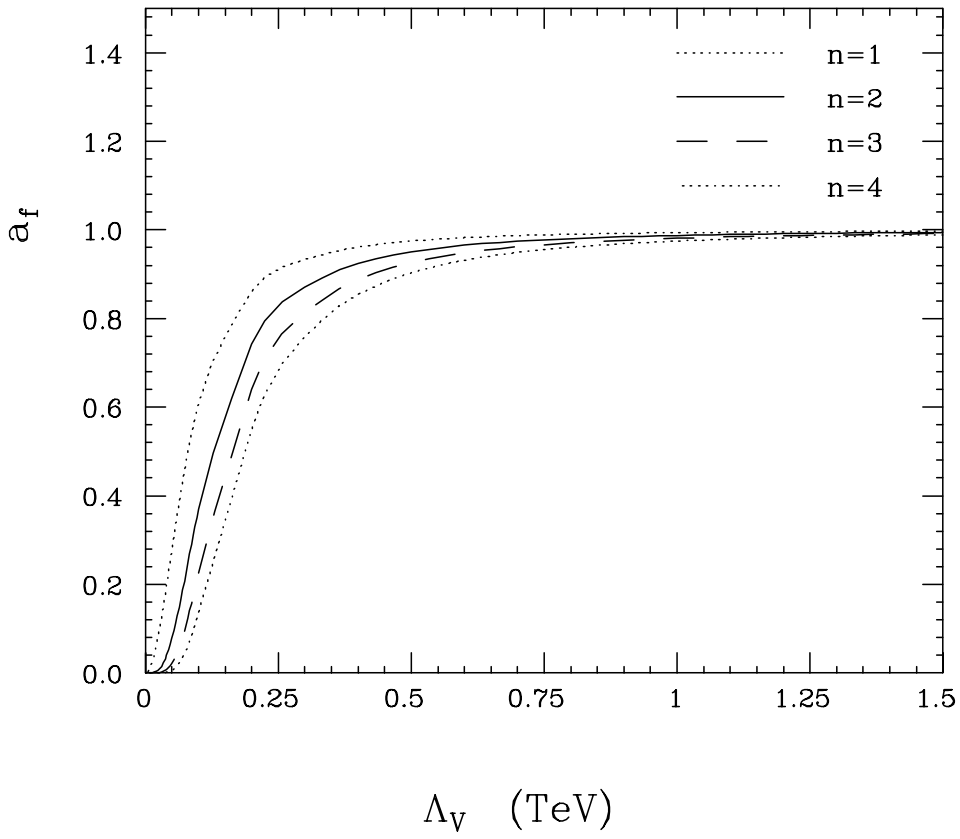

Figure 2.2: Behavior of the generalized dipole form factors as a function of Λ_V ($V = W, Z$), the scale of energy where new physics becomes important in the weak boson sector, for different values of the exponent ($n = 1, 2, 3, 4$) and center of mass energy of $\hat{s} = M_W = 80.2$ GeV. The generic structure function label, a_f, stands for the four anomalous couplings: $a_1 = \kappa - 1, a_2 = \lambda, a_3 = \tilde{\kappa}$ and $a_4 = \tilde{\lambda}$.

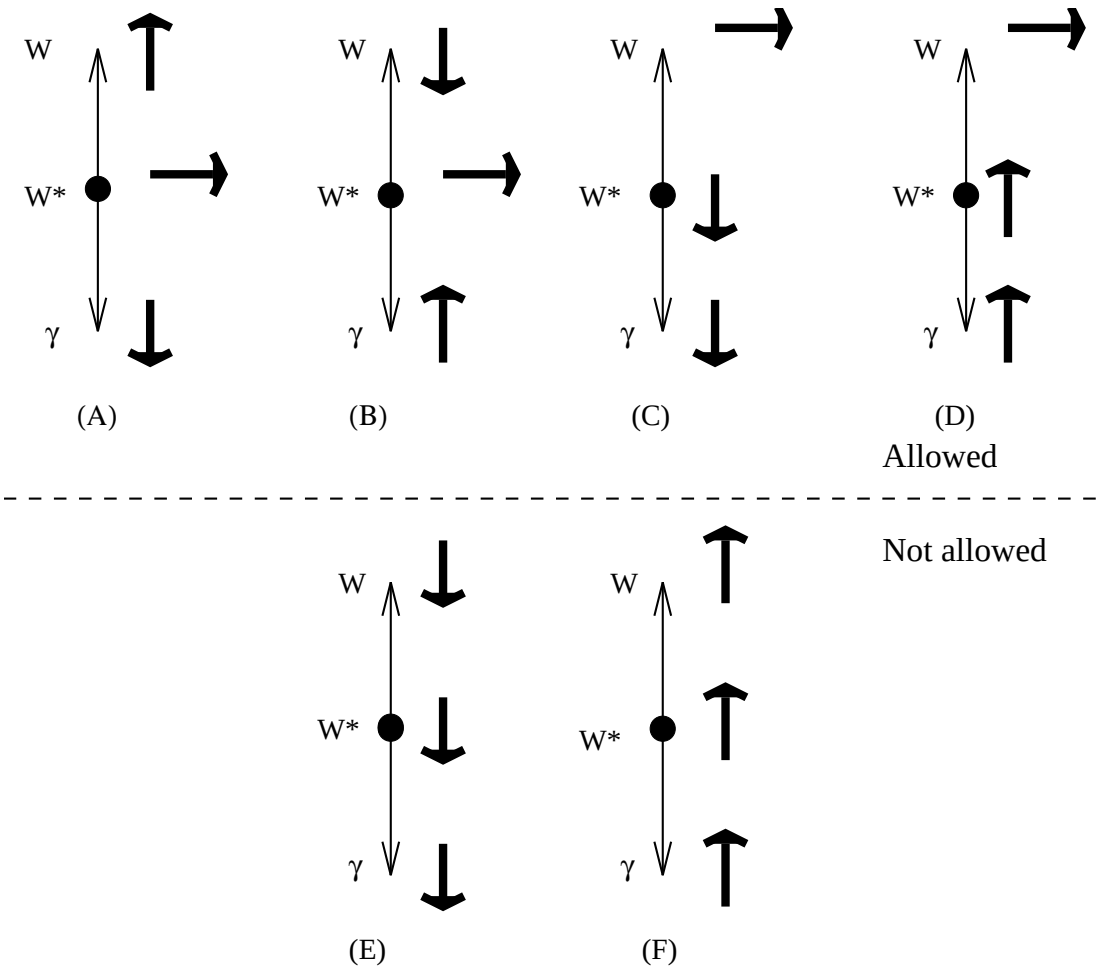

Figure 2.3: The possible helicity states for $W\gamma$ production. The $W^{\star}$ represents an off-shell W boson. The top diagrams (A)-(D) are the allowed helicity combinations, $(\beta_{\gamma}, \beta_{W})$, of the outgoing bosons corresponding to states (-1,1), (1,-1), (-1,0) and (1,0). The bottom diagrams (E)-(F) correspond to the states (-1,-1) and (1,1). They are not allowed because they give a value $J = 2$ to the W boson.

$$d_W^e = \frac{e}{2M_W}(\tilde{\kappa} + \tilde{\lambda}) \tag{2.9}$$

$$Q_W^m = -\frac{e}{M_W^2}(\tilde{\kappa} - \tilde{\lambda}) \tag{2.10}$$

where μ_W is the magnetic dipole moment, Q_W^e is the electric quadrupole moment, d_W^e is the electric dipole moment and Q_W^m is the magnetic quadrupole moment. One

can also relate the mean squared charge radius of the W boson to the anomalous couplings by

$$< R_W^2 >= \frac{1}{M_W^2}(1 + \Delta\kappa + \lambda). \tag{2.11}$$

The sign associated with these quantities indicates their orientation relative to the spin direction.

For an electrically charged spin-**1** particle, $2(\mathbf{1}) + 1 = 3$ $\mathcal{CP}$ conserving[6] electromagnetic moments are allowed [8]. Therefore, the $W^{\pm}$ vector boson is expected to have a magnetic dipole moment and an electric quadrupole moment. All four anomalous couplings are $\mathcal{C}$-even, but $\tilde{\kappa}$ and $\tilde{\lambda}$ are odd under $\mathcal{P}$ while κ and λ are even under $\mathcal{P}$. Therefore, κ and λ are $\mathcal{CP}$ conserving and $\tilde{\kappa}$ and $\tilde{\lambda}$ are $\mathcal{CP}$ violating.

The $W\gamma$ processes shown in Figure 2.1 are produced with different kinematics. For initial-state radiation, the radiation tends to peak along the initial direction of the quark/antiquark. The final state bremsstrahlung tends to peak around the decay lepton. However, in contrast to these two processes, the photons from s-channel or direct $W + \gamma$ production are not correlated with the incoming quarks or decay lepton. All three of these processes produce a photon transverse energy spectrum[7], E_T^{γ}, sharply peaked at low transverse energy and which falls steeply with increasing E_T^{γ}.

Because of the finite width of the W boson, the $W\gamma$ Feynman diagrams cannot be separated and the calculation of the $W\gamma$ cross section must coherently add all the $W\gamma$ amplitudes together to preserve electromagnetic gauge invariance. An interesting consequence of this calculation is that at large photon scattering angles Θ^* in the $W\gamma$ center of mass, where Θ^* is defined as the angle between the photon and the incoming quark, the $u-$ and $t-$channel diagrams interfere destructively with the s-channel diagram. For $cos\,\Theta^* = \mp 1/3$ the differential cross section $d\hat{\sigma}/d(cos\,\Theta^*)$ for $W^{\pm}\gamma$ production goes to zero [3]. This is known as a radiation amplitude zero.

[6] $\mathcal{C}$ stands for the discrete operator of charge conjugation and $\mathcal{P}$ stands for the discrete operation of parity.

[7] The transverse energy of a particle is defined in Chapter 3.

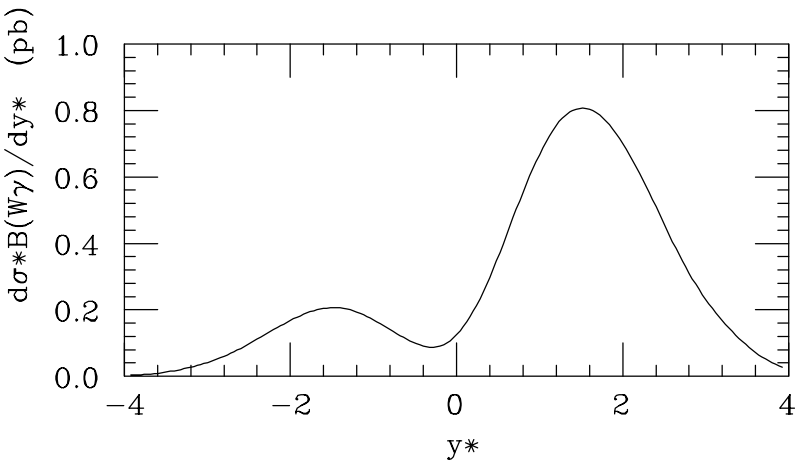

Figure 2.4: The $W\gamma$ differential cross section as a function of the charged-signed rapidity difference, $y^\star = Q_W \cdot (\eta_\gamma - \eta_l)$, where Q_W is the charge of the W boson, η_γ is the rapidity of the photon and η_l is the rapidity of the lepton from the decay of the W boson. The dip that occurs at $y^\star = -1/3$ corresponds to the radiation amplitude zero.

Direct observation of this radiation amplitude zero in the cross section is difficult, and is expected to be partially filled in due to event misreconstruction of the $W\gamma$ rest frame, the two-fold ambiguity of the longitudinal momentum of the neutrino, background processes, higher order QCD corrections and structure function effects. Fortunately, the radiation amplitude zero can be observed in the charged-signed rapidity difference distribution of the $W\gamma$ system in the lab frame, where the rapidity difference is between the photon and decay lepton and that is multiplied by the charge of the W boson or decay lepton [9]. This distribution is shown in Figure 2.4.

All $W\gamma$ kinematic distributions are sensitive to anomalous couplings, but the most sensitive is the photon transverse energy spectrum with the shape and slope of the spectrum being the steepest for standard model values of the couplings [3]. The photon spectrum for different values of anomalous couplings is shown in Figure 2.5 and it shows that the presence of anomalous couplings, with positive or negative

values, will produce an excess of high E_T photons. Limits on the anomalous couplings can be extracted by fitting this spectrum.

In Figure 2.6, we show the lepton-photon separation for $W\gamma$ production with different values of anomalous couplings. Radiative events have small lepton-photon separation and little sensitivity to anomalous couplings. Events with larger lepton-photon separation are from s-channel $W\gamma$ production and are more sensitive to anomalous couplings. The presence of anomalous couplings would produce an excess of $W\gamma$ events with a large lepton-photon separation.

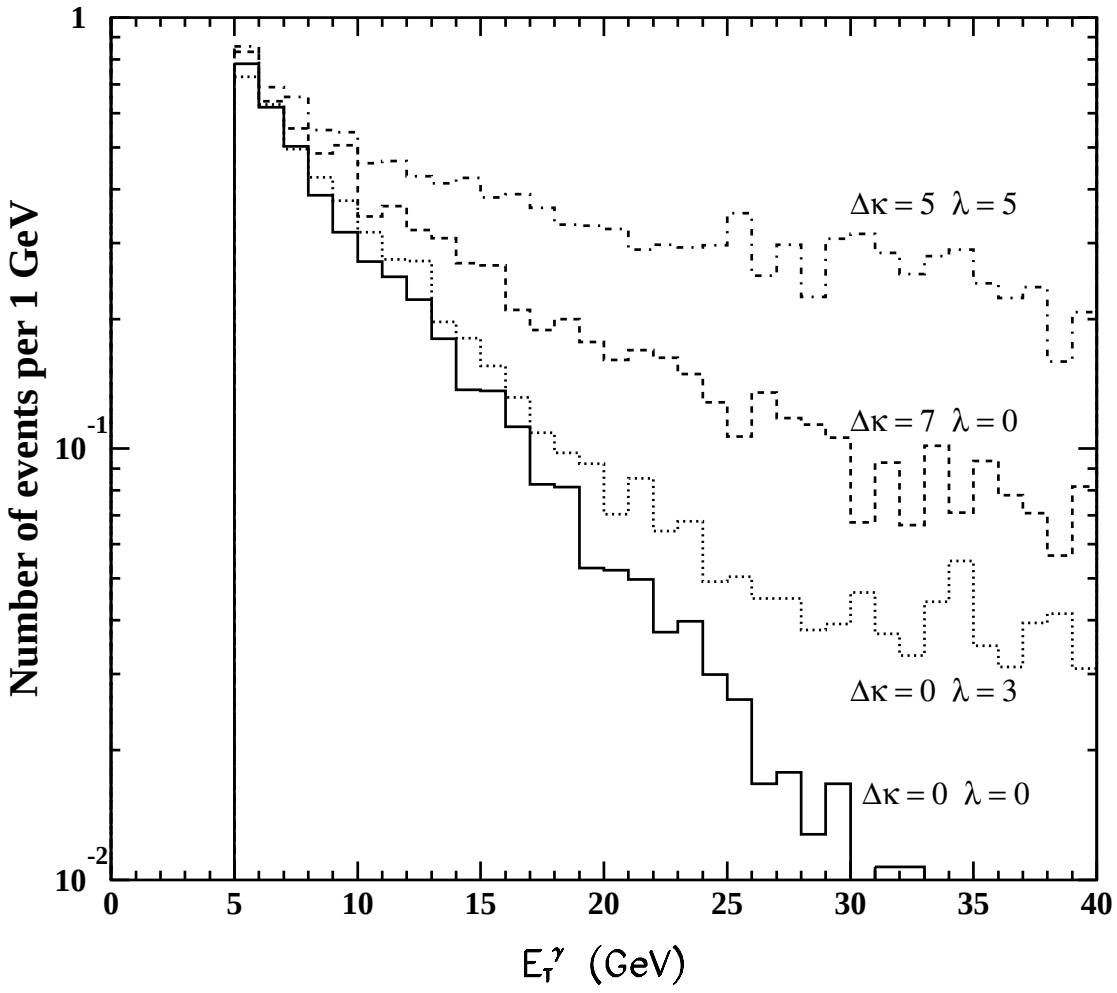

Figure 2.5: The photon E_T spectrum in $W\gamma$ production for different values of anomalous couplings. The shape and slope of the spectrum is steepest for the standard model values of the anomalous couplings. Any anomalous couplings produce an excess of photons with a high transverse energy.

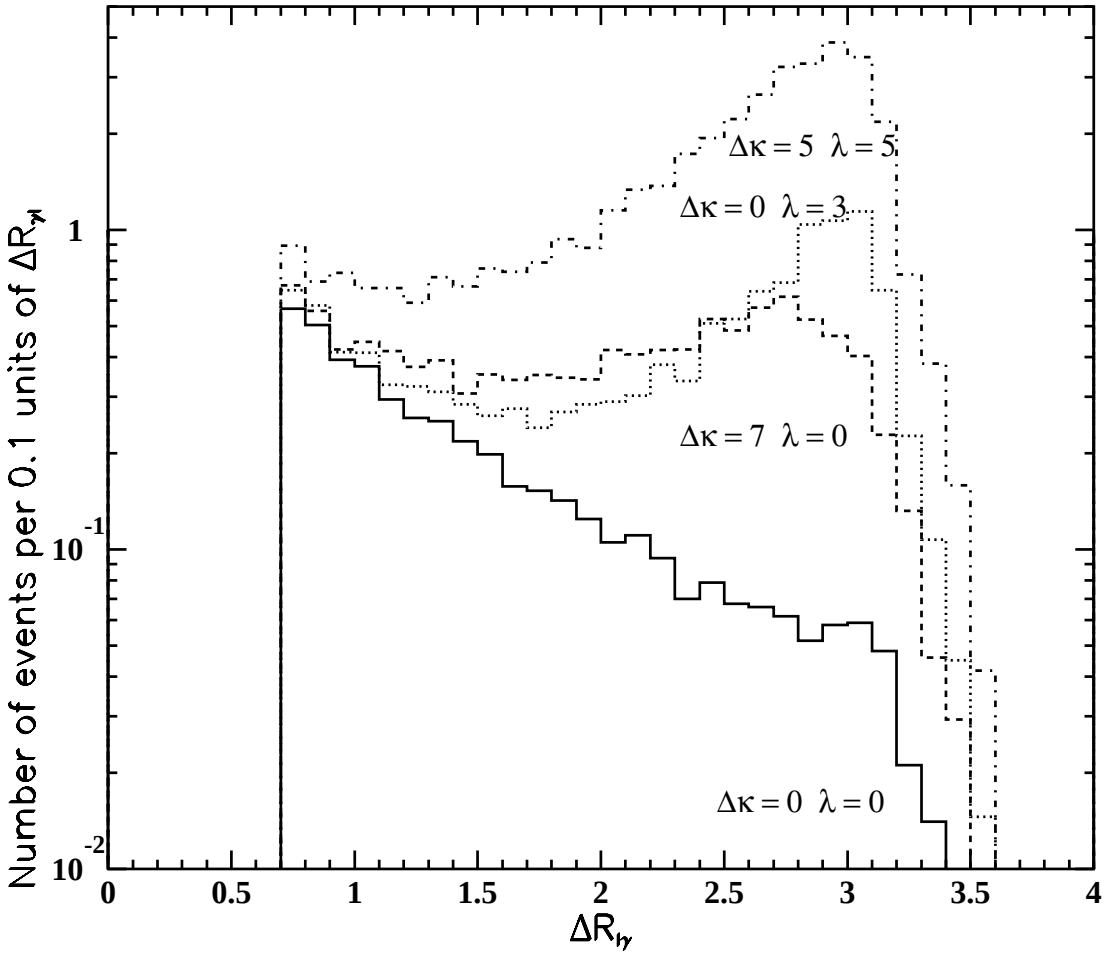

Figure 2.6: The lepton-photon separation in $W\gamma$ production for different values of anomalous couplings. Radiative events populate the smaller lepton-photon region and s-channel production populate the higher lepton-photon region. Any anomalous couplings produce an excess of events with large lepton-photon separation.

2.3 Z γ Production

The tree-level Feynman diagrams for Zγ production are shown in Figure 2.7. The first two diagrams, Figures 2.7(a)-(b), are the u- and t-channel, respectively, and represent initial state radiation from the incoming quark/antiquark. Figure 2.7(c) represents final state radiation or inner bremsstrahlung from either final state lepton. Figure 2.7(d) represents anomalous contributions from $Z\gamma Z$ and $Z\gamma\gamma$ couplings and does not occur in the standard model.

The most general $Z\gamma Z$ vertex function allowed by electromagnetic gauge invariance can be written as [7]

$$
\begin{aligned}
, {}^{\alpha\beta\mu}_{Z\gamma Z}(q_1, q_2, P) &= \left(\frac{P^2 - q_1^2}{M_Z^2}\right)\left[h_1^Z(q_2^\mu g^{\alpha\beta} - q_2^\alpha g^{\mu\beta}) + \frac{h_2^Z}{M_Z^2}P^\alpha(P\cdot q_2 g^{\mu\beta} - q_2^\mu P^\beta)\right. \\
&+ \left. h_3^Z \epsilon^{\mu\alpha\beta\rho} q_{2\rho} + \frac{h_4^Z}{M_Z^2}P^\alpha \epsilon^{\mu\beta\rho\sigma} P_\rho q_{2\sigma}\right] \qquad (2.12)
\end{aligned}
$$

where q_1 and q_2 are the momenta of the outgoing Z boson and γ (Lorentz indicies α and β, respectively), P is the momentum of the incoming Z boson (Lorentz index μ), M_Z is the mass of the Z boson and the h_i^Z are form factors.

The most general anomalous $Z\gamma\gamma$ vertex function can be obtained from the $Z\gamma Z$ vertex function by replacing [7]

$$\frac{P^2 - q_1^2}{M_Z^2} \to \frac{P^2}{M_Z^2} \qquad (2.13)$$

and

$$h_i^Z \to h_i^\gamma \quad i = 1 - 4. \qquad (2.14)$$

The form factors h_i^V, where $V = Z, \gamma$ and $i = 1 - 4$, are dimensionless functions that are taken to have the generalized dipole form [7]

$$h_i^V(P^2 = \hat{s}, q_1^2 = M_Z^2, q_2^2 = 0) = \frac{h_{i0}^V}{(1 + \hat{s}/\Lambda_Z^2)^n} \qquad (2.15)$$

where $\hat{s}$ is the center of mass energy and Λ_Z is the scale of energy where the new physics becomes important in the weak boson sector due to a composite structure of the Z boson. The tree-level standard model predictions for all h_{i0}^V vanish.

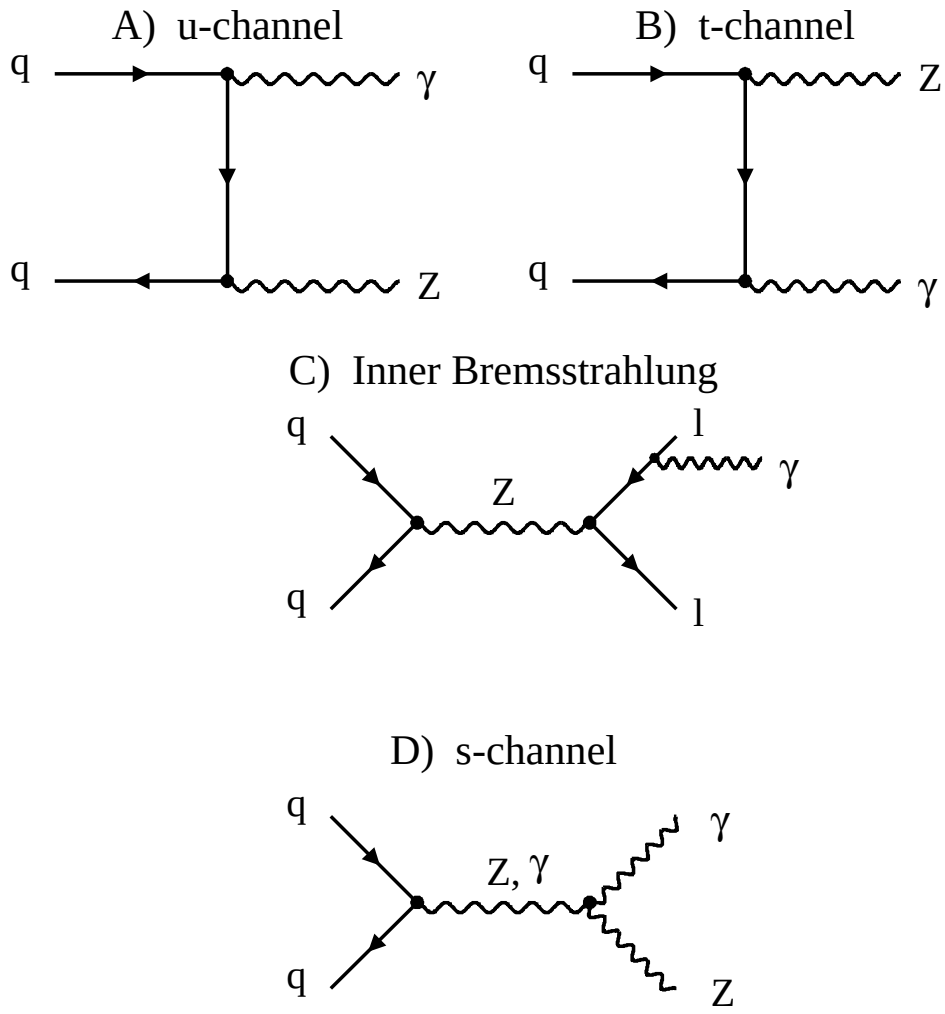

Figure 2.7: Tree-level diagrams for $Z\gamma$ production. Diagrams (A) and (B) represent initial state radiation from the incoming quarks. Diagram (C) represents final state radiation or inner bremsstrahlung from one of the final state leptons. Diagram (D) does not occur in the standard model and represents contributions from anomalous couplings.

Only four parameters are needed to describe the $Z\gamma$ anomalous vertex because the Z boson has a spin of $J = 1$. In the standard model the Z boson is a Majorana particle, which means it is its own antiparticle, and thus cannot have any static electromagnetic moments. Basically, the Z cannot couple directly to the photon because it does not carry electric charge. However, the possibility of transition EM moments exist for nonstandard model $Z\gamma$ couplings. In the static limit, the expressions for the Z transition moments are given by [10]

$$d_{Z_T} = -\frac{e}{M_Z}\frac{1}{\sqrt{2}}\frac{k^2}{M_Z^2}(h_{30}^Z - h_{40}^Z) \quad (2.16)$$

$$Q_{Z_T}^m = \frac{e}{M_Z^2}\sqrt{10}(2h_{30}^Z) \quad (2.17)$$

$$\mu_{Z_T} = -\frac{e}{M_Z}\frac{1}{\sqrt{2}}\frac{k^2}{M_Z^2}(h_{10}^Z - h_{20}^Z) \quad (2.18)$$

$$Q_{Z_T}^e = \frac{e}{M_Z^2}\sqrt{10}(2h_{10}^Z) \quad (2.19)$$

where d_{Z_T} is the electric dipole transition moment, $Q_{Z_T}^m$ is the quadrupole transition moment, μ_{Z_T} is the magnetic dipole transition moment, $Q_{Z_T}^e$ is the electric quadrupole transition moment and k is the energy of the photon, with an exponent related to the Bose prefactor of the vertex function.[8]

All four anomalous couplings are $\mathcal{C}$-odd. The couplings h_{30}^V and h_{40}^V are $\mathcal{P}$-odd and h_{10}^V and h_{20}^V are $\mathcal{P}$-even. Therefore, h_{30}^V and h_{40}^V are $\mathcal{CP}$ conserving and h_{10}^V and h_{20}^V are $\mathcal{CP}$ violating.

Similiar to $W\gamma$, the $Z\gamma$ processes shown in Figure 2.7 are produced with different kinematics. For initial-state radiation, the radiation is peaked along the initial direction of the quark/antiquark. The final state bremsstrahlung will be peaked around the decay leptons. These two processes produce a photon transverse energy spectrum, E_T^γ, sharply peaked at low transverse energy that falls with increasing E_T^γ. Because Figure 2.7(d) does not contribute in the standard model, there is no cancellation between the $u-$ and t-channel diagrams to produce a radiation amplitude zero. Therefore, the E_T^γ spectrum in $Z\gamma$ events does not fall as steeply as the $W\gamma$

[8]These expressions are all leading order in k with $k << M_Z$.

spectrum. The presence of anomalous couplings in $Z\gamma$ production would produce an excess of high E_T photons similiar to $W\gamma$ as shown in Figure 2.5.

2.4 Unitarity

Unitarity is another name for conservation of probability. Any cross section can be expanded in terms of partial waves [12]. From phase relationships of these waves, bounds can be set on their amplitudes which translate into bounds on the total cross section from the optical theorem relation.

Anomalous contributions to $W\gamma$ production in terms of partial wave helicity amplitudes, represented by $\Delta\mathcal{M}_{\beta_\gamma \beta_W}$, can be written as [11]

$$\Delta\mathcal{M}_{\pm 0} = \frac{e^2}{\sin\theta_W}\frac{\sqrt{\hat{s}}}{2M_W}\left[\Delta\kappa + \lambda \mp i(\tilde{\kappa}+\tilde{\lambda})\right]\frac{1}{2}(1 \mp \cos\Theta) \tag{2.20}$$

$$\Delta\mathcal{M}_{\pm\pm} = \frac{e^2}{\sin\theta_W}\frac{1}{2}\left[\frac{\hat{s}}{M_W^2}(\lambda \mp i\tilde{\lambda}) + (\Delta\kappa \mp i\tilde{\kappa})\right]\frac{1}{\sqrt{2}}\sin\Theta \tag{2.21}$$

where Θ is the scattering angle of the photon with respect to the quark direction.

One can see the contributions grow like $(\sqrt{\hat{s}}/M_W)$ and $(\sqrt{\hat{s}}/M_W)^2$. For energies $\sqrt{\hat{s}} >> \Lambda >> M_W$ these terms will dominate over standard model contributions and give infinite contributions at very high energies violating unitarity. This behavior is considered unphysical.

In order to rectify this situation, it is necessary to introduce structure functions that will control these contributions at high energies. The expected behavior of these structure functions is flat for energies below Λ_W and then fall off as the scale Λ_W is reached [6]. This behavior is similiar to the nucleon form factor which is what motivated the generalized dipole form.[9]

The unitary bounds for $WW\gamma$ with anomalous couplings, assuming one coupling is non-zero at a time and $\sqrt{\hat{s}} >> \Lambda_W >> M_W$, are found to be [11]

$$|\,\kappa_0 - 1\,| \;<\; \frac{n^n}{(n-1)^{n-1}}\frac{1.81\,\mathrm{TeV}^2}{\Lambda_W^2} \tag{2.22}$$

[9]The form factor is the Fourier transform of the charge distribution.

$$| \tilde{\kappa}_0 | < \frac{(2n)n^n}{(2n-1)^{n-\frac{1}{2}}} \frac{11.5\,\mathrm{TeV}}{\Lambda_W} \tag{2.23}$$

$$| \lambda_0 |, | \tilde{\lambda}_0 | < \frac{n^n}{(n-1)^{n-1}} \frac{0.96\,\mathrm{TeV}^2}{\Lambda_W^2} \tag{2.24}$$

Solving for the values of n in the denominators which prevent them from being zero or negative shows that a minimum value of $n = 1/2(1)$ ensures that $W\gamma$ production is suppressed at energies $\sqrt{\hat{s}} >> \Lambda_W >> M_W$. Therefore, the standard choice $n = 2$ gaurentees unitarity is preserved.

Similiarly, the unitary bounds for $Z\gamma Z$ using partial wave helicity amplitudes, assuming one coupling is non-zero at a time and $\sqrt{\hat{s}} >> \Lambda_Z >> M_Z$, can be written as [7]

$$| h_{10}^Z |, | h_{30}^Z | < \frac{(\frac{2n}{3})^n}{(\frac{2n}{3}-1)^{n-\frac{3}{2}}} \frac{0.126\,\mathrm{TeV}^3}{\Lambda_Z^3} \tag{2.25}$$

$$| h_{20}^Z |, | h_{40}^Z | < \frac{(\frac{2n}{5})^n}{(\frac{2n}{5}-1)^{n-\frac{5}{2}}} \frac{2.1 \cdot 10^{-5}\,\mathrm{TeV}^5}{\Lambda_Z^5} \tag{2.26}$$

These bounds show that for $n > 3/2$ for $h_{1,3}^V$ and $n > 5/2$ for $h_{2,4}^V$ unitarity is preserved and the high energy behavior is well-behaved for anomalous contributions that grow like $(\sqrt{\hat{s}}/M_Z)^3$ for $h_{1,3}^V$ and $(\sqrt{\hat{s}}/M_Z)^5$ for $h_{2,4}^V$. One can see the growth of the anomalous contributions is encoded into the exponential factor of the denominator.

Chapter 3

The Detector

3.1 Overview

The Collider Detector at Fermilab (CDF) is a 5000 ton magnetic spectrometer that has azimuthal symmetry as well as forward-backward symmetry [13]. The central part of the spectrometer is a movable 2000 ton detector consisting of tracking chambers, electromagnetic and hadron calorimeters, muon chambers and a solenodial magnet. The solenodial magnet is used for the momentum determination of charged particles. It is a 5 m long superconducting coil with a 3 m diameter that produces a uniform 1.5 T field oriented along the proton beam direction.

The proton beam direction defines the $+z$ direction of a right-handed coordinate system with the $+y$ axis pointing vertically upward and the $+x$ axis pointing radially outward from the beamline that is used at CDF. The CDF detector is shown in Figure 3.1. The detector was built to study 1.8 TeV center of mass $p\bar{p}$ collisions at the Fermilab Tevatron.

3.2 The Fermilab Tevatron and Accelerator Complex

The Fermilab Tevatron is a circular accelerator which collides protons and antiprotons at a center-of-mass energy of 1.8 TeV. It is the last stage of an acceleration process which begins with negative hydrogen ions.

These negative hydrogen ions are accelerated using a Cockroft-Walton accelerator

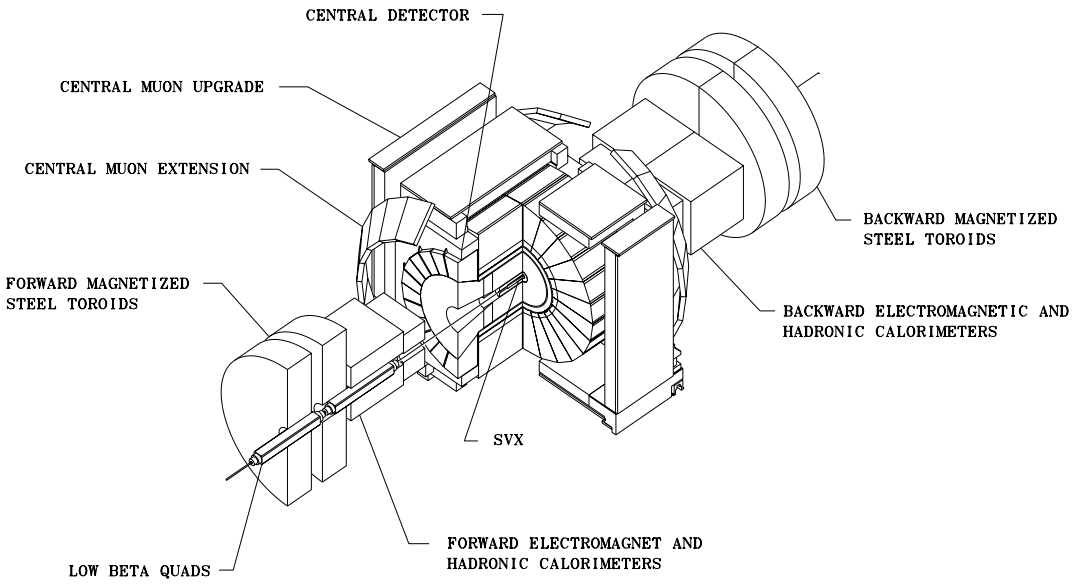

Figure 3.1: A three-dimensional cut away view of the CDF detector. This view shows the azimuthal as well as the forward-backward symmetry of the detector. Various parts of the detector are labeled and discussed in the text.

up to an energy of 750 KeV[1] and then passed through a carbon foil which strips off the orbital electrons. Then the remaining protons are accelerated in a linac up to 400 MeV, inserted into a small synchrotron ring, called the Booster Ring, and accelerated up to 8 GeV.

The protons are then injected into the Main Ring and accelerated up to 150 GeV. Some protons are extracted from this beam and strike a tungsten target creating antiprotons which are momentum selected around 8 GeV and focused with a lithium lens. The antiprotons are then transported from the lithium lens to the Debuncher. The Debuncher is a storage device which reduces the momentum spread of the antiprotons which are then transported to the Antiproton Accumulator ring.

The Antiproton Accumulator stores and accumulates the antiprotons and also

[1]It is common practice to state the numerical value of the energy without explicitly using the phrase "an energy of". We follow this practice in the discussion below to make it more fluid.

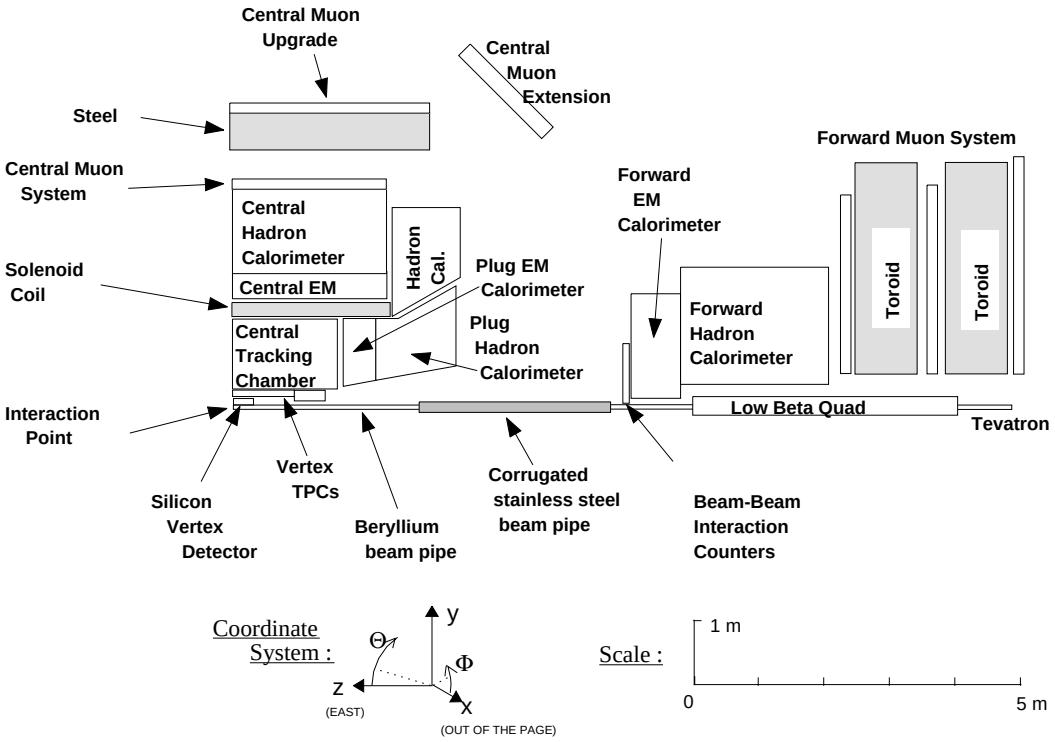

Figure 3.2: A single quadrant of the CDF detector. The coordinate system used by CDF is shown in the lower portion of the diagram with the z direction corresponding to the proton direction. All the detector components are labeled and the scale of the detector is set in the lower right-hand portion of the figure.

reduces their momentum spread by using the method of Stochastic Cooling, a process that uses a set of pick-ups, amplifiers and beam kickers.

When enough antiprotons are collected and cooled ($> 10^{11}$), they are injected back into the Main Ring and accelerated from 8 GeV to 150 GeV. Before the antiprotons are injected back into the Main Ring, six proton bunches are injected into the superconducting accelerator, known as the Tevatron, which sits just below the Main Ring.

Six antiproton bunches are now injected into the Tevatron and the two counter

rotating beams are accelerated up to 900 GeV. The focusing quadrupoles are slowly turned up to full power to obtain the maximum luminosity of 10^{32} cm^{-2}s^{-1}. The protons and antiprotons are then focused upon each other to promote collisions in the CDF detector also known as B0.

3.3 The B0 Detector

The CDF detector, also known as B0, is composed of several detector components. These components consist of various tracking chambers, electromagnetic calorimeters and muon chambers. As shown in Figure 3.2, the coordinate system is defined such that the z-axis points along the incoming proton direction. The polar angle θ is defined with respect to the z-axis with the origin of the coordinate system corresponding to the geometrical center of the detector. The detector pseudorapidity can now be defined as

$$\eta_D = -\log[\tan(\theta/2)] \tag{3.1}$$

The detector rapidity is used to label the location of the detector components.

3.3.1 Tracking

The CDF detector uses three different subdetectors to measure charged particle tracks and momentum. These three subdetectors are the Silicon Vertex Detector (SVX), the Vertex Time Projection System (VTX) and the Central Tracking Chamber (CTC).

SVX

The SVX is located directly outside the 1.9 cm radius beryllium beampipe [14]. It covers a radius from 2.86 to 7.87 cm. It is divided into two identical "barrels" which surround the beampipe at $z = 0$. Each barrel has a length of 25.5 cm giving an overall length of 51 cm allowing tracking to $\mid \eta_D \mid < 2.8$.

The SVX consists of four layers of silicon microstrips with a single hit resolution of $\sigma = 11$ μm. The radii of the four layers are 2.86, 4.26, 5.69 and 7.87 cm. The

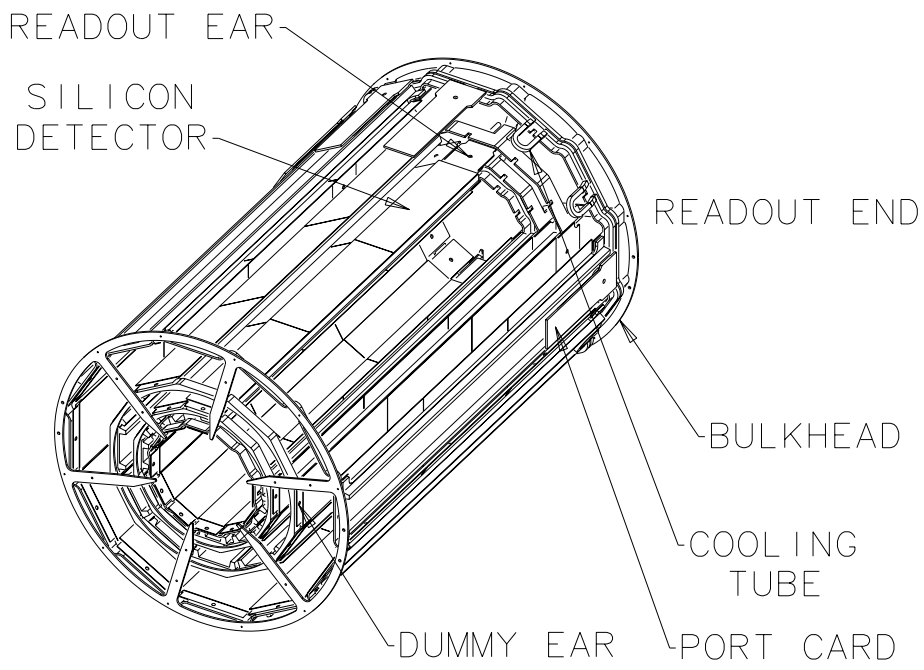

Figure 3.3: A three-dimensional diagram of a single SVX barrel. The barrel directly surrounds the beam pipe. The four layer structure is visible through the left-hand side bulkhead.

strips extend along the z direction and provide $r-\phi$ tracking information. The SVX gives the most precise tracking information of CDF's three tracking chambers, but it only covers 60% of the total possible z interaction region and therefore only used to reconstruct the mean $r-\phi$ of the $p\bar{p}$ store. Half of the SVX is shown in Figure 3.3.

VTX

The VTX consists of eight Vertex Time Projection Chambers (VTPC) that are positioned side by side along the beamline direction [15]. The VTX subtends a radius of 7 to 21 cm. It has an overall length of 2.8 m supplying tracking to $\mid \eta_D \mid < 3.2$. Because

the VTX surrounds the SVX, some modules are smaller in the radial direction.

The VTX is used to determine the primary event vertex (Z_{VTX}). It provides $r-z$ tracking information with a position resolution of $\sigma = 1$ mm and has the ability to identify multiple interactions in the same beam crossing.

CTC

The CTC is a cylindrical drift chamber covering a radius from 0.28 to 1.3 m [16]. It has a length of 3.2 m which allows momentum measurements in the region $\mid \eta_D \mid < 1.1$. The chamber consists of 84 layers of sense wires grouped into nine "superlayers", five axial layers and four stereo layers.

The axial superlayers have 12 radially separated sense wires all parallel to the z axis allowing a $r-\phi$ positional measurement. The stereo superlayers have six sense wires with a 3° stereo angle allowing a combination of $r-\phi$ and $r-z$ measurement. These two layers combined allow the formation of a three-dimensional track with momentum resolution of $\sigma(P_T)/P_T = [(0.0020P_T)^2 + (0.0066)^2]^{1/2}$ where P_T is given in GeV/c. A endview of this chamber is shown in Figure 3.4.

3.3.2 Calorimeters

Calorimeters are particle detection devices which intercept the primary particle and they are of sufficient thickness such that the primary particle interacts and deposits all of its kinetic energy inside the detector volume in a cascade or 'shower' of lower energy particles [17]. The detector signal is proportional to the initial kinetic energy of the particle. Nice features of calorimeters include that they are sensitive to charged and neutral particles, they have different responses to different types of particles and they can be segmented in order to determine the position and angle of the incident particle.

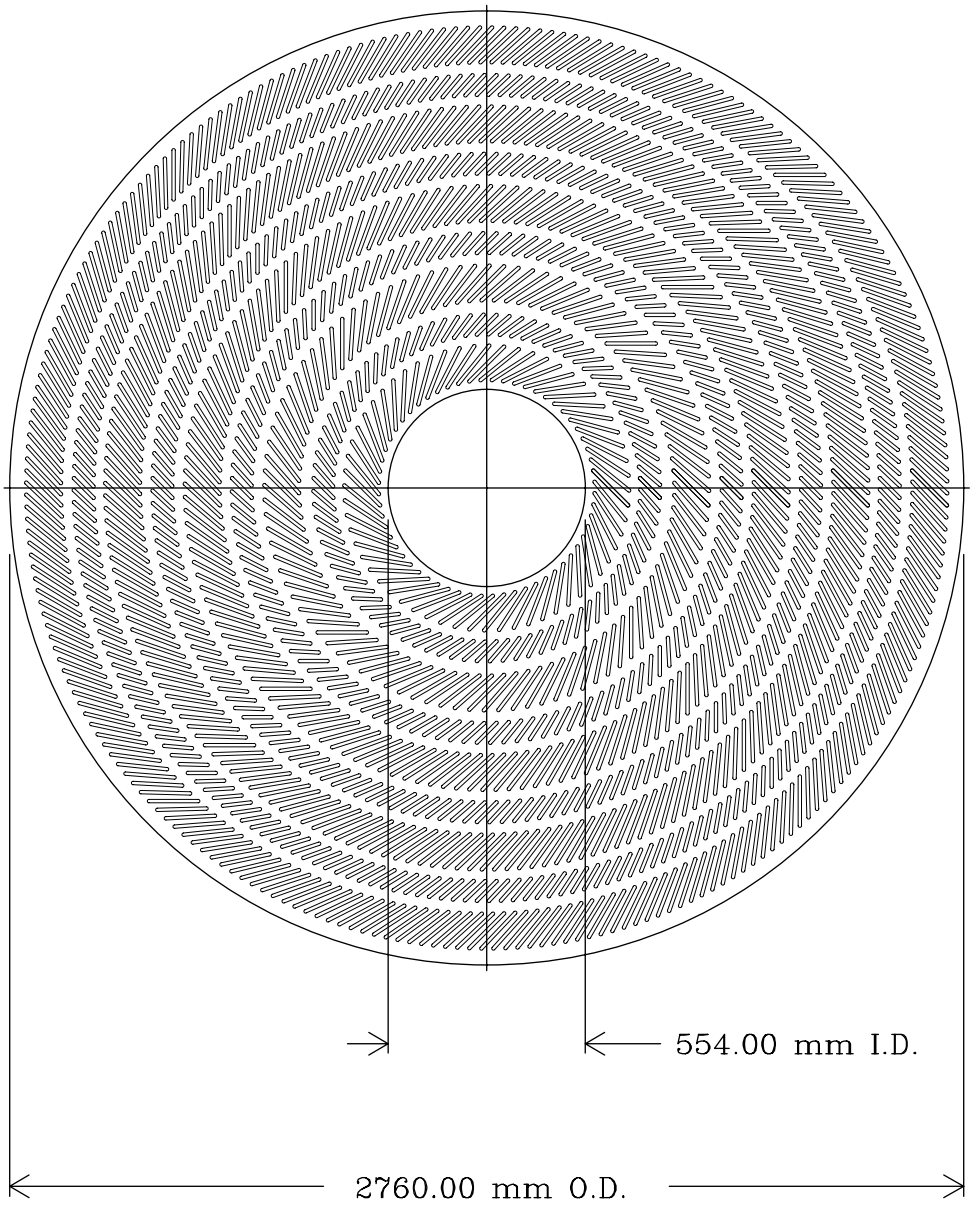

Figure 3.4: Diagram of the CTC endplate. The CTC has nine superlayers. Moving outward from the center, one crosses the superlayers starting with an axial superlayer. Passing further outward, the superlayers alternate between stereo and axial layers.

Electromagnetic Calorimeters

Central The central electromagnetic calorimeter (CEM) is a sampling calorimeter [18]. A sampling calorimeter measures the longitudinal energy deposition in a number of active layers with passive absorber layers interspersed between them.

The CEM is a hybrid design using a plastic scintillator with a wavelength shifter and an embedded strip chamber to measure the electromagnetic cascade. The scintillator is composed of 5 mm thick pieces of SCSN-38 polystyrene assembled to form ten projective towers in a calorimeter wedge. The strip chamber is a series of orthogonal metal strips and wires embedded at the depth corresponding to the maximum of the average transverse shower development and is used to determine the position of the shower at this location in calorimeter depth.

The passive absorber layers are pieces of lead covered with thin pieces of aluminum on each side. High energy electrons lose their energy through bremmstrahlung and photons through pair production in such material. The responses are different for the two particles and allows for particle identification. The CEM calorimeter covers the rapidity range $\mid \eta_D \mid < 1$ with an average energy resolution $\sigma(E)/E$ of $13.5\%/\sqrt{E \sin\theta}$ and position resolution of $\pm$ 2 mm at 50 GeV.

Plug The plug calorimeter (PEM) is a gas sampling calorimeter that allows for a high degree of segmentation [19]. Gas calorimeters work by using charge collection with some degree of internal amplification [17]. The plug calorimeter is 2.8 m in diameter and 50 cm deep with a round disk-shaped geometry. It is made with conductive plastic proportional tubes using lead as the passive absorber. It has full azimuthal coverage and rapidity range $1.1 < \mid \eta_D \mid < 2.4$. It has an energy resolution of $22\%/\sqrt{E \sin\theta}$ and angular resolution $\Delta\theta : 0.04^\circ$ and $\Delta\phi : 0.1^\circ$.

Forward The forward calorimeter (FEM) is also a gas sampling calorimeter [20]. It is located 6.5 m from the interaction point and encloses the beam pipe. It has 30 sampling layers and lead as the passive absorber. The proportional tubes are read

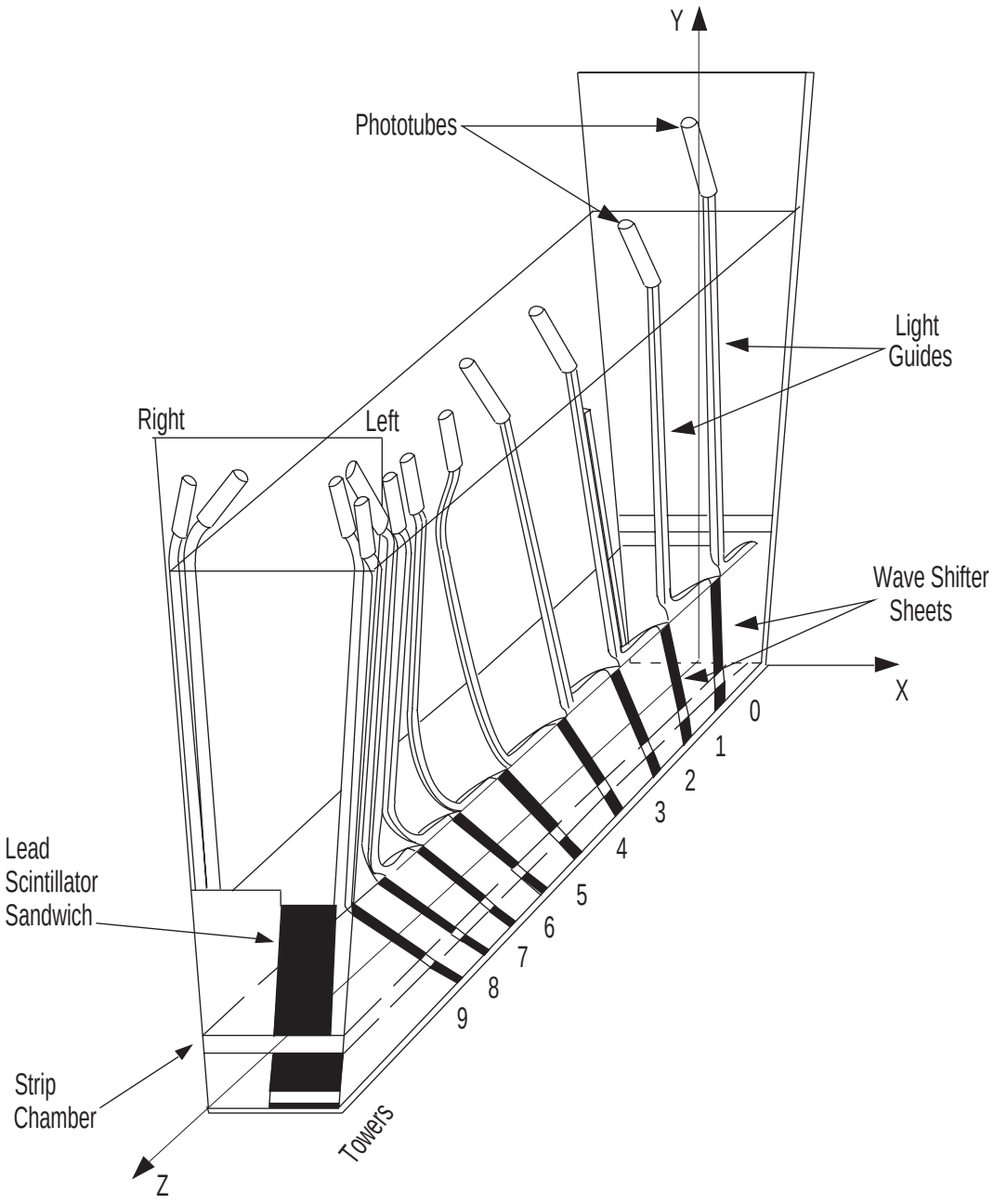

Figure 3.5: Diagram of the light collection system for a central wedge module. The module is divided into 10 projective towers. The strip chamber is located inside the CEM and measures the transverse and longitudinal development of electromagnetic showers.

Calorimeter	Energy Resolution
CEM	$13.7\%/\sqrt{E_T} \oplus 2\%$
PEM	$22\%/\sqrt{E_T} \oplus 2\%$
FEM	$26\%/\sqrt{E_T} \oplus 2\%$
CHA	$50\%/\sqrt{E_T} \oplus 3\%$
WHA	$75\%/\sqrt{E_T} \oplus 4\%$
PHA	$106\%/\sqrt{E_T} \oplus 6\%$
FHA	$137\%/\sqrt{E_T} \oplus 3\%$

Table 3.1: Summary of calorimeter energy resolutions. The FEM and FHA are the forward/backward calorimeters and are not used in this analysis. The $\oplus$ symbol signifies that the error term is added in quadrature.

out through cathode pads. It covers the small angle region between 2° and 10° in polar angle ($2.4 < |\eta_D| < 4$). It has an energy resolution of $\sigma(E)/E = 22\%/\sqrt{E \sin\theta}$ and position resolution between 1 to 4 mm depending on location in the calorimeter.

Hadron Calorimeters

Central The central hadron calorimeter (CHA) consists 48 steel-scintillator modules [21]. It covers the range $0 < |\eta_D| < 0.88$ and has a 2.5 cm sampling length.[2] The scintillator plastic is PMMA doped with 8% naphthalene, 1% butyl-PBD and 0.01% POPOP. The calorimeter is designed with a projective tower geometry with each tower covering 0.1 unit of pseudorapidity and 15° in ϕ with an energy resolution of $\sigma(E)/E = 50\%/\sqrt{E \sin\theta}$ GeV.

Wall and Plug The endwall hadron calorimeter (WHA) and the plug hadron calorimeter (PHA) are the same design as the central calorimeter consisting of 48 steel-scintillator modules with 5.0 cm sampling length [21]. The WHA sits on top of the PHA and together they cover the pseudorapidity range $0.88 < |\eta_D| < 1.31$ with an energy resolution of $75\%/\sqrt{E \sin\theta}$ GeV and $106\%/\sqrt{E \sin\theta}$, respectively.

[2]Sampling length refers to the thickness of the passive absorber.

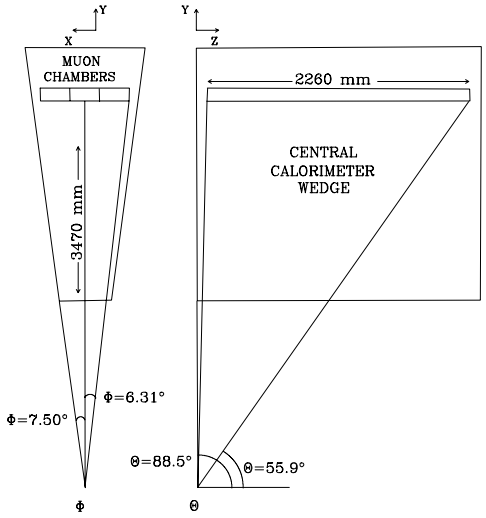

Figure 3.6: Layout of the central muon chambers in one of the central wedges. The left diagram shows a cross-sectional view of a single central wedge and the right diagram shows a side view of the same wedge.

Forward The forward hadron calorimeter (FHA) covers the pseudorapidity range $2.2 < |\eta_D| < 4.2$ with full azimuthal coverage [22]. It is a sampling calorimeter with 27 steel plates as the passive absorber and 27 ionization chambers. It has an energy resolution $\sigma(E)/E = A + BE^{-1/2} + CE^{-1}$ with $A = 8.6 \times 10^{-2}, B = 1.13$ GeV$^{1/2}$ and $C = 2.83$ GeV at $E = 200$ GeV.

3.4 Muon Detection

The muon detection system consists of three independent sets of muon chambers; the Central Muon Chambers (CMU), the Central Muon Upgrade (CMP) and the Central Muon Extension (CMX).

3.4.1 Central Muon System

The CMU is located outside of the central hadron calorimeter at a radius of 347 cm from the beam axis and covers the pseudorapidity range $|\eta_D| < 0.6$ [23]. The

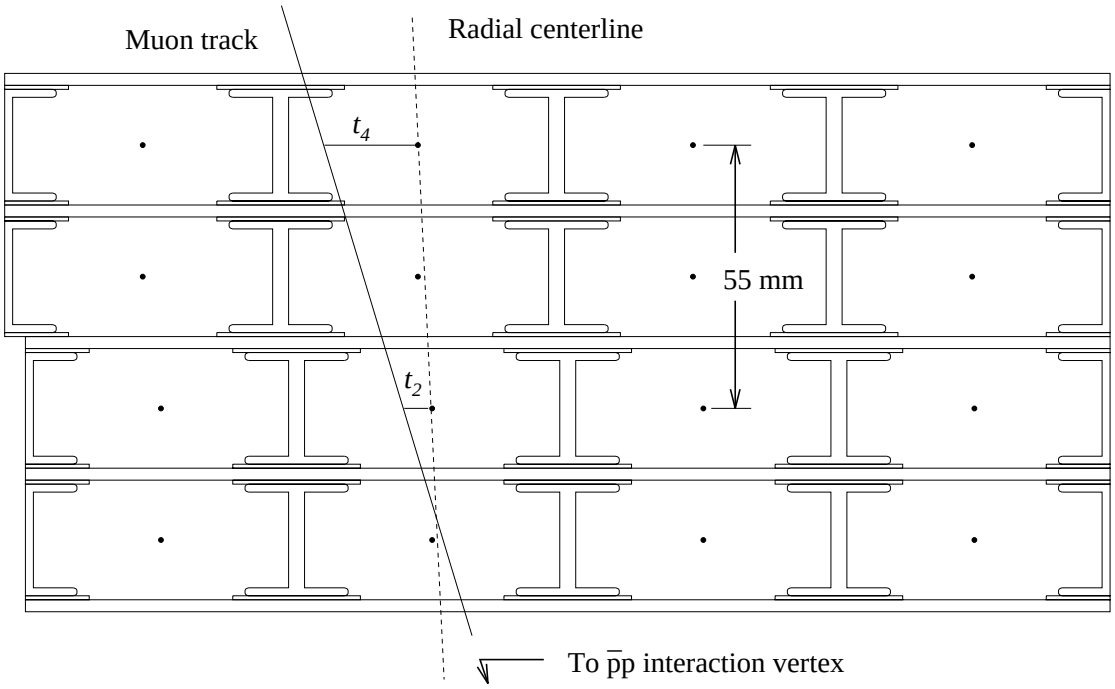

Figure 3.7: A cross sectional view of a CMU chamber. The chamber has four layers of drift cells. The difference between drift times t_2 and t_4 of a charged particle coming from the $p\bar{p}$ interaction vertex is used to determine a rough track momentum.

chambers are arranged into 24 wedges in ϕ for half of the detector ($0 <| \eta_D |< 0.6$). A single wedge is shown Figure 3.6.

Each chamber consists of four layers of drift cells as shown in Figure 3.7. The drift cells are parallel to the z axis with alternating layers radially aligned to provide a rough momentum measurement. Muon tracks are reconstructed using time-to-distance relationships in the drift (ϕ) direction and charge division along the longitudinal (z) direction with corresponding resolutions of $\sigma_\phi = 250$ μm and $\sigma_z = 1.2$ mm.

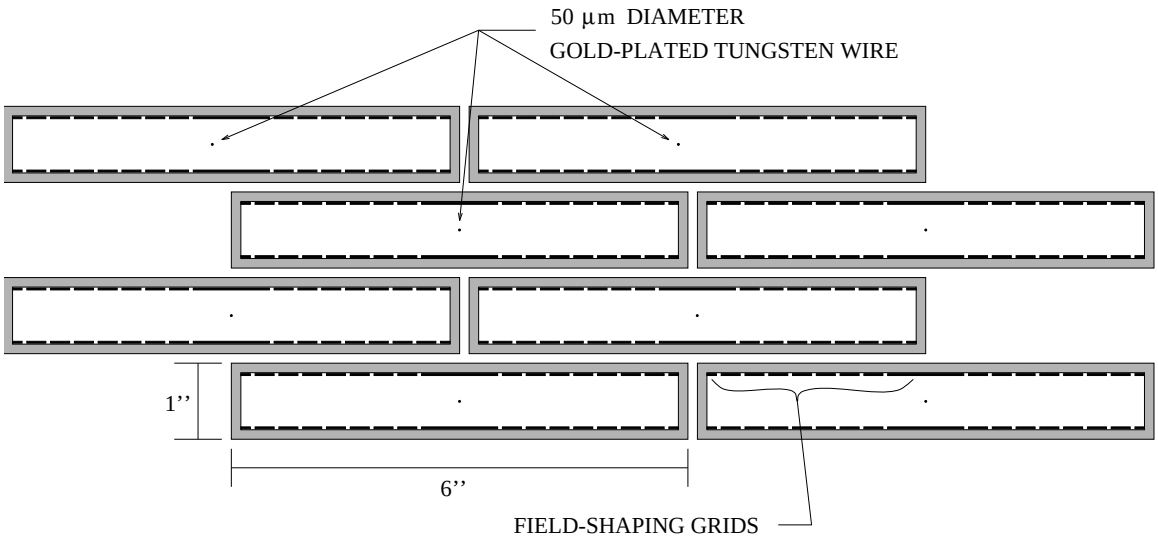

Figure 3.8: A cross sectional view of a CMP chamber. The CMP is located behind the CMU with 60 cm of steel between them. This geometry allows the CMP to be used in coincidence with the CMU to increase the signal-to-noise ratio by decreasing the pion punchthrough.

3.4.2 Central Muon Upgrade

The CMP also consists of four layers of drift cells, but unlike the CMU they are staggered geometrically as shown in Figure 3.8 [24]. An additional 60 cm of steel exists between the CMU and CMP which reduces the region covered by the CMP to $|\eta| \leq 0.5$. This additional steel allows the two detectors to be used in coincidence to increase the signal-to-noise ratio by reducing the number of non-muons penetrating both detectors.[3]

3.4.3 Central Muon Extension

The central muon extension consists of drift chambers (CMX) and scintillation counters (CSX) [24]. The CMX covers a pseudorapidity range of $0.65 \leq |\eta_D| \leq 1.0$. Its wires are radially aligned with the interaction point enabling them to be used in the

[3] A high energy pions can "punch through" the hadron calorimeter and leave a track in the central muon chamber because they did not deposit all their energy in the calorimeter.

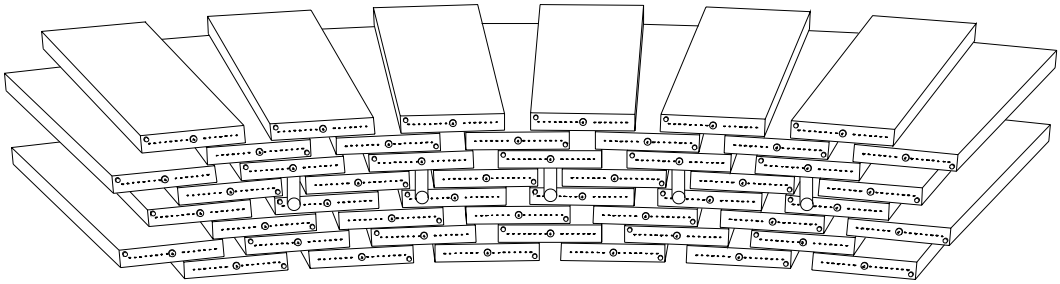

Figure 3.9: A wedge view of the CMX system. The CSX is placed on both sides of this wedge to reduce the background coming from the $p\bar{p}$ collision.

trigger. The CSX was installed on both sides of the CMX to provide timing information to help remove backgrounds from $p\bar{p}$ collision.[4] The total coverage of all three muon systems is shown in Figure 3.10 and the number of hadronic absorption lengths as a function of θ is shown in Figure 3.11.

[4]The CMX is unshielded from both the beamline and forward calorimeters. These two detectors produce a low energy particle spray coming from interactions with small-angle, with respect to the z axis, particles from the $p\bar{p}$ collision.

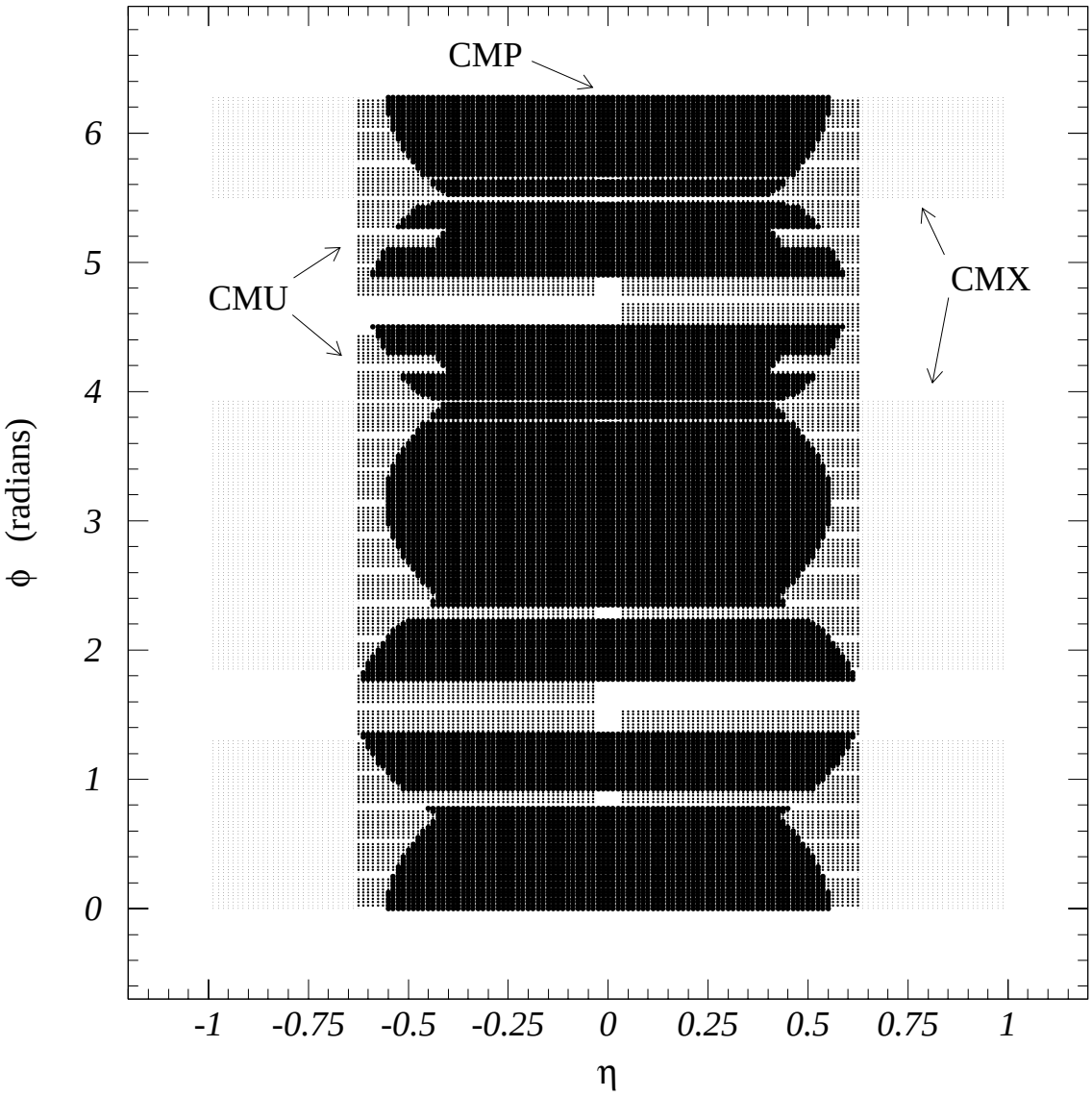

Figure 3.10: Scatter plot of the $\phi - \eta$ coverage of the muon system. This scatter plot shows the individual coverage of each muon system. The CMP coverage is not uniform due to its rectangular geometry in the detector.

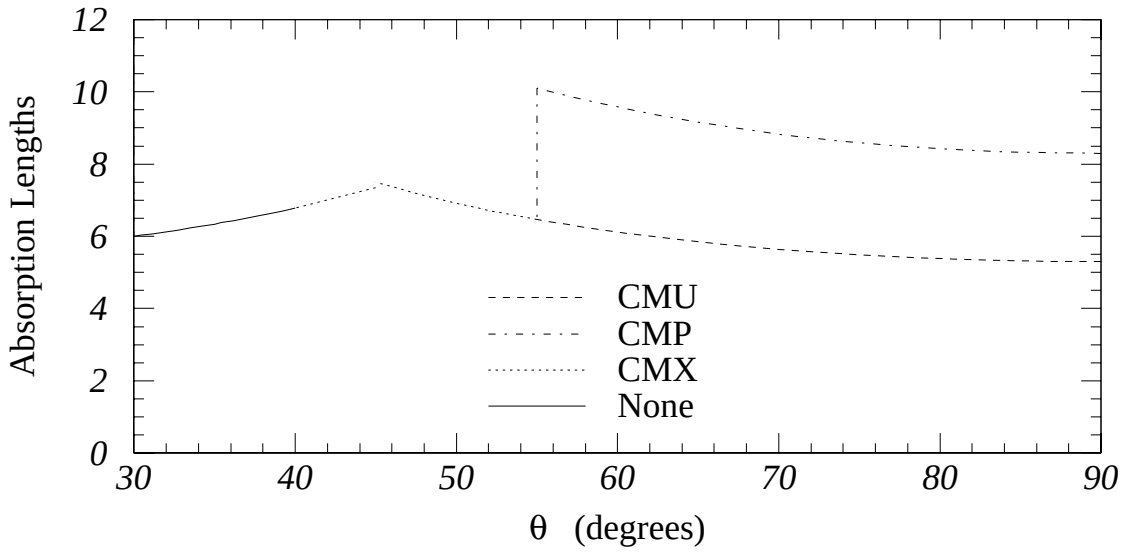

Figure 3.11: The hadronic absorption lengths as a function of θ for the individual muon chambers.

3.5 Trigger

The Tevatron has a high luminosity $p\bar{p}$ bunch crossing time every 3.5 μs with at least one $p\bar{p}$ interaction which corresponds to an interaction rate of 286 kHz. It is not possible to write detector data for every event out to magnetic tape. We can at most write on the order of 20 Hz to tape. In order to accomplish this filtering, CDF uses a three level[5] triggering system to focus primarily on interesting rare events while suppressing background events efficiently [25]. Each trigger level consists of a logical OR of a number of different triggers designed to find many different event topologies.

3.5.1 Level 1

The Level 1 trigger is designed to make its decision before a consecutive beam crossing or within 3.5 μs. It uses the projective geometry of the detector to make a decision based on energy flow. Energy depositions, E_i, in the hadronic and electromagnetic calorimeters are weighted by a hardware encoded $\sin\theta_i$, where θ_i is the angle of the ith calorimeter tower with respect to the center of the detector, to simulate the "transverse energy" of a particle by $E_T^i = E_i \sin\theta_i$. If any tower is above a preset threshold, the Level 1 trigger becomes satisfied. Additional Level 1 triggers include looking for high P_T tracks in the tracking chambers. If the L1 trigger is not satisfied the electronics are cleared for the next beam crossing. If it is satisfied, the detector holds the information and ignores further beam crossings until all further trigger decisions are complete.

3.5.2 Level 2

In Level 2, energy depositions in the calorimeters are used to form clusters in hardware. The hardware uses seed towers or initial clusters of energy that satisfy a preset E_T requirement. Level 2 also uses a hardware track processor called the Central Fast

[5]There is also a Level 0 trigger. It is the requirement that the beam-beam counters (BBCs) fired in order to confirm that a collision occurred in the detector. The BBCs are also used as the primary luminosity monitor [13].

Tracker (CFT) to look for high P_T tracks that match in location to the clusters in the calorimeters. Level 2 takes about 20 μs to make a decision in which the next 6 beam crossings are ignored. If a Level 2 trigger is satisfied, the event is passed on to Level 3. If not, the detector is reset for the next beam crossing. The Level 2 trigger is satisfied at a rate of 20-35 Hz.

3.5.3 Level 3

Level 3 starts to make decisions based on physical objects such as muons, electrons, photons, jets and missing transverse energy. It constructs a crude missing energy vector by summing both electromagnetic and hadronic calorimeter towers and defines a quantity

$$\vec{\not\!\!E}_T = \sum_{Towers} (E_i \sin\theta_i)\hat{n_i} \tag{3.2}$$

where E_i is the energy of the i^{th} tower, $\hat{n_i}$ is a transverse unit vector pointing to the center of each tower and θ_i is the polar angle of the line pointing from $z = 0$ to the i^{th} tower. It does full software reconstruction of the event and makes requirements on P_T, E_T, $\not\!\!E_T$ and the ratio of hadronic to electromagnetic energies for clusters in the calorimeters. If this trigger is satisfied, the event is written out to magnetic tape.

While the first two trigger levels consist of dedicated electronics, the third level is a farm of Silicon Graphics computers that does full event reconstruction. The data samples used in this analysis were taken during two data taking periods. The first period, Run 1A, resulted in an integrated luminosity of 19.3$\pm$0.68 pb^{-1} during 1992-1993. The second period, Run 1B, resulted in 90.1$\pm$7.21 pb^{-1} during 1994-1995.

Chapter 4

The Muon Data Sample

4.1 Trigger Requirements

The Level 1 muon trigger uses timing information from the CMU and CMX chambers. A cross sectional view of the CMU chamber is shown in Figure 3.7. A muon coming from a $\bar{p}p$ collision leaves a track stub in the muon chambers which is a collection of hits in the different layers of the CMU/CMP or CMX chambers. Using drift times from different layers in the chamber the charged particle momentum can be roughly measured from $P_T = (154/\Delta t)$ GeV [26]. In regions where the CMP overlaps the CMU, a track stub is also required in the CMP chamber. This requirement reduces the background from pion punchthrough by a factor of ≈ 20. The Level 1 muon trigger is satisfied if the track stub P_T is above 6 GeV/c.

The Level 2 trigger uses the CFT to search for $r-\phi$ hit patterns in the CTC which correspond with a high P_T charged particle in the magnetic field. The Level 2 trigger is satisfied if a CFT track matches the muon stub within a 5° window in ϕ. This requirement in $\Delta\phi$ corresponds to a $P_T > 9.2$ GeV/c. The Level 3 trigger is a software trigger that does full event reconstruction from event data. The Level 3 requirements for a high P_T muon are[1]

- $P_T^{\mu} > 18$ GeV/c

[1] It is not possible to discuss the selection and construction of the data samples in the detector in a linear fashion, so we state the following trigger requirements and refer the reader to Section 4.2 for their physical description.

- $E^{HAD} < 6.0$ GeV
- CMU $\mid \Delta x \mid < 5$ cm
- CMP $\mid \Delta x \mid < 10$ cm
- CMX $\mid \Delta x \mid < 10$ cm

If these requirements are satisfied, the event is written to tape. The data is then reprocessed offline and the event is reconstructed and required to satisfy the following

- $P_T^{\mu} > 18$ GeV/c
- $E^{HAD} < 6.0$ GeV
- $E^{EM} < 2.0$ GeV
- CMU $\mid \Delta x \mid < 2$ cm
- CMP $\mid \Delta x \mid < 5$ cm
- CMX $\mid \Delta x \mid < 5$ cm

The EM energy cut was not used in the online Level 3 trigger to prevent biasing of analyses which used EM energy information. If these offline requirements are satisfied then the event becomes part of the "inclusive high P_T muon sample".

The following triggers are explained in Appendix A.[2] Using standard Level 1 and Level 3 muon triggers, we required one of the following Level 2 triggers in this analysis:

- For Run 1a, the event must pass one of the following triggers:
  - CMU_CMP_CFT_9_2*,
  - CMUNP_CFT_9_2*,

[2]The * is a wildcard and takes any other trigger combination with the same initial requirements (e.g. CMU_CMP_CFT_9_2).

  - CMUP_CFT_9_2*,
  - No CMX triggers were accepted.

- For Run 1b, the event must pass one of the following triggers:
  - CMNP_CFT_12_5DEG_V*,
  - CMUP_CFT_12_5DEG_V*,
  - CMNP_JET*,
  - CMUP_JET*,
  - CMU_CMP_JET*,
  - CMNP_CFT_12_5DEG_M*,
  - CMUP_CFT_12_5DEG_M*,
  - CMX_CFT_12_5DEG_V*,
  - CMX_JET*,
  - CMX_CFT_12_5DEG_M*,
  - CMX_CFT_12_5DEG_E*.

For example, the CMU_CMP_CFT_9_2* trigger requires a stub in the CMU and CMP (CMU_CMP) which is matched to a CFT track with a $P_T > 9.2$ GeV/c (CFT_9_2).

4.2 Muon Quality Selection Cuts

During data taking periods, it was possible that one or more of the CDF detector components was ill-behaved. To prevent any such biases in this analysis, we required all runs to be listed on a certified list which confirmed that all detector components were operating nominally during the run. We required the event vertex (Z_{VTX}) to be within 60 cm in z of the origin of the detector in order to maintain the projective geometry of the detector. This prevents a systematic bias to the missing transverse energy from particles escaping through detector gaps [27].

With the above two cuts, we constructed a subsample of high-P_T events from the inclusive high P_T muon sample by making the following additional cuts. The muon must be fiducial, which means that it passed through a well understood region of the detector and was well measured. To improve the momentum resolution of the muons, we beam constrained all muon tracks. Beam constraining uses the interaction vertex as an extra point in the track fit and improves the momentum resolution by a factor of two.[3] The muon was required to have a beam constrained momentum of $P_T \geq 20$ GeV/c. This cut suppresses QCD background and has the additional effect of reducing the background from the tauonic decay of the W and Z bosons. The sharing of energy between a larger number of final state particles in the tauonic decay produces a muon momentum spectrum which decreases with P_T while the muon momentum spectrum from W and Z events increases with P_T and peaks at $P_T = M_W(M_Z)/2 \approx 40$ GeV/c.

The muon is also required to have left an energy deposition in the calorimeters consistent with being from a muon or "minimum ionizing" particle. The energy in the CHA must be less than 6.0 GeV and the energy in the CEM must be less than 2.0 GeV. To reduce the effects of multiple scattering, we required the local x extrapolation of the CTC track to the muon chambers and the local x of the track from the muon chamber to be within a certain distance. These are called matching cuts. For the CMU the absolute difference between the tracks had to be less than 3 cm. For the CMP and CMX the absolute difference between the tracks had to be less than 5 cm. Muon identification in the detector is shown in Figure 4.1. The muon must have an isolation less than 0.1. Isolation is defined as the ratio of excess energy (minus the muon energy), in a cone of $\Delta R = \sqrt{\Delta\phi^2 + \Delta\eta^2} = 0.7$ around the muon to the muon's P_T. This reduces backgrounds from QCD which tend to have excess energy around the muon from the semileptonic decay.

In order to reduce the contributions from cosmic rays, we required the muon to pass the cosmic ray filter. The cosmic ray filter uses timing information from the

[3]The resolution scales as $\approx 1/l^2$ where l is the distance over which the fit occurs.

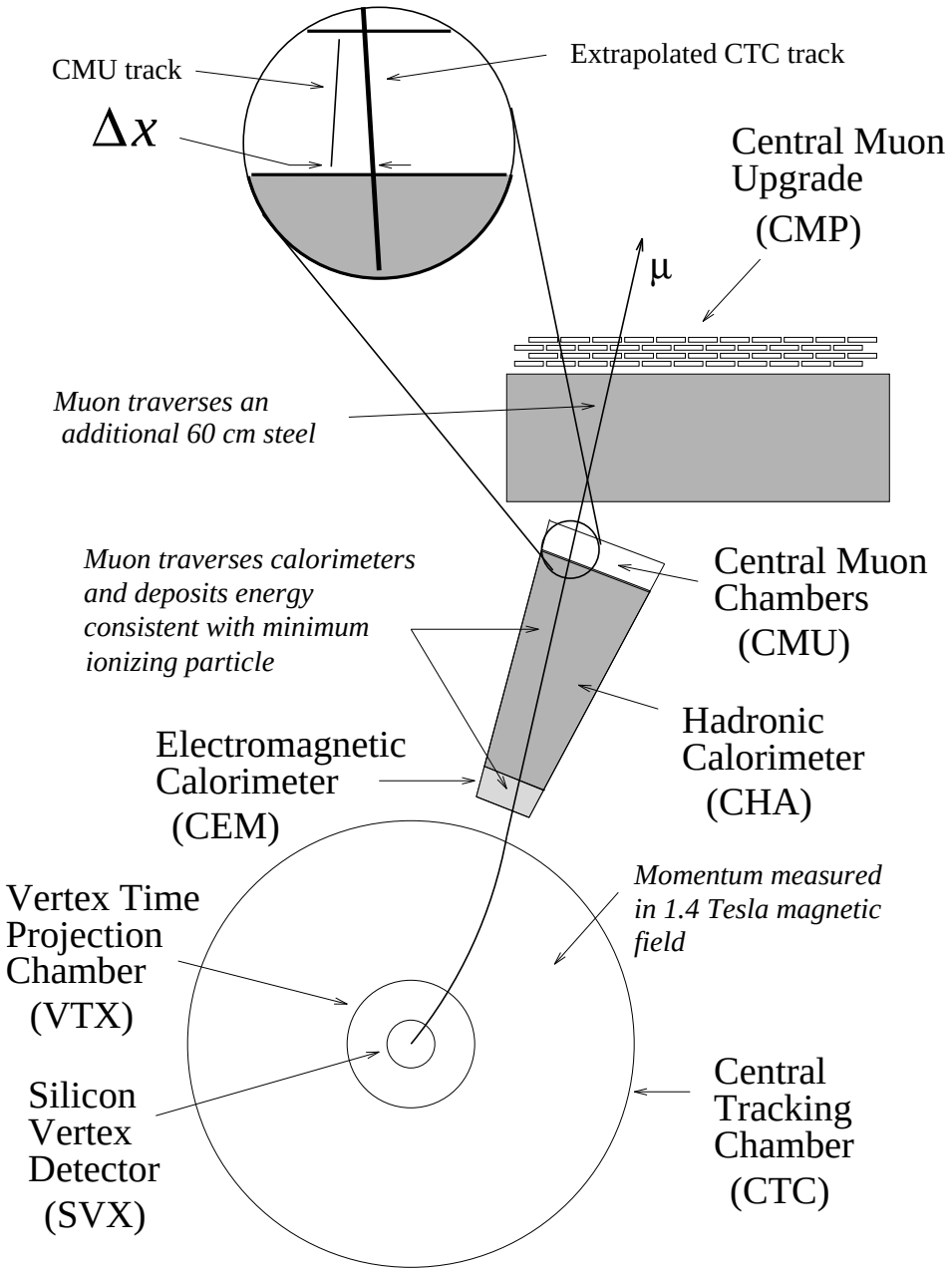

Figure 4.1: The identification of muons. The momentum is measured by the CTC. The muon loses energy in the calorimeters. The CTC track is extrapolated and compared with the track in the muon chambers.

hadron TDCs and requires that the time of the energy deposition in the calorimeters occurs within a window corresponding to a $p\bar{p}$ collision. Since cosmic rays are not correlated with the event vertex, we made an impact parameter requirement - in the $r-\phi$ plane - from a good vertex be less than 0.2 cm. Also, the Z_0 position as determined by the muon chambers must be with 5 cm of a high quality vertex as measured by the VTX (Z_{VTX}).

If any muon satisfied the above requirements, we called it a "golden" muon and saved the event for further analysis. We show some event distributions in Figure 4.2 and summarize the cuts in Table 4.1.

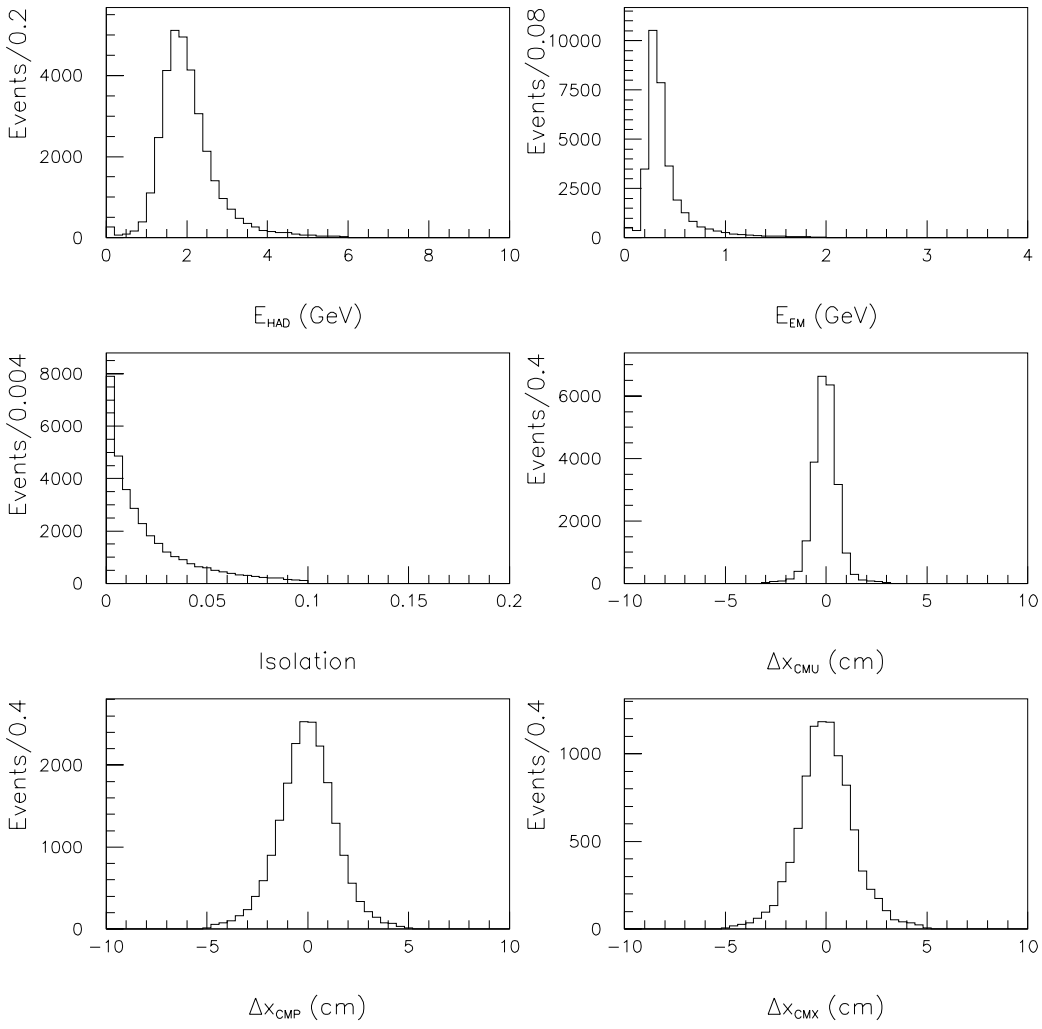

Figure 4.2: Distributions for muon identification. The first three plots are part of the minimum ionization requirements. The next three plots are matching requirements. The cuts are applied in these histograms.

Good run	
Event vertex fiducial	$\mid Z_{VTX} \mid \leq 60.0$ cm
Fiduciality	
Transverse momentum	$P_T^{BC} \geq 20.0$ GeV/c
Hadron energy	$E_{HAD} \leq 6.0$ GeV
EM energy	$E_{EM} \leq 2.0$ GeV
Isolation	$I \equiv (E_{\Delta R=0.4}^{Excess})/P_T^{BC} \leq 0.10$
ΔX_{CMU}	$\mid \Delta X_{CMU} \mid < 3$ cm
ΔX_{CMP}	$\mid \Delta X_{CMP} \mid < 5$ cm
ΔX_{CMX}	$\mid \Delta X_{CMX} \mid < 5$ cm
Cosmic ray filter	
Impact parameter	$\mid d_0 \mid \leq 0.2$ cm
Track near good vertex	$\mid Z_0 - Z_{VTX} \mid \leq 5.0$ cm

Table 4.1: Summary of muon quality requirements.

The CDF detector has three regions for muon detection: the central muon chambers (CMU), the central muon upgrade chambers (CMP), and the central muon extension (CMX). A muon in an event gets classified according to which detectors the muon has passed through: 1=CMU, 2=CMP, 3=CMU/CMP, 4=CMX, 5=CMU/CMP/CMX, 6=CMP/CMX, 7=CMU, 8=CMIO. A CMIO is a high P_T track with no corresponding track in any of the three muon detectors.

To facilitate comparison between data and Monte Carlo, we classified muons by a different basis. This reclassification of events is based on the muon ϕ and the detector η. The new classification is as follows: CMUP, CMNP, CMX, PMIO. The CMUP ($\mid \eta \mid \leq 0.62$) corresponds to the upgraded muon region of the detector where the CMU region overlaps with the CMP region, CMNP ($\mid \eta \mid \leq 0.62$) is the non-upgraded region where only CMU coverage exists, CMX ($0.62 \leq \mid \eta \mid \leq 1.00$) is the region cover by the CMX extension and PMIO ($1.00 \leq \mid \eta \mid$) which has no muon detector coverage

and consists of CMIO muons. CMIO muons will be reclassified into one of the above 4 types.

The data sample used in this analysis was constructed from the combined data set from CDF's Run 1a and Run 1b. The two data sets combined give an integrated luminosity of 107 pb^{-1}, with Run 1a consisting of 18.3 pb^{-1} and Run 1b consisting of 88.4 pb^{-1}. We show the luminosity broken down into regions in Table 4.2. The method for determining the luminosity using the beam-beam counters is discussed in [28, 29].

Data Sample	Region	$\int \mathcal{L}dt$
Inclusive Muon 1A	CMUP	18.33 ± 0.66
	CMNP	19.22 ± 0.69
Inclusive Muon 1B	CMUP	88.35 ± 3.62
	CMNP	89.20 ± 3.66
	CMX	88.98 ± 3.65

Table 4.2: Luminosity of the muon channel broken down by region. This corresponds to a total of 110 pb^{-1} of integrated luminosity for Run 1.

The muon Z and W event samples used in this analysis are generated from the Baur Monte Carlos. They are passed through a detector simulation which yields the theoretical predictions for cross sections and event yields. We refer the reader to Chapter 6 for a more detailed discussion.

4.2.1 Muon Channel Z Event Selection

A Z boson can decay to two muons. After we found a golden muon, we searched for a second muon that satisfied the following requirements.

- Minimum beam constrained transverse momentum : $P_T \geq 20.0$ GeV/c,
- Maximum EM energy : $E_{EM} \leq 2.0$ GeV,
- Maximum HAD energy : $E_{HAD} \leq 6.0$ GeV,

- Maximum isolation : $I \leq 0.10$.

Any second muon passing these cuts was labeled a "silver" muon. These cuts are looser than golden cuts in order to increase the acceptance. Additionally, we also required:

- The charge of each leg used to construct the Z is of opposite sign,
- The separation between the z vertex positions of the muons must be below a minimum requirement: $\mid z_1^{\mu} - z_2^{\mu} \mid \leq 5.0$ cm,
- Minimum dimuon mass: $M_{\mu\mu} \geq 65.0$ GeV/c^2.

After all the selection cuts, we found 3969 events the passed the all requirements from the Run 1 data. The dimuon mass distribution is shown in Figure 4.6 and the event yields are shown in Table 4.3. We have plotted additional kinematical distributions in Figures 4.3- 4.5.

Classification	Run 1A	Run 1B	Total
CMUP-CMUP	107	733	840
CMUP-CMNP	63	284	347
CMUP-CMX	105	877	982
CMUP-PMIO	138	579	717
CMNP-CMNP	34	106	140
CMNP-CMX	33	206	239
CMNP-PMIO	49	150	199
CMX-CMX	-	227	227
CMX-PMIO	-	278	278
Total	529	3440	3969

Table 4.3: Yields from the Run 1 Inclusive Muon Z Sample separated into the Diboson classification scheme.

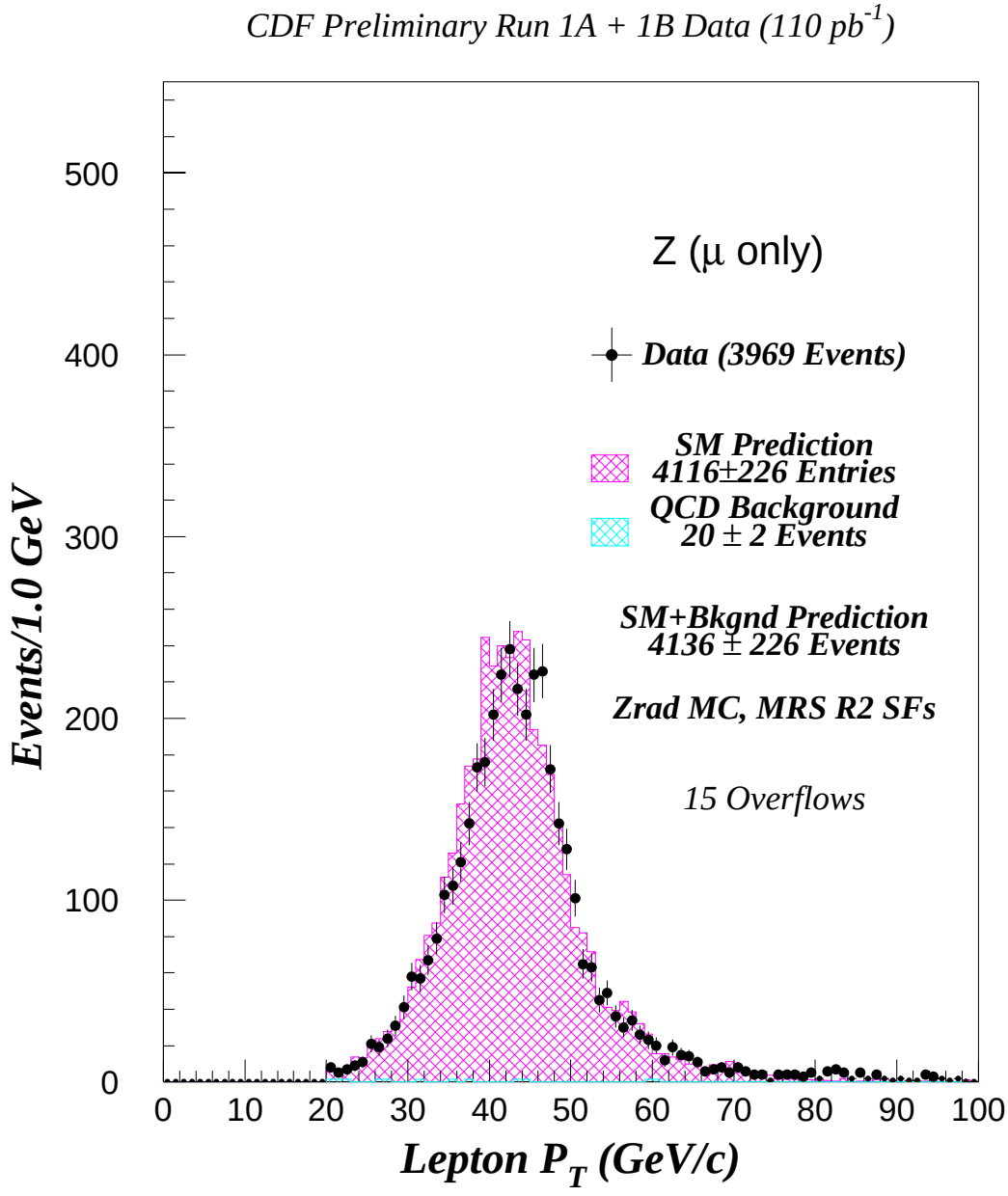

Figure 4.3: The muon transverse momentum for Z events from the inclusive muon sample overlaid on the standard model prediction + background expectation. Note that both legs of the Z are plotted.

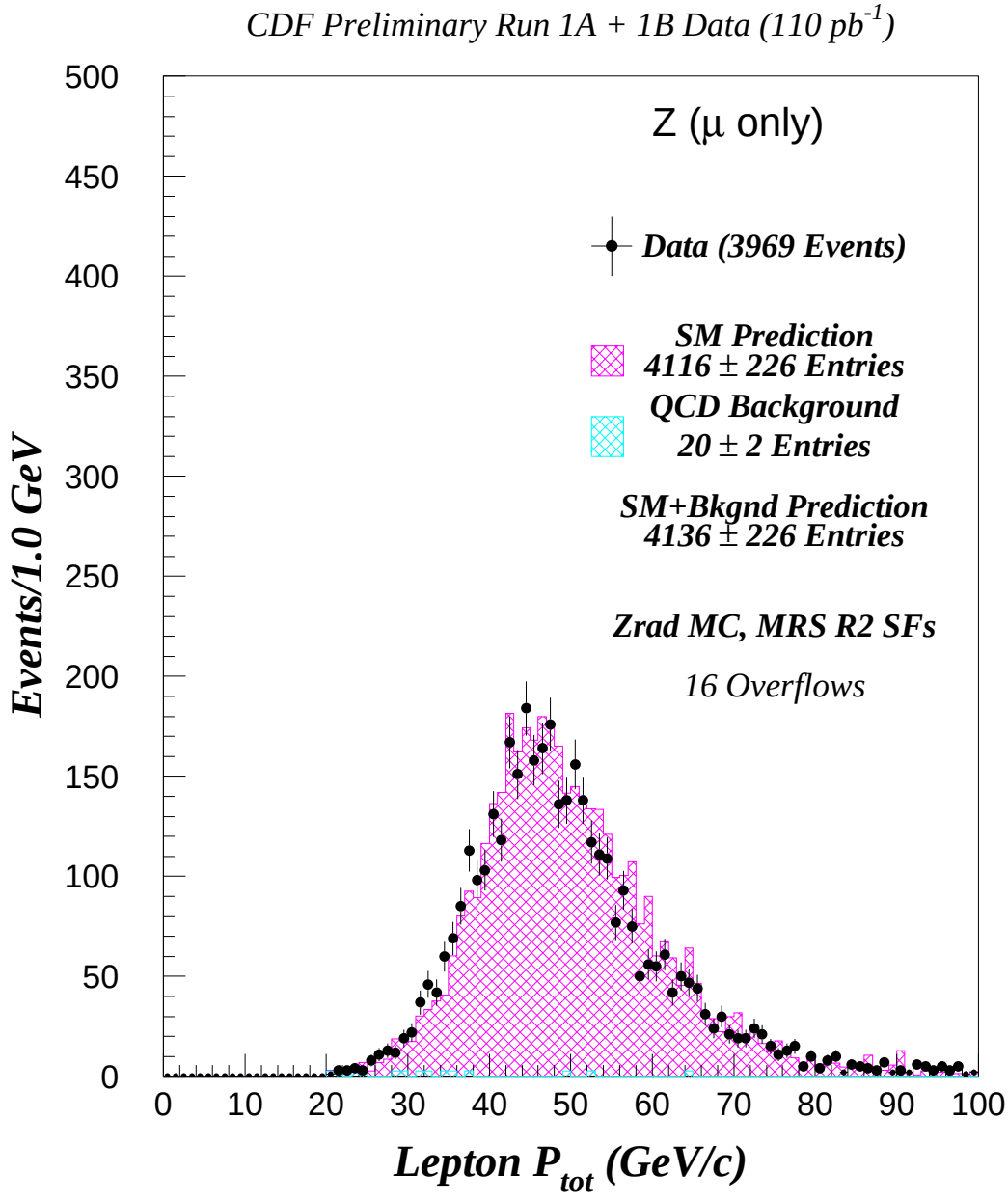

Figure 4.4: The muon total momentum for Z events from the inclusive muon sample overlaid on the standard model prediction + background expectation. Note that both legs of the Z are plotted.

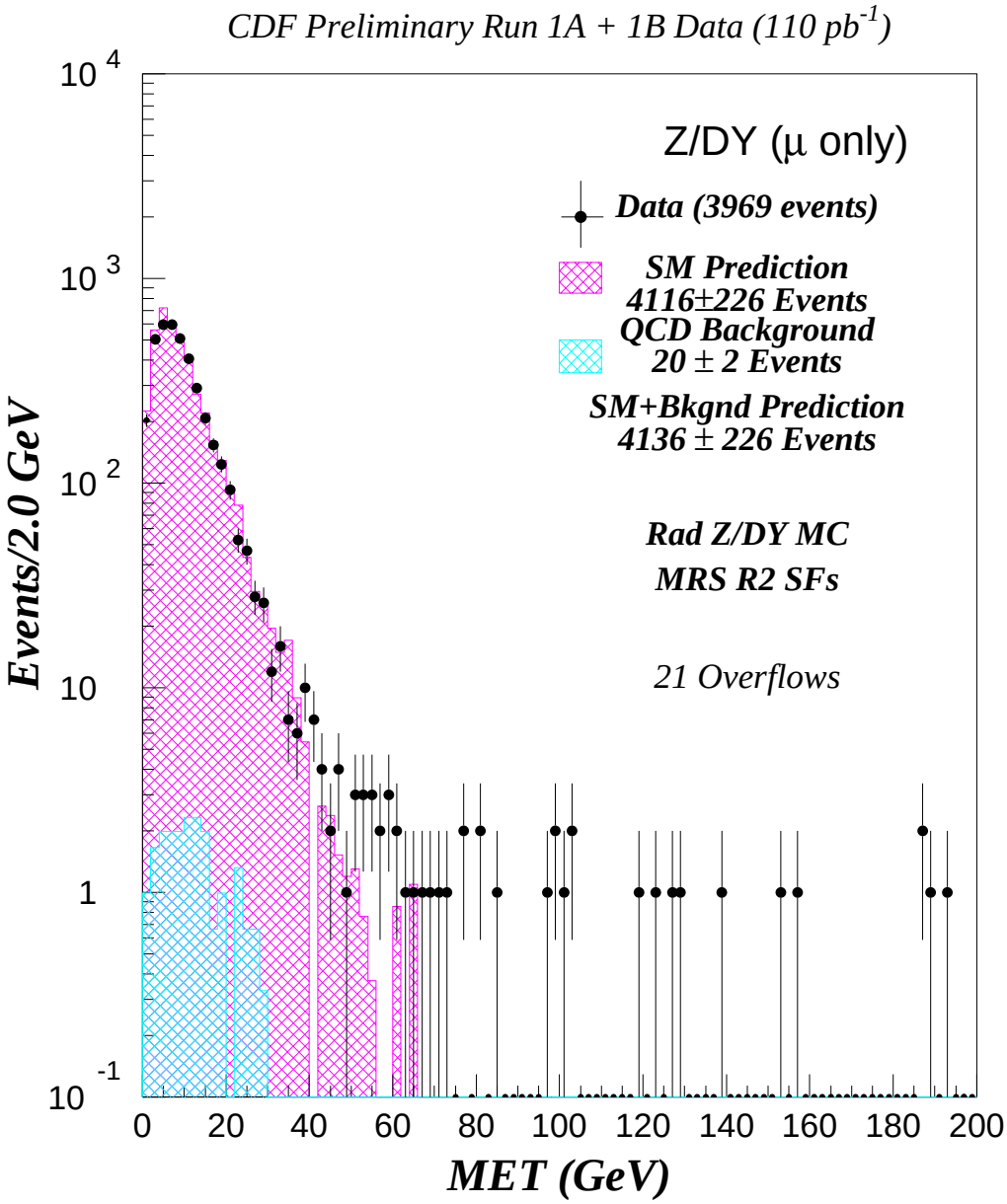

Figure 4.5: The missing transverse energy for Z events from the inclusive muon sample on a logarithmic scale overlaid on the standard model prediction + background expectation.

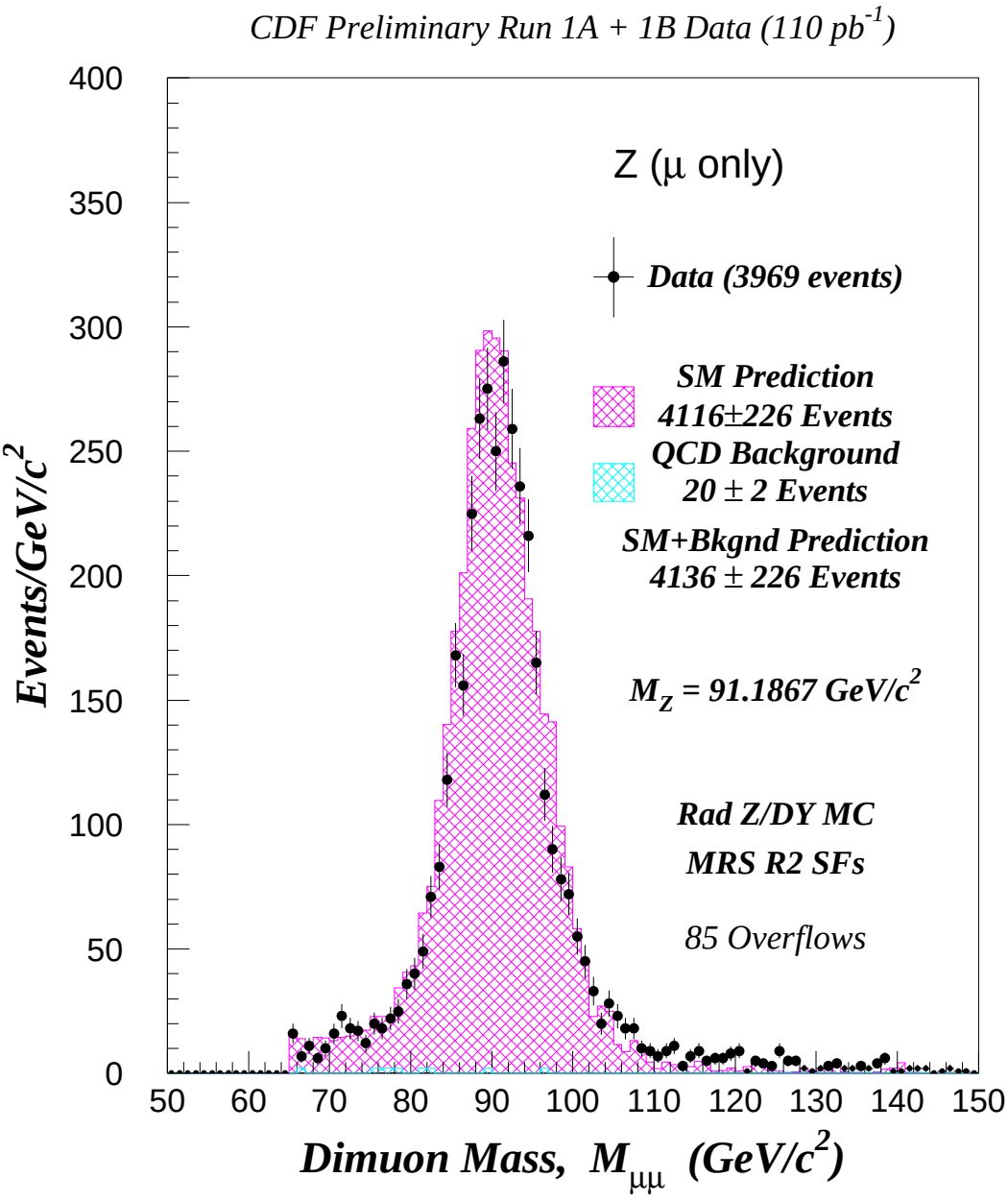

Figure 4.6: The dimuon mass for Z events from the inclusive muon sample overlaid on the standard model prediction + background expectation.

4.2.2 Muon Channel W Event Selection

The W boson can decay into a muon and muon neutrino. The accompanying neutrino cannot be detected in the detector but its presence is inferred from the energy imbalance or missing transverse energy in the detector.

The simple missing $\not\!\!E_T$ calculation discussed in Chapter 3 suffers from two defects: for events with multiple primary vertices, the $\not\!\!E_T$ is frequently calculated using the wrong vertex, and a simple sum of tower energies fails to properly include our knowledge of the differing response of the calorimeter to electromagnetic and hadronic energy deposits [30].

The increased luminosity gives a higher probability of multiple primary vertices for a given event. We calculated the $\not\!\!E_T$ according to the correction used in [30] and is as follows:

$$\vec{\not\!\!E}_T = -\sum(\vec{E}_e + \vec{E}_\gamma + \vec{E}_\mu + \vec{E}_{jet} + \kappa * \vec{E}_{uncl}) \tag{4.1}$$

where $\vec{E}_e$ is the electron energies, $\vec{E}_\gamma$ the photon energies, $\vec{E}_\mu$ the muon energies, $\vec{E}_{jet}$ is the jet energies in a cone $\Delta R = \sqrt{(\Delta\eta)^2 + (\Delta\phi)^2} = 0.4$ cone size with minimum jet E_T of 10 GeV, κ is a scale factor which scales the unclustered energy $\vec{E}_{uncl}$. The motivation and the code used is fully described in [30, 31]. These corrections were applied to all events in both Run 1b and Run 1a data.

From the golden sample discussed above the requirements for W's are as follows:

- Minimum missing transverse energy: $\not\!\!E_T > 20.0$ GeV,
- Minimum transverse mass of the W: $M_T > 40.0$ GeV/c^2 (This requirement further suppresses tauonic decay of the W and tauonic decay of a one-legged Z.),
- The event is not consistent with a Z or a one-legged Z[4].

[4] A one-legged Z is where a Z boson decays such that one the legs has a $\mid \eta \mid > 1.1$ and the leg is not detected by the CTC. This mismeasurement mimics a missing transverse energy signal.

where the W transverse mass is defined as

$$M_W^T = \sqrt{2P_T^\mu P_T^\nu [1 - \cos(\phi_\mu - \phi_\nu)]}. \tag{4.2}$$

After all these quality cuts, we found 38,606 muon W events and shown in Table 4.4. The W transverse mass for W events from the inclusive muon sample is shown in Figure 4.11. Additional kinematical plots for W events from the inclusive muon sample are shown in Figures 4.7- 4.10.

Classification	Run 1A	Run 1B	Total
CMUP	3925	18916	22841
CMNP	1473	4932	6405
CMX	-	9360	9360
Muon Total	5398	33208	38606

Table 4.4: Yields from the Run 1 Inclusive Muon W Sample separated into the Diboson classification scheme.

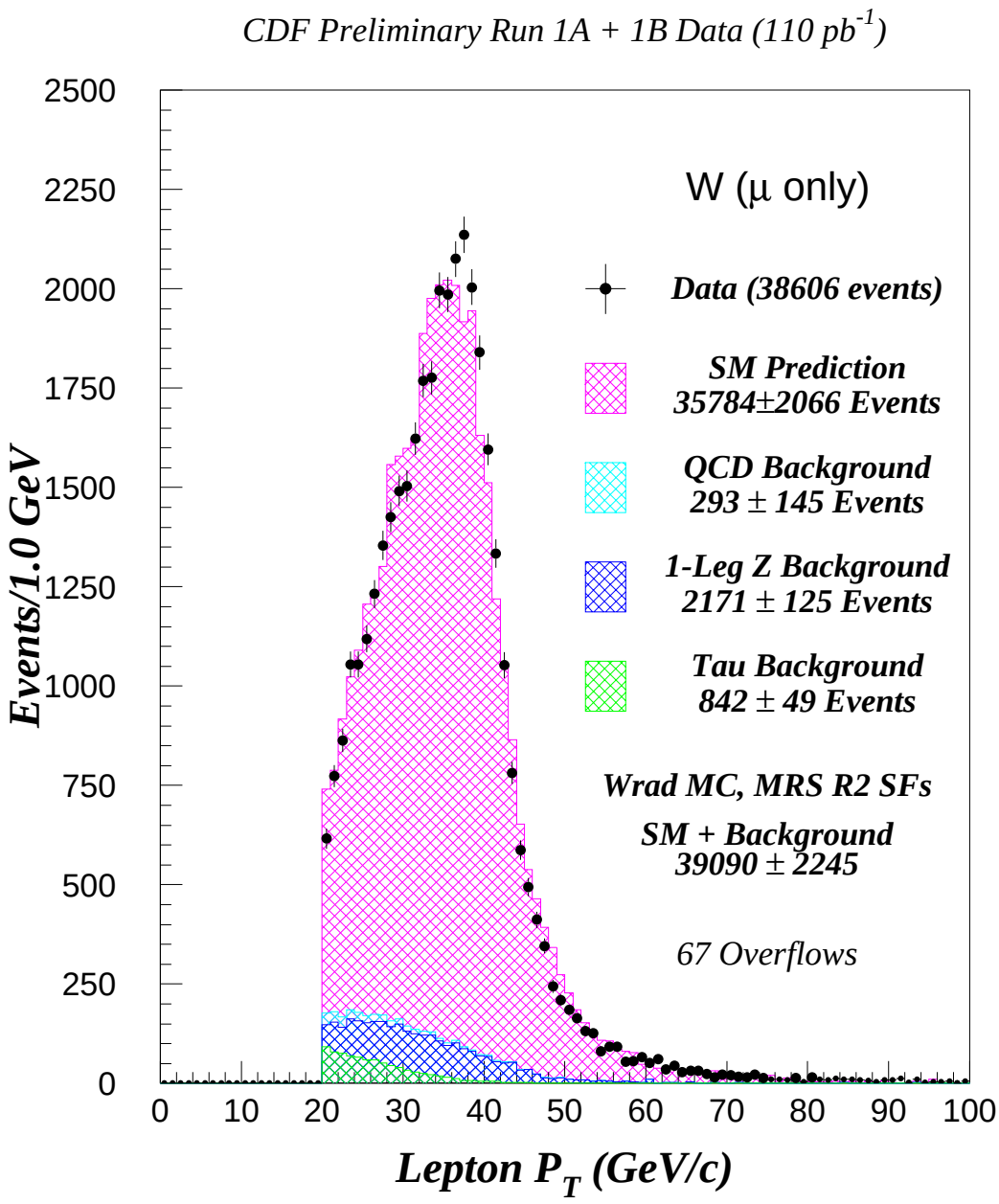

Figure 4.7: The muon transverse momentum for W events from the inclusive muon sample overlaid on the standard model prediction + background expectation.

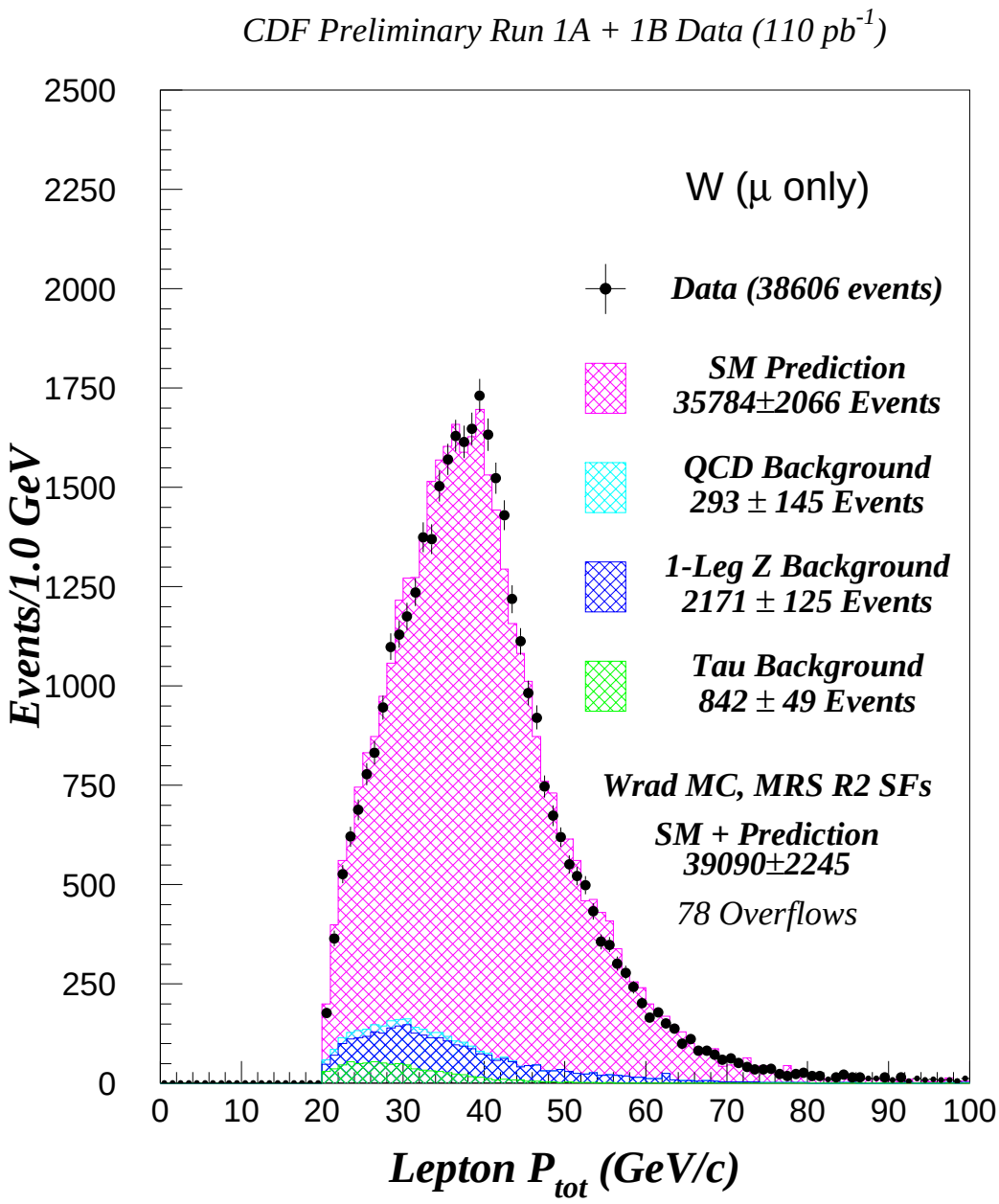

Figure 4.8: The muon total momentum for W events from the inclusive muon sample overlaid on the standard model prediction + background expectation.

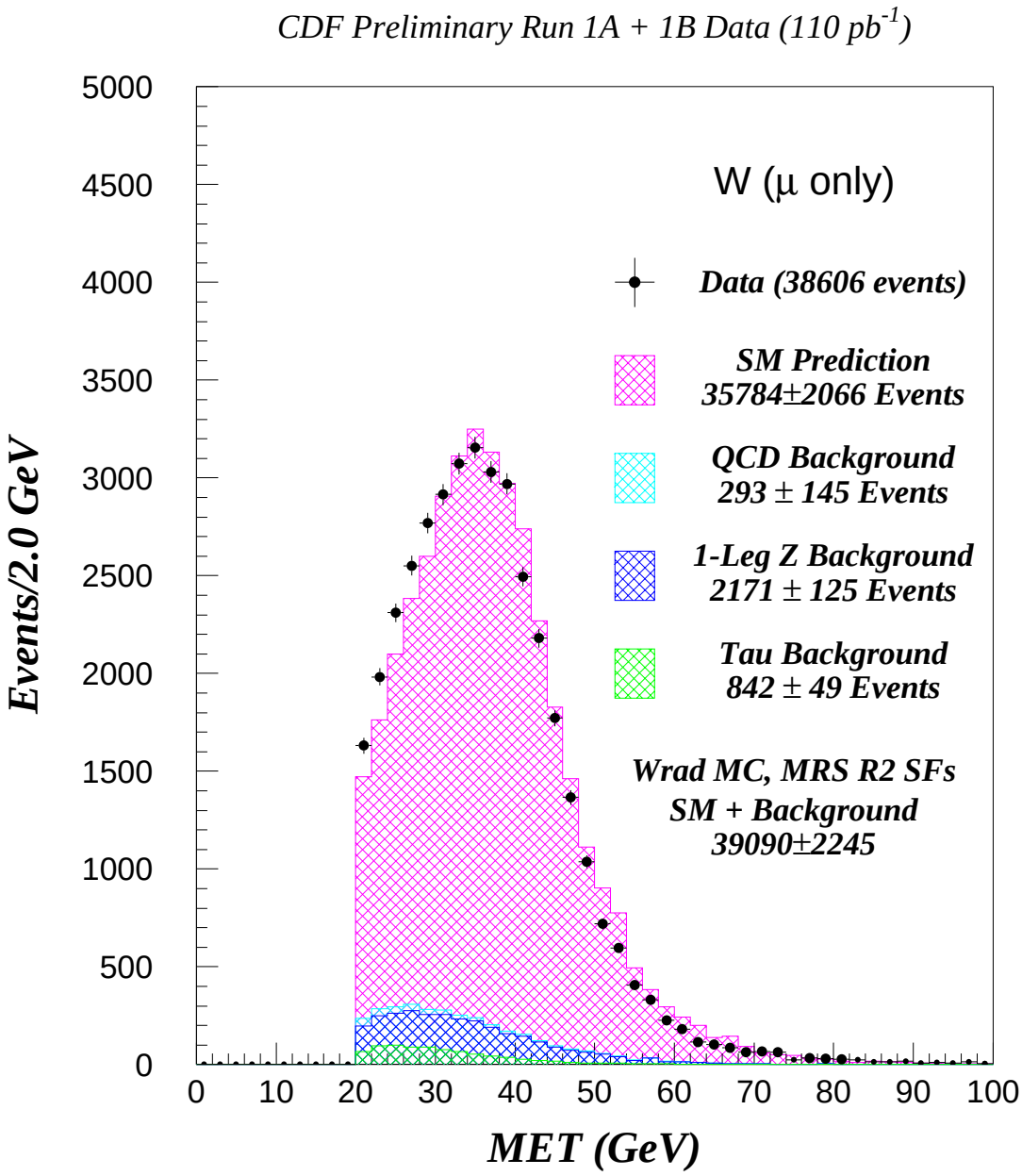

Figure 4.9: The missing transverse energy for W events from the inclusive muon sample on a linear scale overlaid on the standard model prediction + background expectation.

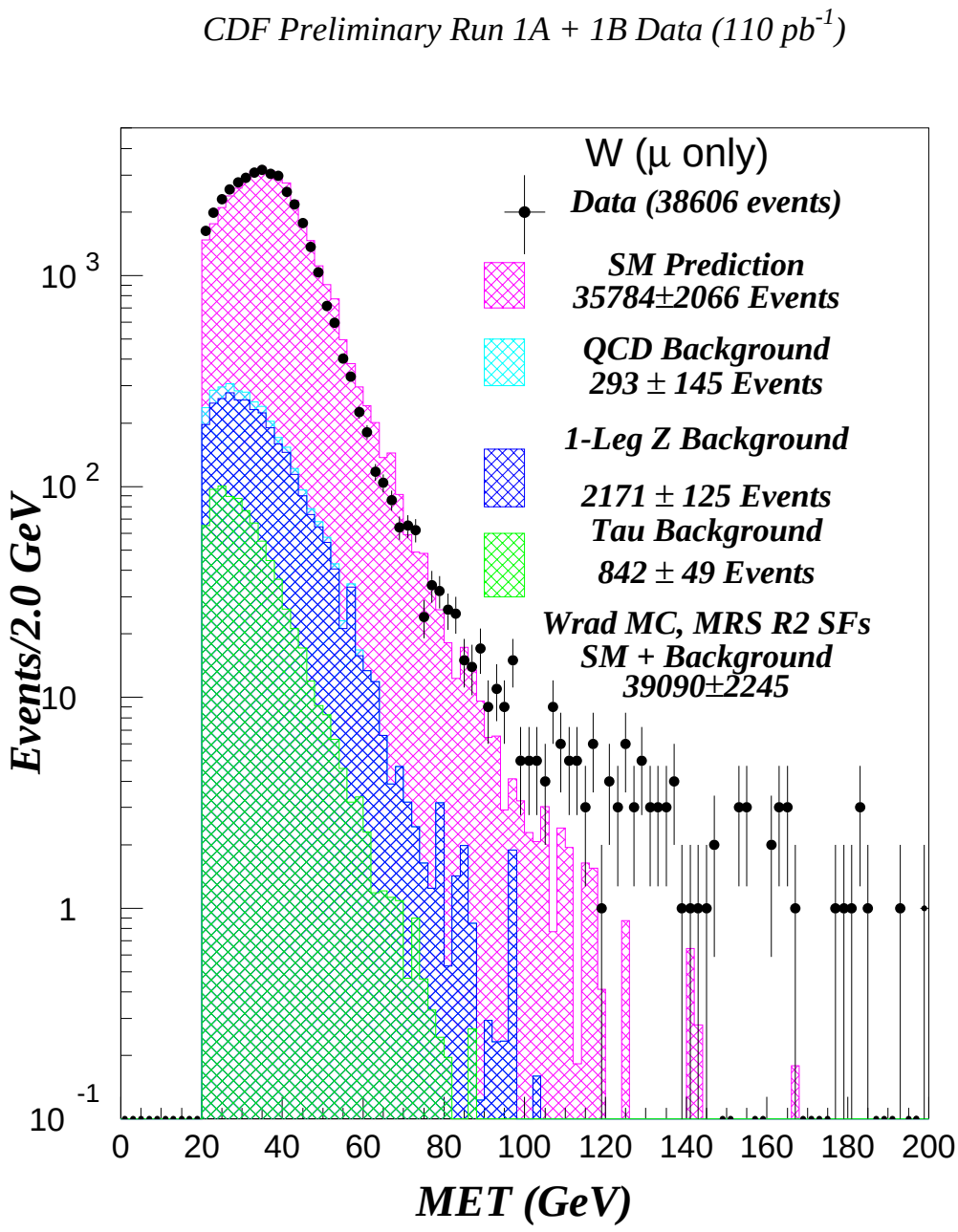

Figure 4.10: The missing transverse energy for W events from the inclusive muon sample on a logarithmic scale overlaid on the standard model prediction + background expectation.

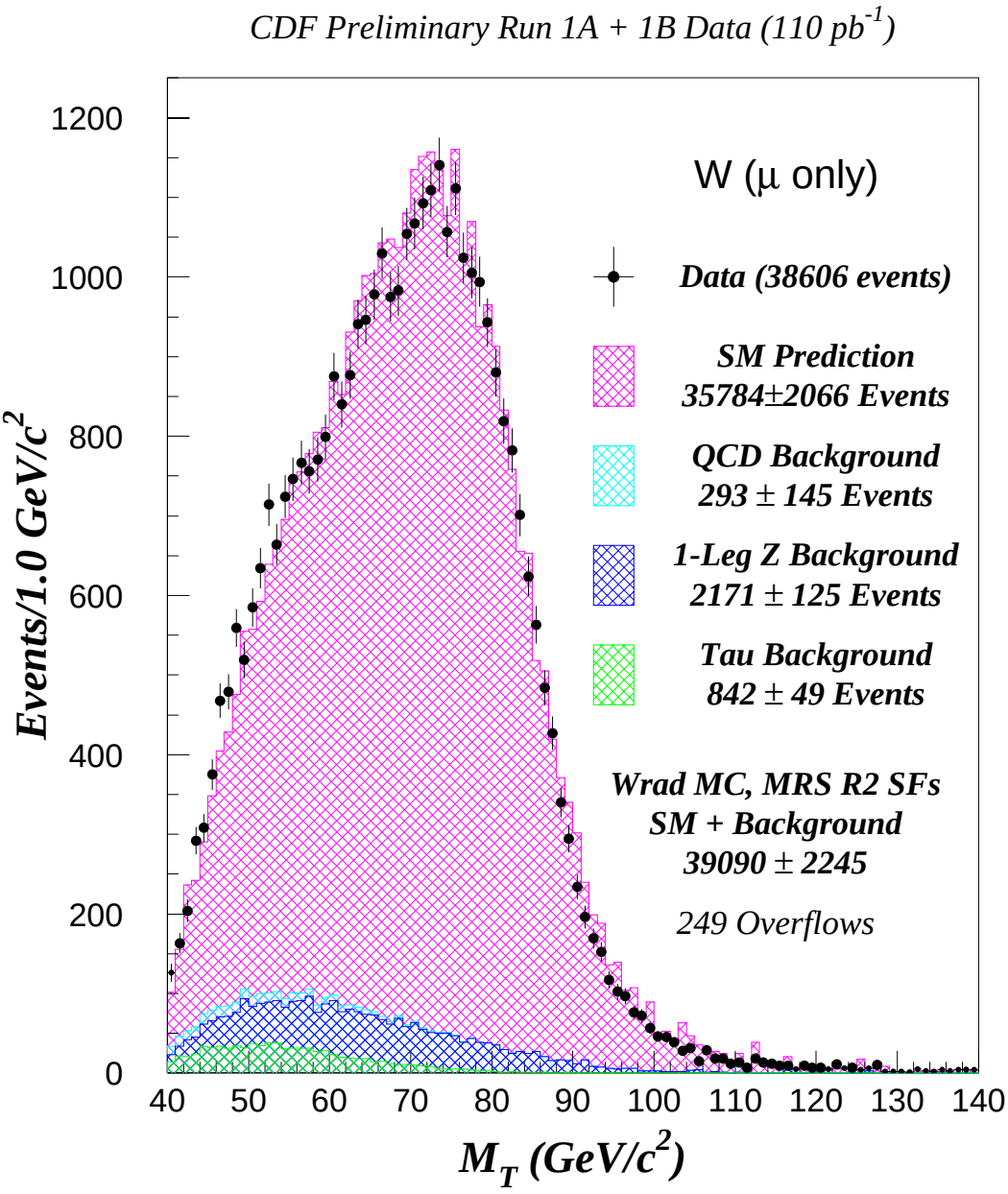

Figure 4.11: The W transverse mass for W events from the inclusive muon sample overlaid on the standard model prediction + background expectation.

4.3 Muon Efficiencies

In this analysis, a variety of event selection requirements were made in order to obtain nearly pure samples of W and Z bosons. Making quality cuts has the effect of reducing background contributions in the event samples and therefore increases the signal-to-noise (S/N) ratio. In the next section, we will estimate the background contribution in the inclusive data samples.

Now we ask the related question of how many real events fail due the quality requirements. Real events can fail these requirements because the energy loss mechanisms are statistical in nature. In order to calculate the cross section, we must know the real number of events that were produced.

To accomplish this, we needed to construct a sample of leptons and then study their response to the selection requirements. This was done using the second leg of Z boson events requiring a golden lepton in the event and then looking for a second lepton that satisfied the requirements: the dilepton mass be within 75 GeV/c^2 $< M_{ll} <$ 105 GeV/c^2, the leptons must have opposite charge sign and both legs must come from the same vertex $\mid Z^1_{VTX} - Z^2_{VTX} \mid <$ 5 cm. These requirements actually create a fairly clean sample of Z events. We then ask if the second leg passes a specific cut and use that ratio of the number of events that pass the selection requirement to the total number found to calculate the efficiency of that cut.

Denoting the efficiency for finding a lepton by ϵ, four possibilites must be considered:

- Both muons pass all the requirement: $\epsilon * \epsilon$
- The first leg passes the cut and the second does not: $\epsilon * (1 - \epsilon)$
- The first fails the cut and the second passes the cut: $(1 - \epsilon) * \epsilon$
- Neither leg passes the cut: $(1 - \epsilon) * (1 - \epsilon)$

Because of situation four, we are not able to measure the true number of events that were produced due to the inefficiency of the first leg. We only measure the first three

possibilities. Denoting the total number of Z events that were produced by N_{total}, we can calculate the total number that we will pass our cuts by

$$N_{find} = N_{total}(\epsilon^2 + \epsilon(1-\epsilon) + (1-\epsilon)\epsilon) \tag{4.3}$$

In order to determine the efficiency of the specific cut, we require that the cut is satisfied. So a subsample of these events will satisfy the cut. Therefore the

$$N_{pass} = N_{total} * \epsilon^2 \tag{4.4}$$

and defining the ratio R_c we then get

$$R_c = \frac{N_{pass}}{N_{find}} = \frac{N_{total}\epsilon^2}{N_{total}[\epsilon^2 + \epsilon(1-\epsilon) + (1-\epsilon)\epsilon]} \tag{4.5}$$

and solving for the efficiency of the cut we find

$$\epsilon = \frac{2 * R_c}{1 + R_c} \tag{4.6}$$

Due to the different detector regions the second lepton can pass through, we must determine the overall efficiencies for each region (e.g. CMUP, CMNP and CMX for muons).

4.3.1 Muon Identification Efficiencies

For golden muons the total overall efficiency, ϵ_{gold}, is determined from

$$\epsilon_{gold} = \epsilon_{had} \cdot \epsilon_{em} \cdot \epsilon_{iso} \cdot \epsilon_{trk} \cdot \epsilon_{stub} \cdot \epsilon_{dx} \cdot \epsilon_{cosmic} \tag{4.7}$$

where ϵ_{had} is the hadron energy cut efficiency, ϵ_{em} is the electromagnetic energy cut efficiency, ϵ_{iso} is the isolation cut efficiency, ϵ_{trk} is the CTC track finding efficiency, ϵ_{stub} is the stub reconstruction efficiency, ϵ_{dx} is the matching cut efficiency and ϵ_{cosmic} is the cosmic ray muon filter efficiency. For silver muons the overall efficiency, ϵ_{silver}, is determined from

$$\epsilon_{silver} = \epsilon_{had} \cdot \epsilon_{em} \cdot \epsilon_{iso} \cdot \epsilon_{trk} \tag{4.8}$$

Using the technique discussed in Section 7.1, we measured the efficiencies of the individual cuts and they summarized in Tables 4.5- 4.6. The silver efficiencies are summarized in Table 4.7.

The CTC track efficiency was determined from the electron W sample by identifying the W using the calorimeter only and then looking for a corresponding track [56]. It was measured to be $\epsilon_{trk} = 0.997 \pm 0.001$. The stub finding efficiency was measured in earlier studies [56] and was found to be $\epsilon_{stub} = 0.971^{+0.014}_{-0.022}$.

	CMUP		CMNP		CMX	
	R	ϵ	R	ϵ	R	ϵ
ϵ_{had}	708/739	$0.9786^{+0.0039}_{-0.0045}$	220/232	$0.9735^{+0.0076}_{-0.0099}$	571/597	$0.9777^{+0.0043}_{-0.0052}$
ϵ_{em}	684/739	$0.9613^{+0.0052}_{-0.0058}$	210/232	$0.9502^{+0.0107}_{-0.0130}$	559/597	$0.9671^{+0.0054}_{-0.0063}$
ϵ_{iso}	693/739	$0.9679^{+0.0047}_{-0.0055}$	213/232	$0.9573^{+0.0099}_{-0.0122}$	571/597	$0.9777^{+0.0043}_{-0.0052}$
ϵ_{cosmic}	710/739	$0.9800^{+0.0038}_{-0.0044}$	219/232	$0.9712^{+0.0081}_{-0.0103}$	592/597	$0.9958^{+0.0019}_{-0.0028}$
ϵ_{dx}	680/739	$0.9584^{+0.0056}_{-0.0061}$	208/232	$0.9455^{+0.0112}_{-0.0135}$	589/597	$0.9933^{+0.0025}_{-0.0032}$
ϵ_{cuts}	537/739	$0.8417^{+0.0112}_{-0.0117}$	156/232	$0.8041^{+0.0228}_{-0.0240}$	500/597	$0.9116^{+0.0090}_{-0.0098}$

Table 4.5: Golden muon identification efficiencies for Run 1B.

	CMUP		CMNP		CMX	
	R	ϵ	R	ϵ	R	ϵ
ϵ_{had}	98/102	$0.9800^{+0.0096}_{-0.0155}$	41/42	$0.9880^{+0.0101}_{-0.0269}$	93/94	$0.9947^{+0.0045}_{-0.0123}$
ϵ_{em}	98/102	$0.9800^{+0.0096}_{-0.0155}$	37/42	$0.9367^{+0.0285}_{-0.0410}$	87/94	$0.9613^{+0.0145}_{-0.0203}$
ϵ_{iso}	96/102	$0.9697^{+0.0122}_{-0.0179}$	39/42	$0.9630^{+0.0207}_{-0.0347}$	92/94	$0.9892^{+0.0070}_{-0.0139}$
ϵ_{cosmic}	98/102	$0.9800^{+0.0096}_{-0.0155}$	37/42	$0.9367^{+0.0285}_{-0.0410}$	94/94	$1.0000^{+0.0000}_{-0.0096}$
ϵ_{dx}	93/102	$0.9538^{+0.0156}_{-0.0205}$	40/42	$0.9756^{+0.0161}_{-0.0312}$	94/94	$1.0000^{+0.0000}_{-0.0096}$
ϵ_{cuts}	75/102	$0.8475^{+0.0304}_{-0.0339}$	27/42	$0.7826^{+0.0600}_{-0.0655}$	85/94	$0.9497^{+0.0169}_{-0.0225}$

Table 4.6: Golden muon identification efficiencies for Run 1A. The CMX values are not used in the Run 1a analysis.

	Run 1B		Run 1A	
Region	R	ϵ	R	ϵ
CMUP	1226/1424	$0.9253^{+0.0054}_{-0.0056}$	150/175	$0.9230^{+0.0156}_{-0.0184}$
CMNP	300/365	$0.9023^{+0.0124}_{-0.0135}$	56/65	$0.9256^{+0.0254}_{-0.0327}$
CMX	898/1077	$0.9094^{+0.0069}_{-0.0073}$	138/159	$0.9293^{+0.0157}_{-0.0188}$
PMIO	1004/1120	$0.9454^{+0.0051}_{-0.0055}$	187/207	$0.9492^{+0.0114}_{-0.0139}$

Table 4.7: Silver muon identification efficiencies in different regions for Run 1.

4.3.2 Muon Trigger Efficiencies

We only summarize the trigger efficiencies for muons and electrons. The overall trigger efficiency, T, is determined from

$$T = \epsilon_{L1} \cdot \epsilon_{L2} \cdot \epsilon_{L3} \tag{4.9}$$

where ϵ_{L1} is the Level 1 trigger efficiency, ϵ_{L2} is the Level 2 trigger efficiency and ϵ_{L3} is the Level 3 trigger efficiency. They were determined using the same method as above and are shown in Table 4.8. A more detailed study of the muon Run 1B average L2 trigger efficiencies is discussed in [52].

	Run 1B	Run 1A
CEM	0.938±0.002	0.952±0.003
CMUP	0.818±0.017	0.869±0.017
CMNP	0.639±0.043	0.873±0.017
CMX	0.571±0.021	-

Table 4.8: Overall lepton trigger efficiencies, T, for muons and electrons in Run 1.

4.4 Backgrounds in the Inclusive Muon W and Z Samples

4.4.1 Electroweak

The largest background to inclusive W production in the muon channel comes from Z decay where one of the muons is not detected by the CTC and produces a missing transverse energy signal mimicing a W event. This is called a one-legged Z event. The background is large because the CTC has limited η coverage $\mid \eta \mid < 1.7$ and the efficiency for finding a track falls with increasing $\mid \eta \mid$ for $\mid \eta \mid > 1.0$. We show the CTC tracking efficiency in Figure 4.12. Additionally, we rejected all events in the W sample that had a second muon passing the minimum ionization cuts with a momentum over 10 GeV/c^2, opposite charge to the golden muon and had a z position within 5 cm of the golden muon.

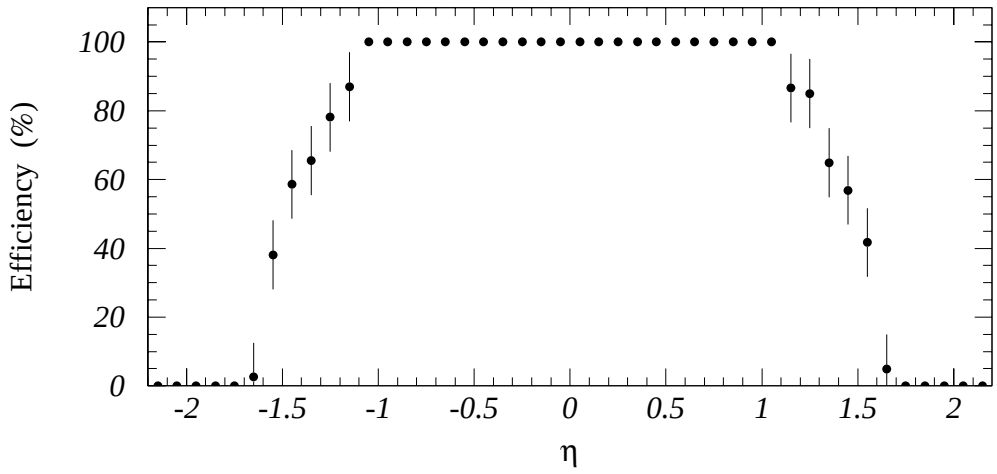

Figure 4.12: The CTC tracking efficiency as a function of η.

There also exists an additional class of residual one-legged muon Z events which arise from the inefficiencies of the identification cuts. The second leg can fail either the the minimum ionizing EM energy cut, the minimum ionizing HAD energy cut or the isolation requirement due to internal or external bremsstrahlung as the muon passed through the calorimeters. Since we do not simulate this, we removed events from the W sample in which the second leg failed ONLY one of the minimum ionizing cuts. This second leg was also required to have opposite sign and z position within 5 cm of the golden muon.

Another background is from the tauonic decay of a $W \rightarrow \tau\nu_\tau$ where the tauon decays into a muon faking real muonic W decay. Since the energy is shared by four final state particles, the P_T spectrum of the muon will be softer. Our P_T and transverse mass cuts reduce this background contribution. These backgrounds are estimated from Monte Carlo studies and shown in Table 4.13.

4.4.2 QCD in the Inclusive Muon W Sample

QCD dijet production, where one of the jets fluctuates to fake a lepton and the other jet is mismeasured to produce a fake missing E_T is a background to the inclusive W sample. We use two methods to measure the QCD background contribution.

The first method we used is similiar to the method in the W mass analysis as discussed in [32]. This method uses the angle between the lepton and the highest E_T jet in the event as the discriminating distribution.[5] If the event is W+jet, the decay of the W is not correlated with the jet; therefore, the angular distribution between the lepton and the jet will be flat. For a QCD dijet event, where the jets are back-to-back, we expect the angle between the jet which fluctuated to look like a lepton and the jet which produced the missing E_T to be peaked around 180°. In Figures 4.14- 4.15, we see the $\Delta\phi(l, jet)$ distribution for $E_T^{JET} > 7$ GeV for different muon regions (CMUP,CMNP and CMX). We removed events that had an electromagnetic fraction greater than 0.8 to prevent brem around the lepton simulating a QCD jet. The EM fraction is shown in Figure 4.13.

The lower end of the distribution (which should be flat) tapers off. This is due to the isolation requirement on the lepton. The distribution rises and levels off. The slight peak around 180° is from QCD dijets. We then fit the flat part of the distribution and extrapolated the line into the high $\Delta\phi$ region. The excess events above the line in the last two bins were taken to be the QCD background contribution. The results are shown in Table 4.9.

The second method used the lepton isolation. We relaxed the requirement on the lepton isolation. We then made the assumption that events with isolation greater than 0.1 are from QCD background. Strictly speaking, this region consists of QCD background events and W+jets. In Chapter 5, we discuss a method for estimating the W+jet fraction. We could not apply this method to the muon channel due to low statistics. We then extrapolated this fit into the signal region (isolation < 0.1).

[5] All jets are JTC96S corrected.

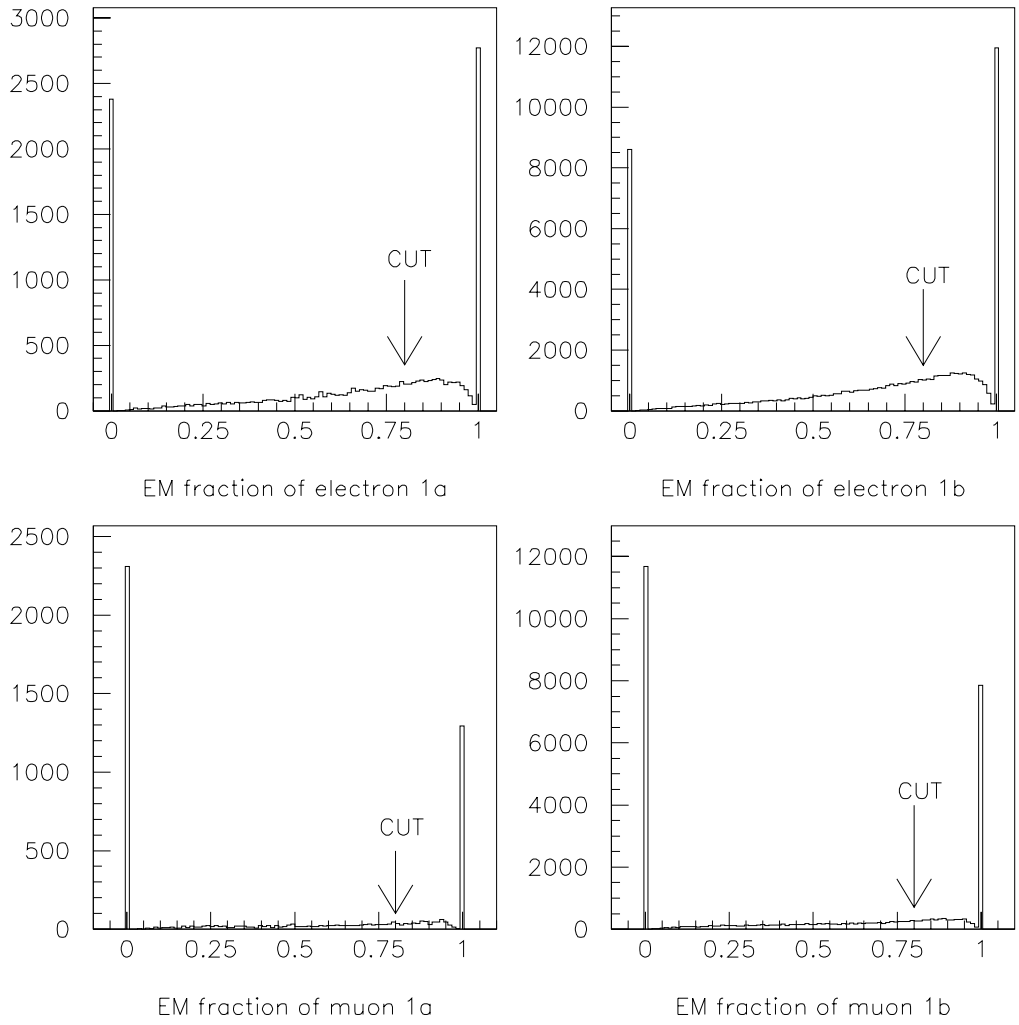

Figure 4.13: Electromagnetic fraction of the excess energy around the lepton in a cone $\Delta R = 0.7$. The upper plots are for electrons and the lower plots are for muons.

	Classification	% Background
Run 1b	CMUP	$0.66 \pm 0.26 \pm 0.09$
	CMNP	$0.98 \pm 0.52 \pm 0.46$
	CMX	$0.53 \pm 0.34 \pm 0.54$
Run 1a	CMUP	$1.53 \pm 0.62 \pm 0.02$
	CMNP	$0.70 \pm 0.96 \pm 0.53$

Table 4.9: The QCD percent background fraction in the W inclusive sample for muons using a linear fit to $\Delta\phi$ distribution between the lepton and the highest E_T jet and extrapolating to high $\Delta\phi$.

	Classification	% Background
Run 1b	CMUP	$0.25 \pm 0.22 \pm 0.08$
	CMNP	$0.64 \pm 0.80 \pm 0.27$
	CMX	$0.27 \pm 0.18 \pm 0.19$
Run 1a	CMUP	$0.56 \pm 0.54 \pm 0.21$
	CMNP	$1.11 \pm 0.16 \pm 0.27$

Table 4.10: The QCD percent background fraction in the W inclusive samples for muons using a single exponential fit to the high isolation region (non-signal) and extrapolating into the low isolation region (signal).

The number of events under this line gives an estimate of the QCD background contribution. The results of the fits are shown if Figures 4.16- 4.17 and are listed in Table 4.10.

4.4.3 QCD in the Inclusive Muon Z Sample

Similiar to the Ws, in the Z inclusive sample we relaxed the isolation requirement. We then fit the high isolation region and extrapolated into the signal region. The number of events under this extrapolated line gives us an estimate of the QCD background in the inclusive Z data. To estimate a systematic, we varied the slopes of the extrapolated distribution. Using this method for Zs gives an upper bound on the

	Classification	% Background
Run 1b	muon	$0.38 \pm 0.03 \pm 0.61$
Run 1a	muon	$1.29 \pm 0.11 \pm 0.17$

Table 4.11: The QCD percent background fraction in the Z inclusive samples for muons using a single exponential fit to the high isolation region (non-signal) and extrapolating into the low isolation region (signal).

QCD contribution. Actually, we expect the QCD background in the Z sample to be less than the W sample because of the requirement of two high P_T leptons which is harder to fake. The results of the fits are shown in Figure 4.18 and listed in Table 4.11.

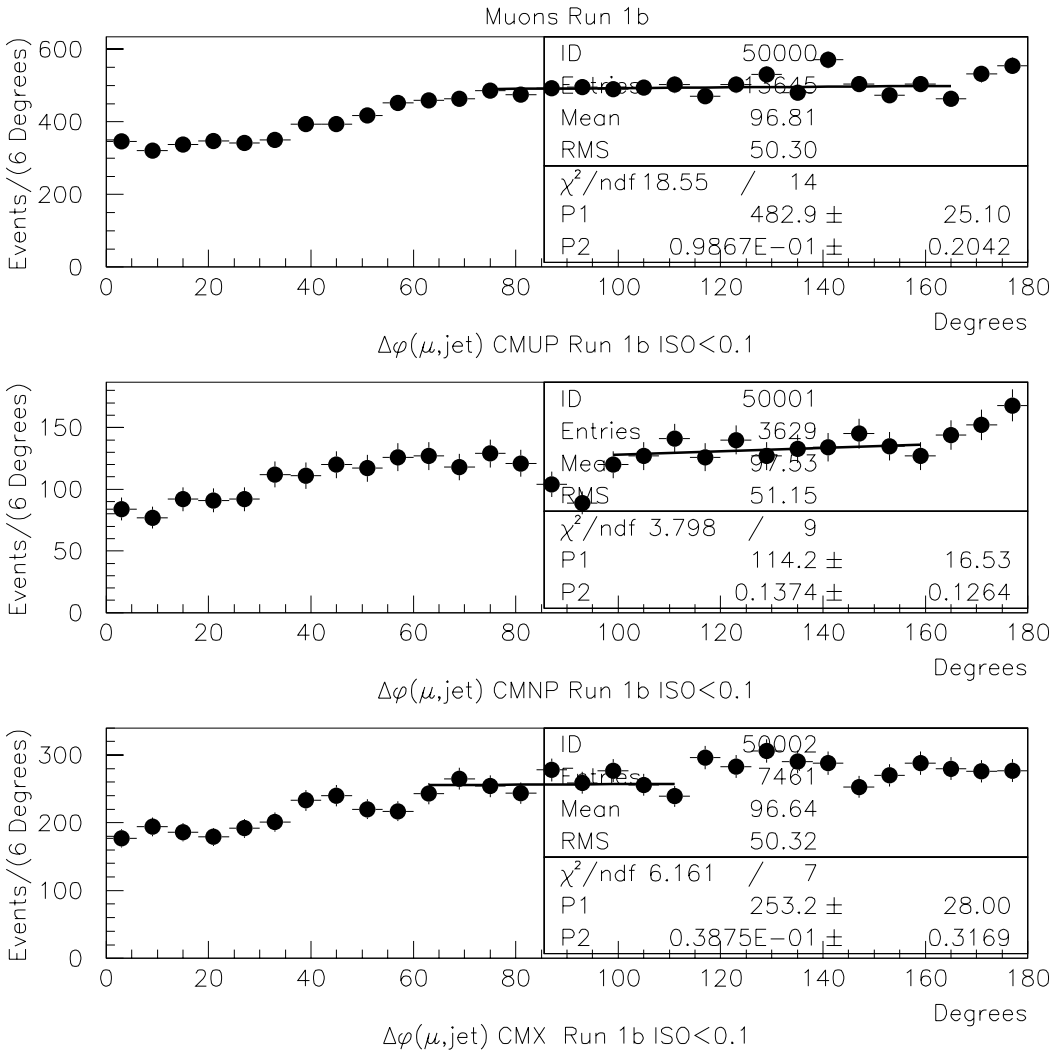

Figure 4.14: These distributions show the angle between the muon and the highest E_T jet in W events from Run 1b; the top diagram is for CMUP muons, the middle diagram is for CMNP muons and the bottom diagram is for CMX muons. Each distribution is fitted with a linear fit. The ranges of the fit were chosen to produce the lowest positive slope from the data.

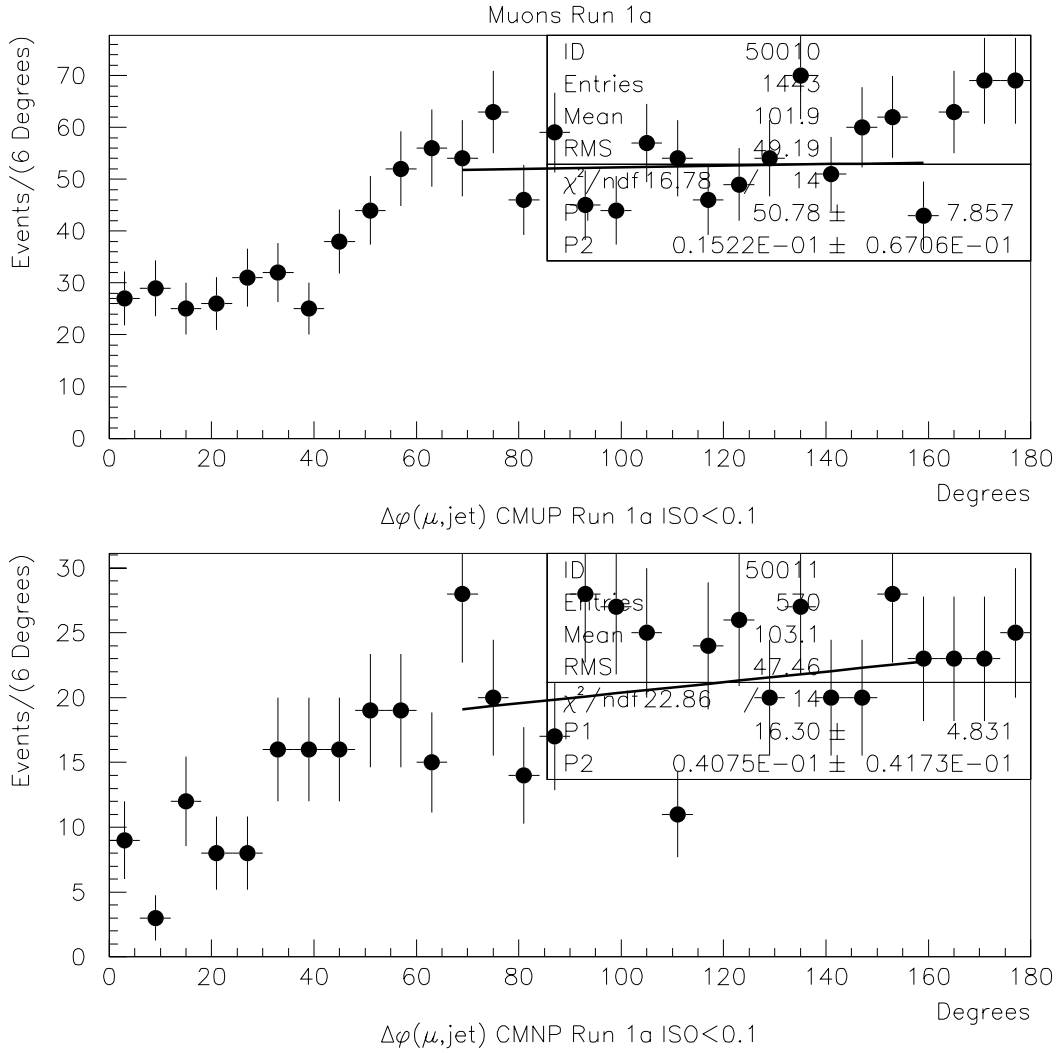

Figure 4.15: These distributions show the angle between the muon and the highest E_T jet in W events from Run 1a; the upper diagram is for CMUP muons and the lower diagram is for CMNP muons. Each distribution is fitted with a linear fit. The ranges of the fit were chosen to produce the lowest positive slope from the data.

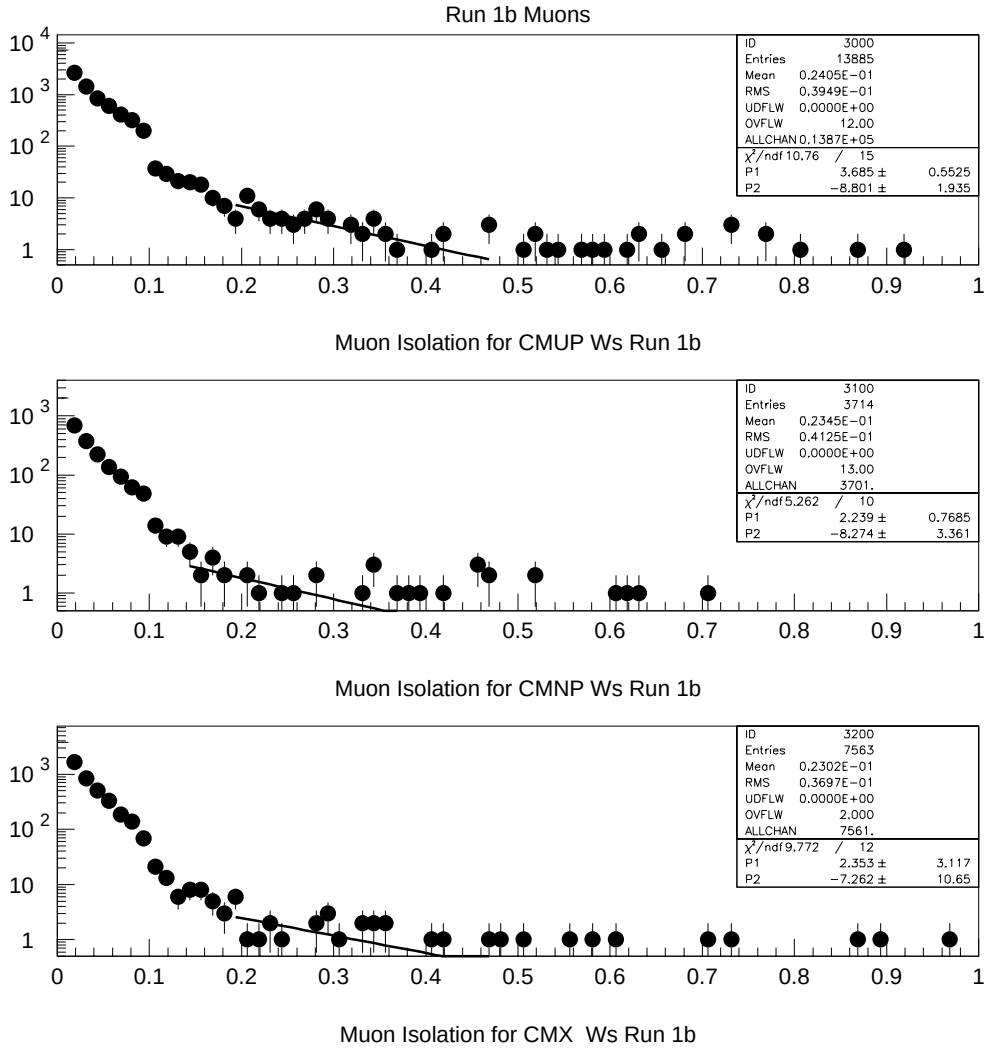

Figure 4.16: These distributions show the muon isolation for W events from Run 1b; the top diagram is for CMUP muons, the middle diagram is for CMNP muons, and the bottom diagram is for CMX muons. The high isolation region (nonsignal region) is fitted with an exponential and then extrapolated into the signal region to estimate the QCD background.

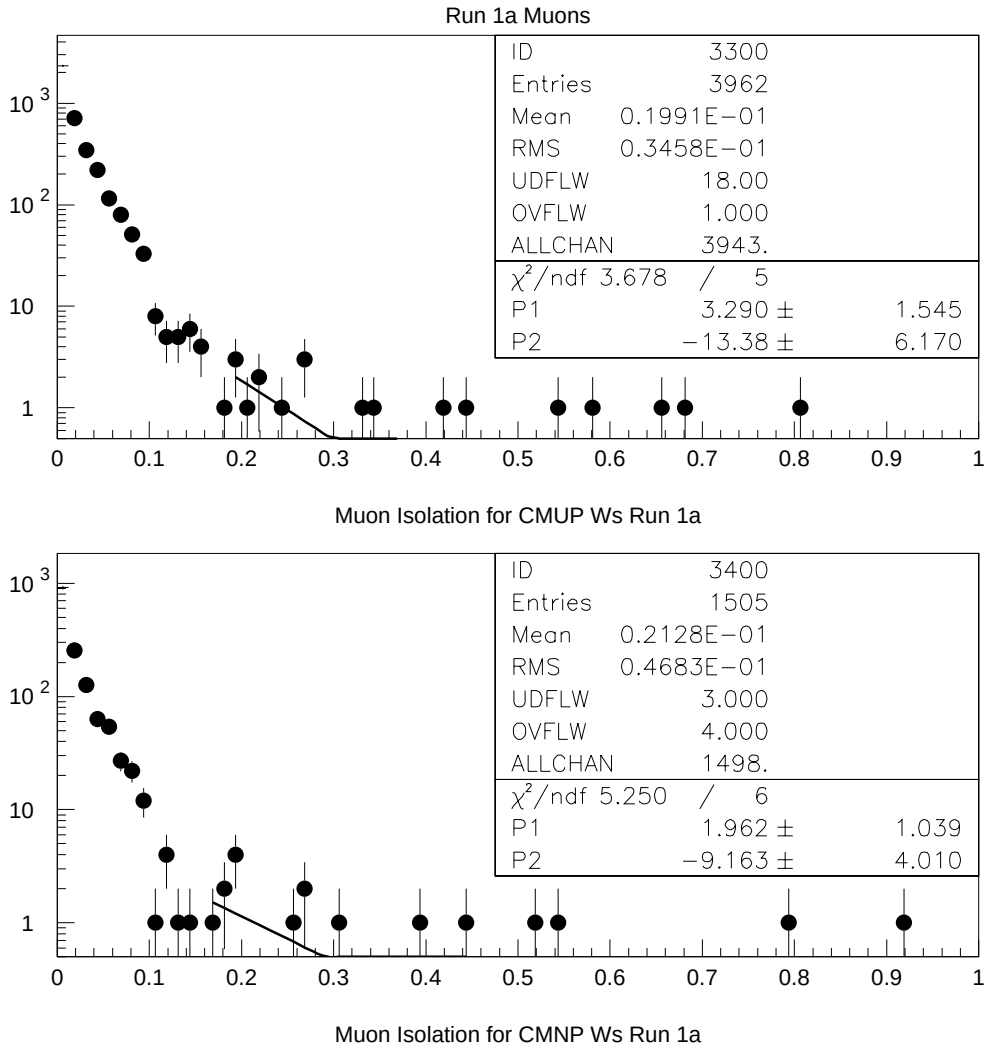

Figure 4.17: These distributions show the muon isolation for W events from Run 1a; the upper diagram is for CMUP muons and the lower diagram is for CMNP muons. The high isolation region (nonsignal region) is fitted with an exponential and then extrapolated into the signal region to estimate the QCD background.

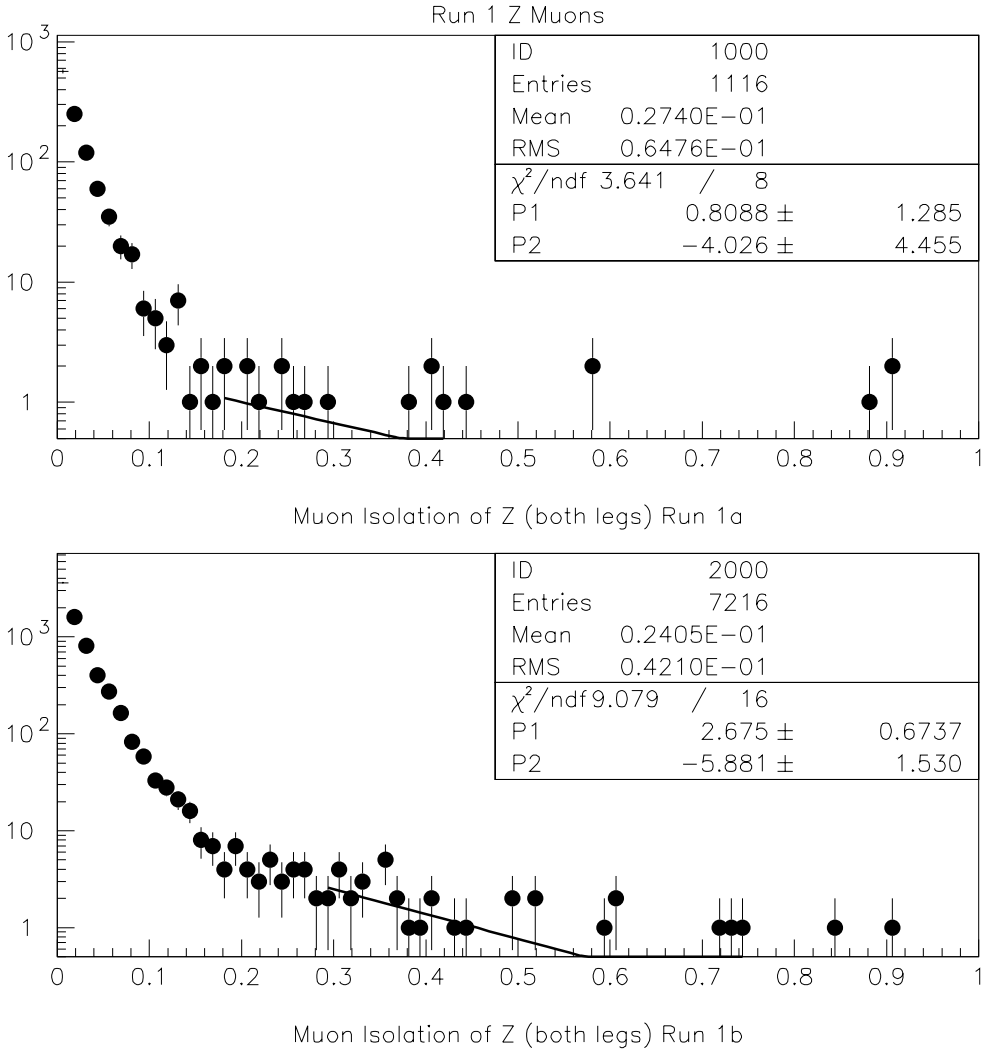

Figure 4.18: These distributions show the muon isolation for Z events (both legs) from Run 1a; the upper diagram is for CMUP muons and the lower diagram is for CMNP muons. The high isolation region (nonsignal region) is fitted with an exponential and then extrapolated into the signal region to estimate the QCD background.

4.5 Summary of Inclusive Muon Channel W/Z Results

We have described the construction and analysis of 110 pb^{-1} of inclusive muon data. We applied the standard quality cuts and constructed a Z and W sample. Using the data, we estimated the QCD background. The electroweak backgrounds were determined from Monte Carlo studies. We have plotted various kinematical distributions and find excellent agreement between data and standard model plus background predictions in the muon channel. We summarize our results numerically in Tables 4.12- 4.13. These samples will be used as a starting point for the construction of the muon $Z + \gamma$ and $W + \gamma$ samples.

Process	Run 1B	Run 1A	Total
Z	3548.7 ± 193.0	566.8 ± 33.4	4115.5 ± 226.4
QCD	13.1 ± 1.0	6.8 ± 0.6	19.9 ± 1.6
SM Total	3561.8 ± 193.0	573.6 ± 33.4	4135.4 ± 226.4
Data	3440	529	3969

Table 4.12: Comparison of inclusive Z yields between the standard model plus background expectation and data in the muon channel.

Process	Run 1B	Run 1A	Total
W	30976.1 ± 1768.6	4807.5 ± 297.3	35783.6 ± 2065.9
QCD	222.8 ± 106.7	70.4 ± 38.5	293.2 ± 145.2
OLZ	1901.0 ± 108.3	269.8 ± 16.7	2170.8 ± 125.0
$W \to \tau$	729.1 ± 41.6	112.6 ± 7.0	841.7 ± 48.6
SM Total	33829.0 ± 1921.5	5260.3 ± 323.3	39089.3 ± 2244.2
Data	33208	5398	38606

Table 4.13: Comparison of inclusive W yields between the standard model plus background expectation and data in the muon channel.

Chapter 5

The Electron Data Sample

5.1 Trigger Requirements

We will only summarize the electron requirements and results for completeness. The Level 1 trigger for electrons requires that one trigger tower (two physical towers) be above an 8 GeV threshold. At Level 2, the detector makes a decision based on whether the cluster is an electron or photon. For electrons, the ratio of hadronic to electromagnetic energy must be less the 1.125 and a stiff track of transverse momentum $P_T > 9.2$ GeV/c is matched to the cluster. At Level 3, a three-dimensional track with $P_T > 13$ GeV/c must point to the electron cluster with $E_T > 18$ GeV. Events passing these trigger requirements compose the "high P_T inclusive electron sample".

Using this sample, we made the additional requirements:

- The run must be on the good run list,
- For Run 1a, the event must pass one of the following Level 2 triggers:
  - CEM_9_SEED_SH_7_CFT_9_2,
  - CEM_16_ISO,
- For Run 1b, the event must pass one of the following Level 2 triggers:
  - CEM_16_ISO,
  - CEM_16_ISO_XCES,

- CEM_23_ISO_XCES,
- CEM_16_CFT_12,
- CEM_8_CFT_7_5,
- CEM_8_CFT_7_5_XCES,

These triggers are discussed in detail in Appendix A.

5.2 Electron Quality Selection Cuts

To improve the quality of events used in this analysis, we made the following offline requirements:

- Minimum transverse energy of the cluster (after all corrections are applied): $E_T \geq 20.0$ GeV,
- The location of the CEM cluster was required to be in a good fiducial region of the central calorimeter, as defined by the position determined from CES shower centroid information (11-channel clustering) and FIDELE fiducial cuts, with $|X_{ces}^{local}| \leq 21.0$ cm and $9.0 \leq |Z_{ces}| \leq 230.0$ cm (first 1/2 of CEM Tower 9).
- Maximum isolation of cluster: $I \equiv (E_{\Delta R=0.4}^{Excess})/E_T^{Cluster} \leq 0.10$,
- The cluster must satisfy the sliding HAD/EM relation: $HAD/EM < 0.055 + 0.00045 * E$,
- The χ_{ces}^2 in the CES of the cluster must be less than 10: $\chi_{ces}^2 < 10$,
- The lateral three tower shower shape of the cluster must be less than 0.2: $L_{SHR} < 0.2$, where $L_{SHR} = 0.14 \cdot \sum_i \frac{E_i^{meas} - E_i^{pred}}{\sqrt{0.14E^2 + \sigma^2(E_i^{pred})}}$,
- The E_c/P_{BC} ratio of the cluster, where E_c is the corrected energy and P_{BC} is the beam constrained momentum, must fall within certain limits: $0.5 \leq E_c/P_{BC} \leq 2.0$,

- Matching cuts between the CES shower profile of the cluster and the related CTC track must fall within appropriate limits: $|\Delta x| < 1.5$ cm, $|\Delta z| < 3.0$ cm,
- Required the Z_{vtx} position of the track related to the cluster be within the fiducial region of the detector: $|Z_{vtx}| \leq 60.0$ cm.

If at least one electromagnetic cluster in the event satisfied these quality requirements, we kept the event and then labeled the cluster as a "golden" electron.

The data sample used in this analysis was constructed from the combined data set from CDF's Run 1a and Run 1b. The two data sets combined give an integrated luminosity of 110 pb^{-1}, with Run 1a consisting of 19.7 pb^{-1} and Run 1b consisting of 90.4 pb^{-1}. We give the break down for each region in Table 5.1. The method for determining the luminosity using the beam-beam counters is discussed in [28, 29]. The Z and W event samples used in this analysis are generated from the Baur Monte

Data Sample	Region	$\int \mathcal{L}dt$
Inclusive Electron 1A	CEM	19.65 ± 0.71
Inclusive Electron 1B	CEM	90.35 ± 3.70

Table 5.1: Luminosity of the electron channel broken down by region. This corresponds to a total of 110 pb^{-1} of integrated luminosity for Run 1.

Carlos. They are passed through a detector simulation which yields the theoretical predictions for cross sections and event yields. We refer the reader to Chapter 6 for a more detailed discussion.

5.2.1 Electron Z Event Selection

We extracted Z events from the inclusive electron sample by requiring a second electron in either the central, plug or forward region of the detector. The second EM cluster had to satisfy the following requirements:

- The transverse energy of the second cluster in the CEM/PEM/FEM regions must be greater than 20/15/10 GeV, respectively,

- The second cluster must be isolated: $ISO4 \equiv \frac{E_{T,\Delta R=0.4} - E_{T,cluster}}{E_{T,cluster}} < 0.1$,
- The ratio of hadronic to electromagnetic energy of the second cluster must be less than 10% for all three regions: $HAD/EM < 0.1$,
- If the second cluster is in the central region, it must have an energy to momentum ratio less than 2.0: $E/P < 2.0$,
- If the second cluster is in the plug region, it must have a 3×3 tower χ^2 less than 3.0: $\chi^2_{3\times3} < 3.0$.

If a second cluster satisfies these requirements it is called a "silver" electron. For the event to be a Z, we also required:

- The charge of each leg must be of the opposite sign (central-central only): $Q_{gold} * Q_{silver} < 0$,
- The separation between the z vertex positions of the electrons must be below a minimum requirement: $\mid z_1 - z_2 \mid \leq 5.0$ cm,
- A minimum dielectron mass[1] greater than 70.0 GeV/c^2: $M_Z \geq 70.0$ GeV/c^2.

After all selection cuts, we found 7979 events that passed the Z requirements from the Run 1 data. We have displayed several kinematical distributions from the electron Z sample in Figures 5.1- 5.4. We also give the breakdown by region in Table 5.2.

[1]The dilepton mass requirement in the electron channel is higher than the muon channel because the detector has better resolution for electrons (i.e. the width of the dielectron mass peak is smaller).

Classification	Run 1A	Run 1B	Total
CEM-CEM	562	2499	3061
CEM-PEM	719	3323	4042
CEM-FEM	172	704	876
Total	1453	6526	7979

Table 5.2: Z yields from the Run 1 Inclusive Electron Sample separated by region.

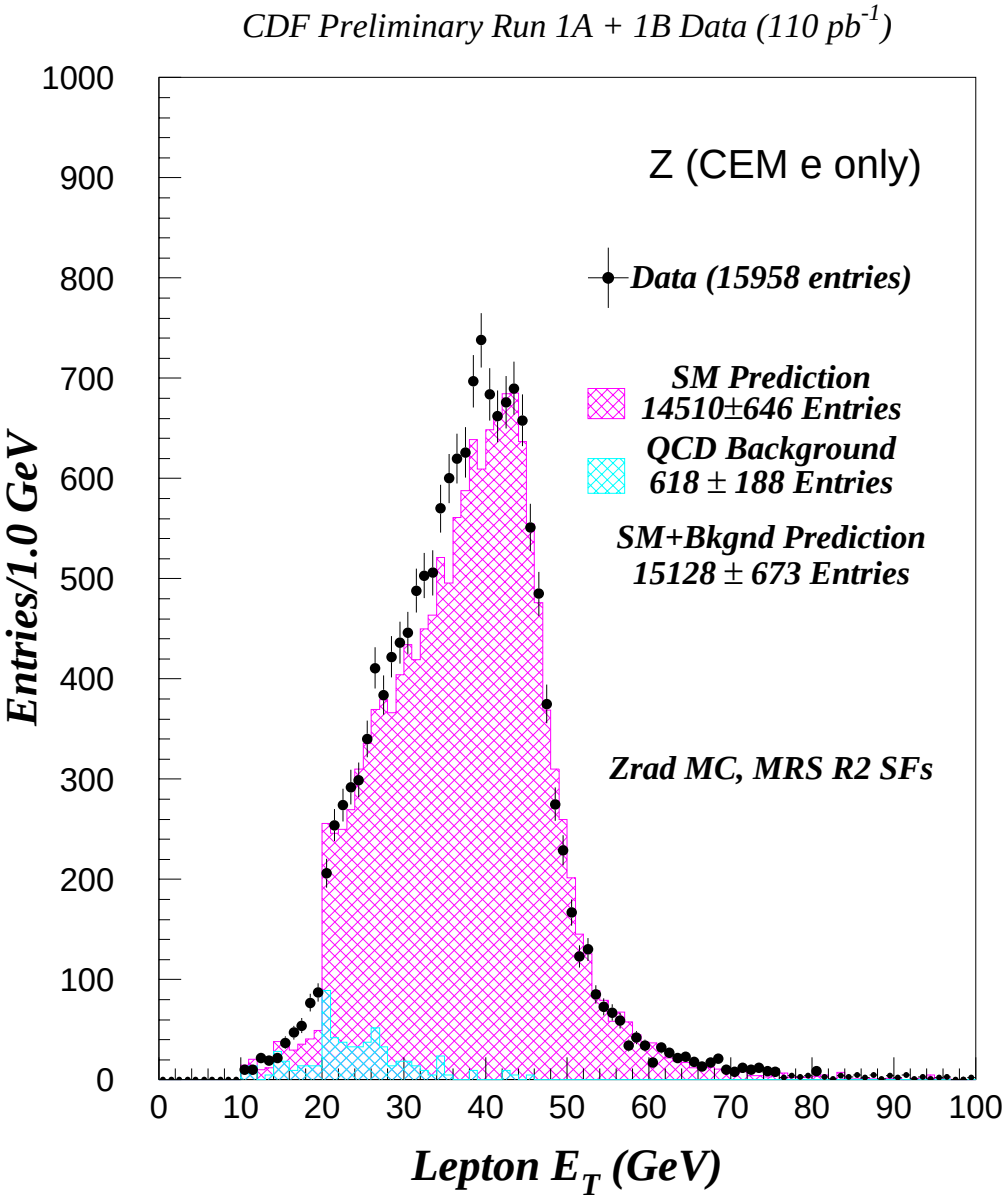

Figure 5.1: The electron transverse energy for Z events (both legs) from the inclusive electron sample overlaid on the standard model prediction plus background expectation.

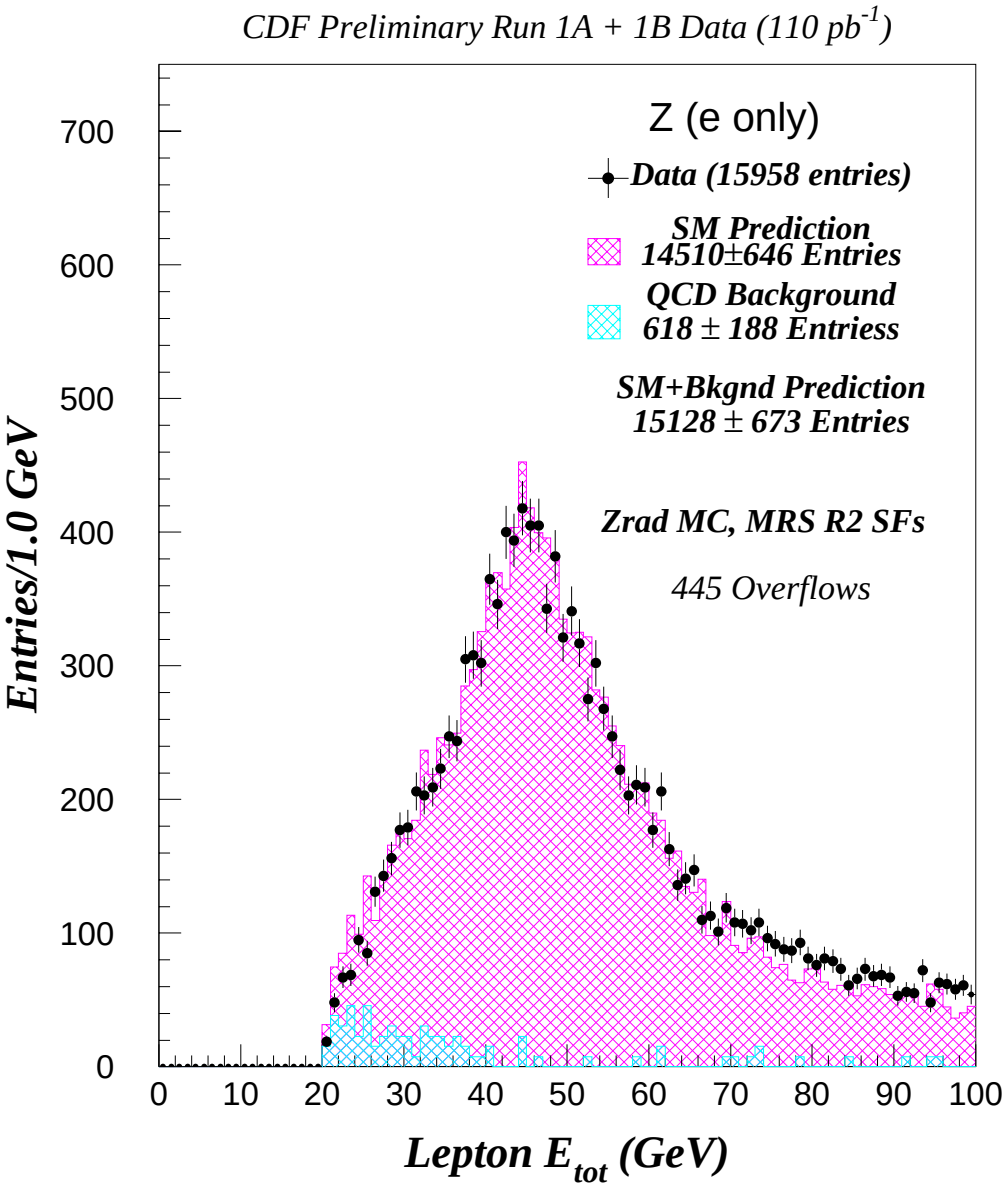

Figure 5.2: The electron total energy for Z events (both legs) from the inclusive electron sample overlaid on the standard model prediction plus background expectation.

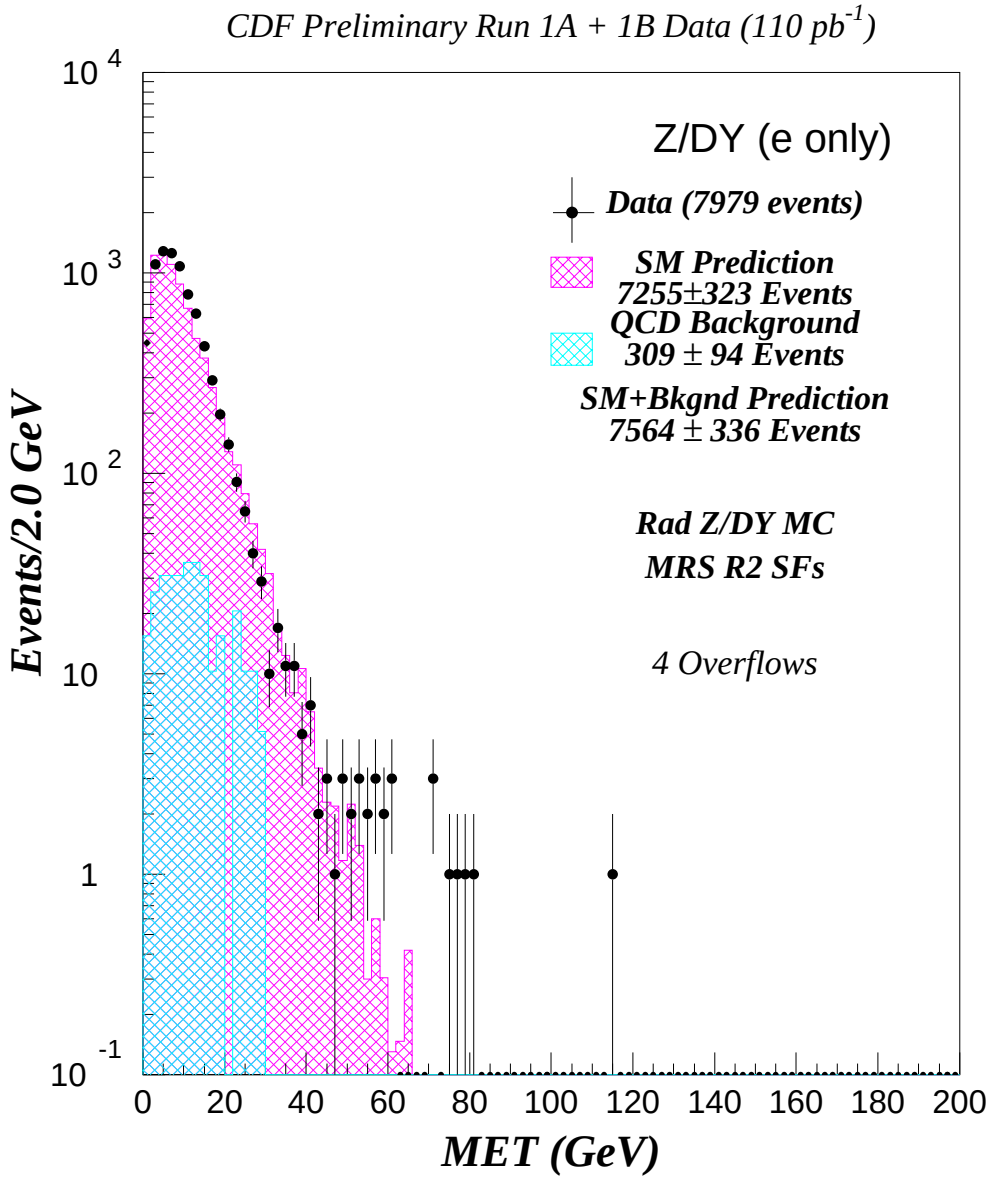

Figure 5.3: The missing transverse energy for Z events from the inclusive electron sample on a logarithmic scale overlaid on the standard model prediction plus background expectation.

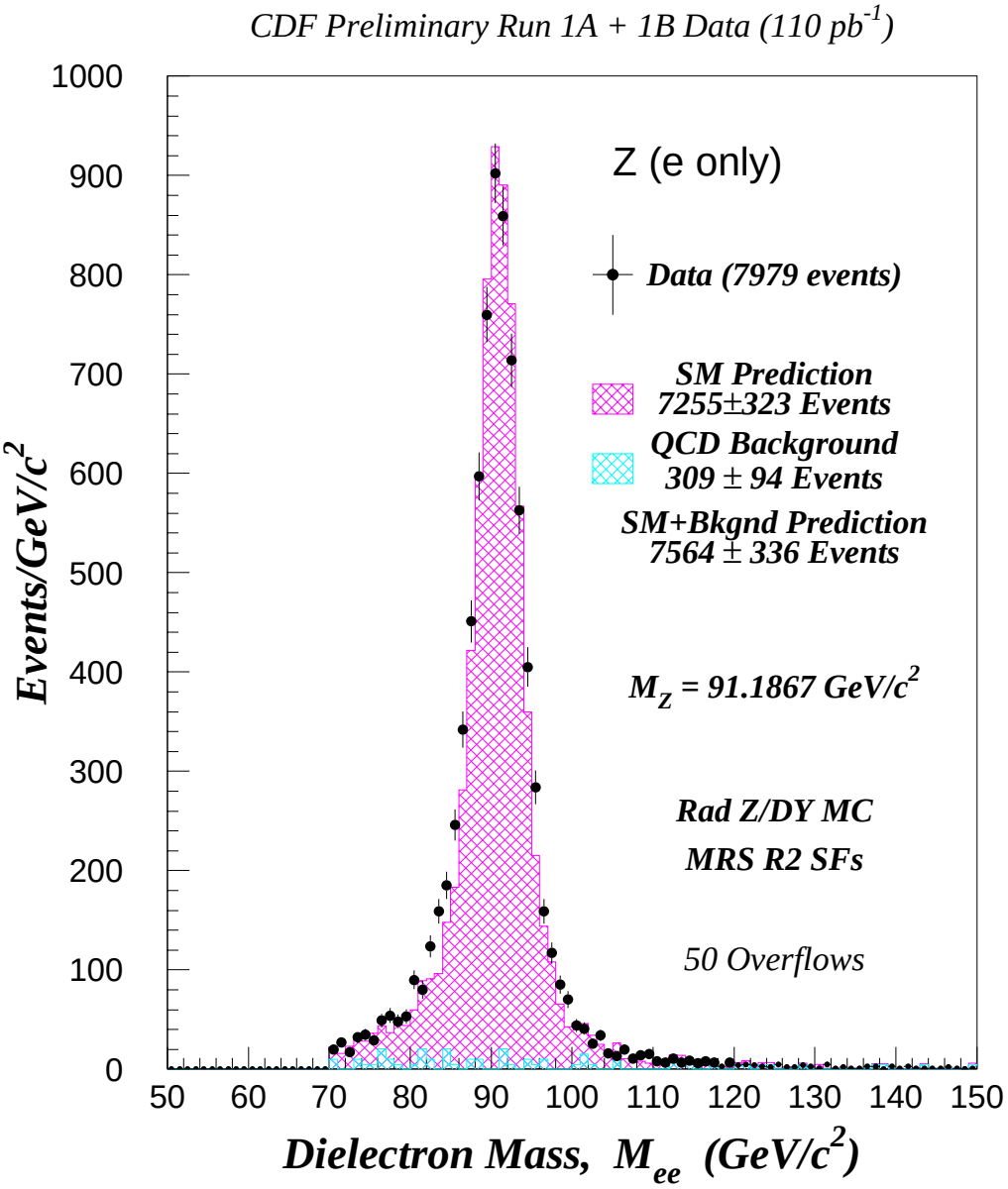

Figure 5.4: The dielectron mass for Z events from the inclusive electron sample overlaid on the standard model prediction plus background expectation.

5.2.2 Electron W Event Selection

After the missing transverse energy correction, we made the additional requirements on the golden electron sample:

- Minimum missing transverse energy: $\not\!\!E_T > 20.0$ GeV,
- Minimum transverse mass of the W: $M_T > 40.0$ GeV/c^2.
- The event is NOT consistent with a Z or a one-legged Z,

After all these quality cuts, we found 73118 events as shown in Table 5.3. We have plotted some kinematic distributions of the W events in Figures 5.5- 5.9.

Classification	Run 1A	Run 1B	Total
CEM	13290	60073	73363

Table 5.3: W yields from the Run 1 Inclusive Electron Sample.

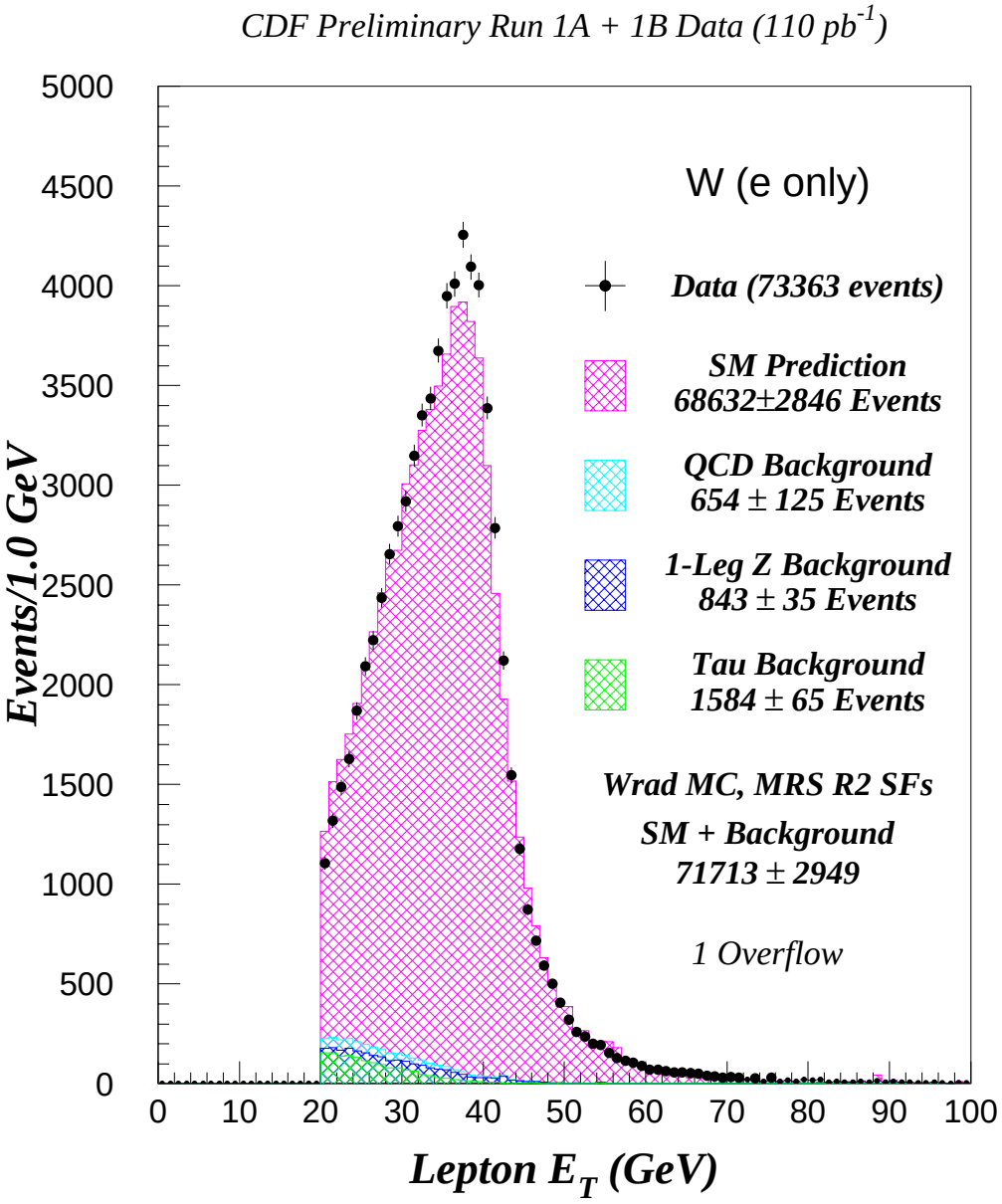

Figure 5.5: The electron transverse energy for W events from the inclusive electron sample overlaid on the standard model prediction plus background expectation.

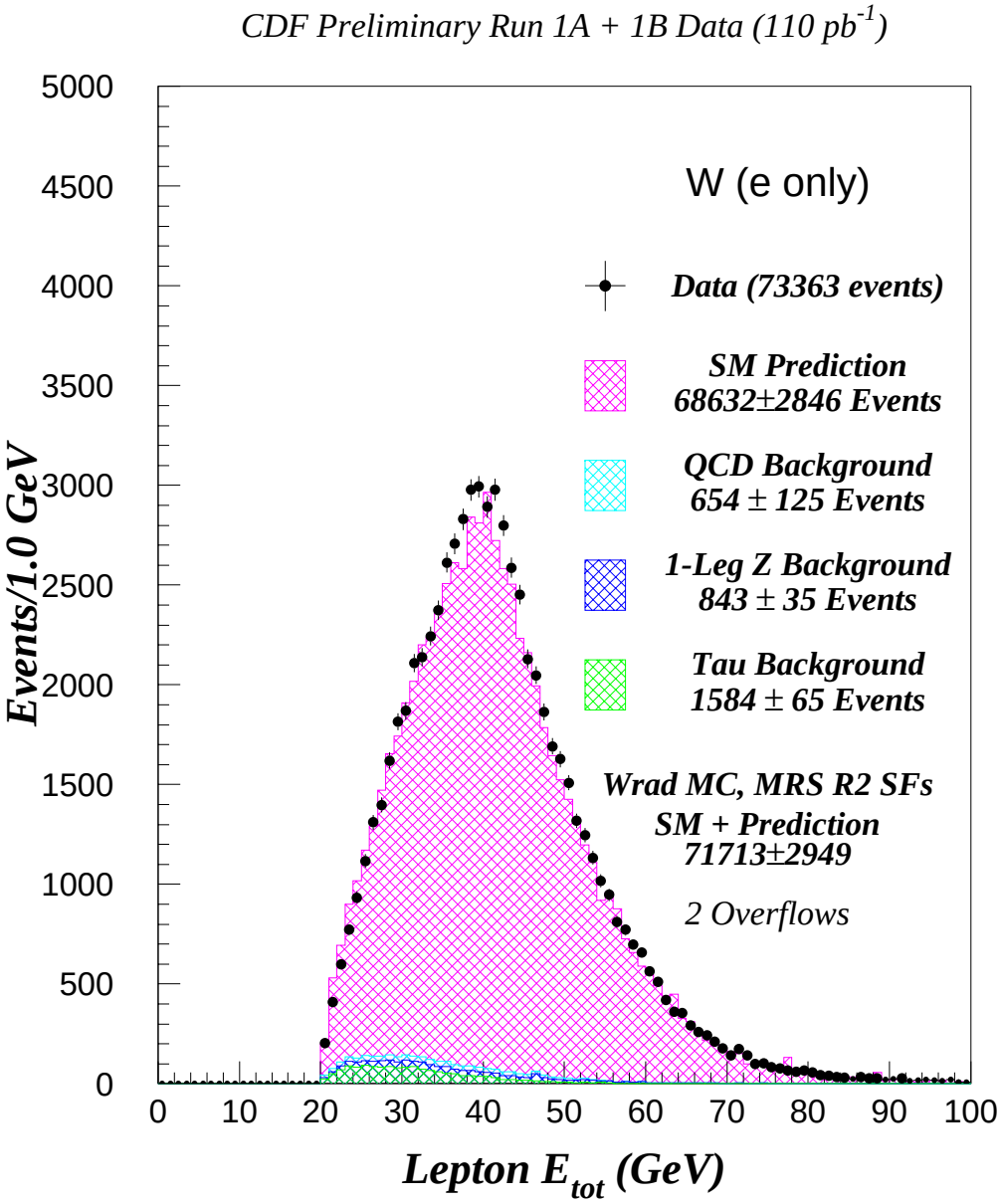

Figure 5.6: The total electron energy for W events from the inclusive electron sample overlaid on the standard model prediction plus background expectation.

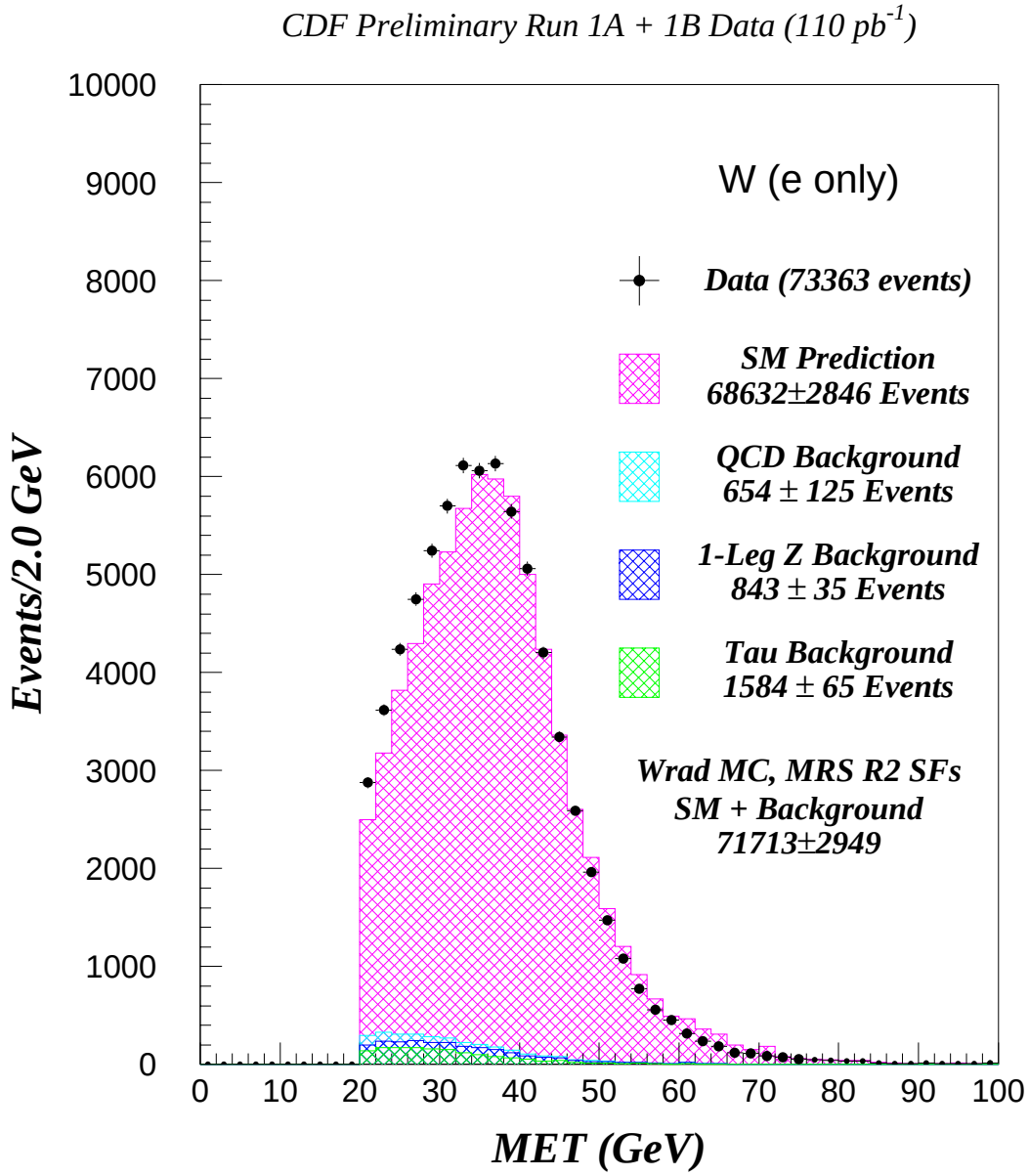

Figure 5.7: The missing transverse energy for W events from the inclusive electron sample on a linear scale overlaid on the standard model prediction plus background expectation.

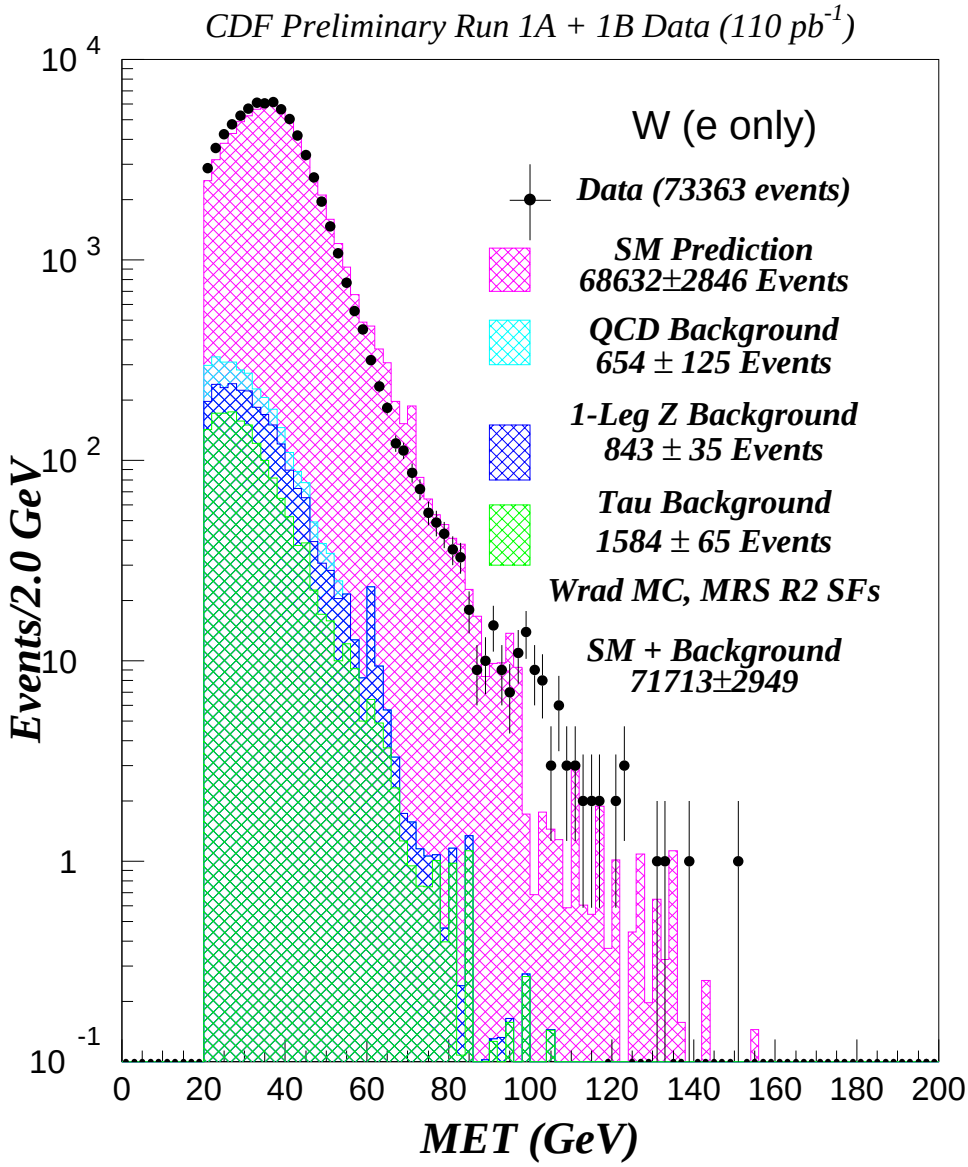

Figure 5.8: The missing transverse energy for W events from the inclusive electron sample on a logarithmic scale overlaid on the standard model prediction plus background expectation.

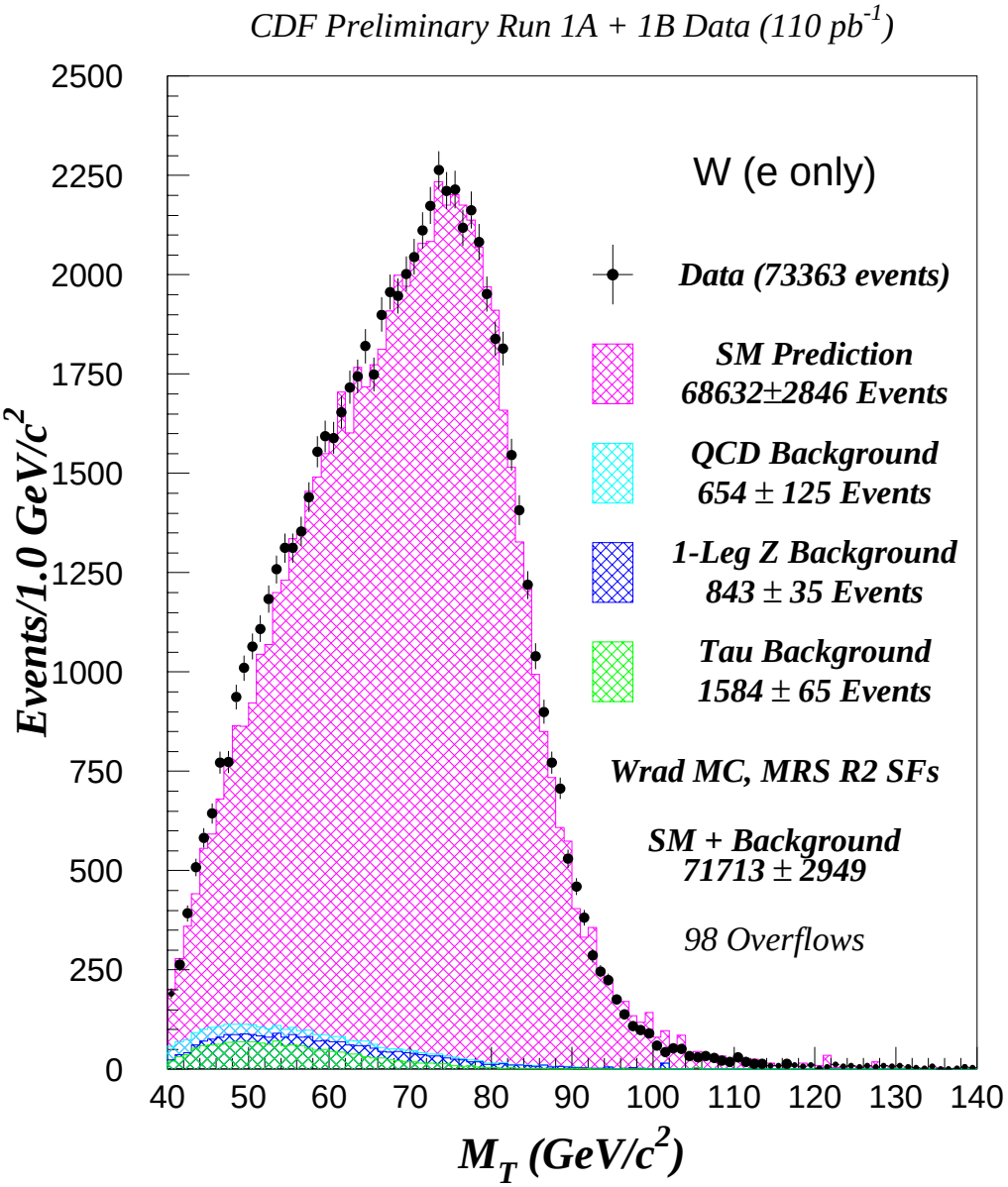

Figure 5.9: The W transverse mass for W events from the inclusive electron sample overlaid on the standard model prediction plus background expectation.

5.3 Electron Efficiencies

We summarize the electron efficiencies for completeness. The efficiency on the golden leg is computed from

$$\epsilon_{gold} = \epsilon_{had/em} \cdot \epsilon_{iso} \cdot \epsilon_{E/P} \cdot \epsilon_{lshr} \cdot \epsilon_{dx} \cdot \epsilon_{dz} \cdot \epsilon_{\chi^2_{strip}} \tag{5.1}$$

where $\epsilon_{had/em}$ is the efficiency of the hadron to electromagnetic energy ratio cut, ϵ_{iso} is the isolation cut efficiency, $\epsilon_{E/P}$ is the efficiency of the electron energy to momentum cut, ϵ_{lshr} is the transverse shower development cut efficiency, ϵ_{dx} and ϵ_{dz} are track matching cut efficiencies and $\epsilon_{\chi^2_{strip}}$ is the CES strip chi-squared cut efficiency.

Similiar to muons, the second leg for electron Zs can be in three different regions. For the silver leg in the central region

$$\epsilon^{CEM}_{silver} = \epsilon_{had/em} \cdot \epsilon_{iso} \cdot \epsilon_{E/P} \tag{5.2}$$

where these efficiencies are defined above. For the plug region

$$\epsilon^{PEM}_{silver} = \epsilon_{had/em} \cdot \epsilon_{iso} \cdot \epsilon_{\chi^2_{3\times3}} \tag{5.3}$$

where $\epsilon_{\chi^2_{3\times3}}$ is the efficiency for the pad 3×3 requirement. For the forward region

$$\epsilon^{FEM}_{silver} = \epsilon_{had/em} \cdot \epsilon_{iso} \tag{5.4}$$

where these efficiencies are defined above. The identification efficiencies for Run 1B are summarized in Table 5.4. The silver electron efficiencies for Run 1 are listed in Table 5.5.

5.4 Backgrounds in the Inclusive Electron W and Z Samples

5.4.1 Electroweak

The electroweak backgrounds in the inclusive electron W and Z samples are completely equivalent to the muon sample. The one-legged Z events are removed by rejecting events with a second isolated track with $P_T > 10$ GeV/c, opposite charge

	R	ϵ
$\epsilon_{had/em}$	1621/1639	$0.9945^{+0.0012}_{-0.0017}$
ϵ_{iso}	1545/1639	$0.9705^{+0.0031}_{-0.0034}$
ϵ_{lshr}	1592/1639	$0.9855^{+0.0021}_{-0.0025}$
$\epsilon_{E/P}$	1361/1639	$0.9073^{+0.0055}_{-0.0059}$
ϵ_{dx}	1626/1639	$0.9960^{+0.0012}_{-0.0015}$
ϵ_{dz}	1636/1639	$0.9991^{+0.0005}_{-0.0009}$
$\epsilon_{\chi^2_{strip}}$	1510/1639	$0.9590^{+0.0036}_{-0.0038}$
ϵ_{cuts}	1163/1639	$0.8301^{+0.0078}_{-0.0079}$

Table 5.4: Individual golden electron identification efficiencies for Run 1B.

	Run 1B	Run 1A
CEM	0.903±0.005	0.917±0.008
PEM	0.902±0.009	0.909±0.014
FEM	0.875±0.028	0.858±0.044

Table 5.5: Silver electron identification efficiencies for Run 1.

sign to the golden electron, Z_{VTX} position difference less than 5 cm and dielectron mass less than 70 GeV/c^2. The one-legged Z background in the electron channel is not the largest as in the muon channel because the acceptance for electrons is greater.

Again, another background is from the tauonic decay of a $W \rightarrow \tau\nu_\tau$ where the tauon decays into a electron faking real electron W decay. Since the energy is shared by four final state particles, the P_T spectrum of the electron will be softer. Our P_T and transverse mass cuts reduce this background contribution. These backgrounds are estimated from Monte Carlo studies and shown in Table 5.11.

5.4.2 QCD in the Inclusive Electron W Sample

We have used the same methodology for determining the QCD background in the electron sample as discussed in Chapter 4. Using the first method, we plotted the

$\Delta\phi(l, jet)$ for the respective electron regions for Run 1 in Figure 5.10. The results of these fits are shown in Table 5.6.

Using the second method, we plotted the isolation for the respective electron regions for Run 1 in Figure 5.11. We have added a refinement due to the increased statistics in the electron channel. Originally, we made the assumption that all events with isolation greater than 0.1 are from QCD. Actually, these events are composed of QCD and real W+jet events. If all events were from QCD, then plotting $\Delta\phi(l, jet)$ for these events should produce a peak around 180°. This distribution is shown in Figure 5.12. This is indeed the case, but the peaking of this distribution occurs on top of a flat component. This flat component is the W+jet background contribution to the high isolation data. We fitted this distribution to obtain an estimate of the W+jet contribution. The results for the corrected QCD background estimate are shown in Table 5.7. The numbers for the W+jet background fraction in the high isolation data are shown in Table 5.8.

	Classification	% Background
Run 1b	Central	$0.993 \pm 0.142 \pm 0.312$
Run 1a	Central	$0.431 \pm 0.297 \pm 0.367$

Table 5.6: The QCD percent background fraction in the W inclusive sample for electrons using a linear fit to $\Delta\phi$ distribution between the electron and the highest E_T jet and extrapolating to high $\Delta\phi$.

	Classification	% Background
Run 1b	Central	$2.7 \pm 1.1 \pm 0.31$
Run 1a	Central	$1.6 \pm 0.3 \pm 0.32$

Table 5.7: The QCD percent background fraction in the W inclusive sample for electrons using a single exponential fit to the high isolation region (nonsignal) and extrapolating into the signal region. The numbers have been corrected for the W+jet contribution.

	Classification	% Background
Run 1b	Central	0.46±0.06±0.02
Run 1a	Central	0.41±0.14±0.07

Table 5.8: The W+jet percentage background fraction in the high isolation tail for W inclusive electron events.

5.4.3 QCD in the Inclusive Electron Z Sample

Identically to the muons, in the electron Z sample we relaxed the isolation requirement. We then fit the high isolation region and extrapolated into the signal region. The number of events under this extrapolated line gives us an estimate of the QCD background in the inclusive Z data. To estimate a systematic, we varied the slopes of the extrapolated distribution. Using this method for Zs gives an upper bound on the QCD contribution. The results of the fits are shown in Figure 5.13 and listed in Table 5.9.

	Classification	% Background
Run 1b	electron	3.66 ± 0.95 ± 1.24
Run 1a	electron	4.84 ± 2.20 ± 0.65

Table 5.9: The QCD percent background fraction in the Z inclusive sample for electrons using a single exponential fit to the high isolation region (nonsignal) and extrapolating into the signal region.

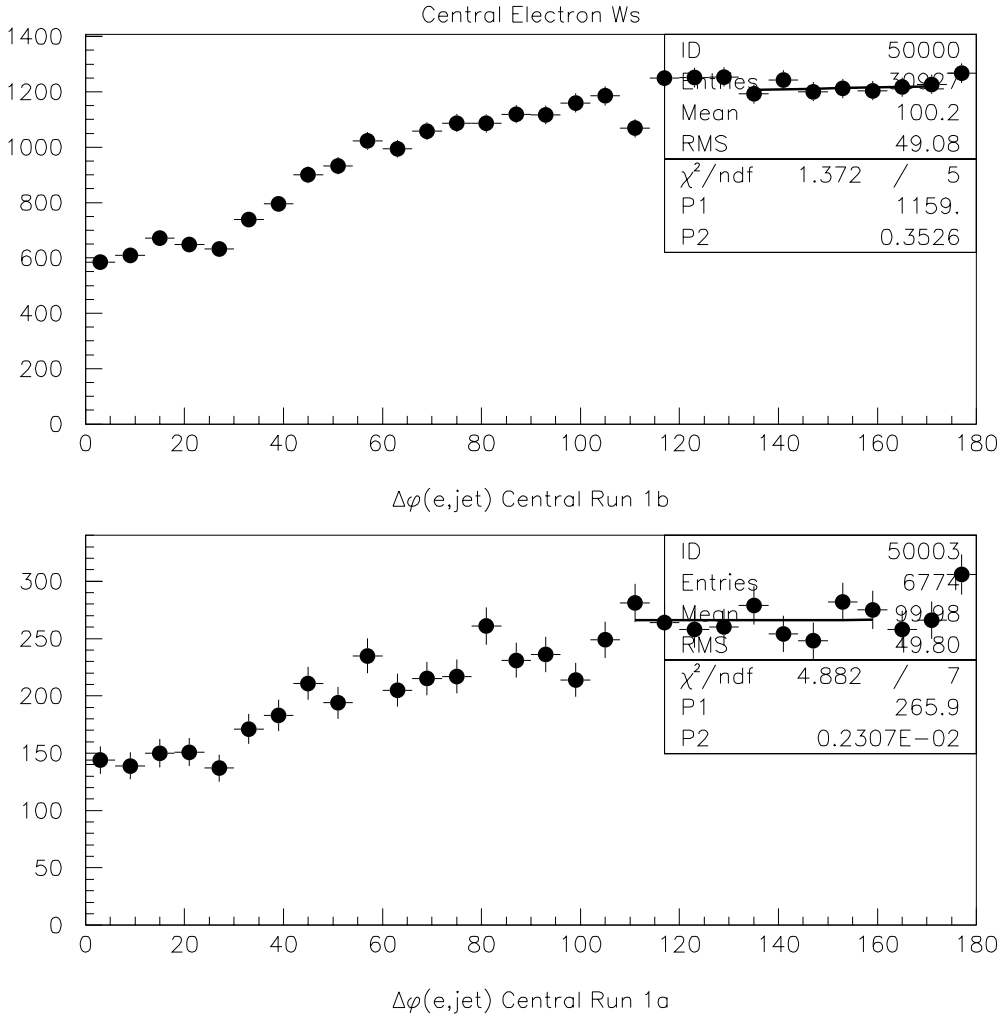

Figure 5.10: These distributions show the angle between the electron and the highest E_T jet in W events for Run 1; the top diagram is for central electrons in Run 1b and the bottom diagram is for central electrons in Run 1a. Each distribution is fitted with a linear fit. The ranges of the fit were chosen to produce the lowest positive slope from the data.

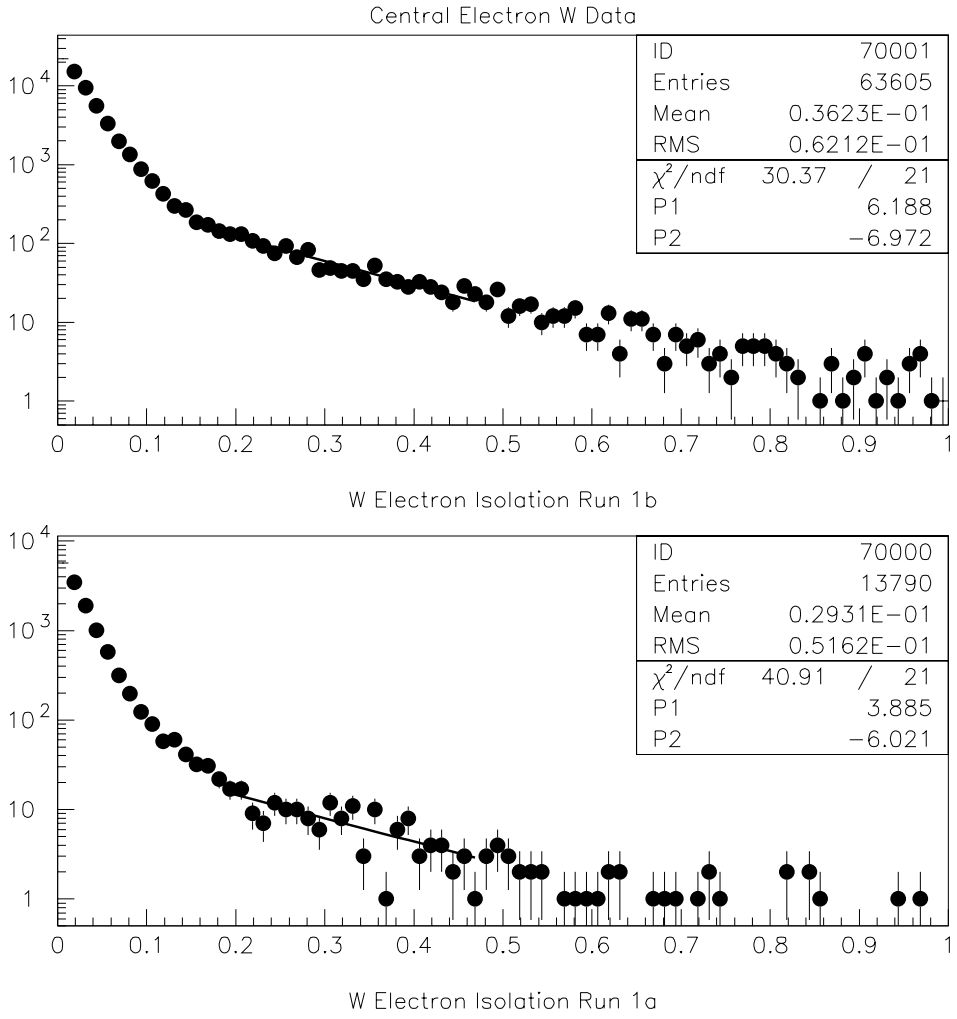

Figure 5.11: These distributions show the angle between the electron and the highest E_T jet in W events for Run 1; the top diagram is for central electrons in Run 1b and the bottom diagram is for central electrons in Run 1a. The high isolation region (nonsignal region) is fitted with an exponential and then extrapolated into the signal region to estimate the QCD background.

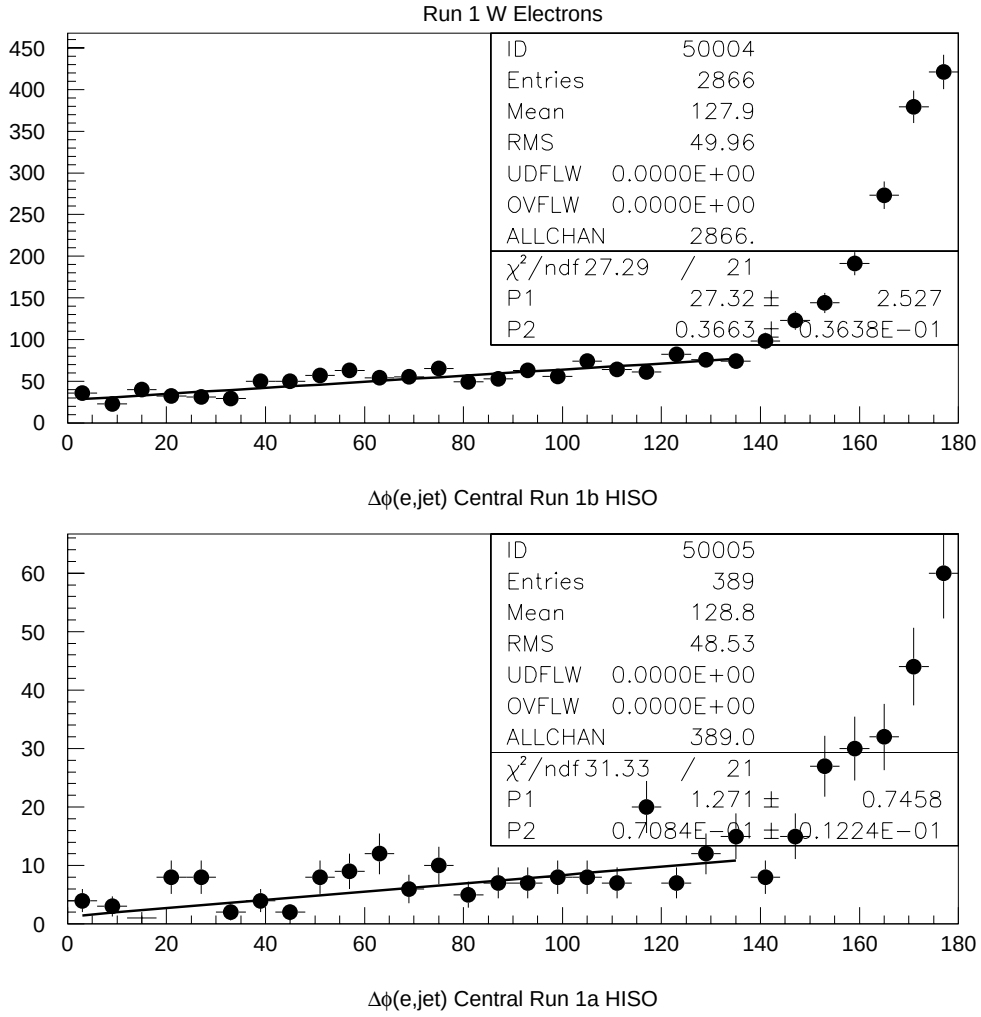

Figure 5.12: These distributions show the angle between the electron and the highest E_T jet for events with high isolation (ISO$>$ 0.1) in Run 1; the top diagram is for central electrons in Run 1b and the bottom diagram is for central electrons in Run 1a. Each distribution is fitted with a linear fit. The peak at 180° is the QCD contribution and the flat component is the W+jet contribution.

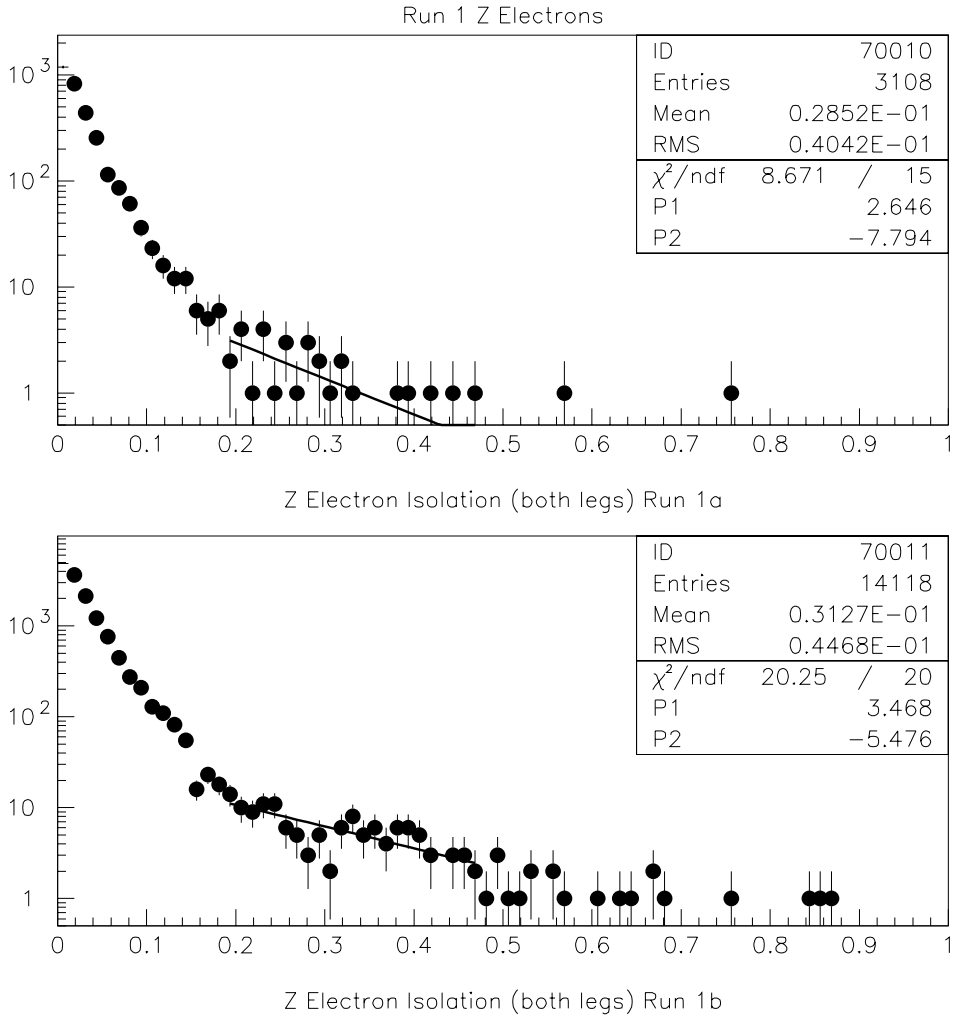

Figure 5.13: These distributions show the electron isolation for Z events (both legs) from Run 1a; the upper diagram is for central electrons in Run 1b and the lower diagram is for Run 1a. The high isolation region (nonsignal region) is fitted with an exponential and then extrapolated into the signal region to estimate the QCD background.

5.5 Summary of Inclusive Electron Channel W/Z Results

We have described the construction and analysis of 110 pb^{-1} of inclusive electron data. We applied the standard quality cuts and constructed a Z and W sample. Using the data, we estimated the QCD background. The electroweak backgrounds were determined from Monte Carlo studies. We have plotted various kinematical distributions and find excellent agreement between data and standard model plus background predictions in the electron channel. We summarize our results numerically in Tables 5.10- 5.11. These samples will be used as a starting point for the construction of the $Z + \gamma$ and $W + \gamma$ sample.

Process	Run 1B	Run 1A	Total
Z	5932.4 ± 263.2	1322.2 ± 59.8	7254.6 ± 323.0
QCD	238.9 ± 62.0	70.3 ± 32.0	309.2 ± 94.0
SM Total	6171.3 ± 270.4	1392.5 ± 67.8	7563.8 ± 336.4
Data	6526	1453	7979

Table 5.10: Break down of inclusive Z yields from the standard model in the electron channel.

Process	Run 1B	Run 1A	Total
W	56162.6 ± 2357.6	12469.1 ± 488.2	68631.7 ± 2845.8
QCD	596.5 ± 85.3	57.3 ± 39.5	653.8 ± 124.8
OLZ	693.0 ± 29.1	149.7 ± 5.9	842.7 ± 35.0
$W \to \tau$	1296.3 ± 53.3	287.8 ± 11.3	1584.1 ± 64.6
SM Total	58748.4 ± 2441.5	12963.9 ± 506.8	71712.3 ± 2948.0
Data	60073	13290	73363

Table 5.11: Break down of inclusive W yields from the standard model in the electron channel.

Chapter 6

The $W + \gamma$ and $Z/DY + \gamma$ Data Samples

6.1 Photon Selection

After we selected muon and electron channel inclusive W and Z boson data sets, we applied a common set of selection cuts to these four samples to search for W/Z events accompanied by high energy photons. This analysis extends previous CDF $V + \gamma$ analyses by searching for photons with high rapidity in the plug region of the detector. We summarize the photon selection requirements and refer the reader to [35] for a more detailed discussion of these cuts. For the CEM, we required a localized cluster to satisfy the following:

- A three tower cluster of electromagnetic energy of at least $E_T \geq 7.0$ GeV deposited in the central calorimeter, after position response and CEM energy scale corrections.

- The location of the CEM cluster was required to be in a good fiducial region of the central calorimeter, as defined by the position determined from CES shower centroid information (11-channel clustering) and FIDELE fiducial cuts, with $|X_{ces}^{local}| \leq 21.0$ cm and $9.0 \leq |Z_{ces}| \leq 230.0$ cm (first 1/2 of CEM Tower 9).

- Calorimeter Isolation ("Iso4" cut): The extra transverse energy deposited in a cone of $\Delta R = 0.4$ centered on the CEM cluster, but not including the EM cluster, divided by the E_T of the cluster ($ET4/E_T$) must be less than 0.15.

- Tracking Isolation ("SumPt4" cut): The extra summed transverse momentum ($\sum PT4$) due to charged tracks within a cone of $\Delta R = 0.4$ centered on the CEM cluster must be less than 2.0 GeV. The tracks participating in the sum must have $|Z_{vtx} - Z_0| < 10$ cm.

- Tracking Isolation ("N3D" cut): At most one 3-D CTC track (originating from *any* vertex) pointing at the EM cluster (N3D ≤ 1).

- $HAD/EM < 0.055 + 0.00045 * E$ where E was the total energy of the EM cluster in GeV.

- A three tower lateral shower-shape for the CEM cluster of $L_{shr} < 0.5$.

- Using 11-channel clustering, the average of the CES strip and wire chi-squares of a fit of the testbeam electron transverse shower profiles to the leading CES cluster profile in each of these views, must be less than 20.0.

- The absence of 2^{nd} CES strip/wire clusters (within the CEM cluster) was required to further suppress π^0 and multi-photon backgrounds. For $E_T^{EM} <$ 17.88 GeV, we required $E_{2^{nd}\ CES} < -0.0094544 + (0.144330 * E_T^{EM})$. For $E_T^{EM} \geq 17.88$ GeV, we required $E_{2^{nd}\ CES} < 2.3918 + (0.010018 * E_T^{EM})$. This choice of a sliding no-2^{nd} CES cut was made to make the efficiency of this cut independent of E_T^{EM}.

For the PEM, we required a localized cluster to satisfy the following:

- A three tower cluster of electromagnetic energy deposited in the plug calorimeter of at least $E_T \geq 7.0$ GeV, after position response and PEM energy scale corrections.

- The location of the PEM cluster was required to be in a good fiducial region of the plug calorimeter, as defined by the position determined from PEM (or PES, where applicable) shower centroid information and FIDELE fiducial cuts.

- Calorimeter Isolation ("Iso4" cut): The extra transverse energy deposited in a cone of $\Delta R = 0.4$ centered on the PEM cluster, but not including the EM cluster, divided by the E_T of the cluster($ET4/E_T$) must be less than 0.15.

- Tracking Isolation ("VTX Occ" cut): We required that the VTX Occupancy in both the normal and radial-board views be less than 0.4.

- $HAD/EM < 0.028 + 0.00019 * E$ where E was the total energy of the EM cluster in GeV.

- The PEM 3×3 Pad chi-square was required to be less than 5.0.

- If the PEM cluster was also in the PES region ($1.28 \leq |\eta_{EM}| \leq 1.78$), then we additionally required both the PES theta and phi transverse shower profile chi-squares to be less than 20.0.

After all photon selection cuts were applied, we made an additional cut:

- An angular separation between the W/Z decay lepton(s) and the photon of $\Delta R_{l\gamma} = \sqrt{\Delta\eta^2 + \Delta\phi^2} > 0.7$. This cut is designed to suppress the contribution from radiative W/Z decay.

We had 122 (213) muon (electron) $W\gamma$ candidate events and 36 (43) muon (electron) $Z\gamma$ candidate events that passed all the above requirements. In Figures 6.1- 6.2, we show a typical $W + \gamma$ event in the CDF detector. The development of the muon $W\gamma$ and $Z\gamma$ samples is shown in Figures 6.3- 6.18 and summarized in Tables 6.1- 6.2. The total event yields from the combined muon and electron channels are shown in Table 6.3. We also show some kinematic properties of the combined muon and electron $W\gamma$ and $Z\gamma$ candidate event samples overlaid on the standard model prediction plus background expectation in Figures 8.2- 8.14.

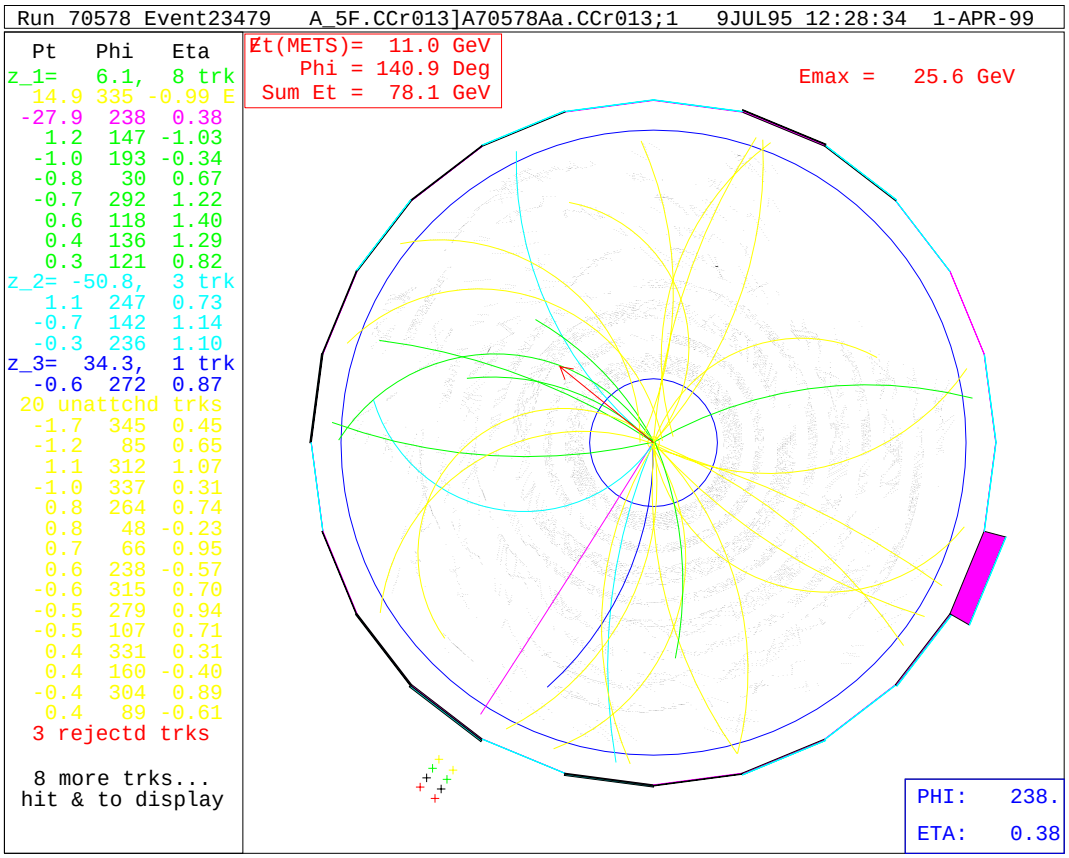

Figure 6.1: A CTC event display of a muon $W\gamma$ event. The crosses in the lower left side of the picture represent hits in the CMU chamber with a track pointing to the center of the detector. The photon can be seen in the lower right as a red block on the outer circle.

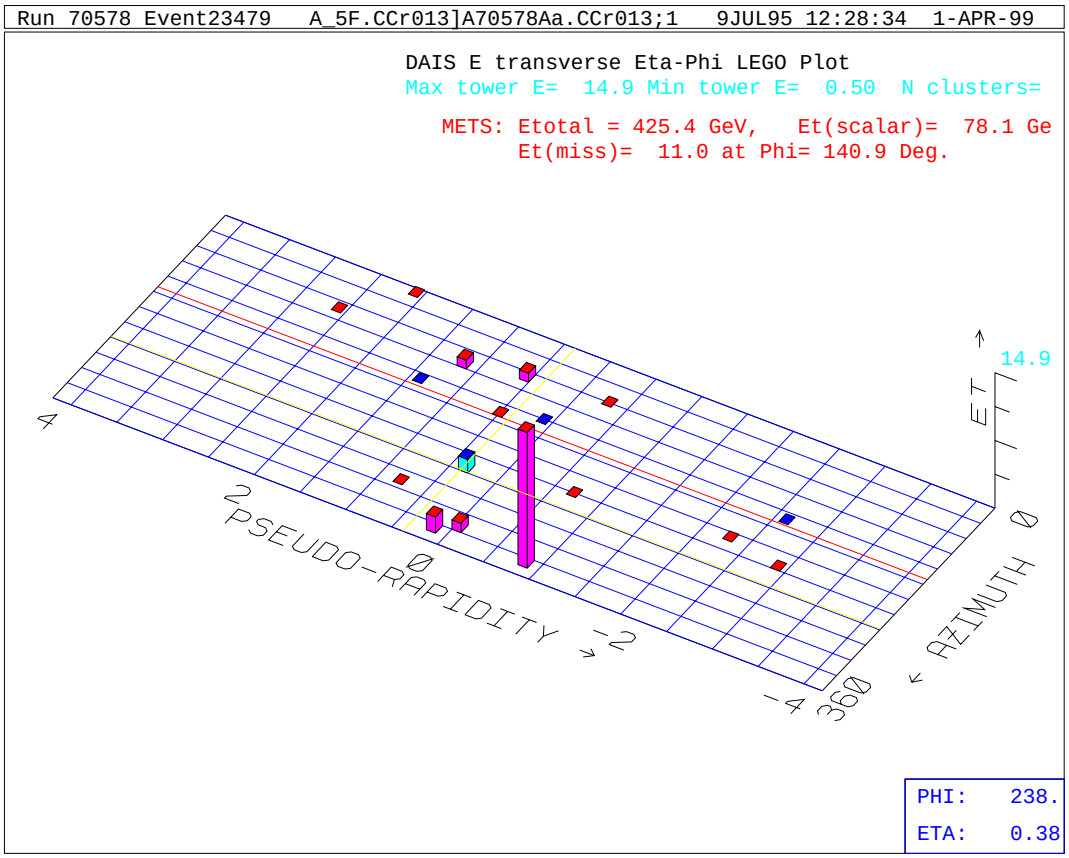

Figure 6.2: A LEGO event display of a muon $W\gamma$ event. This is an (η, ϕ) projection of the central calorimeter. The height of the block corresponding to the photon is directly related to its energy ($E_T^{\gamma} = 15.4$ GeV).

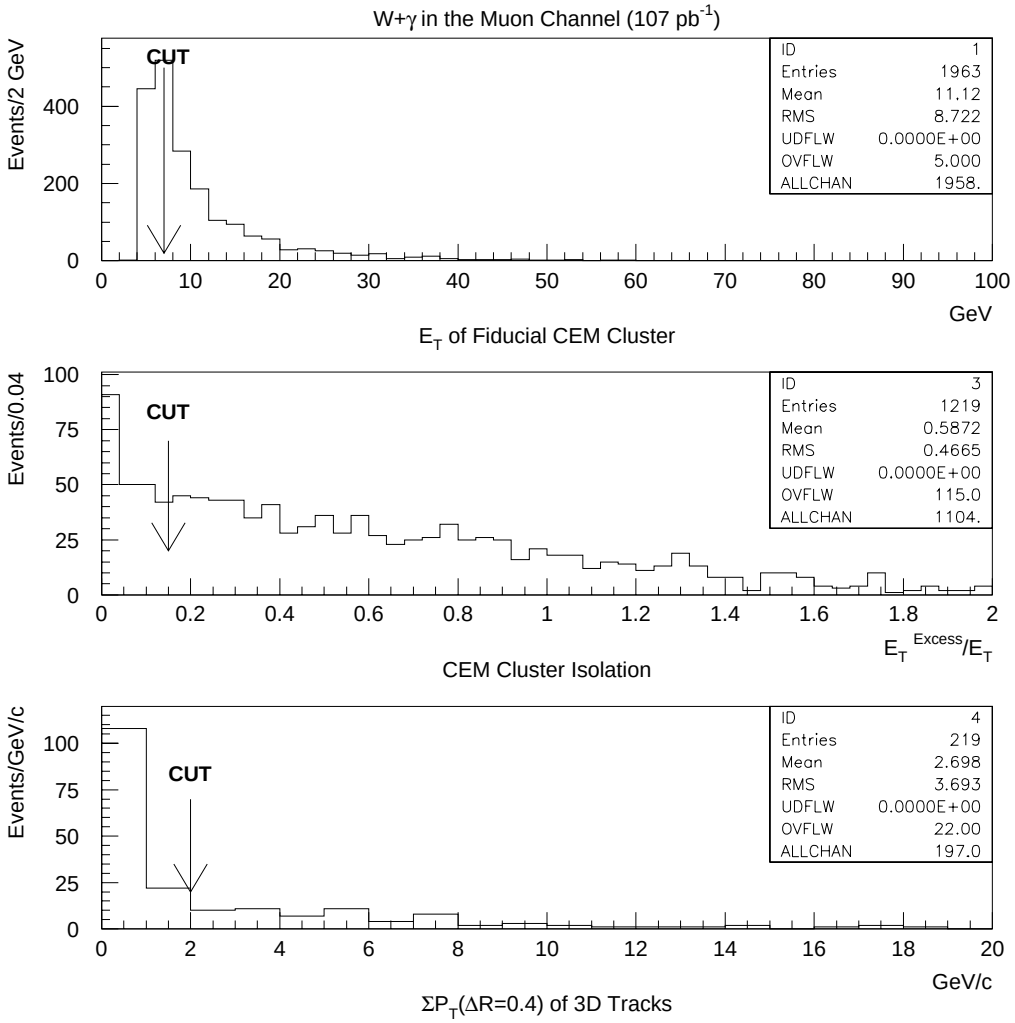

Figure 6.3: The development of the $W\gamma$ event sample in the muon channel for CEM clusters as the photon selection cuts are applied to the inclusive muon W sample. The top histogram displays the E_T of the CEM cluster, the middle histogram shows the cluster isolation and the bottom histogram displays the tracking isolation associated with the CEM cluster. The arrows on the histograms visually show the cuts discussed in the text.

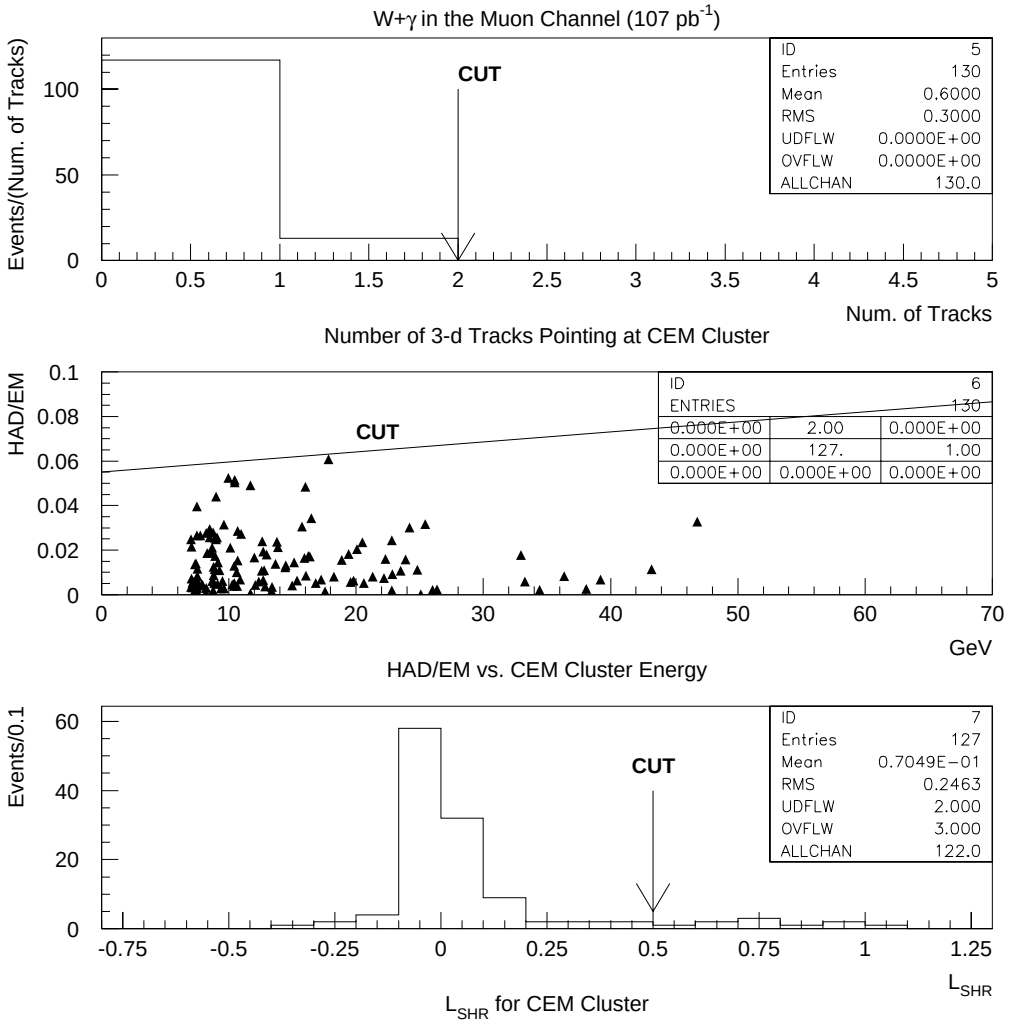

Figure 6.4: The development of the $W\gamma$ event sample in the muon channel for CEM clusters as the photon selection cuts are applied to the inclusive muon W sample. The top histogram displays the number of three-dimensional tracks pointing towards the CEM cluster, the middle histogram shows the ratio of hadronic to electromagnetic energy of the CEM cluster and the bottom histogram displays the lateral shower shape of the CEM cluster. The arrows on the histograms visually show the cuts discussed in the text.

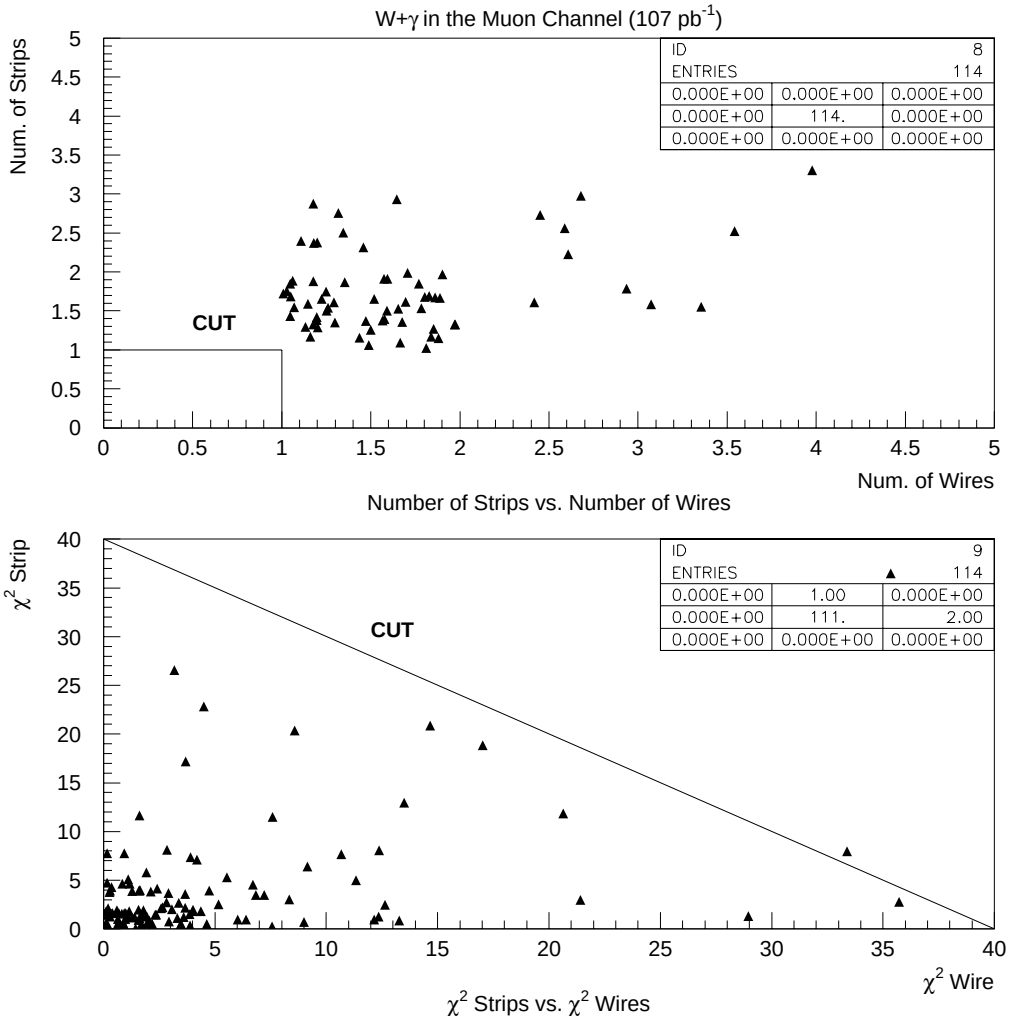

Figure 6.5: The development of the $W\gamma$ event sample in the muon channel for CEM clusters as the photon selection cuts are applied to the inclusive muon W sample. The upper histogram displays the number of strips and the number of wires for the CEM cluster and the lower histogram shows the chi-squares for the strips and wires for the CEM cluster. The arrows on the histograms visually show the cuts discussed in the text.

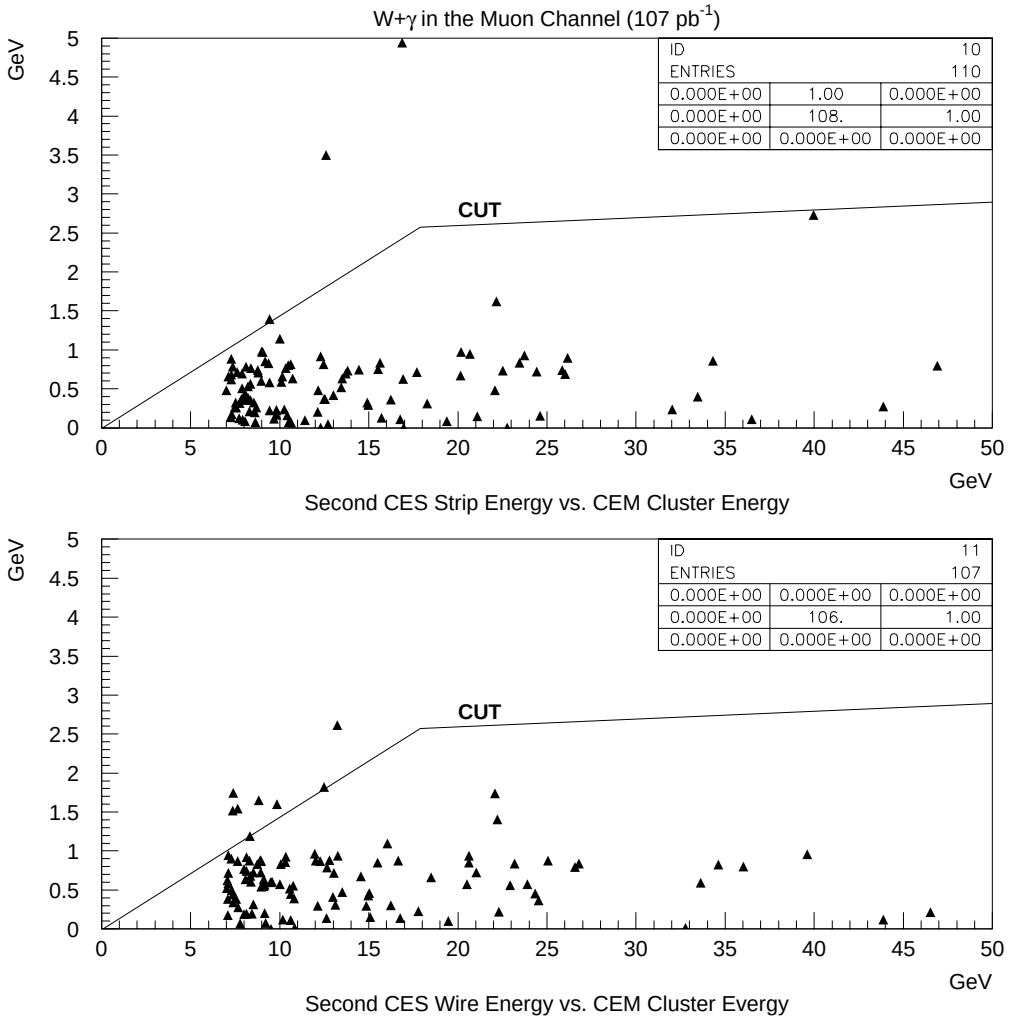

Figure 6.6: The development of the $W\gamma$ event sample in the muon channel for CEM clusters as the photon selection cuts are applied to the inclusive muon W sample. The upper histogram displays the strip energy for a second CES cluster near the candidate EM cluster and the lower histogram shows the wire energy for a second CES cluster near the candidate EM cluster. The arrows on the histograms visually show the cuts discussed in the text.

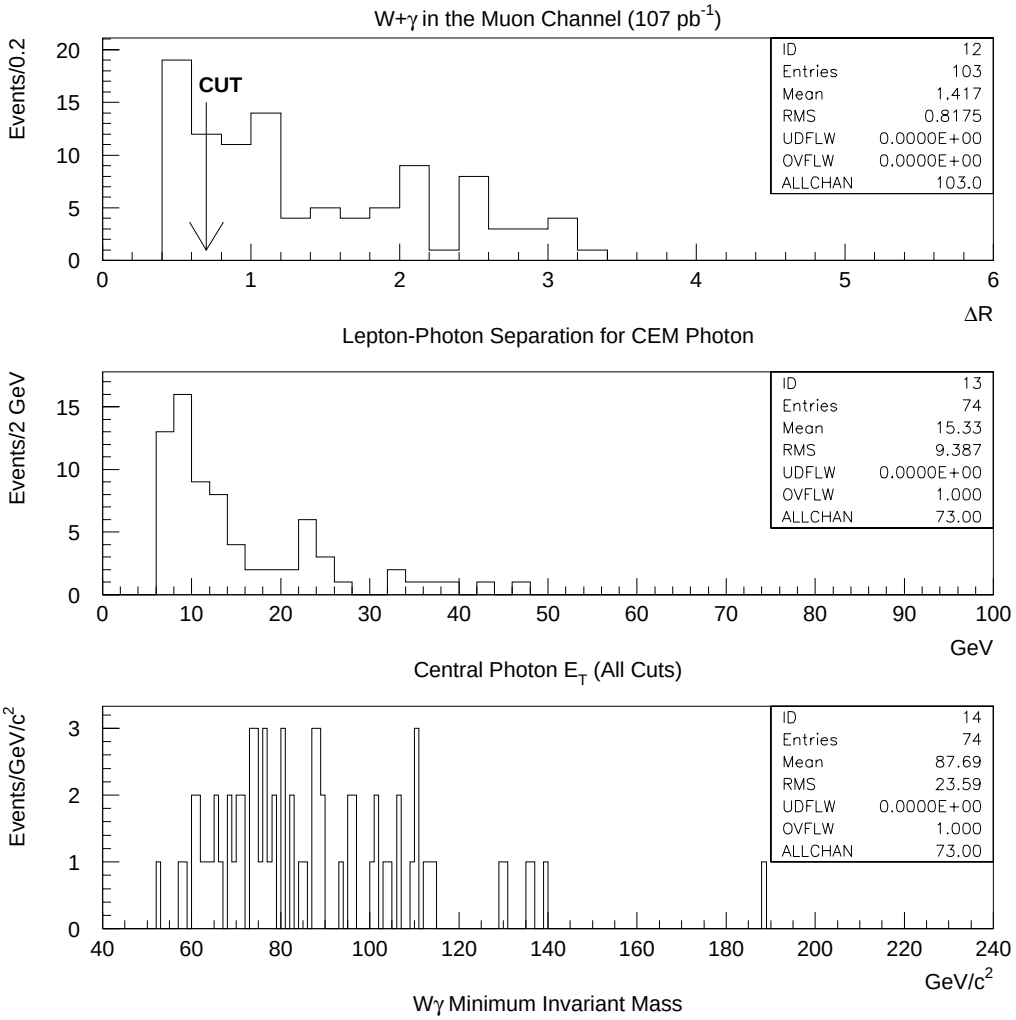

Figure 6.7: The development of the $W\gamma$ event sample in the muon channel for CEM clusters as the photon selection cuts are applied to the inclusive muon W sample. The top histogram displays the angular separation between the lepton and CEM photon, the middle histogram shows the photon E_T after all cuts are applied and the bottom histogram displays the $W\gamma$ minimum invariant mass. The arrow on the upper histogram visually shows the cut discussed in the text.

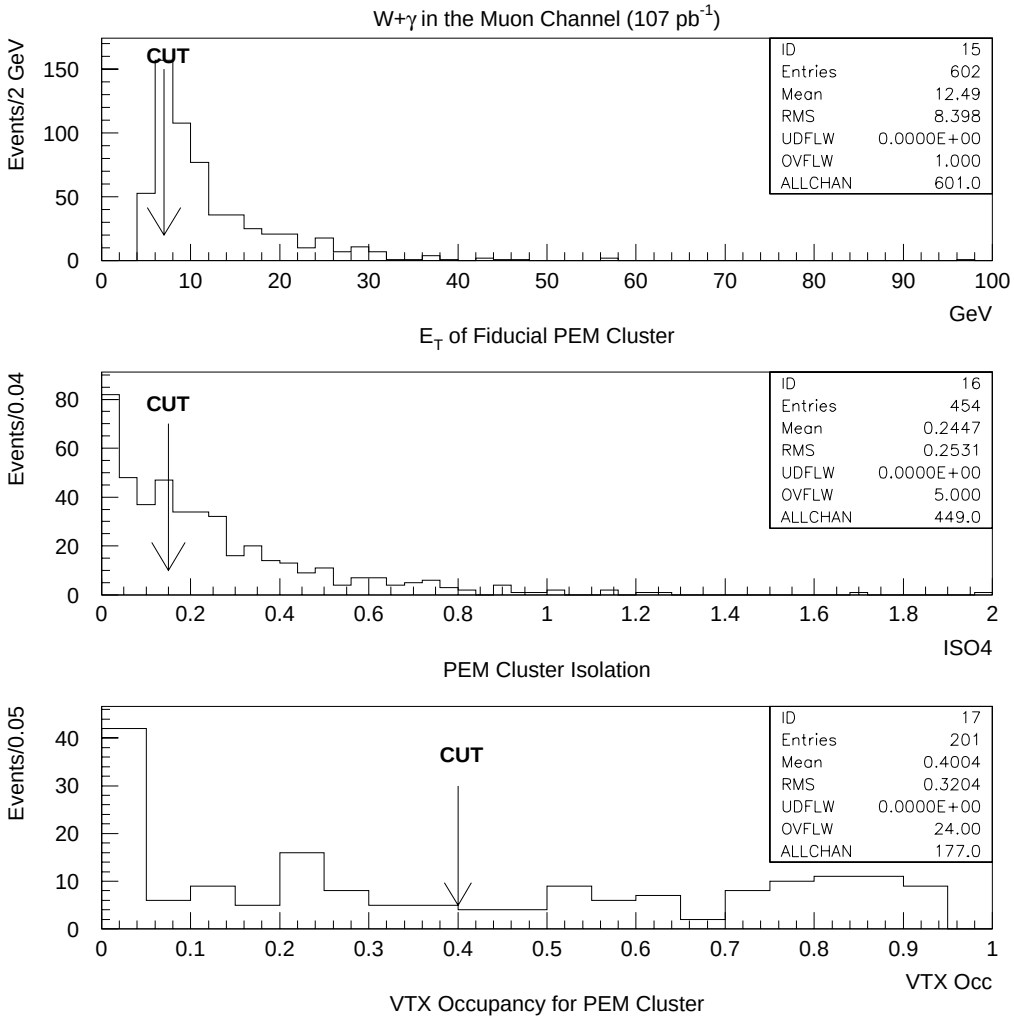

Figure 6.8: The development of the $W\gamma$ event sample in the muon channel for PEM clusters as the photon selection cuts are applied to the inclusive muon W sample. The top histogram displays the E_T of the PEM cluster, the middle histogram shows the cluster isolation and the bottom histogram displays the VTX occupancy associated with the cluster. The arrows on the histograms visually show the cuts discussed in the text.

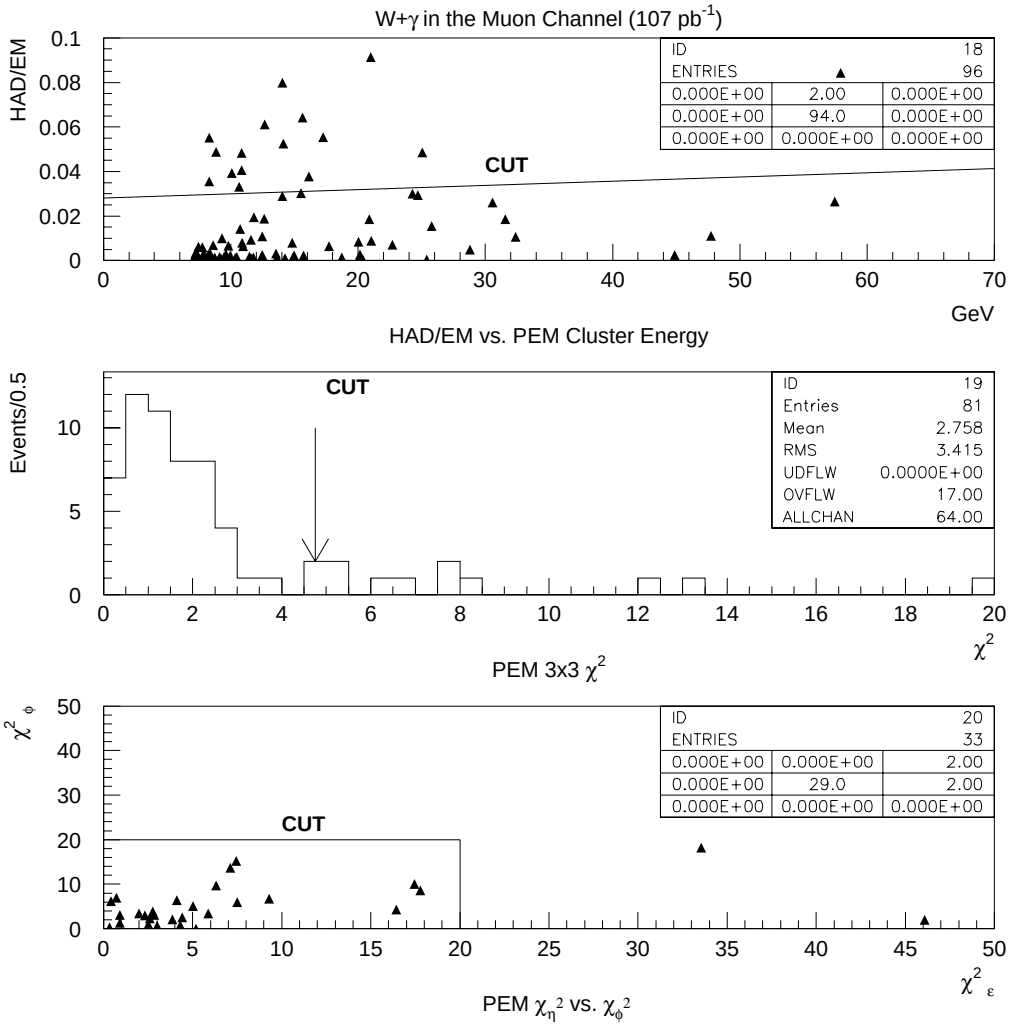

Figure 6.9: The development of the $W\gamma$ event sample in the muon channel for PEM clusters as the photon selection cuts are applied to the inclusive muon W sample. The upper histogram displays the ratio of hadronic to electromagnetic energy of the PEM cluster, the middle histogram shows the 3×3 chi-squares for the cluster and the lower histogram displays the chi-squares for clusters that fall within the region were the plug has wire chambers. The arrows on the histograms visually show the cuts discussed in the text.

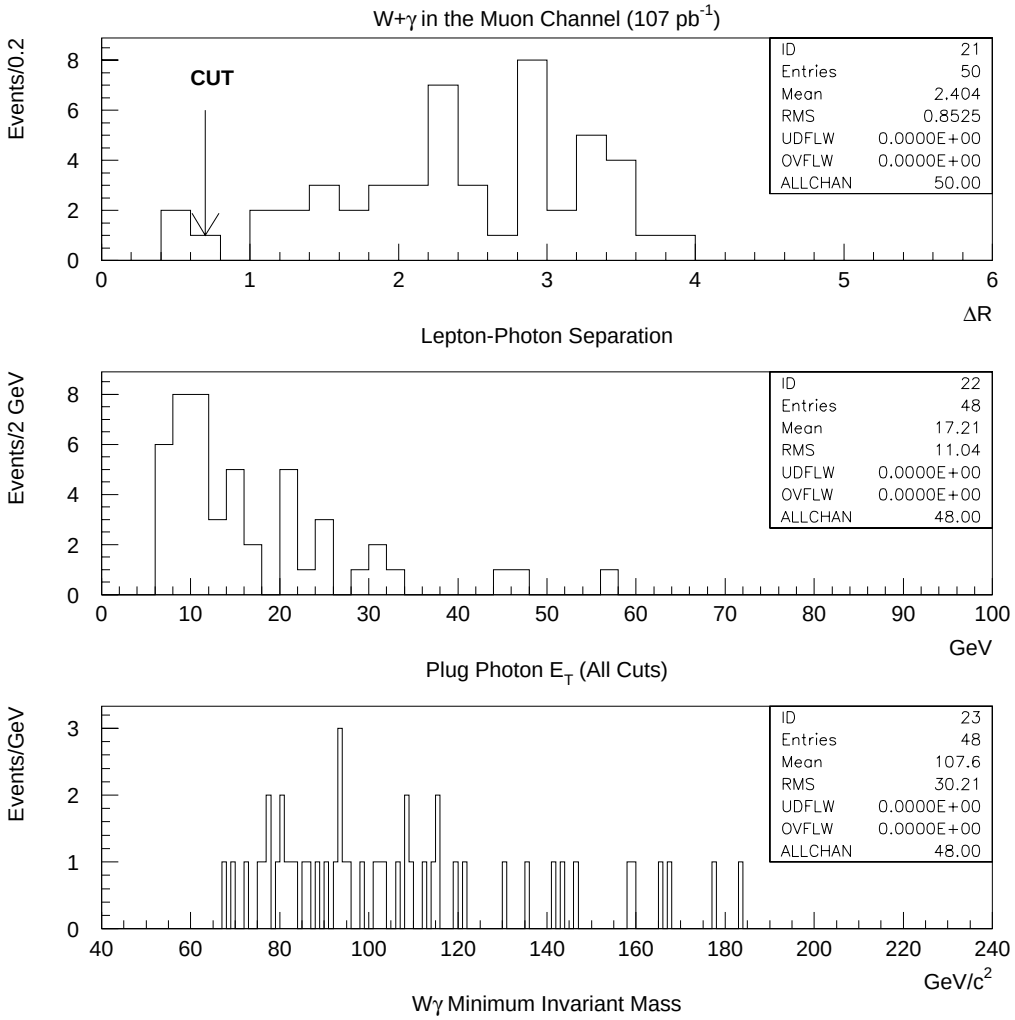

Figure 6.10: The development of the $W\gamma$ event sample in the muon channel for PEM clusters as the photon selection cuts are applied to the inclusive muon W sample. The top histogram displays the angular separation between the lepton and PEM photon, the middle histogram shows the photon E_T after all cuts are applied and the bottom histogram displays the $W\gamma$ minimum invariant mass. The arrow on the upper histogram visually shows the cut discussed in the text.

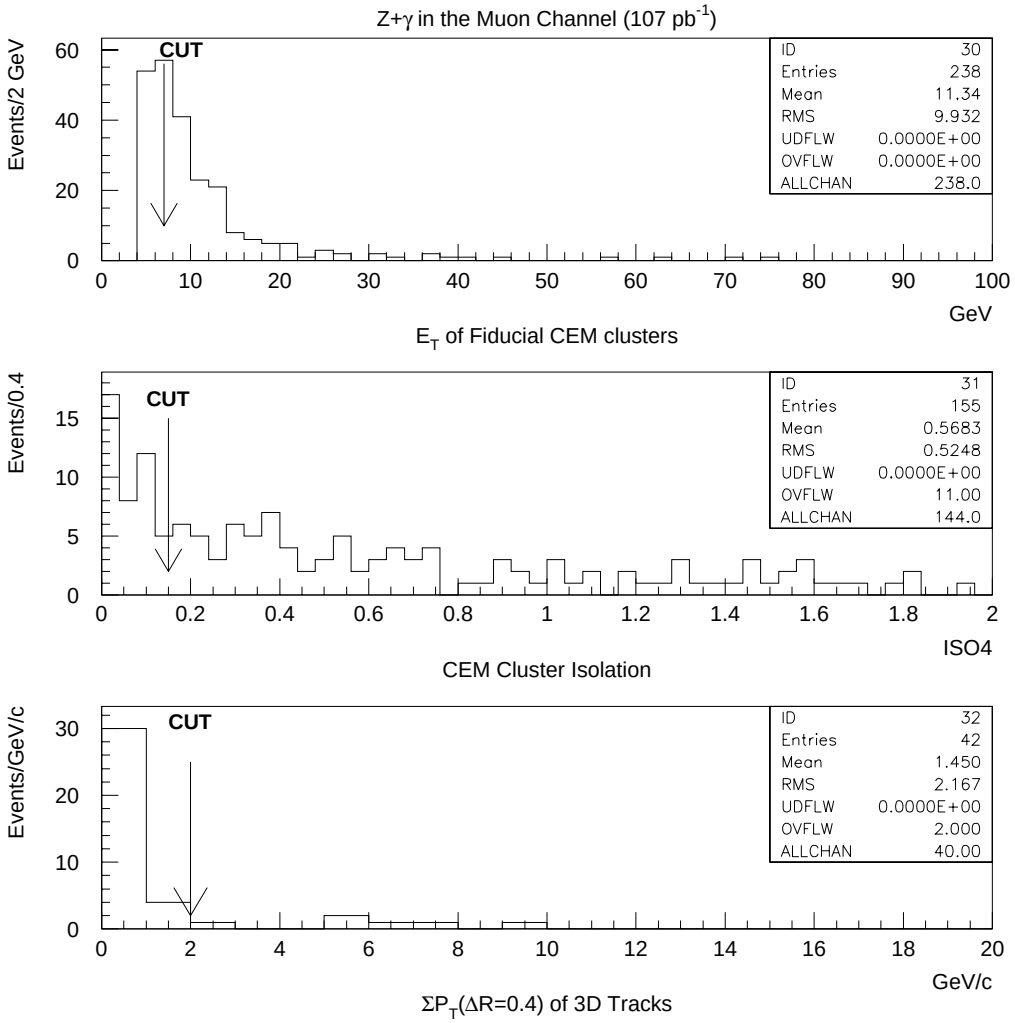

Figure 6.11: The development of the $Z\gamma$ event sample in the muon channel for CEM clusters as the photon selection cuts are applied to the inclusive muon Z sample. The top histogram displays the E_T of the CEM cluster, the middle histogram shows the cluster isolation and the bottom histogram displays the tracking isolation associated with the CEM cluster. The arrows on the histograms visually show the cuts discussed in the text.

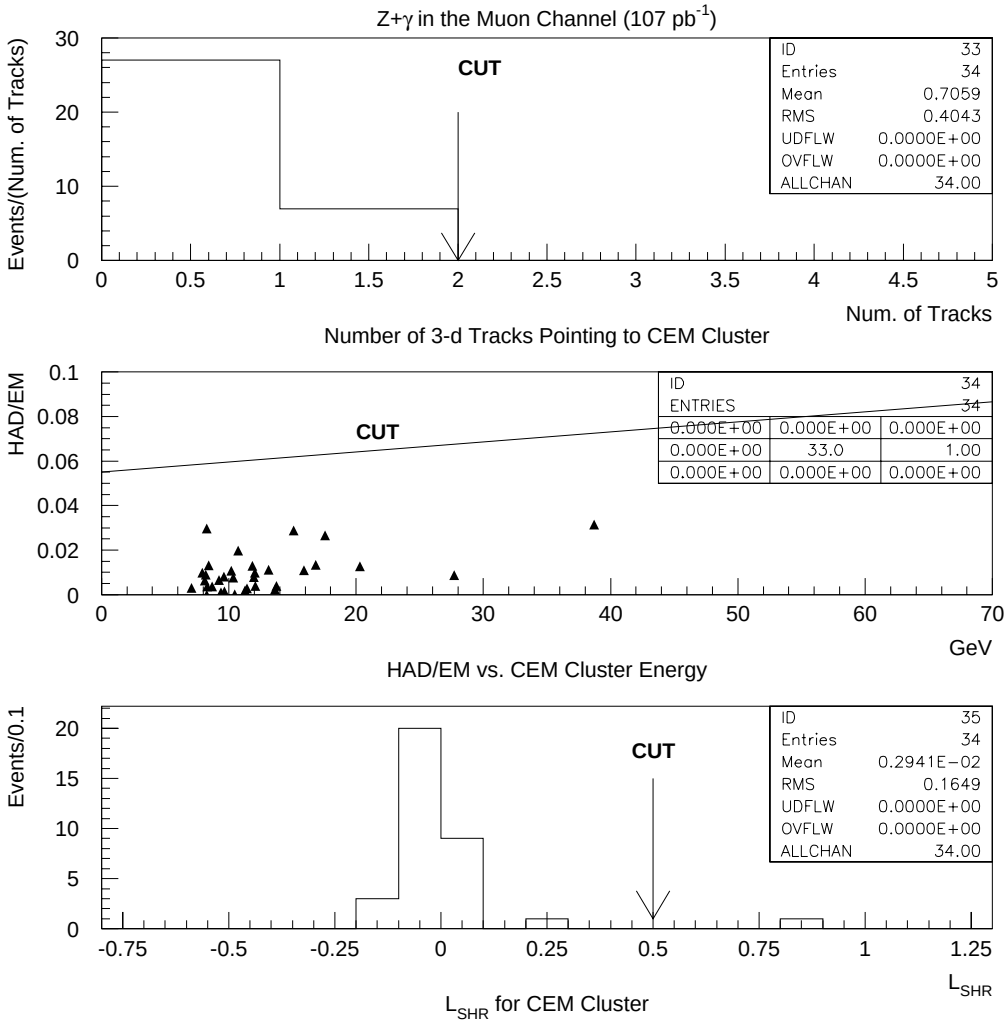

Figure 6.12: The development of the $Z\gamma$ event sample in the muon channel for CEM clusters as the photon selection cuts are applied to the inclusive muon Z sample. The top histogram displays the number of three-dimensional tracks pointing towards the CEM cluster, the middle histogram shows the ratio of hadronic to electromagnetic energy of the CEM cluster and the bottom histogram displays the lateral shower shape of the CEM cluster. The arrows on the histograms visually show the cuts discussed in the text.

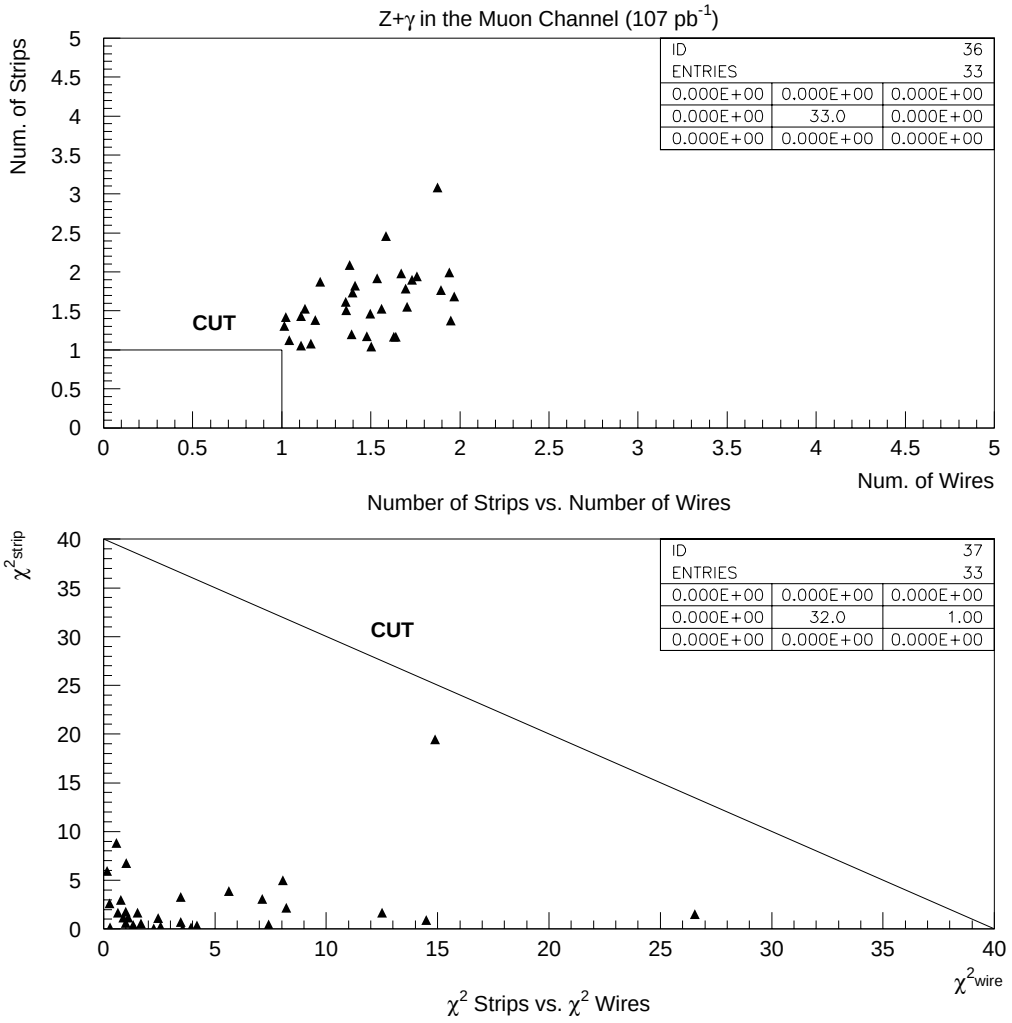

Figure 6.13: The development of the $Z\gamma$ event sample in the muon channel for CEM clusters as the photon selection cuts are applied to the inclusive muon Z sample. The upper histogram displays the number of strips and the number of wires for the CEM cluster and the lower histogram shows the chi-squares for the strips and wires for the CEM cluster. The arrows on the histograms visually show the cuts discussed in the text.

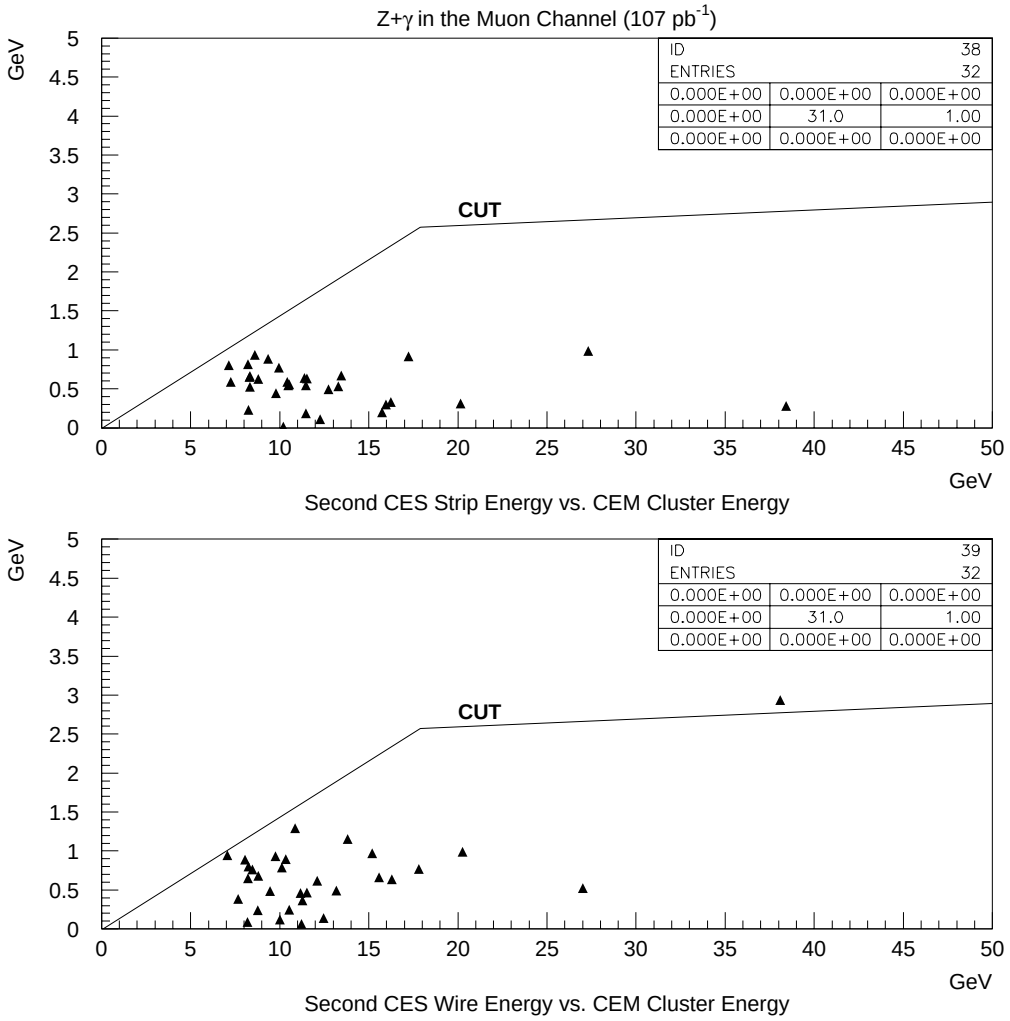

Figure 6.14: The development of the $Z\gamma$ event sample in the muon channel for CEM clusters as the photon selection cuts are applied to the inclusive muon Z sample. The upper histogram displays the strip energy for a second CES cluster near the candidate EM cluster and the lower histogram shows the wire energy for a second CES cluster near the candidate EM cluster. The arrows on the histograms visually show the cuts discussed in the text.

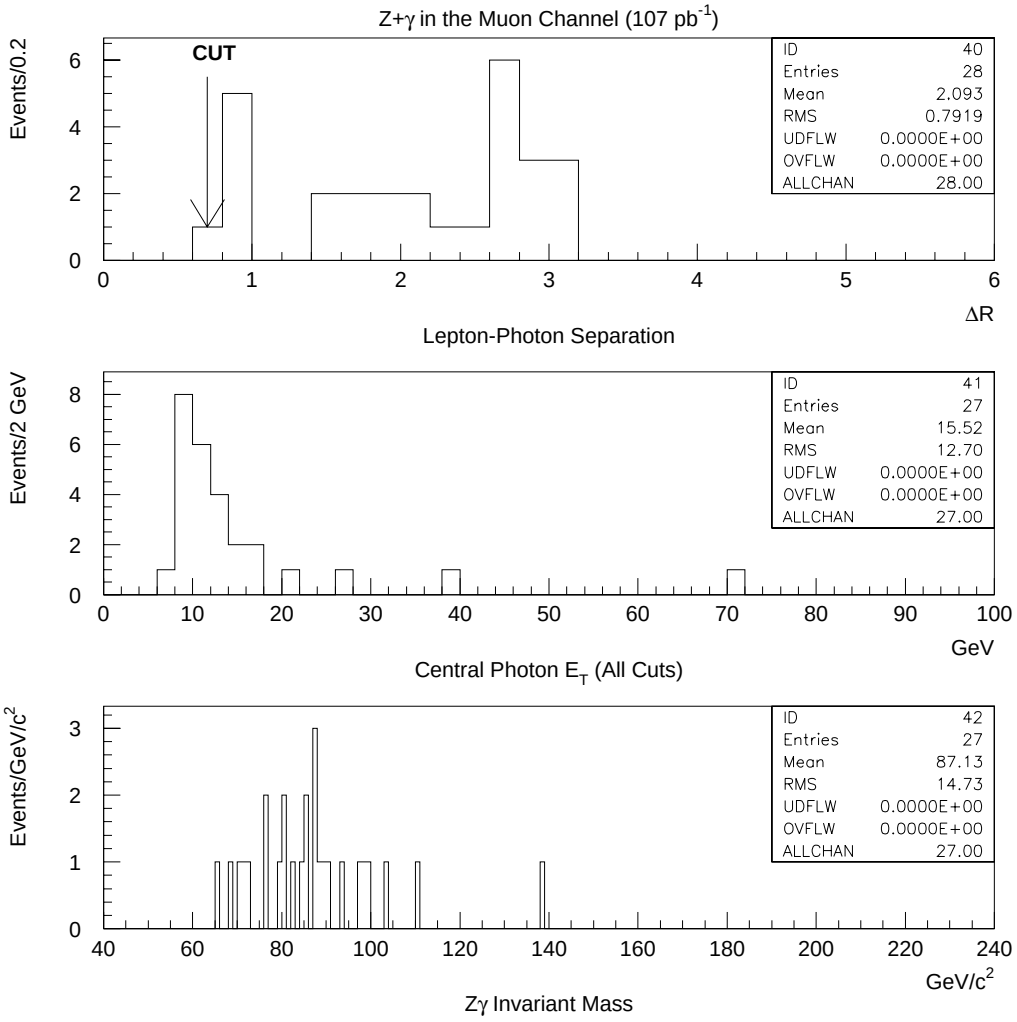

Figure 6.15: The development of the $Z\gamma$ event sample in the muon channel for CEM clusters as the photon selection cuts are applied to the inclusive muon Z sample. The top histogram displays the angular separation between the lepton and CEM photon, the middle histogram shows the photon E_T after all cuts are applied and the bottom histogram displays the $Z\gamma$ minimum invariant mass. The arrow on the upper histogram visually shows the cut discussed in the text.

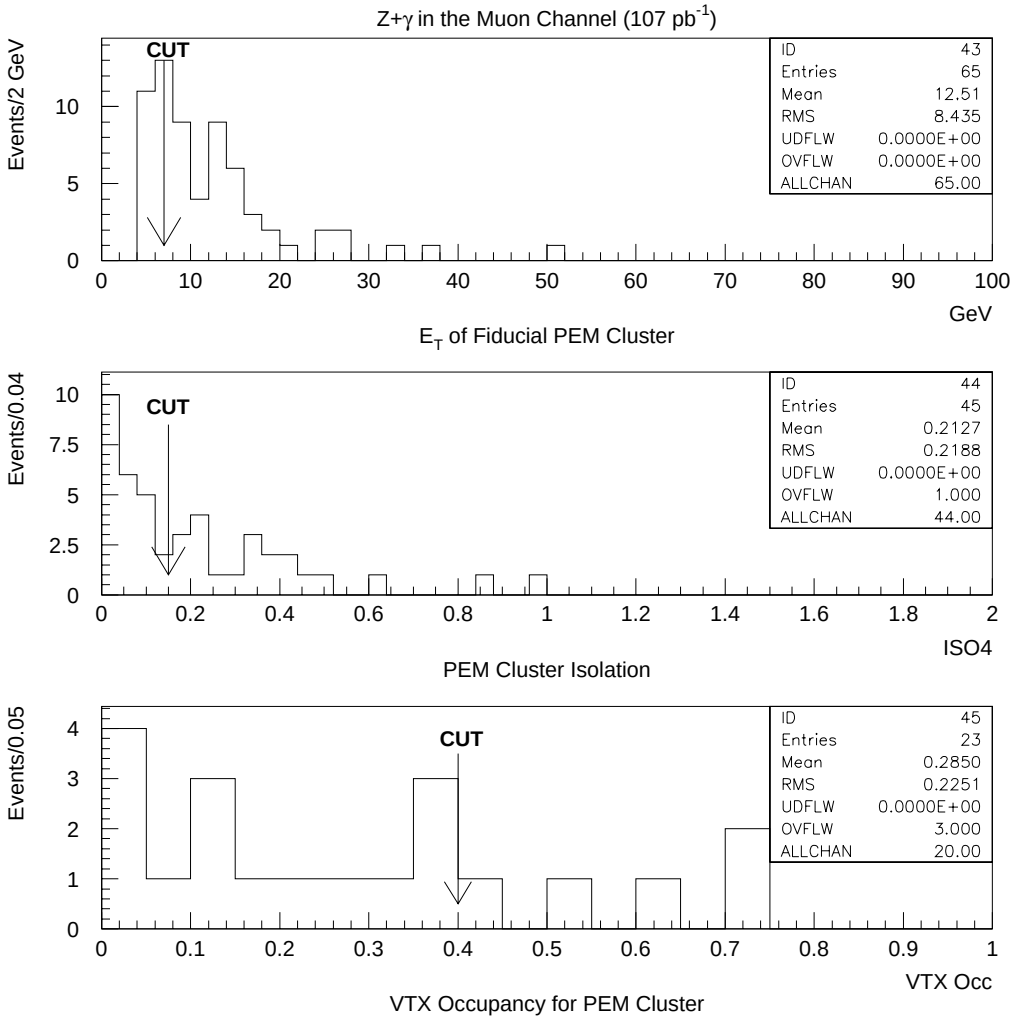

Figure 6.16: The development of the $Z\gamma$ event sample in the muon channel for PEM clusters as the photon selection cuts are applied to the inclusive muon Z sample. The top histogram displays the E_T of the PEM cluster, the middle histogram shows the cluster isolation and the bottom histogram displays the VTX occupancy associated with the cluster. The arrows on the histograms visually show the cuts discussed in the text.

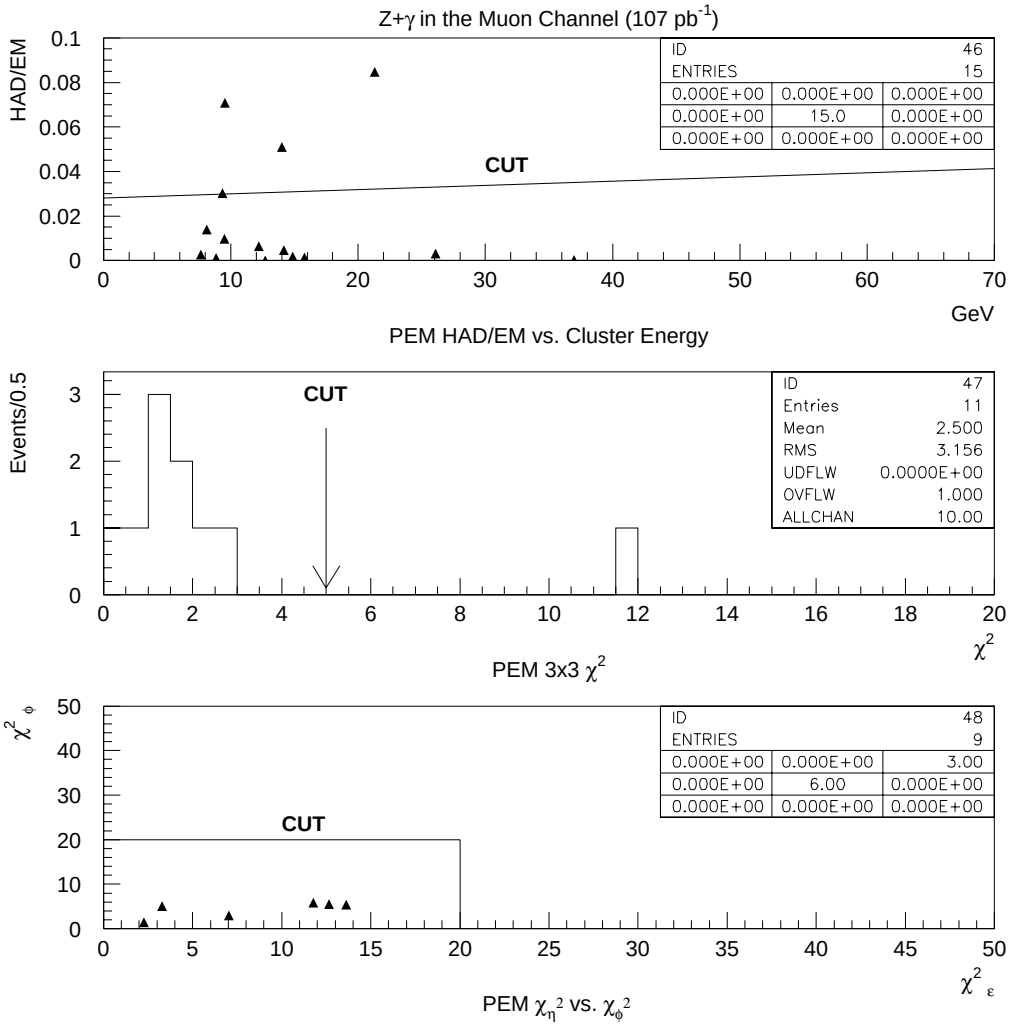

Figure 6.17: The development of the $Z\gamma$ event sample in the muon channel for PEM clusters as the photon selection cuts are applied to the inclusive muon Z sample. The upper histogram displays the ratio of hadronic to electromagnetic energy of the PEM cluster, the middle histogram shows the 3x3 chi-squares for the cluster and the lower histogram displays the chi-squares for clusters that fall within the region were the plug has wire chambers. The arrows on the histograms visually show the cuts discussed in the text.

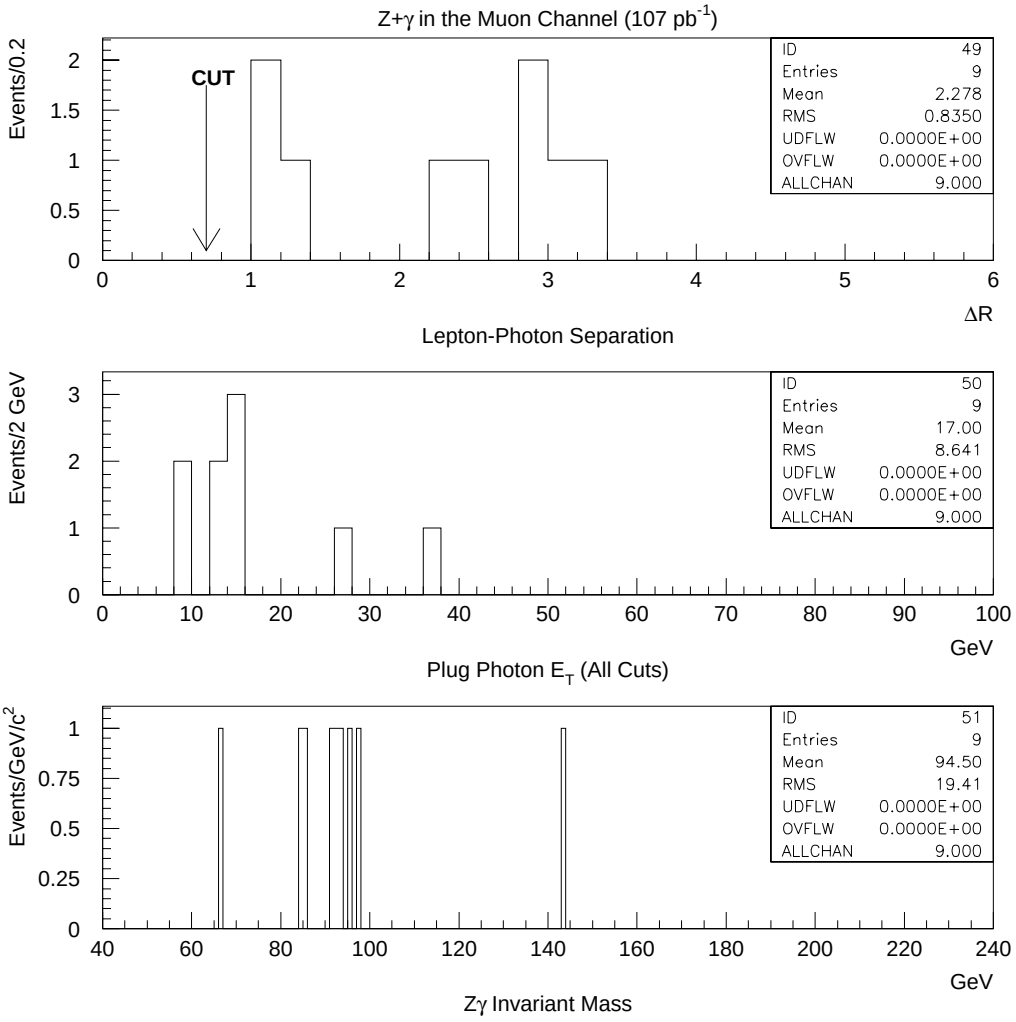

Figure 6.18: The development of the $Z\gamma$ event sample in the muon channel for PEM clusters as the photon selection cuts are applied to the inclusive muon Z sample. The top histogram displays the angular separation between the lepton and PEM photon, the middle histogram shows the photon E_T after all cuts are applied and the bottom histogram displays the $Z\gamma$ minimum invariant mass. The arrow on the upper histogram visually shows the cut discussed in the text.

	$W_\mu\gamma$	$Z_\mu\gamma$
Inclusive W/Z Data Samples	-	-
Fiduciality	1963	238
$E_T \geq 7$ GeV	1219	155
Isolation ($\Delta R = 0.4$)	219	42
$\Sigma P_T(\Delta R = 0.4) \leq 2.0$ GeV/c	130	34
$N3D \leq 1$	130	34
HAD/EM	127	34
L_{SHR}	114	33
χ^2_{avg}	110	32
2^{nd} Strip Energy	107	32
2^{nd} Wire Energy	103	28
$\Delta R_{l\gamma} > 0.7$	74	27

Table 6.1: Summary of Run 1 muon $W\gamma$ and $Z\gamma$ CEM candidates passing successive photon cuts.

	$W_\mu\gamma$	$Z_\mu\gamma$
Inclusive W/Z Data Samples	-	-
Fiduciality	602	65
$E_T \geq 7$ GeV	454	45
Isolation ($\Delta R = 0.4$)	201	23
VTX Occupancy	96	15
HAD/EM	81	11
$\chi^2_{3\times 3}$	77	9
χ^2_η, χ^2_ϕ	50	9
$\Delta R_{l\gamma} > 0.7$	48	9

Table 6.2: Summary of Run 1 muon $W\gamma$ and $Z\gamma$ PEM candidates passing successive photon cuts.

	$W\gamma$		$Z\gamma$	
	CEM	PEM	CEM	PEM
Muon	74	48	27	9
Electron	128	85	36	7

Table 6.3: Summary of Run 1 muon + electron $W\gamma$ and $Z\gamma$ CEM and PEM candidates passing all photon requirements.

6.2 Photon Identification Efficiencies

The overall efficiency for central photons, ϵ_{γ}^{CEM}, was determined from the individual efficiencies of the CEM photon cuts:

$$\epsilon_{\gamma}^{CEM} = \epsilon_{ISO4}^{\gamma} \cdot \epsilon_{PT4}^{\gamma} \cdot \epsilon_{N3D}^{\gamma} \cdot \epsilon_{had/em}^{\gamma} \cdot \epsilon_{lshr}^{\gamma} \cdot \epsilon_{\chi^2_{stp}+\chi^2_{wir}}^{\gamma} \cdot \epsilon_{2^{nd}CES}^{\gamma} \cdot \mathcal{P}_{\overline{conv}}^{\gamma} \cdot \mathcal{S}_{e\to\gamma}^{CEM} \qquad (6.1)$$

where ϵ_{ISO4}^{γ} is the efficiency of the isolation requirement cut, ϵ_{PT4}^{γ} is the track isolation cut efficiency, ϵ_{N3D}^{γ} is the efficiency of the three-dimensional track cut, $\epsilon_{had/em}^{\gamma}$ is the hadron to electromagnetic ratio cut efficiency, ϵ_{lshr} is the transverse shower development cut efficiency, $\epsilon_{\chi^2_{stp}+\chi^2_{wir}}$ is the average strip+wire chi-squared cut efficiency, $\epsilon_{2^{nd}CES}^{\gamma}$ is the efficiency of the second CES cluster cut efficiency, $\mathcal{P}_{\overline{conv}}^{\gamma}$ is the photon survival probability and $\mathcal{S}_{e\to\gamma}^{cem}$ is the photon versus electron shower development correction factor, since electrons were used in the CDF testbem. This factor was determined from EGS/QFL Monte Carlo simulations of the CDF electromagnetic calorimeter.

The efficiencies ϵ_{lshr}^{γ}, $\epsilon_{\chi^2_{stp}+\chi^2_{wir}}^{\gamma}$, $\epsilon_{had/em}^{\gamma}$ and $\epsilon_{2^{nd}CES}^{\gamma}$ were determined from electron test-beam data of various energies. These efficiencies have a slight E_T dependence as shown in Table 6.4. The inclusive electron and muon W and Z samples were used to measure the efficiencies of the two isolation cuts ($\Sigma PT4$ and $ISO4$) and the 3D track requirement ($N3D$). Cones of size 0.4 in ΔR are pointed in random directions in the central region of the detector ($|\eta| < 1.1$) with the requirement that these cones are separated from the lepton(s) by at least 0.7 units in ΔR. This separation is the same separation between photons and the lepton(s) used in the analysis and it

prevents overlap between the cone and the lepton. Within each cone the $\Sigma PT4$ values centered on the cone axis and the number of three-dimensional tracks are measured and their efficiencies are taken to be the ratio of the number of cones which contain summed track P_T less than 2 GeV or the number of cones with less than two tracks, respectively, to the total number of cones used.

Data Sample	$\epsilon^{\gamma}_{Had/EM}$	ϵ^{γ}_{Lshr}	$\epsilon^{\gamma}_{\chi^2_{stp}+\chi^2_{wir}}$	$\epsilon^{\gamma}_{no\ 2^{nd}\ CES}$
5 GeV e Test Beam	$98.9 \pm 0.2\%$	$99.9 \pm 0.1\%$	$97.3 \pm 0.3\%$	$98.0 \pm 0.1\%$
10 GeV e Test Beam	$99.6 \pm 0.1\%$	$98.8 \pm 0.4\%$	$96.2 \pm 0.4\%$	$97.9 \pm 0.1\%$
18 GeV e Test Beam	$99.1 \pm 0.9\%$	$100.0\ ^{+0.0}_{-1.7}\%$	$98.2 \pm 1.8\%$	$98.2 \pm 1.6\%$
30 GeV e Test Beam	$98.9 \pm 0.9\%$	$100.0\ ^{+0.0}_{-1.1}\%$	$99.2 \pm 0.7\%$	$98.2 \pm 1.0\%$
50 GeV e Test Beam	$98.0 \pm 0.3\%$	$99.9 \pm 0.1\%$	$99.2 \pm 0.2\%$	$97.6 \pm 0.2\%$

Table 6.4: CEM photon efficiency determination for EM shower variables.

The $ISO4 = ET4/E_T$ efficiency also has a dependence on the E_T of the cluster. We determined the $ISO4$ efficiency by the following method. First, the number of cones containing $X < ET4 < (X + 0.25$ GeV) are counted. The variable X ranges from 0-10 GeV and this method forms energy bins of width 0.25 GeV from 0 to 10 GeV. Using this distribution, the efficiency for $ET4 < X$ is the number of all cones containing $ET4$ less than X divided by the total number of cones. Therefore, the efficiency for $ISO4 = ET4/E_T < 0.15$ can be calculated directly. The $ISO4$ efficiency for a photon with $E_T = 10$ GeV is determined from the the number of cones passing $ET4/E_T < 0.15$ ($ET4 < 1.5$ GeV) requirement. This allows a determination of the isolation efficiency up to $10/E_T = 0.15$ ($E_T = 150$ GeV).

The overall E_T dependent photon selection efficiency used in this analysis is shown in Table 6.6. We show the total photon efficiency as a function of transverse photon energy for CEM and PEM photons for Run I in Figure 6.19. The final photon efficiencies used in this analysis combined the E_T independent efficiencies with the E_T dependent $ISO4$ efficiencies weighted by the standard model $W\gamma$ photon spectrum.

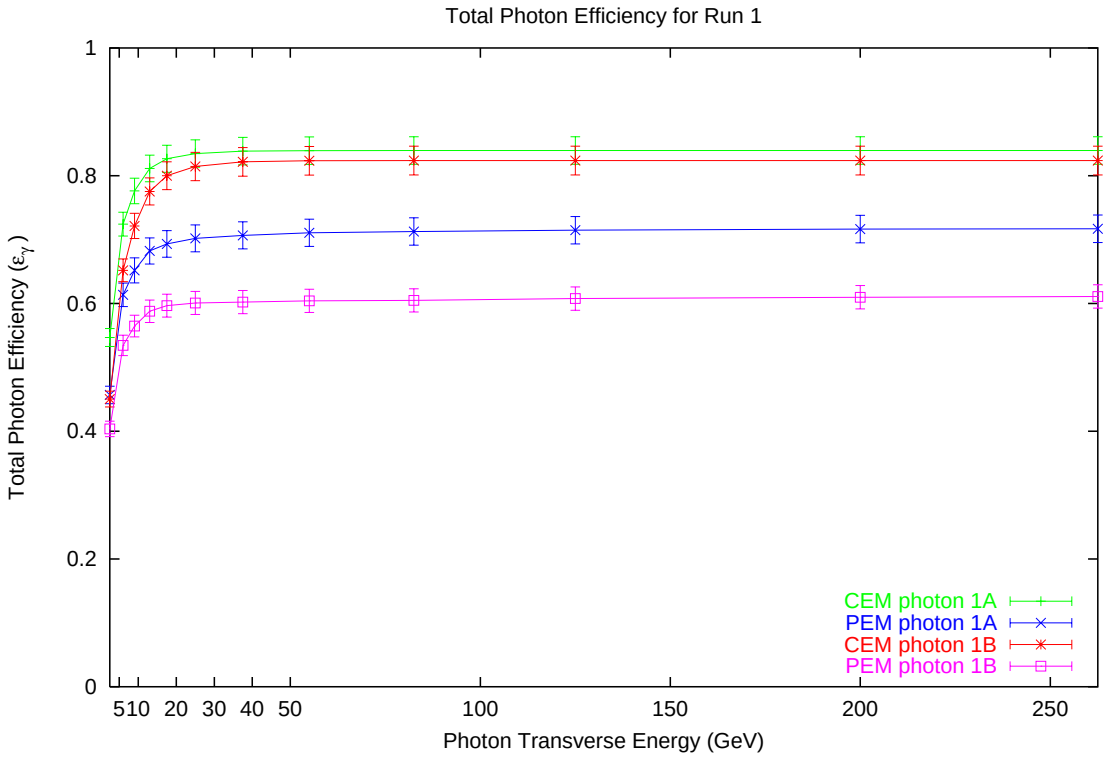

Figure 6.19: Photon efficiency for CEM and PEM photons for Run 1a and Run 1b. Efficiencies for Run 1b are lower than Run 1a due to the higher luminosity in Run 1b.

CEM Photon Cut	Efficiency
$\epsilon^{\gamma}_{had/em}$	$0.9916 \pm 0.0094 \pm 0.0075$
ϵ^{γ}_{lshr}	$0.9990 \pm 0.0004 \pm 0.0025$
$\epsilon^{\gamma}_{\chi^2_{stp}+\chi^2_{wir}}$	$0.9837 \pm 0.0012 \pm 0.0085$
$\epsilon^{\gamma}_{2^{nd}CES}$	$0.9626 \pm 0.0071 \pm 0.0104$
$\mathcal{P}^{\gamma}_{\overline{conv}}$	$0.9344 \pm 0.0012 \pm 0.0045$
$\mathcal{S}^{CEM}_{e\rightarrow\gamma}$	$1.0027 \pm 0.0056 \pm 0.0100$

Table 6.5: The E_T independent efficiencies of CEM photon.

	Run 1A		Run 1B	
	CEM	PEM	CEM	PEM
0-5	54.7±1.4%	45.7±1.4%	45.0±1.2%	40.4±1.2%
5-7	72.6±1.9%	61.3±1.8%	65.1±1.8%	53.4±1.6%
7-11	77.8±2.0%	65.2±2.0%	72.1±2.0%	56.5±1.7%
11-15	81.2±2.1%	68.2±2.1%	78.5±2.1%	58.8±1.8%
15-20	82.6±2.1%	69.3±2.1%	80.0±2.2%	59.7±1.8%
20-30	83.6±2.1%	70.2±2.1%	81.4±2.2%	60.1±1.8%
30-45	83.9±2.2%	70.7±2.1%	82.1±2.2%	60.2±1.8%
45-65	83.9±2.2%	71.1±2.1%	82.3±2.2%	60.4±1.8%
65-100	84.0±2.2%	71.3±2.1%	82.3±2.2%	60.5±1.8%
100-150	84.0±2.2%	71.5±2.1%	82.3±2.2%	60.8±1.8%
150-250	83.9±2.2%	71.6±2.2%	82.3±2.2%	61.0±1.8%
250-10000	83.9±2.2%	71.7±2.2%	82.3±2.2%	61.1±1.8%

Table 6.6: The E_T dependent total photon efficiency.

	CEM	PEM
Run 1A	79.93±2.06%	67.12±2.01%
Run 1B	75.79±2.07%	58.03±1.74%

Table 6.7: Final photon efficiencies weighted average of E_T bins.

These values are shown in Table 6.7.

The photon survival probability is the probability that a photon will pass through all the material associated with the detector corresponding to $6.8 \pm 0.2\%$ of a conversion length, χ_o^γ, without converting to a e^+e^- pair. The photon shower development correction factor, $\mathcal{S}_{e\to\gamma}^{cem}$, is defined as the ratio of the products of photon selection efficiencies to electron selection efficiencies. It is determined from a CDF detector simulation called QFL and accounts for any differences in the overall photon efficiency because electron testbeam data was used to measure photon cut efficiencies.

PEM Photon Cut	Efficiency
ϵ^{γ}_{VTX}	$0.8650 \pm 0.0030 \pm 0.0030$
$\epsilon^{\gamma}_{had/em}$	$0.9430 \pm 0.0090 \pm 0.0140$
$\epsilon^{\gamma}_{\chi^2_{3\times3}}$	$0.9650 \pm 0.0090 \pm 0.0150$
$\mathcal{P}^{\gamma}_{\overline{conv}}$	$0.9131 \pm 0.0058 \pm 0.0065$
$\mathcal{S}^{PEM}_{e\to\gamma}$	$1.0027 \pm 0.0056 \pm 0.0100$

Table 6.8: Efficiencies of PEM photon cuts.

The results for CEM photon efficiencies are summarized in Table 6.5.

The overall efficiency for plug photons, ϵ^{PEM}_{γ}, was determined from the individual efficiencies from the PEM photon cuts:

$$\epsilon^{PEM}_{\gamma} = \epsilon^{\gamma}_{ISO4} \cdot \epsilon^{\gamma}_{VTX} \cdot \epsilon^{\gamma}_{had/em} \cdot \epsilon^{\gamma}_{\chi^2_{3\times3}} \cdot \mathcal{P}^{\gamma}_{\overline{conv}} \cdot \mathcal{S}_{e\to\gamma} \tag{6.2}$$

where ϵ^{γ}_{VTX} is the VTX occupancy cut efficiency and $\epsilon^{\gamma}_{\chi^2_{3\times3}}$ is the pad 3×3 tower cut efficiency. These efficiencies are determined similiar to central photons and are discussed in [35]. The E_T independent efficiencies are summarized in Table 6.8. The final photon efficiencies are shown in Figure 6.7.

Chapter 7

Monte Carlo Studies and Background Determination for the $W + \gamma$ and $Z/DY + \gamma$ Data Samples

7.1 The Event Generator and Detector Simulation

The Baur $W + \gamma$ and $Z + \gamma$ Monte Carlo event generators [6, 7] perform complete helicity calculations of all the tree level Feynman diagrams shown in Chapter 2. It also has the ability to decay the final state W/Z boson into the electron, muon and tauon channels. The kinematic phase space integration is performed using the VEGAS adaptive multidimensional integration code [36]. The default structure functions used in this analysis are MRS R2 which are found to best match the W decay asymmetry at CDF [43].

Higher order QCD effects such as $q + \overline{q} \rightarrow g + V + \gamma$ and $q + g \rightarrow q + V + \gamma$ are approximated by a "k-factor" [34] of $[1 + \frac{8\pi}{g}\alpha_s(M_V^2)] \approx 1.33$, where V represents a W or Z vector boson, $\alpha_s(M_V^2)$ is the strong coupling constant at $Q^2 = M_V^2$, Q is the $q\overline{q}$ momentum transfer and M_V is the vector boson mass. The Baur Monte Carlos include all parton-parton luminosities and the Cabibbo-Kobayashi-Maskawa [45] quark mixing matrix elements.

The Baur Monte Carlos produce weighted events. The event weight is related to the probability that such an event would occur in an experiment. On the order of three million events were generated. Each sample can be generated with a different set of anomalous couplings as input parameters.

During Monte Carlo generation, loose geometrical and kinematical selection re-

quirements are made to prevent creating artificial kinematic biases on the leptons and photons. These are that the photon $E_T > 1$ GeV, lepton $P_T(E_T) > 1$ GeV/c, the lepton-photon separation $\Delta R_{\gamma l}$ must be greater than 0.3 and the maximal photon, lepton and neutrino rapidity was set to ± 6.0.

The four-vector information associated with the final state particles for each monte carlo event are fed into a "fast" Monte Carlo detector simulation program which parameterizes details of the muon, electron, missing E_T and photon responses in the CDF detector and Gaussian smears the event four vectors. All detector resolutions, efficiencies and geometrical information are entered into the program and therefore must be measured elsewhere. The fast detector Monte Carlo boosts the $W\gamma(Z\gamma)$ system according to the W and Z P_T distributions as measured by CDF [49]. The effect of the underlying event (min-bias) is included as in the actual CDF measured data.

The fast detector MC produces the final kinematic and geometrical acceptances for $W\gamma$ and $Z\gamma$ events and the predicted cross section times branching ratio after all analysis cuts. Electroweak backgrounds (one-legged $Z + \gamma$ and tauonic decays of $W + \gamma$s) were generated from the Baur Monte Carlos. The Baur Monte Carlos generate $W\gamma$ and $Z\gamma$ events with some overall cross section based on the matrix elements that describe the production of these types of events.

The standard model Baur Monte Carlo event generator outputs a cross section times branching ratio, $\sigma \cdot BR(V+\gamma)_{gen}$, before any experimental cuts are applied. After passing these Monte Carlo events through the fast Monte Carlo detector simulation program, which includes all experimental efficiencies, geometrical acceptances and imposes all experimental cuts, a cross section times branching ratio, $\sigma \cdot BR(V + \gamma)_{cuts}$, is obtained.

The predicted number of events for either $W\gamma$ or $Z\gamma$ processes can be related to both cross sections:

$$N_{pred}^{V\gamma} = \sigma \cdot BR(V + \gamma)_{cuts} \cdot \int \mathcal{L}dt \cdot (A \cdot \epsilon)_{V\gamma} \tag{7.1}$$

$$N_{pred}^{V\gamma} = \sigma \cdot BR(V+\gamma)_{gen} \cdot \int \mathcal{L}dt \cdot (A' \cdot \epsilon')_{V\gamma} \tag{7.2}$$

where A is the overall kinematic and geometrical acceptance discussed in Chapter 7, ϵ is the total efficiency for all analysis requirements and A' is the overall kinematic and geometrical acceptance for finding central photons with $E_T > 7$ GeV and $\Delta R > 0.7$ from the generated samples with the relaxed kinematic requirements on the photon mentioned above. Both acceptances are generated from the "fast" monte carlo.

One can relate the cross section after all selection cuts, $\sigma \cdot BR(V+\gamma)_{cuts}$, to $\sigma \cdot BR(V+\gamma)_{gen}$ through the following relationship

$$\sigma \cdot BR(V+\gamma)_{cuts} = \sigma \cdot BR(V+\gamma)_{gen} \cdot \left(\frac{A' \cdot \epsilon'}{A \cdot \epsilon}\right) \tag{7.3}$$

The predicted cross sections in Chapter 8 are obtained from the fast Monte Carlo detector simulation using this relationship. The inclusive samples are generated in a completely analogously fashion as discussed above.

7.2 Acceptances

The total acceptance for $W\gamma$ events can be represented as

$$A_{W\gamma} = A_W \cdot f_W^{\gamma} \cdot A^{\gamma} \tag{7.4}$$

where A_W is the fraction of all $W\gamma$ events where the lepton is in the CMU (CEM), CMNP and CMX (Run 1B only) fiducial regions with the lepton having $P_T > 20$ GeV/c, the event having $\not\!\!E_T > 20$ GeV and $M_T^W > 40$ GeV/c^2. The variable f_W^{γ} is the fraction of all $W\gamma$ events in which the photon is within the central(plug) region of the detector and A^{γ} is the fraction of all central(plug) photons which have $E_T > 7$ GeV and are separated from the lepton by $\Delta R > 0.7$. Each combination of regions is treated as a separate experiment.

The acceptance for $Z\gamma$ is more complicated by the fact that there are two leptons in the event. The full equation for $A \cdot \epsilon$ - these two terms are not factorizable - in $Z\gamma$

events is given by

$$A_{Z\gamma} \cdot \epsilon_{Z\gamma} = \frac{1}{f_{DY}} \cdot \epsilon_{zvx} \cdot A_{M_Z} \cdot (T \cdot \epsilon_{gold})$$
$$\times \sum_{cem,pem} [f_{Zcc} \cdot (2\epsilon^{CEM}_{silver} - T \cdot \epsilon_{gold}) \cdot (f^{\gamma}_{Zcc} \cdot A^{\gamma}_{Zcc} \cdot \epsilon^{\gamma})$$
$$+(f_{Zcp} \cdot \epsilon^{PEM}_{silver}) \cdot (f^{\gamma}_{Zcp} \cdot A^{\gamma}_{Zcp} \cdot \epsilon^{\gamma})$$
$$+(f_{Zcf} \cdot \epsilon^{FEM}_{silver}) \cdot (f^{\gamma}_{Zcf} \cdot A^{\gamma}_{Zcf} \cdot \epsilon^{\gamma})] \quad (7.5)$$

where the term $\frac{1}{f_{DY}}$ is a theoretical correction factor (98.5% for electrons and 97.0% for muons) which explicitly takes into account the removal of the Drell-Yan contribution,[1] ϵ_{zvx} is the efficiency for the event vertex cut and A_{M_Z} is the fraction of events with $M_Z > 70$ GeV/c^2. The f^{γ}_{Zcx} is the fraction of all photons in $Z\gamma$ events that are in the central or plug region of the detector with the two legs in the corresponding region central-central (cc), central-plug (cp) or central-forward (cf), f_{Zcx} is the fraction of all $Z\gamma$ events where the first leg is in the central region of the detector and the second leg is in the central (c), or plug (p) or forward (f) region, ϵ^{γ} is the efficiency for finding a photon in the central or plug region. We refer the reader to the analogous discussion for muons in [53].

7.2.1 Acceptance × Efficiency

The total acceptances discussed above give the probability of detecting $W\gamma$ or $Z\gamma$ events based on the overall detector geometry and the kinematic requirements. This quantity is needed to calculate the cross section for the relevant process. We summarize the acceptance × efficiency for the inclusives and $V + \gamma$ processes in Tables 7.1- 7.4.

[1] Strictly speaking, it applies to a window cut, but it approximates the Drell-Yan contribution with the lower bound cut we used in this analysis.

Region	Run 1B	Run 1A
CEM	0.257±0.002	0.262±0.004
CMUP	0.077±0.002	0.080±0.003
CMNP	0.025±0.002	0.027±0.002
CMX	0.043±0.002	-

Table 7.1: Acceptance × efficiency for inclusive W events.

Region	Run 1B	Run 1A
CEM	0.294±0.005	0.302±0.008
CMUP	0.124±0.004	0.126±0.005
CMNP	0.040±0.002	0.036±0.002
CMX	0.033±0.001	-

Table 7.2: Acceptance × efficiency for inclusive Z events.

	CEM γ		PEM γ	
Region	Run 1B	Run 1A	Run 1B	Run 1A
CEM	0.050±0.001	0.051±0.002	0.029±0.001	0.034±0.001
CMUP	0.016±0.001	0.017±0.001	0.008±0.000	0.010±0.001
CMNP	0.005±0.000	0.005±0.004	0.003±0.000	0.003±0.000
CMX	0.008±0.000	-	0.005±0.000	-

Table 7.3: Acceptance × efficiency for $W\gamma$ events.

	CEM γ		PEM γ	
	Run 1B	Run 1A	Run 1B	Run 1A
Electrons	0.046±0.001	0.047±0.002	0.020±0.001	0.023±0.001
Muons	0.034±0.002	0.026±0.002	0.012±0.001	0.010±0.001

Table 7.4: Acceptance × efficiency for $Z\gamma$ events.

7.3 Systematic Uncertainties on Standard Model Monte Carlo Predictions

7.3.1 The Effect of Structure Function Choice

We ran the Baur Monte Carlos with four different structure functions: the default MRS R2, MRSD-', CTEQ3M and CTEQ4M. We then passed the events through the fast Monte Carlo and recorded the number of events and the cross section. To estimate the systematic uncertainty, we took the average of the differences from the default set of structure functions. For $W\gamma$ it is 13.0 events, which represents a 6.5% uncertainty in the SM prediction of 200.75 events (based on MRS R2). For $Z\gamma$ the number of events vary by 3.9 events, which represents a 5.5% uncertainty in the 70.35 events predicted by the SM. The average of the differences between the cross sections for these structure functions is 1.2 pb for $W\gamma$ and 0.3 pb for $Z\gamma$. We summarize the results below in Table 7.5.

7.3.2 The Effect of Q^2 Scale Variation

The Q^2 of the $W\gamma$ and $Z\gamma$ processes refers to the four-momentum of the intermediate W or Z boson in Figures 2.1(c-d) and 2.4(c-d), respectively. The default values used for Q^2 are the mass of the W squared $((80.2\ \mathrm{GeV/c^2})^2)$ and mass of the Z squared $((91.1\ \mathrm{GeV/c^2})^2)$ for the $W\gamma$ and $Z\gamma$ Monte Carlos, respectively. Two other values are used, $4M_V^2$ and $M_V^2/4$, where $V = W$ or Z, to determine the effect that Q^2 have on the theoretical predictions. The results for $W\gamma$ are differences of 2.0 events and 0.2 pb for cross sections, while for $Z\gamma$ the differences are 0.7 events and 0.05 pb. These are small systematic uncertainties and represents a contribution of 1%. We summarize the results below in Table 7.5.

7.3.3 The Effect P_T Boosting

We used the measured P_T spectra of the W and Z bosons [54], and the $d\sigma/dP_T(W/Z)$ distributions agree well with theoretical predictions [55] and we make the assumption

that the expected shapes of the P_T distributions for $W/Z+\gamma$ are similar to the shape of the W/Z P_T distributions because most of the photons in the diboson event samples have E_T values which are fairly low. We show the measured P_T spectrum for $W+\gamma$ and $Z/DY+\gamma$ in Figures 7.1- 7.2.

To determine how the predicted cross sections and event yields vary with P_T boosts of the $W\gamma$ or $Z\gamma$ systems, the Monte Carlo $P_T(V_l+\gamma)$ distributions are varied within 1σ high and 1σ low limits from the fit to the shape of the $d\sigma/dP_T(W/Z)$ distributions. Other values were the nominal and no P_T boost at all. The $W\gamma$ cross section varies by 0.8 pb and the number of events varies by 8.9. The $Z\gamma$ cross section varies by 0.2 pb and the number of events varies by 3.1. We summarize the results below in Table 7.5.

	$W\gamma$		$Z\gamma$	
	$\sigma_{\sigma\cdot B}$	$\sigma_{N_{SM}}$	$\sigma_{\sigma\cdot B}$	$\sigma_{N_{SM}}$
SF	1.2 pb	13.0	0.3 pb	3.9
Q^2	0.2 pb	2.0	0.05 pb	0.7
P_T boost	0.8 pb	8.9	0.2 pb	3.1
Sum in Quadrature	1.5 pb	15.9	0.4 pb	5.0

Table 7.5: The systematic uncertainties in $W\gamma$ and $Z\gamma$ standard model production cross sections and event yield predictions.

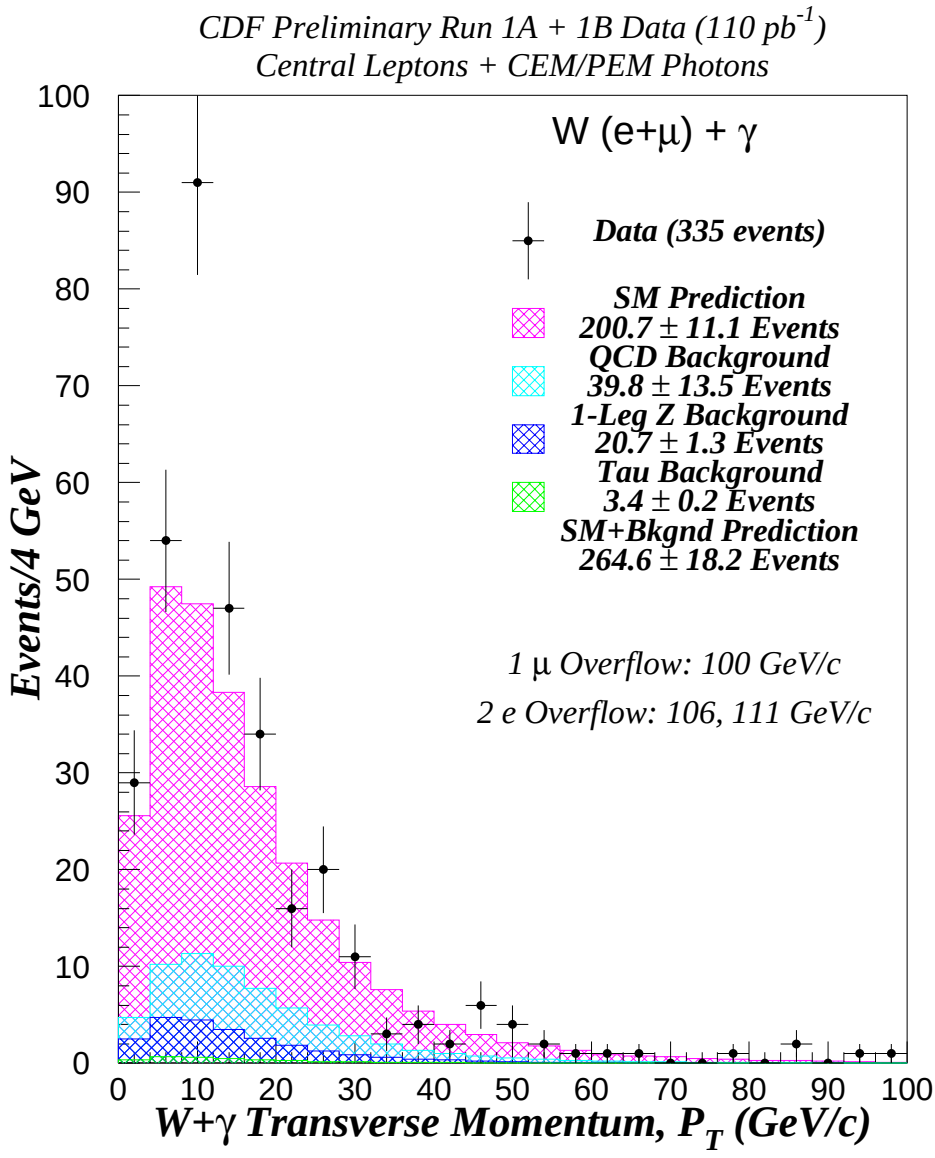

Figure 7.1: Transverse momentum of the $W + \gamma$ system overlaid on the standard model plus background expectation.

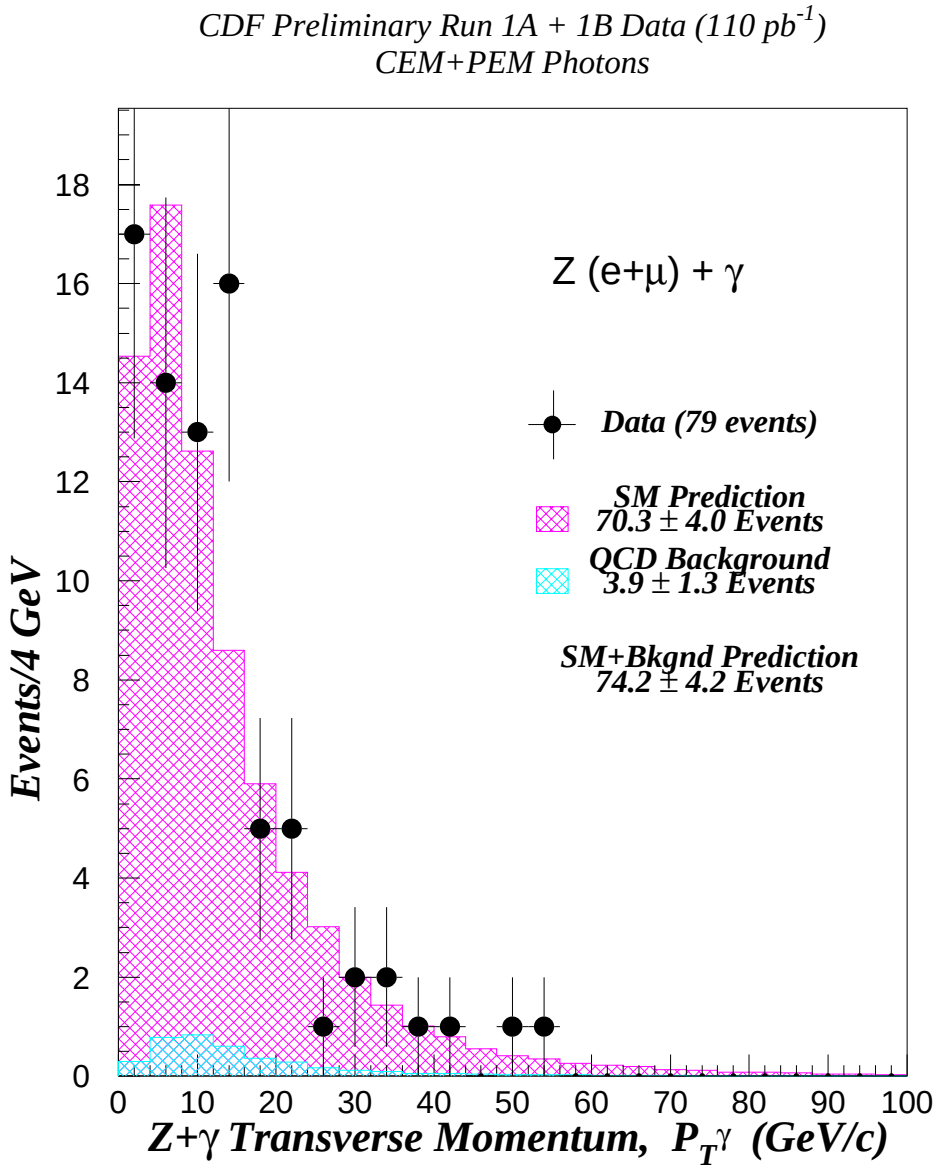

Figure 7.2: Transverse momentum of the $Z/DY + \gamma$ system overlaid on the standard model plus background expectation.

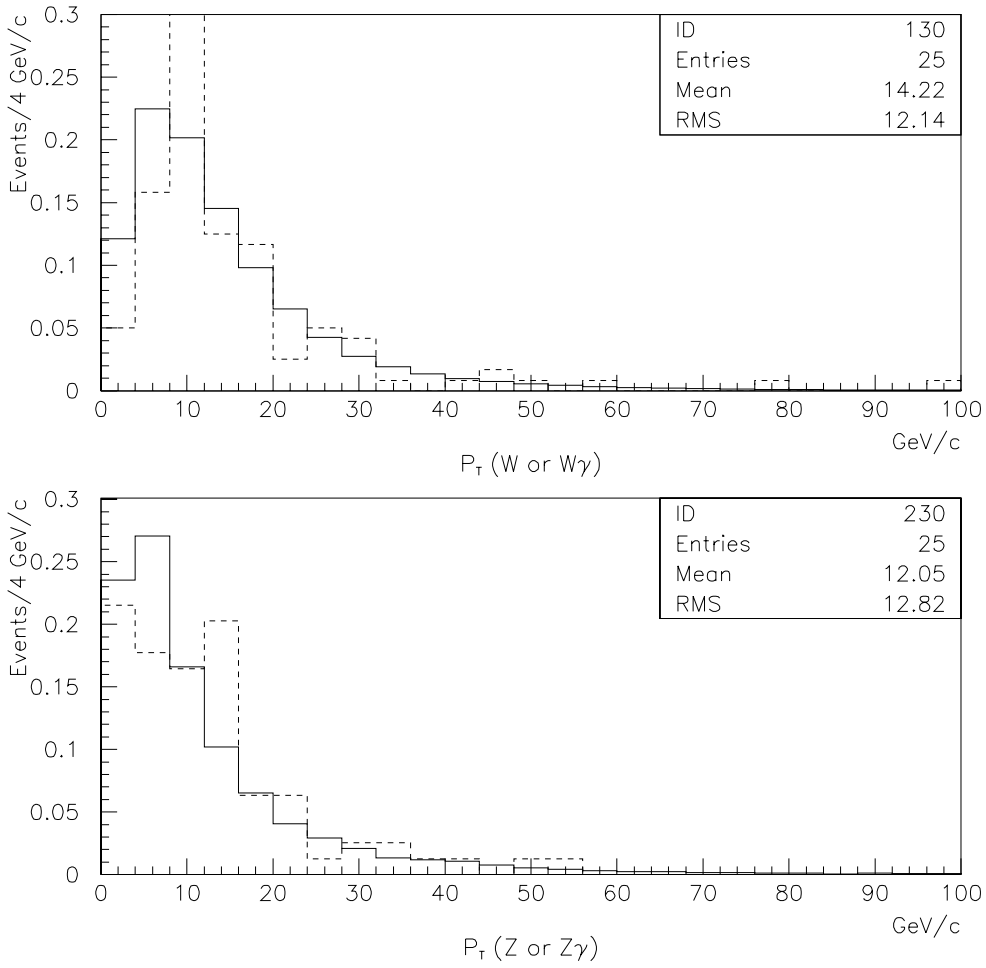

Figure 7.3: The normalized transverse momentum of the $V+\gamma$ system compared with the V system. The top histogram is the comparison of W and $W+\gamma$. The solid line is the W P_T spectrum and the dotted line is the $W+\gamma$ P_T spectrum. The bottom histogram is the comparison of Z/DY and $Z/DY+\gamma$. The solid line is the Z P_T spectrum and the dotted line is the $Z+\gamma$ P_T spectrum.

7.4 Backgrounds in the $V + \gamma$ Sample

7.4.1 QCD Jet Fragmentation

Jets in inclusive W and Z events can fragment into a leading π^0 or η. These neutral mesons can subsequently decay into two photons. If one of the two photons escapes detection or they are too close for the EM calorimeter to resolve them, as such the jet will look like a real photon. Therefore, a jet has a probability to fake a real photon. This probability will depend on the E_T of the jet and the region (central or plug) in which the jet is produced.

We obtained independent estimates of this probability by using two "non-signal"[2] data samples: Photon-23 and QCD jet data samples. The Photon-23 (P23) data required the unprescaled Level 2 isolated CEM 23 GeV (CEM_23_ISO_XCES) trigger to be satisfied. Additionally, we rejected all diphoton triggers (e.g. TWO_CEM*). The QCD jet data samples consisted of the unprescaled Jet-100 and the prescaled Jet-70, Jet-50 and Jet-20 data samples. These data samples required the Level 2 triggers JET_100, JET_70, JET_50 and JET_20, respectively. We rejected all events in the jet samples that satisfied the P23 trigger to prevent the overlap of the two data samples.

From these data samples we constructed two classes of non-leading[3] or extra jets. The first class consisted of jets which had an associated CEM(PEM) tight EM cluster - a cluster which passed all CEM(PEM) photon cuts - and was within $\Delta R \leq 0.7$ of the jet. The second class consisted of all non-leading jets.

More specifically, we selected central or plug jets which were $\Delta R > 1.4$ away from the EM (Jet) trigger jet in P23 (Jet) events. Each jet was required to have $E_T > 7.0$ GeV after JTC96S corrections and a fiducial z-vertex ($\mid Z_{VTX} \mid < 60$ cm). The trigger jet was not used in this analysis to prevent possible biases. The non-leading jets were then ordered in E_T with the highest E_T jet designated the 2^{nd} jet, the next highest

[2]Non-signal means the data samples do not contain our W or Z events.
[3]A non-leading jet means the jet was not the trigger jet.

CEM Data Sample	Numerator	Denominator
Jet 345	1781	2072683
Jet 2^{nd}-only	793	1413819
P23 345	531	420954
P23 2^{nd}-only	1173	485042

Table 7.6: Summary of event yields for the raw CEM jet probability. Individual estimates were made using only the second jet (2^{nd}-only) and all jets of higher order (345).

PEM Data Sample	Numerator	Denominator
Jet 345	2102	1938861
Jet 2^{nd}-only	1828	693796
P23 345	376	464258
P23 2^{nd}-only	1005	313743

Table 7.7: Summary of event yields for the raw PEM jet probability. Individual estimates were made using only the second jet (2^{nd}-only) and all jets of higher order (345).

E_T jet as the 3^{rd} jet, etc. The angular separation between all jets in the event was required to be greater than 1.4 ($\Delta R > 1.4$) because the jets were clustered with a cone size of $\Delta R = 0.7$.

The raw probability for a central(plug) jet to fake a photon is given by

$$\mathcal{P}_{Jet \to fake\gamma}(E_T^{Jet}) = \frac{N^{MatchedJet}(E_T^{Jet})}{N^{ExtraJet}(E_T^{Jet})} \tag{7.6}$$

where $N^{MatchedJet}(E_T^{Jet})$ is the number of central(plug) jets for a given E_T^{Jet} that are matched to a tight CEM(PEM) cluster and $N^{ExtraJet}(E_T^{Jet})$ is the number of all extra central(plug) jets for this same E_T^{Jet}. The raw numbers are shown in Tables 7.6-7.7

Some of these photons are not from QCD jets but are real/prompt photons. We will only summarize the methods used to measure the prompt photon fraction and refer the reader to a more detailed discussion in [41, 50]. For the low E_T region

Region	Et7 *vs.* $< \chi^2_{ces} >$	Iso4 *vs.* $< \chi^2_{ces} >$
A	Et7 $>$ 15.0 GeV, $< \chi^2_{ces} >$ $<$ 5.0	Iso4 $>$ 0.50, $< \chi^2_{ces} >$ $<$ 5.0
B	Et7 $>$ 15.0 GeV, $< \chi^2_{ces} >$ $>$ 20.0	Iso4 $>$ 0.50, $< \chi^2_{ces} >$ $>$ 20.0
C (signal)	Et7 $<$ 5.0 GeV, $< \chi^2_{ces} >$ $<$ 5.0	Iso4 $<$ 0.15, $< \chi^2_{ces} >$ $<$ 5.0
D	Et7 $<$ 5.0 GeV, $< \chi^2_{ces} >$ $>$ 20.0	Iso4 $<$ 0.15, $< \chi^2_{ces} >$ $>$ 20.0

Table 7.8: Band-Gap Cuts for CEM prompt photon/QCD jet background fraction determination.

Region	Et7 *vs.* $\chi^2_{3\times3}$	Iso4 *vs.* $\chi^2_{3\times3}$
A	Et7 $>$ 15.0 GeV, $\chi^2_{3\times3}$ $<$ 2.5	Iso4 $>$ 0.50, $\chi^2_{3\times3}$ $<$ 2.5
B	Et7 $>$ 15.0 GeV, $\chi^2_{3\times3}$ $>$ 10.0	Iso4 $>$ 0.50, $\chi^2_{3\times3}$ $>$ 10.0
C (signal)	Et7 $<$ 7.5 GeV, $\chi^2_{3\times3}$ $<$ 2.5	Iso4 $<$ 0.15, $\chi^2_{3\times3}$ $<$ 2.5
D	Et7 $<$ 7.5 GeV, $\chi^2_{3\times3}$ $>$ 10.0	Iso4 $<$ 0.15, $\chi^2_{3\times3}$ $>$ 10.0

Table 7.9: Band-Gap Cuts for PEM prompt photon/QCD jet background fraction determination.

($E_T < 50$ GeV), we used two "conjugate" variables, such as the CEM cluster isolation or the excess E_T in a cone $\Delta R = 0.7$ versus the CES $< \chi^2_{strip} + \chi^2_{wire} >$ as a function of E_T^{EM} for the central region and the PEM cluster isolation or the excess E_T in a cone $\Delta R = 0.7$ versus the PEM pad $\chi^2_{3\times3}$ for the plug region.

These scatter plots were divided into four regions also called band-gapped regions as shown for CEM photons in Figure 7.4. One region consisted predominantly of signal and the others essentially of pure photons. This division into regions is shown in Tables 7.8- 7.9.

Let N_A, N_B, N_C and N_D be the number of observed events in each of the four regions A, B, C and D, respectively. Using the assumptions that the QCD background in Region B (high isolation, high χ^2) is distributed identically to that in Region D

(low isolation, high χ^2) and that the QCD background in Region A (high isolation, low χ^2) is distributed identically to that in Region C (low isolation, low χ^2), then the following relation between ratios of the number of events in each region is given by:

$$\frac{N_C^{Pred\ QCD}}{N_A} = \frac{N_D}{N_B}$$

Thus, by measuring the number of events in regions A, B and D (all of which are QCD background), we can compute the number of QCD background events expected in Region C:

$$N_C^{Pred\ QCD} = N_A \left(\frac{N_D}{N_B}\right)$$

and hence the QCD background fraction, F_{QCD}, and prompt photon fraction, F_γ, are given by

$$F_{QCD} = \frac{N_C^{Pred\ QCD}}{N_C}, \qquad F_\gamma = 1 \ - \ F_{QCD} \qquad \text{since} \qquad F_{QCD} \ + \ F_\gamma \ \equiv \ 1$$

The results for this method are shown in Tables 7.10- 7.11.

For the high E_T region ($E_T > 15$ GeV), we used the CPR technique[4] as discussed in [51]. It uses the fact that one of the two photons from a leading π^0 or η will convert in the coil material around 85% of the time, while a single prompt/photon will convert about 70% of the time. The data is a mixture of the two and the relevant fractions are determined from:

$$N_\gamma^{true} \ = \ \frac{\mathcal{P}_{conv}^{QCD} \cdot N_{\overline{conv}}^{true} \ - \ \mathcal{P}_{\overline{conv}}^{QCD} \cdot N_{conv}^{true}}{\mathcal{P}_{\overline{conv}}^{\gamma} \ - \ \mathcal{P}_{\overline{conv}}^{QCD}}$$

$$N_{QCD}^{true} \ = \ \frac{\mathcal{P}_{\overline{conv}}^{\gamma} \cdot N_{conv}^{true} \ - \ \mathcal{P}_{conv}^{\gamma} \cdot N_{\overline{conv}}^{true}}{\mathcal{P}_{\overline{conv}}^{\gamma} \ - \ \mathcal{P}_{\overline{conv}}^{QCD}}$$

where N_γ^{true} is the true number of prompt photons, N_{QCD}^{true} is the number of photons from QCD jets, $\mathcal{P}_{conv}^{QCD}(\mathcal{P}_{\overline{conv}}^{QCD})$ is the probability for photons from QCD jets to convert (not to convert) in the CPR and $\mathcal{P}_{conv}^{\gamma}(\mathcal{P}_{\overline{conv}}^{\gamma})$ is the probability for a prompt photon to convert (not to convert) in the CPR.

[4]The CPR analysis only applies to central photons.

JET 345 χ^2_{ces} Data	Et7 vs. $<\chi^2>_{ces}$	Iso4 vs. $<\chi^2>_{ces}$	<Et7+Iso4> vs. $<\chi^2>_{ces}$
$7 < E_T^{EM} \leq 11$ GeV	0.581 ± 0.100	0.612 ± 0.086	0.597 ± 0.093
$11 < E_T^{EM} \leq 19$ GeV	0.345 ± 0.080	0.300 ± 0.063	0.323 ± 0.072
$E_T^{EM} > 19$ GeV	0.055 ± 0.071	0.044 ± 0.070	0.050 ± 0.081
P23 2345 χ^2_{ces} Data	Et7 *vs.* $<\chi^2>_{ces}$	Iso4 *vs.* $<\chi^2>_{ces}$	<Et7+Iso4> *vs.* $<\chi^2>_{ces}$
$7 < E_T^{EM} \leq 11$ GeV	0.826 ± 0.151	0.568 ± 0.085	0.697 ± 0.118
$11 < E_T^{EM} \leq 19$ GeV	0.374 ± 0.085	0.358 ± 0.071	0.366 ± 0.078
$E_T^{EM} > 19$ GeV	0.167 ± 0.058	0.205 ± 0.093	0.186 ± 0.076
JET 2-Only χ^2_{ces} Data	Et7 *vs.* $<\chi^2>_{ces}$	Iso4 *vs.* $<\chi^2>_{ces}$	<Et7+Iso4> *vs.* $<\chi^2>_{ces}$
$7 < E_T^{EM} \leq 11$ GeV	0.697 ± 0.235	0.799 ± 0.193	0.748 ± 0.214
$11 < E_T^{EM} \leq 19$ GeV	0.668 ± 0.205	0.239 ± 0.054	0.454 ± 0.130
$E_T^{EM} > 19$ GeV	0.148 ± 0.049	0.169 ± 0.040	0.159 ± 0.145
P23 2-Only χ^2_{ces} Data	Et7 *vs.* $<\chi^2>_{ces}$	Iso4 *vs.* $<\chi^2>_{ces}$	<Et7+Iso4> *vs.* $<\chi^2>_{ces}$
$7 < E_T^{EM} \leq 11$ GeV	0.686 ± 0.183	0.520 ± 0.111	0.603 ± 0.147
$11 < E_T^{EM} \leq 19$ GeV	0.380 ± 0.110	0.340 ± 0.080	0.360 ± 0.095
$E_T^{EM} > 19$ GeV	0.150 ± 0.060	0.210 ± 0.090	0.180 ± 0.075

Table 7.10: QCD background fraction, F_{QCD} for CEM region, with low E_T^{EM}.

JET 345 χ^2_{ces} Data	Et7 vs. $<\chi^2>_{ces}$	Iso4 vs. $<\chi^2>_{ces}$	<Et7+Iso4> vs. $<\chi^2>_{ces}$
$7 < E_T^{EM} \leq 11$ GeV	0.462 ± 0.080	0.310 ± 0.046	0.387 ± 0.062
$11 < E_T^{EM} \leq 19$ GeV	0.304 ± 0.066	0.196 ± 0.045	0.246 ± 0.054
$E_T^{EM} > 19$ GeV	0.240 ± 0.065	0.054 ± 0.044	0.145 ± 0.053
P23 345 χ^2_{ces} Data	Et7 vs. $<\chi^2>_{ces}$	Iso4 vs. $<\chi^2>_{ces}$	<Et7+Iso4> vs. $<\chi^2>_{ces}$
$7 < E_T^{EM} \leq 11$ GeV	0.480 ± 0.160	0.320 ± 0.063	0.399 ± 0.110
$11 < E_T^{EM} \leq 19$ GeV	0.217 ± 0.104	0.263 ± 0.101	0.241 ± 0.102
$E_T^{EM} > 19$ GeV	0.222 ± 0.150	0.536 ± 0.632	0.243 ± 0.200
JET 2-Only χ^2_{ces} Data	Et7 *vs.* $<\chi^2>_{ces}$	Iso4 *vs.* $<\chi^2>_{ces}$	<Et7+Iso4> *vs.* $<\chi^2>_{ces}$
$7 < E_T^{EM} \leq 11$ GeV	0.370 ± 0.105	0.424 ± 0.135	0.402 ± 0.120
$11 < E_T^{EM} \leq 19$ GeV	0.824 ± 0.204	0.342 ± 0.080	0.408 ± 0.166
$E_T^{EM} > 19$ GeV	0.164 ± 0.224	0.266 ± 0.326	0.217 ± 0.160
P23 2-Only χ^2_{ces} Data	Et7 *vs.* $<\chi^2>_{ces}$	Iso4 *vs.* $<\chi^2>_{ces}$	<Et7+Iso4> *vs.* $<\chi^2>_{ces}$
$7 < E_T^{EM} \leq 11$ GeV	0.581 ± 0.080	0.404 ± 0.071	0.492 ± 0.075
$11 < E_T^{EM} \leq 19$ GeV	0.512 ± 0.069	0.339 ± 0.049	0.424 ± 0.059
$E_T^{EM} > 19$ GeV	0.126 ± 0.020	0.083 ± 0.032	0.103 ± 0.028

Table 7.11: QCD background fraction, F_{QCD} for PEM region, with low E_T^{EM}.

All conversion probabilities are determined from Monte Carlo which used detailed studies of the amount of radiator material between the active volume of the CTC and the CPR. N_{conv}^{true} is determined by CPR charge deposition. If a photon converted in the material upstream of the CPR, it would deposit $Q > 500$ fC in the CPR. So for all tight CEM clusters found, we looked at the corresponding charge deposition in the CPR. No charge deposition with the tight CEM cluster meant the photon did

not convert ($N_{\overline{conv}}^{true}$). Corrections are made for the underlying event and the CPR inefficiency [41]. The results are shown in Table 7.12. The final prompt photon subtracted probability as a function of E_T is shown in Figures 7.5- 7.6.

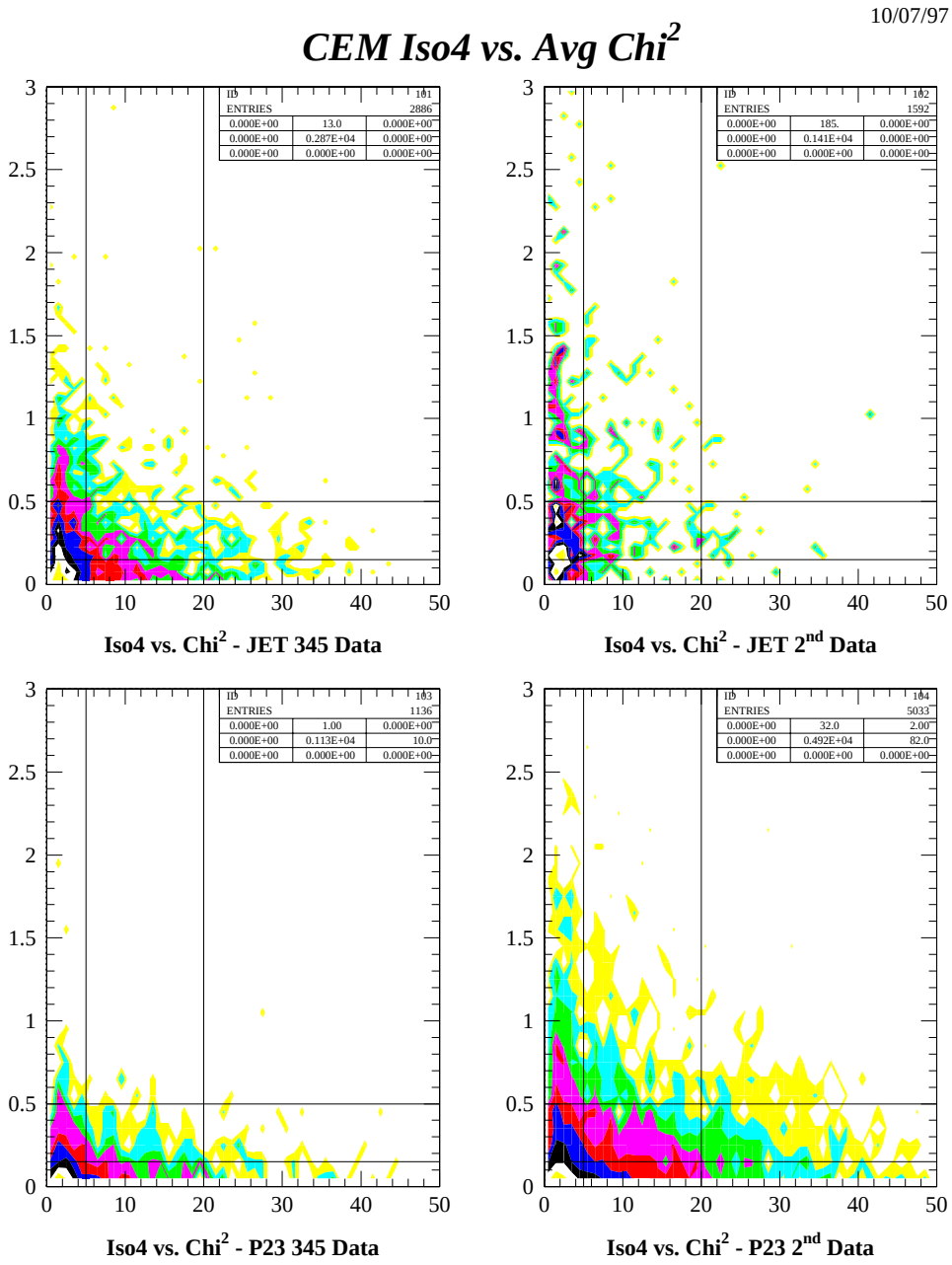

Figure 7.4: Iso4 versus CES $< \chi^2 >$ for JET and P23 CEM clusters associated with 345 and 2-only jets.

JET 345 χ^2_{ces} Data	Et7 vs. $<\chi^2>_{ces}$	Iso4 vs. $<\chi^2>_{ces}$	<Et7+Iso4> vs. $<\chi^2>_{ces}$
$15 < E_T^{EM} \leq 19$ GeV	0.243 ± 0.102	0.160 ± 0.065	Avg'd w/ Q_{cpr} Data
$19 < E_T^{EM} \leq 40$ GeV	0.103 ± 0.079	0.129 ± 0.116	(See below)
$40 < E_T^{EM} \leq 60$ GeV	–	–	–
$E_T^{EM} > 60$ GeV	–	–	–
JET 345 Q_{cpr} Data	Et7 *vs.* Q_{cpr}	Iso4 *vs.* Q_{cpr}	<Et7+Iso4> *vs.* Q_{cpr}
$15 < E_T^{EM} \leq 19$ GeV	0.227 ± 0.142	0.362 ± 0.118	0.248 ± 0.107
$19 < E_T^{EM} \leq 40$ GeV	0.461 ± 0.176	0.439 ± 0.143	0.279 ± 0.128
$40 < E_T^{EM} \leq 60$ GeV	–	–	–
$E_T^{EM} > 60$ GeV	–	–	–
P23 2345 χ^2_{ces} Data	Et7 vs. $<\chi^2>_{ces}$	Iso4 vs. $<\chi^2>_{ces}$	<Et7+Iso4> vs. $<\chi^2>_{ces}$
$15 < E_T^{EM} \leq 19$ GeV	–	–	–
$19 < E_T^{EM} \leq 40$ GeV	–	–	–
$40 < E_T^{EM} \leq 60$ GeV	–	–	–
$E_T^{EM} > 60$ GeV	–	–	–
P23 2345 Q_{cpr} Data	Et7 vs. Q_{cpr}	Iso4 vs. Q_{cpr}	<Et7+Iso4> vs. Q_{cpr}
$15 < E_T^{EM} \leq 19$ GeV	0.308 ± 0.142	0.392 ± 0.110	0.350 ± 0.107
$19 < E_T^{EM} \leq 40$ GeV	0.290 ± 0.176	0.424 ± 0.009	0.357 ± 0.128
$40 < E_T^{EM} \leq 60$ GeV	0.034 ± 0.191	0.104 ± 0.174	0.069 ± 0.183
$E_T^{EM} > 60$ GeV	-0.251 ± 0.454	0.154 ± 0.362	-0.100 ± 0.325
JET 2-Only χ^2_{ces} Data	Et7 vs. $<\chi^2>_{ces}$	Iso4 vs. $<\chi^2>_{ces}$	<Et7+Iso4> vs. $<\chi^2>_{ces}$
$15 < E_T^{EM} \leq 19$ GeV	0.320 ± 0.152	0.109 ± 0.039	Avg'd w/ Q_{cpr} Data
$19 < E_T^{EM} \leq 40$ GeV	0.354 ± 0.164	0.182 ± 0.062	(See below)
$40 < E_T^{EM} \leq 60$ GeV	0.086 ± 0.058	0.155 ± 0.145	
$E_T^{EM} > 60$ GeV	–	–	–
JET 2-Only Q_{cpr} Data	Et7 vs. Q_{cpr}	Iso4 vs. Q_{cpr}	<Et7+Iso4> vs. Q_{cpr}
$15 < E_T^{EM} \leq 19$ GeV	0.026 ± 0.262	0.232 ± 0.155	0.172 ± 0.152
$19 < E_T^{EM} \leq 40$ GeV	0.660 ± 0.360	0.306 ± 0.178	0.378 ± 0.191
$40 < E_T^{EM} \leq 60$ GeV	0.245 ± 0.351	0.180 ± 0.223	0.173 ± 0.174
$E_T^{EM} > 60$ GeV	0.310 ± 0.224	0.458 ± 0.184	0.384 ± 0.204
P23 2-Only χ^2_{ces} Data	Et7 vs. $<\chi^2>_{ces}$	Iso4 vs. $<\chi^2>_{ces}$	<Et7+Iso4> vs. $<\chi^2>_{ces}$
$15 < E_T^{EM} \leq 19$ GeV	–	–	–
$19 < E_T^{EM} \leq 40$ GeV	–	–	–
$40 < E_T^{EM} \leq 60$ GeV	–	–	–
$E_T^{EM} > 60$ GeV	–	–	–
P23 2-Only Q_{cpr} Data	Et7 *vs.* Q_{cpr}	Iso4 *vs.* Q_{cpr}	<Et7+Iso4> *vs.* Q_{cpr}
$15 < E_T^{EM} \leq 19$ GeV	0.379 ± 0.144	0.427 ± 0.121	0.403 ± 0.133
$19 < E_T^{EM} \leq 40$ GeV	0.307 ± 0.116	0.447 ± 0.097	0.377 ± 0.107
$40 < E_T^{EM} \leq 60$ GeV	0.034 ± 0.191	0.104 ± 0.174	0.069 ± 0.183
$E_T^{EM} > 60$ GeV	-0.251 ± 0.454	0.154 ± 0.362	-0.049 ± 0.408

Table 7.12: QCD background fraction, F_{QCD} for CEM region, high E_T^{EM}.

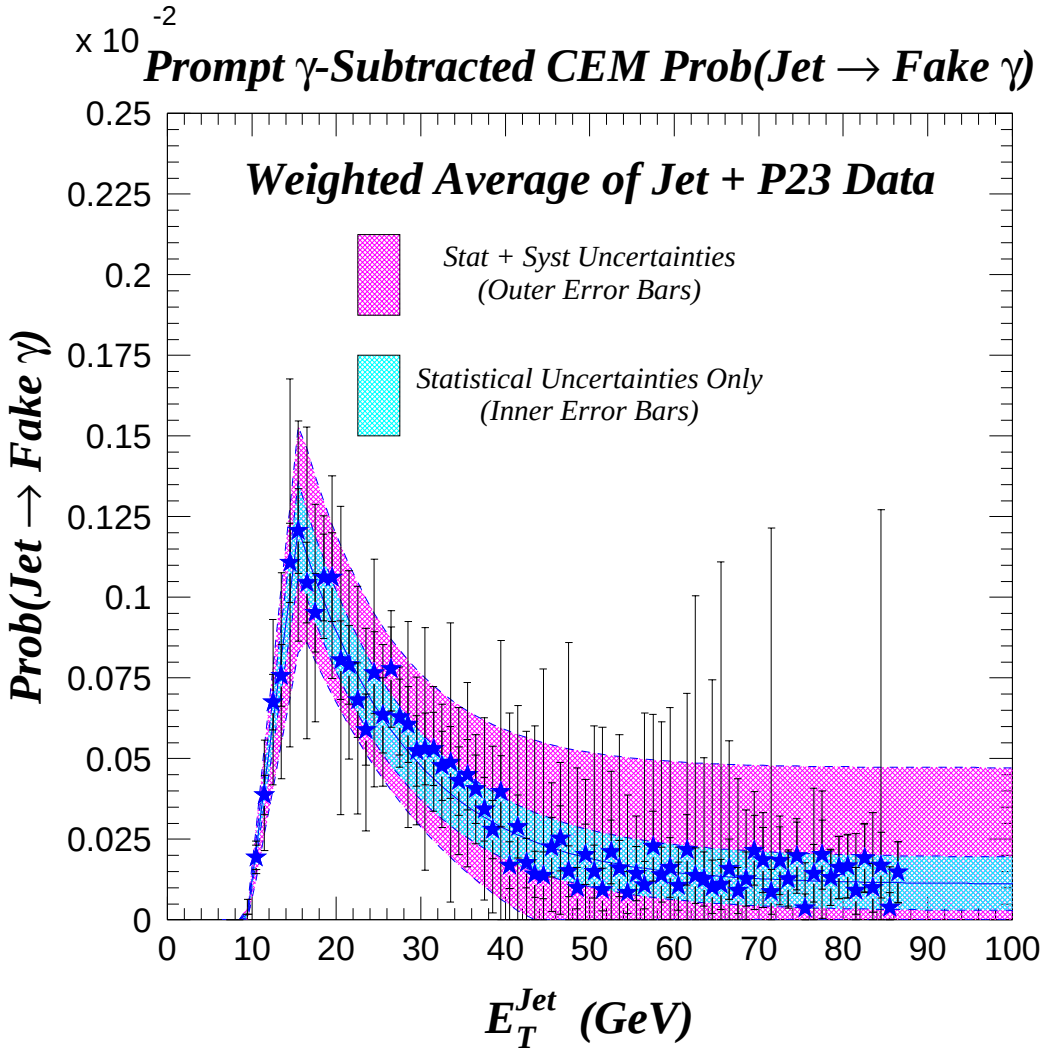

Figure 7.5: Prompt photon-subtracted probability for a CEM jet to fake a photon from the JET and P23 data samples.

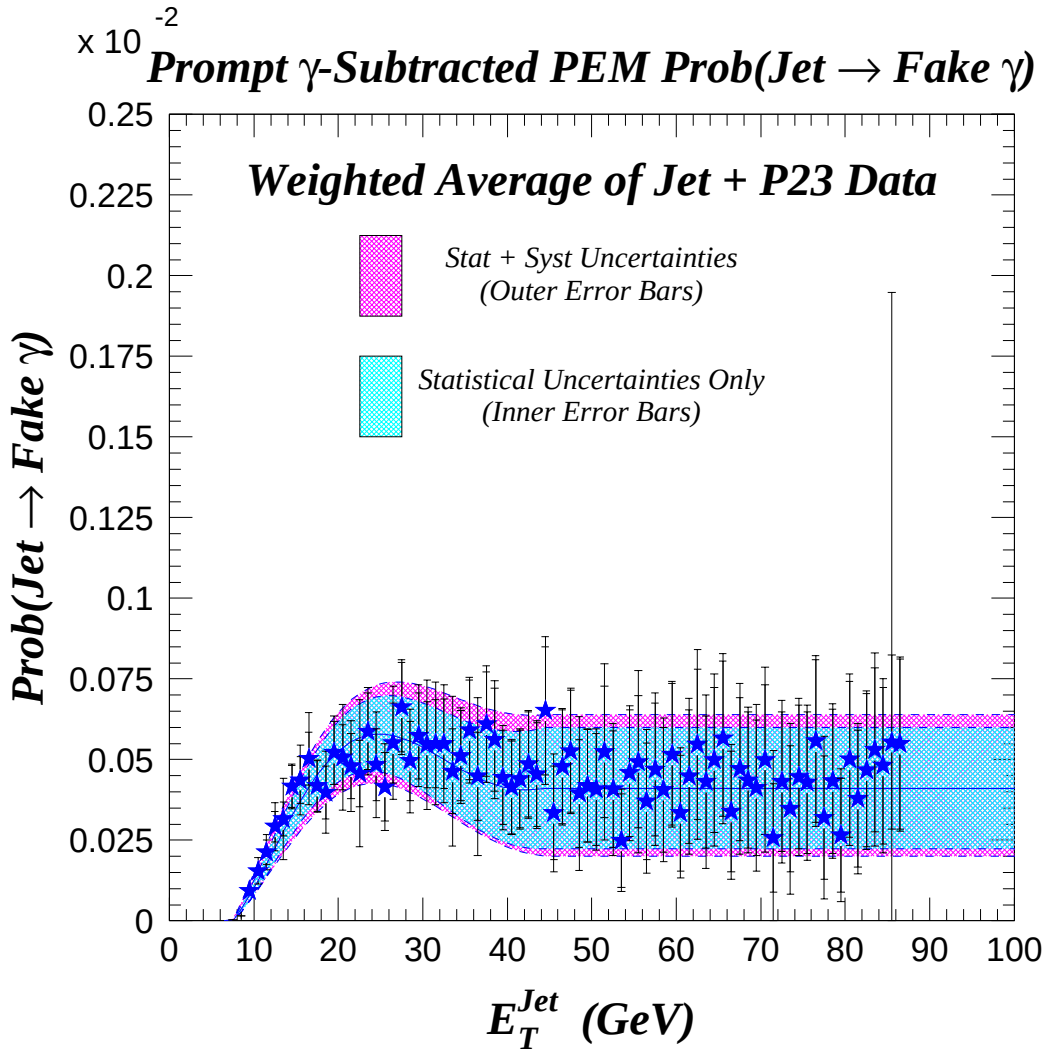

Figure 7.6: Prompt photon-subtracted probability for a PEM jet to fake a photon from the JET and P23 data samples.

The detailed information as to how a central (plug) QCD jet with transverse energy, E_T^{JET}, fragments in such a way as to fake a CEM (PEM) photon with EM transverse energy, $E_T^{EM} \leq E_T^{JET}$ is contained in the correlation information associated with the CEM (PEM) E_T^{EM} versus E_T^{JET} scatterplots (after prompt photon subtraction) as shown in Figure 7.7. However, a more convenient and equivalent choice of variables to express this fragmentation correlation is the CEM (PEM) $Z \equiv E_T^{EM}/E_T^{JET}$ versus E_T^{JET} scatterplot. The physical meaning of the variable Z is that it is the fractional amount of transverse energy of the fake photon from the parent QCD jet. The Z versus E_T^{JET} scatterplot can be normalized in order to convert it to a probability density function. Thus, we can define a two-dimensional QCD jet $\rightarrow$ fake photon "fragmentation" function, $\mathcal{D}(Z, E_T^{JET})$, such that $\int_0^1 \mathcal{D}(Z, E_T^{JET})dZ = 1$. For a given E_T^{JET}, $\mathcal{D}(Z, E_T^{JET})$ is the probability that a jet of E_T^{JET} fragments in such a way as to fake a photon of $E_T^{EM} \leq E_T^{JET}$. These distributions are shown for central and plug jet in Figure 7.8.

Given that a central(plug) QCD jet of E_T^{JET} does fragment in such a way as to fake a CEM (PEM) photon with prompt photon subtracted probability $\mathcal{P}_{\text{JET}\rightarrow\text{fake }\gamma}(E_T^{JET})$, it fragments with 100% probability to a "tight" central (plug) EM cluster with $E_T^{EM} \leq E_T^{JET}$. The CEM (PEM) "fragmentation" function, $\mathcal{D}(Z, E_T^{JET})$ contains the information on precisely how the central (plug) QCD jets fragment to a CEM (PEM) fake photon, respectively.

The QCD jet fake-photon background in each of the e/μ $W + \gamma$ and $Z + \gamma$ data samples was then obtained by convoluting the central (plug) jet E_T^{JET} distributions associated with the inclusive e/μ W/Z data samples with the prompt photon subtracted CEM (PEM) $\mathcal{P}_{\text{JET}\rightarrow\text{fake }\gamma}(E_T^{JET})$ probability distributions and using the CEM (PEM) $\mathcal{D}(Z, E_T^{Jet})$ jet "fragmentation" distributions, respectively.

Operationally, each central (plug) jet in the inclusive e/μ W/Z data samples having $E_T^{JET} > 7$ GeV and W/Z decay lepton-jet angular separation $\Delta R_{\ell-Jet} > 0.7$ was assigned an event weight, W, equal to the prompt photon-subtracted value of CEM (PEM) $\mathcal{P}_{\text{Jet}\rightarrow\text{fake }\gamma}(E_T^{Jet})$, the probability that this central (plug) jet fragmented

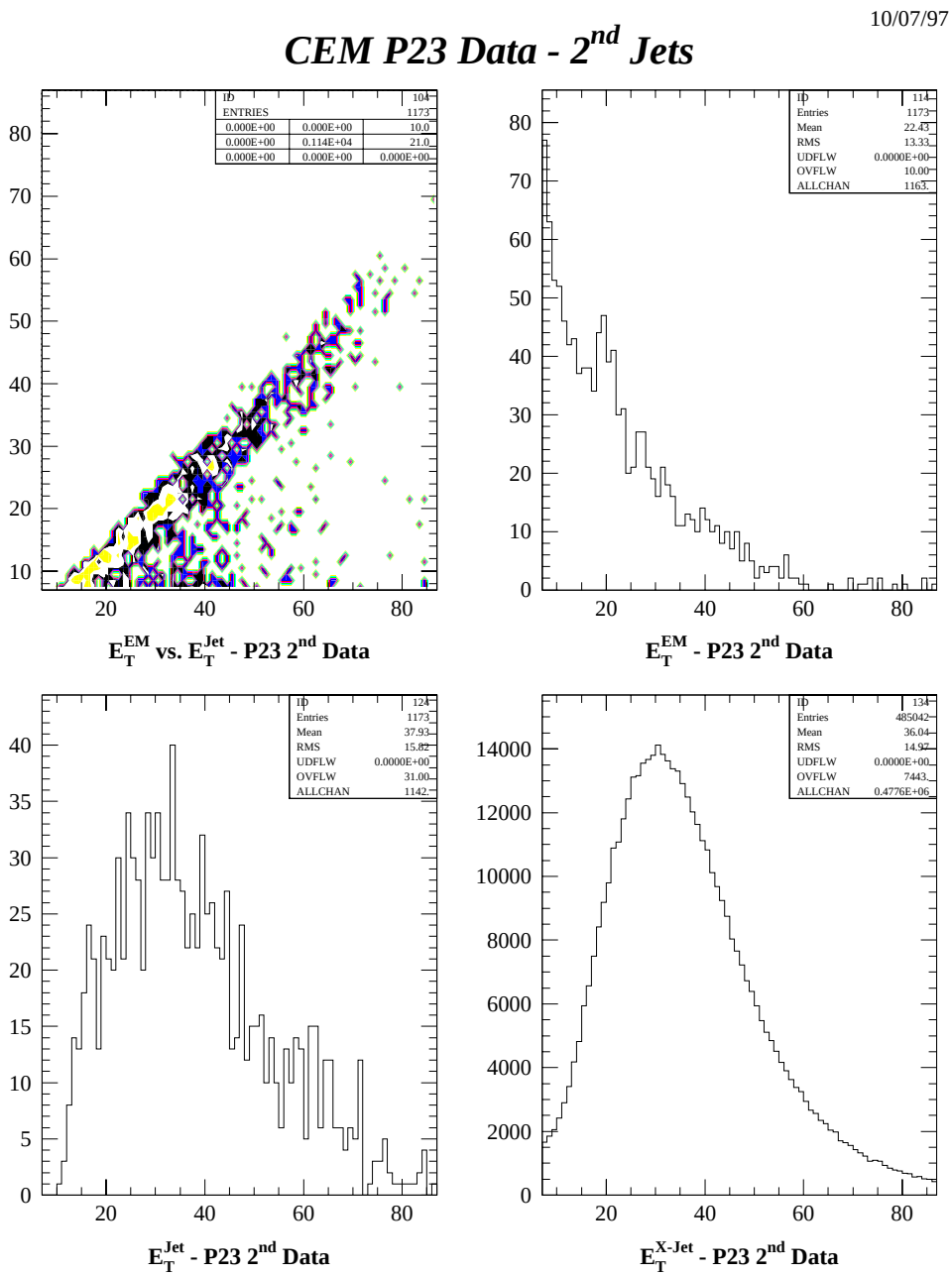

Figure 7.7: E_T^{EM} versus E_T^{JET} scatterplot, the projections onto each axis and the E_T^{Jet} spectrum associated with the unmatched "extra" jets for the CEM P23 2-only jets data sample.

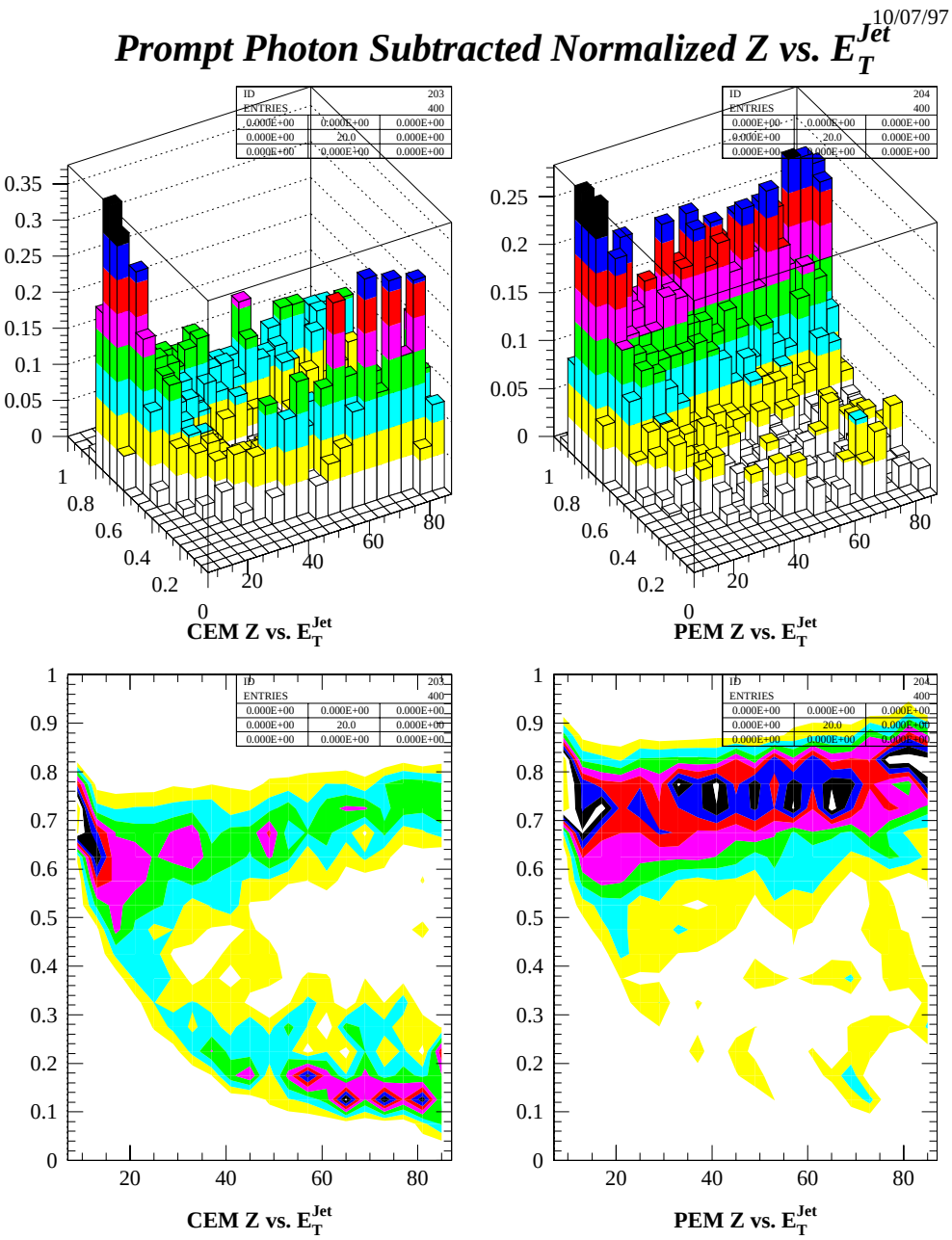

Figure 7.8: The combined JET + P23 prompt photon subtracted and normalized CEM/PEM Z versus E_T^{JET} distributions for "tight" CEM/PEM clusters matched to central/plug jets.

in such a way as to mimic a photon passing our $V + \gamma$ photon cuts. We show the inclusive jet spectra for inclusive W and Z bosons in Figure 7.9 and the results are shown in Tables 8.9- 8.10.

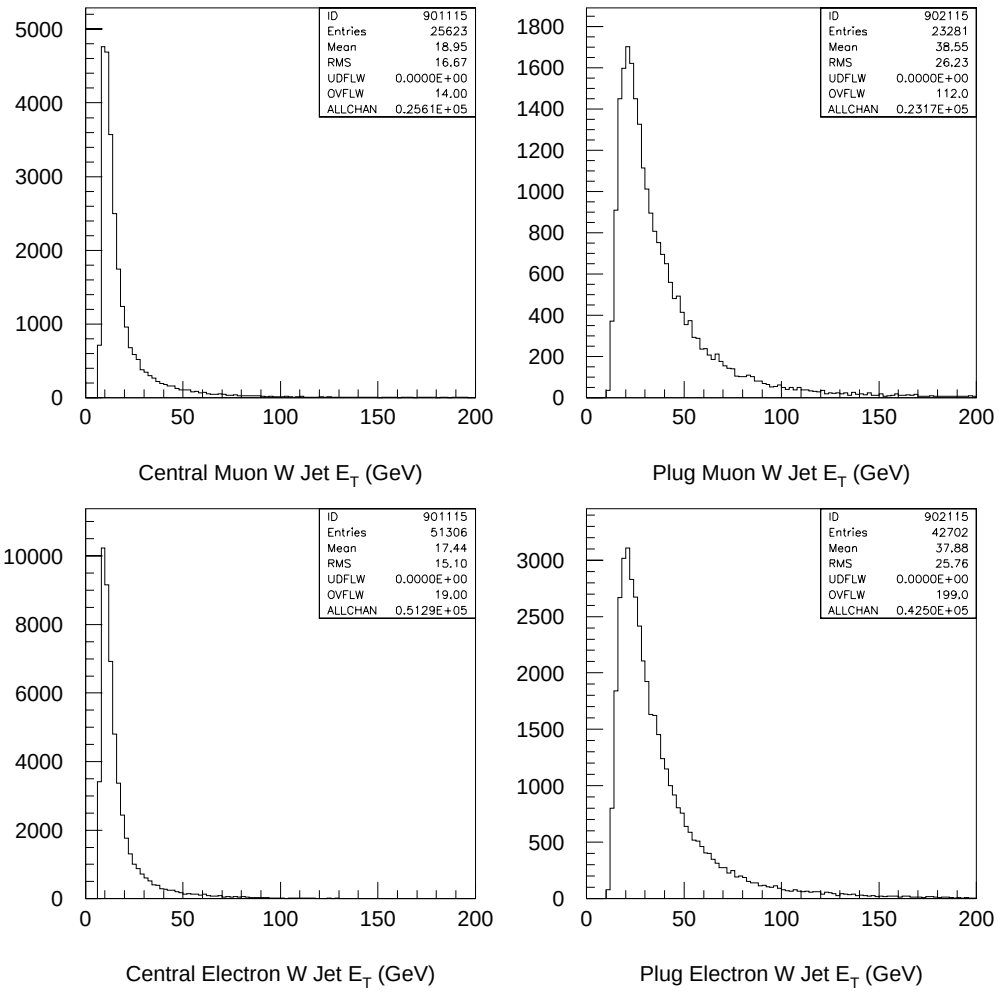

Figure 7.9: Jet transverse energy spectra for central and plug jets in inclusive electron + muon channel W data. The top histograms are from muon W data and the bottom histograms are from electron W data.

The correlation information contained in the prompt photon-subtracted CEM (PEM) normalized $\mathcal{D}(Z, E_T^{JET})$ scatterplot(s) was then used to "fragment" (with unit probability) this central (plug) jet with transverse energy E_T^{JET} to a fake CEM (PEM) photon with transverse energy $E_T^{EM} \leq E_T^{JET}$, respectively, using hybrid Monte Carlo techniques. Since the four-vector information associated with each such jet is known, and the angular separation (ΔR) distribution between "tight" EM cluster matched to "extra" non-leading central (plug) jets is strongly peaked at $\Delta R = 0$, we also obtain from this hybrid Monte Carlo simulation the four-vector information of the fragmented, fake photon, along with its event weight (equal to the value of the $\mathcal{P}_{\mathrm{JET}\to\mathrm{fake}\ \gamma}(E_T^{JET})$ for this input jet).

Thus, by using all such jets in the inclusive e/μ W/Z data samples, we are able to obtain the QCD jet background in the e/μ $W+\gamma$ and $Z+\gamma$ data samples for any $V+\gamma$ kinematic distribution of interest, not just the E_T^{γ} distribution(s), but also the $W+\gamma$ cluster transverse mass (M_{CT}) distribution, the $Z+\gamma$ 3-body mass ($M_{\ell^+\ell^-\gamma}$) distribution, the charge-signed rapidity difference ($Q^{\ell}\cdot\Delta\eta_{\gamma-\ell}$) distributions, the $\cos\theta^*$ distributions, etc.

7.4.2 Electroweak Backgrounds

Other backgrounds to the $W\gamma$ sample include one-legged Zs with an associated photon and tauon decay of the W boson with an associated photon. These two backgrounds have already been discussed in Chapter 4 and Chapter 5.

Chapter 8

$V + \gamma$ Standard Model Comparisons

8.1 The $V + \gamma$ Standard Model Event Yield Comparison

We have described the construction and analysis of 110 pb^{-1} of inclusive high P_T muon and electron data. After constructing inclusive muon and electron channel Z and W samples, we applied our CEM and PEM photon quality requirements and constructed muon and electron channel $Z + \gamma$ and $W + \gamma$ samples. Using inclusive Z+jets and W+jets data, we estimated the QCD to fake photon background in the $Z + \gamma$ and $W + \gamma$ samples. The electroweak backgrounds in these samples were determined from Monte Carlo studies. We summarize our results numerically in Tables 8.1- 8.10. In Figure 8.1, we graphically summarize all the channels in the analysis and their deviations.

We calculated the deviations from the standard model predictions using the following formula:

$$\Delta = \frac{N_{obs} - N_{pred}^{tot}}{N_{pred}^{tot}} \tag{8.1}$$

where N_{obs} is the number of observed events, in the respective channel (inclusive V and $V + \gamma$), and N_{pred}^{tot} is the total number of predicted signal plus background expectation. The statistical significance of these results is discussed in Chapter 9.

Process	Run 1B	Run 1A	Total
$Z\gamma$	17.62 ± 1.07	2.99 ± 0.19	20.61 ± 1.26
Jet$\rightarrow \gamma$	0.72 ± 0.28	0.10 ± 0.04	0.82 ± 0.32
SM Total	18.34 ± 1.11	3.09 ± 0.19	21.43 ± 1.30
Data	23	4	27

Table 8.1: Comparison of muon channel $Z\gamma$ event yields between the standard model plus background expectation and data for CEM photons using the default $V+\gamma$ cuts.

Process	Run 1B	Run 1A	Total
$W\gamma$	38.05 ± 2.39	6.47 ± 0.44	44.52 ± 2.83
Jet$\rightarrow \gamma$	7.93 ± 2.90	1.23 ± 0.44	9.16 ± 3.34
$OLZ + \gamma$	8.38 ± 0.53	1.23 ± 0.08	9.61 ± 0.61
$W \rightarrow \tau + \gamma$	0.59 ± 0.04	0.10 ± 0.01	0.69 ± 0.05
SM Total	54.95 ± 4.14	9.03 ± 0.69	63.98 ± 4.83
Data	63	11	74

Table 8.2: Comparison of muon channel $W\gamma$ event yields between the standard model plus background expectation and data for CEM photons using the default $V+\gamma$ cuts.

Process	Run 1B	Run 1A	Total
$Z\gamma$	6.11 ± 0.38	1.09 ± 0.07	7.20 ± 0.45
Jet$\rightarrow \gamma$	0.38 ± 0.11	0.05 ± 0.02	0.43 ± 0.11
SM Total	6.49 ± 0.40	1.14 ± 0.07	7.63 ± 0.46
Data	7	2	9

Table 8.3: Comparison of muon channel $Z\gamma$ event yields between the standard model plus background expectation and data for PEM photons using the default $V+\gamma$ cuts.

Process	Run 1B	Run 1A	Total
$W\gamma$	21.15 ± 1.36	3.68 ± 0.25	24.83 ± 1.61
Jet$\rightarrow \gamma$	3.86 ± 1.15	0.58 ± 0.17	4.44 ± 1.32
$OLZ + \gamma$	4.64 ± 0.30	0.68 ± 0.05	5.32 ± 0.35
$W \rightarrow \tau + \gamma$	0.43 ± 0.03	0.08 ± 0.01	0.51 ± 0.04
SM Total	30.08 ± 2.04	5.02 ± 0.35	35.10 ± 2.40
Data	43	5	48

Table 8.4: Comparison of muon channel $W\gamma$ event yields between the standard model plus background expectation and data for PEM photons using the default $V+\gamma$ cuts.

Process	Run 1B	Run 1A	Total
$Z\gamma$	23.98 ± 1.23	5.65 ± 0.30	29.63 ± 1.53
Jet$\rightarrow \gamma$	1.50 ± 0.54	0.30 ± 0.11	1.80 ± 0.65
SM Total	25.48 ± 1.34	5.95 ± 0.32	31.43 ± 1.66
Data	29	7	36

Table 8.5: Comparison of electron channel $Z\gamma$ event yields between the standard model plus background expectation and data for CEM photons using the default $V + \gamma$ cuts.

Process	Run 1B	Run 1A	Total
$W\gamma$	67.26 ± 3.37	15.81 ± 0.75	83.07 ± 4.12
Jet$\rightarrow \gamma$	14.84 ± 5.26	3.02 ± 1.10	17.86 ± 6.36
$OLZ + \gamma$	2.92 ± 0.15	0.64 ± 0.03	3.56 ± 0.18
$W \rightarrow \tau + \gamma$	1.05 ± 0.05	0.24 ± 0.01	1.29 ± 0.06
SM Total	86.07 ± 6.36	19.71 ± 1.35	105.78 ± 7.71
Data	108	20	128

Table 8.6: Comparison of electron channel $W\gamma$ event yields between the standard model plus background expectation and data for CEM photons using the default $V + \gamma$ cuts.

Process	Run 1B	Run 1A	Total
$Z\gamma$	10.27 ± 0.55	2.64 ± 0.14	12.91 ± 0.69
Jet$\rightarrow \gamma$	0.70 ± 0.20	0.14 ± 0.04	0.84 ± 0.24
SM Total	10.97 ± 0.59	2.78 ± 0.15	13.75 ± 0.73
Data	6	1	7

Table 8.7: Comparison of electron channel $Z\gamma$ event yields between the standard model plus background expectation and data for PEM photons using the default $V + \gamma$ cuts.

Process	Run 1B	Run 1A	Total
$W\gamma$	38.41 ± 1.98	9.90 ± 0.49	48.31 ± 2.47
Jet$\rightarrow \gamma$	6.88 ± 2.04	1.41 ± 0.42	8.29 ± 2.46
$OLZ + \gamma$	1.74 ± 0.09	0.41 ± 0.02	2.15 ± 0.11
$W \rightarrow \tau + \gamma$	0.75 ± 0.04	0.19 ± 0.01	0.94 ± 0.05
SM Total	47.78 ± 2.93	11.91 ± 0.67	59.69 ± 3.60
Data	64	21	85

Table 8.8: Comparison of electron channel $W\gamma$ event yields between the standard model plus background expectation and data for PEM photons using the default $V + \gamma$ cuts.

Process	Run 1B	Run 1A	Total
$Z\gamma$	57.98 ± 3.21	12.37 ± 1.30	70.35 ± 4.51
Jet$\rightarrow \gamma$	3.30 ± 1.13	0.59 ± 0.20	3.89 ± 1.33
SM Total	61.28 ± 3.40	12.96 ± 1.32	74.24 ± 4.70
Data	65	14	79

Table 8.9: Comparison of muon plus electron channel $Z\gamma$ event yields between the standard model plus background expectation and data using the default $V+\gamma$ cuts.

Process	Run 1B	Run 1A	Total
$W\gamma$	164.89 ± 9.02	35.86 ± 1.93	200.75 ± 10.95
Jet$\rightarrow \gamma$	33.52 ± 11.35	6.25 ± 2.13	39.77 ± 13.48
$OLZ + \gamma$	17.69 ± 1.05	2.96 ± 0.18	20.65 ± 1.23
$W \rightarrow \tau + \gamma$	2.82 ± 0.15	0.61 ± 0.04	3.43 ± 0.19
SM Total	218.92 ± 15.27	45.68 ± 3.03	264.60 ± 18.30
Data	278	57	335

Table 8.10: Comparison of muon plus electron channel $W\gamma$ event yields between the standard model plus background expectation and data using the default $V+\gamma$ cuts.

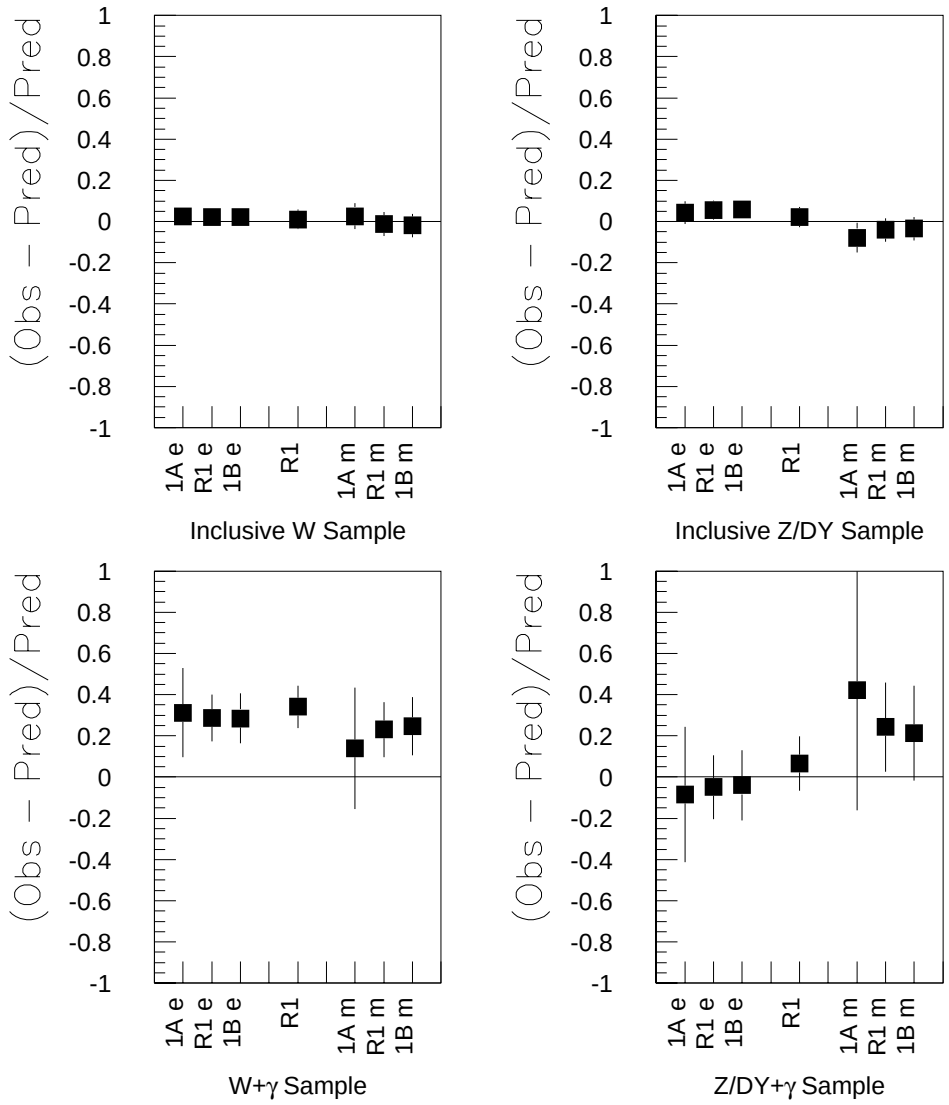

Figure 8.1: A graphical summary of all channels in this analysis and their deviations from standard model predictions using the default $V + \gamma$ cuts.

8.2 $V + \gamma$ Kinematic Distributions

8.2.1 Standard Studies

In Figures 8.2- 8.3, the $Z\gamma$ photon transverse energy spectrum is plotted on a linear and logarithmic scale, respectively.[1] The data exhibits the sharply falling behavior as expected. We discuss the statistical significance of this distribution in Chapter 9. The three-body mass, $M_{\ell\ell\gamma}$, is displayed in Figure 8.4. Non-zero anomalous $ZZ\gamma/Z\gamma\gamma$ couplings would tend to broaden this distribution and produce events with high three-body masses. One event with spectacular properties does occur with a very high three-body mass. This event has a three-body mass of 423 GeV/c^2, with photon $E_T = 193$ GeV ($= P_T^Z$), and is discussed in detail in [44].

In Figures 8.5- 8.6, we show scatterplots of the three-body mass versus the dilepton or pair mass on a linear and logarithmic z scale, respectively. The vertical lines at $M_Z = 65$ GeV/c^2 and 110 GeV/c^2 delineate the standard Z mass window cut for older analyses. We have replaced this Z mass window cut with a lower bound $M_Z > 65(70)$ GeV/c^2 in order to increase statistics and to be sensitive to new physics which would occur with high pair masses (e.g. leptoquarks, excited leptons, etc.). The diagonal line with slope equal to one is used to guide the eye and is the dividing line in which all events occur above due to the 7 GeV requirement on the photon. The horizontal line at a three-body mass of 100 GeV/c^2 is used as a lower cut in charged-signed rapidity studies to suppress radiative events which populate the region below it. The events in the upper right region are from Drell-Yan + photon. It can be seen from these scatterplots that these three $Z/DY + \gamma$ events are exceedingly improbable to have occurred, and are also exceedingly unlikely to be background. The event at a three-body mass of 300 GeV/c^2 and pair mass of 163 GeV/c^2 is the famous $e^+e^-\gamma\gamma$ + MET event [38].

[1] Linear plots emphasize the peak of the distribution while logarithmic plots emphasize the tails of the distribution.

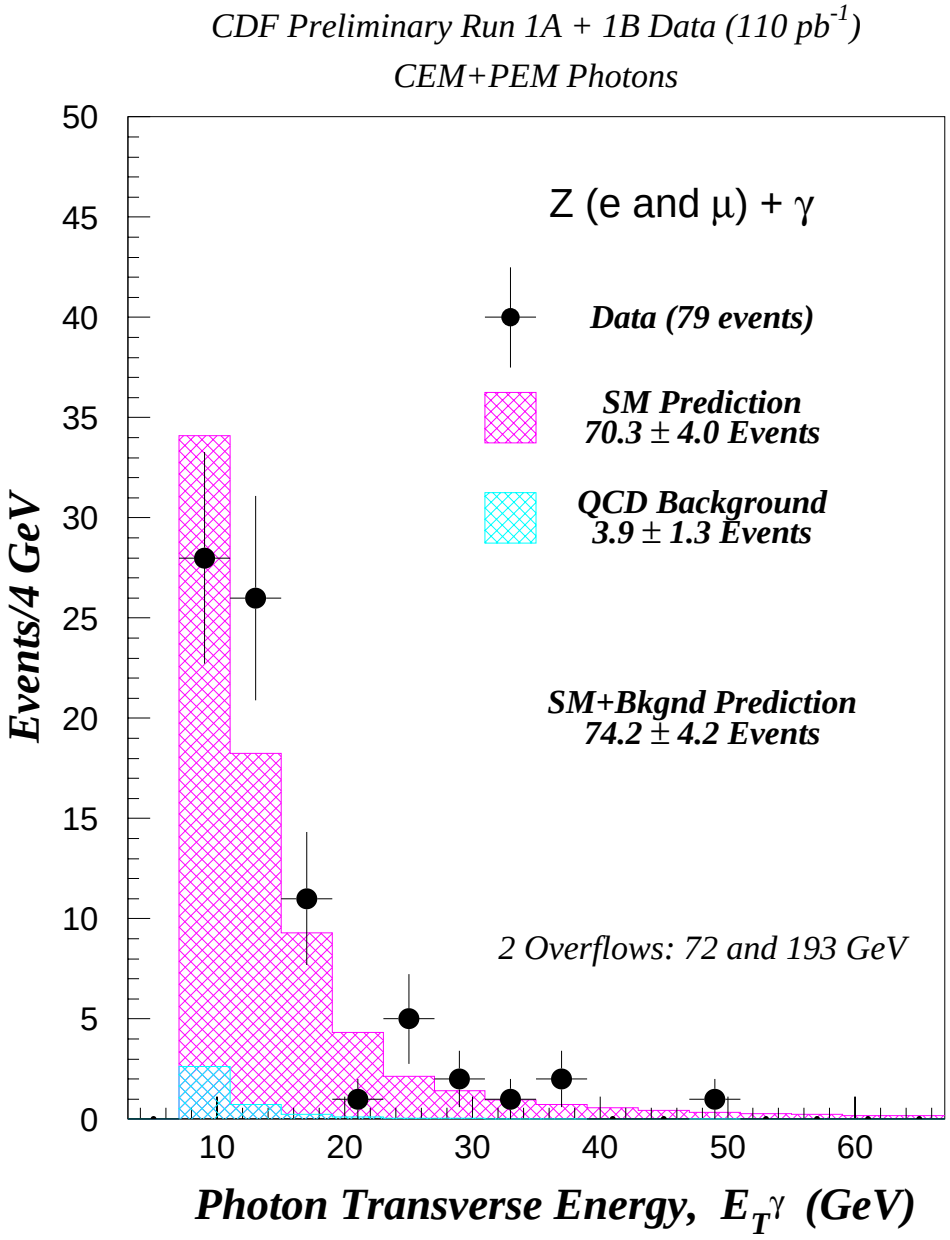

Figure 8.2: $Z/DY + \gamma$ transverse E_T^γ overlaid on the standard model prediction plus background expectation on a linear scale.

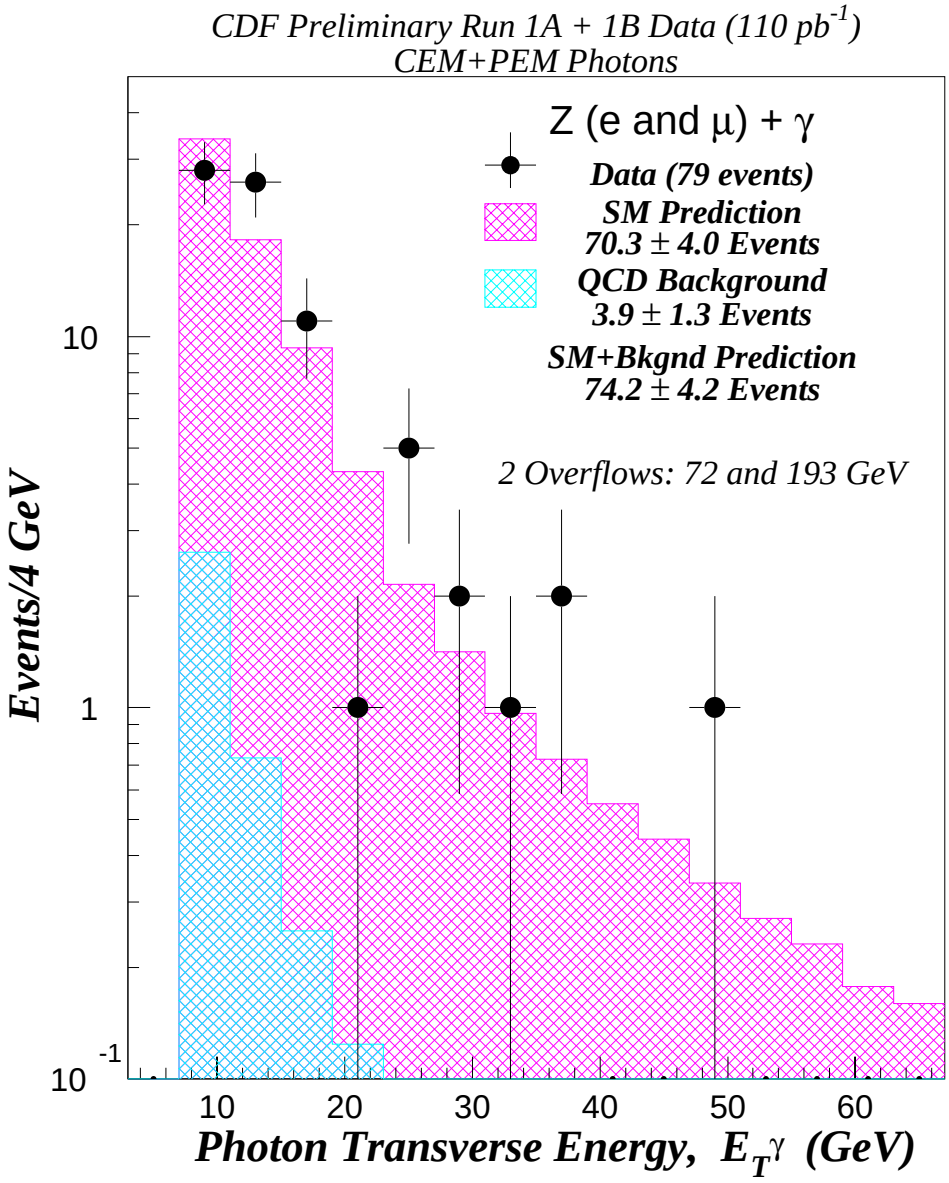

Figure 8.3: $Z/DY + \gamma$ transverse E_T^γ overlaid on the standard model prediction plus background expectation on a logarithmic scale.

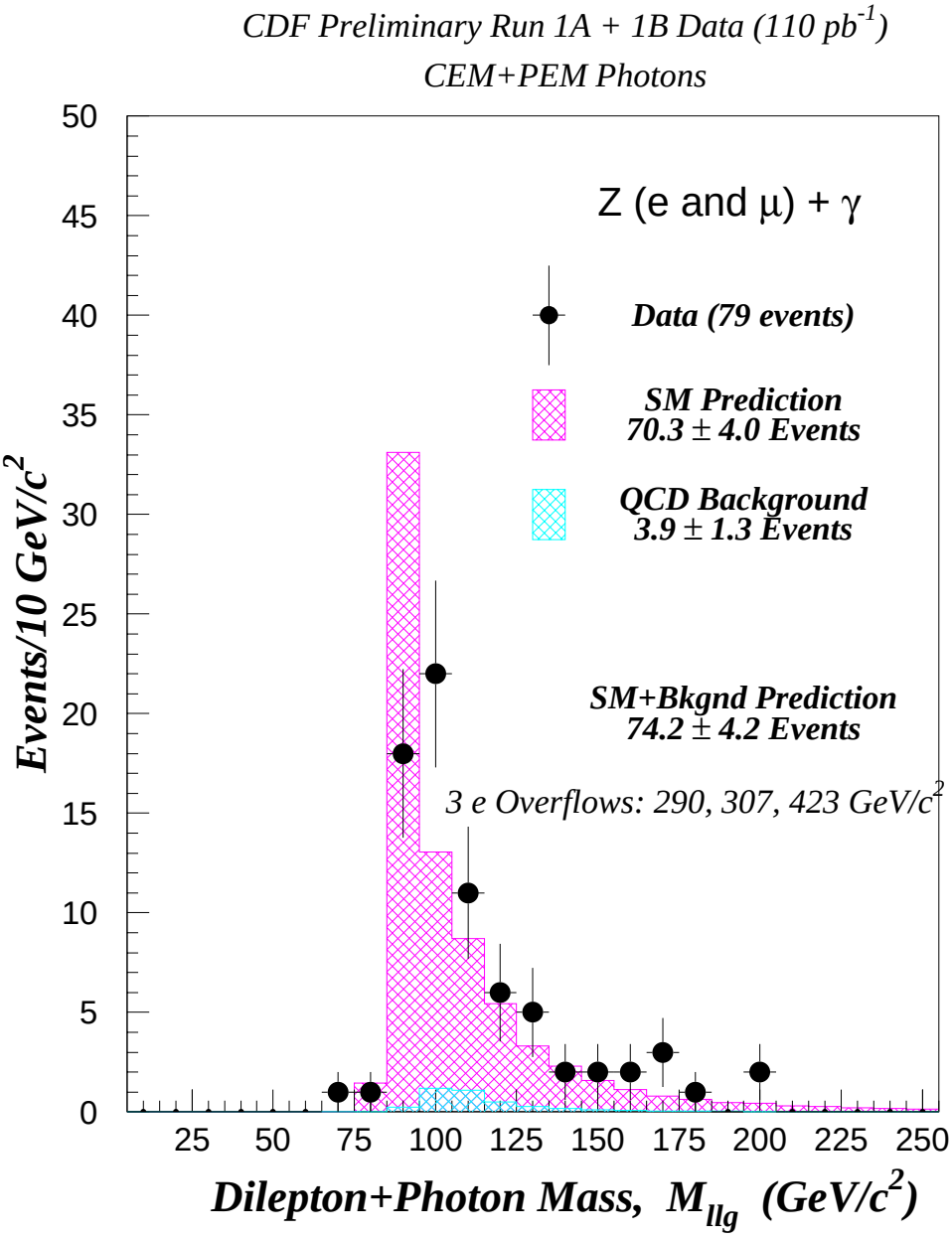

Figure 8.4: $Z/DY+\gamma$ three-body mass $M_{ll\gamma}$ overlaid on the standard model prediction plus background expectation.

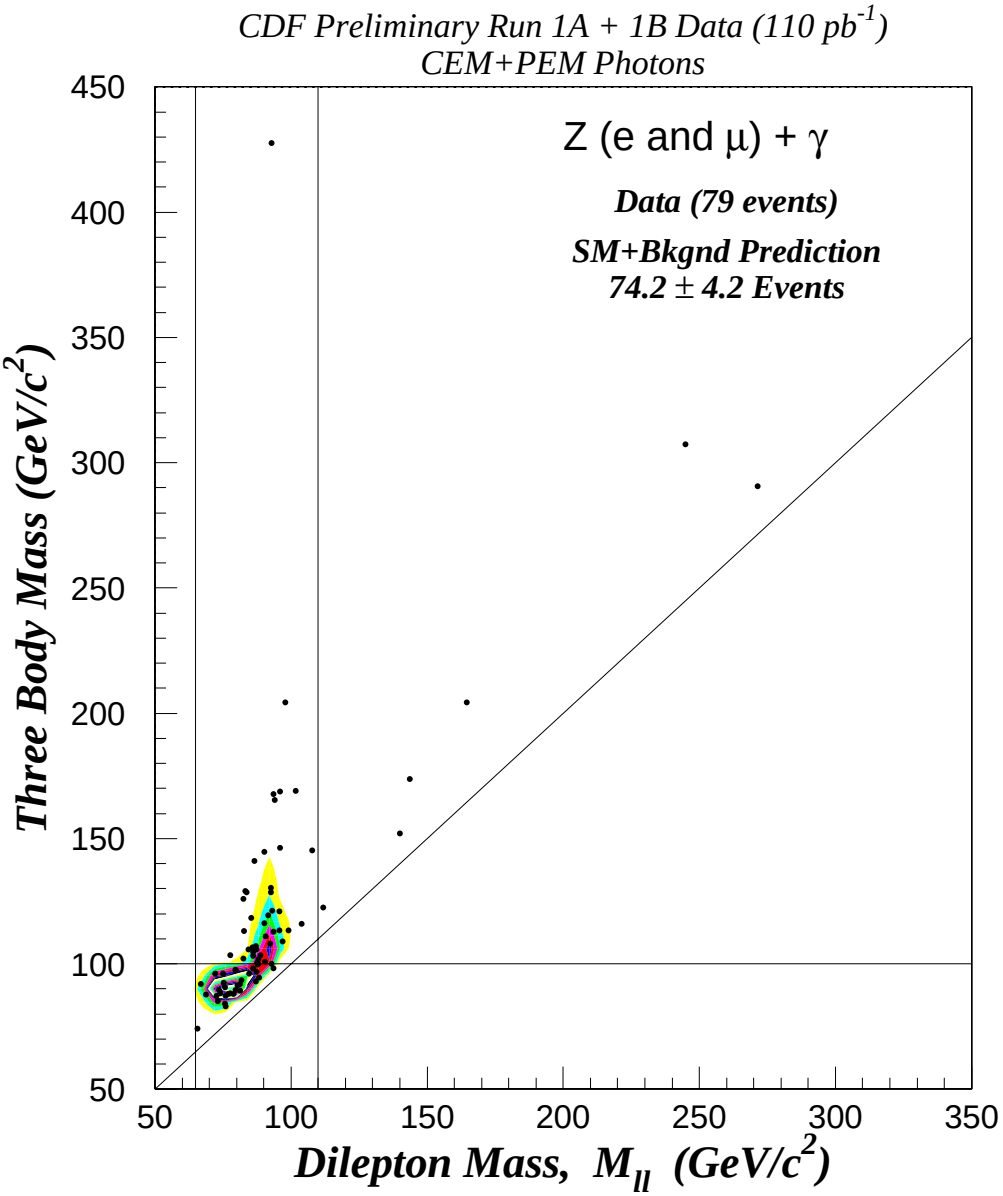

Figure 8.5: $Z/DY + \gamma$ three-body mass versus dilepton pair mass overlaid on the standard model prediction plus background expectation on a linear z scale.

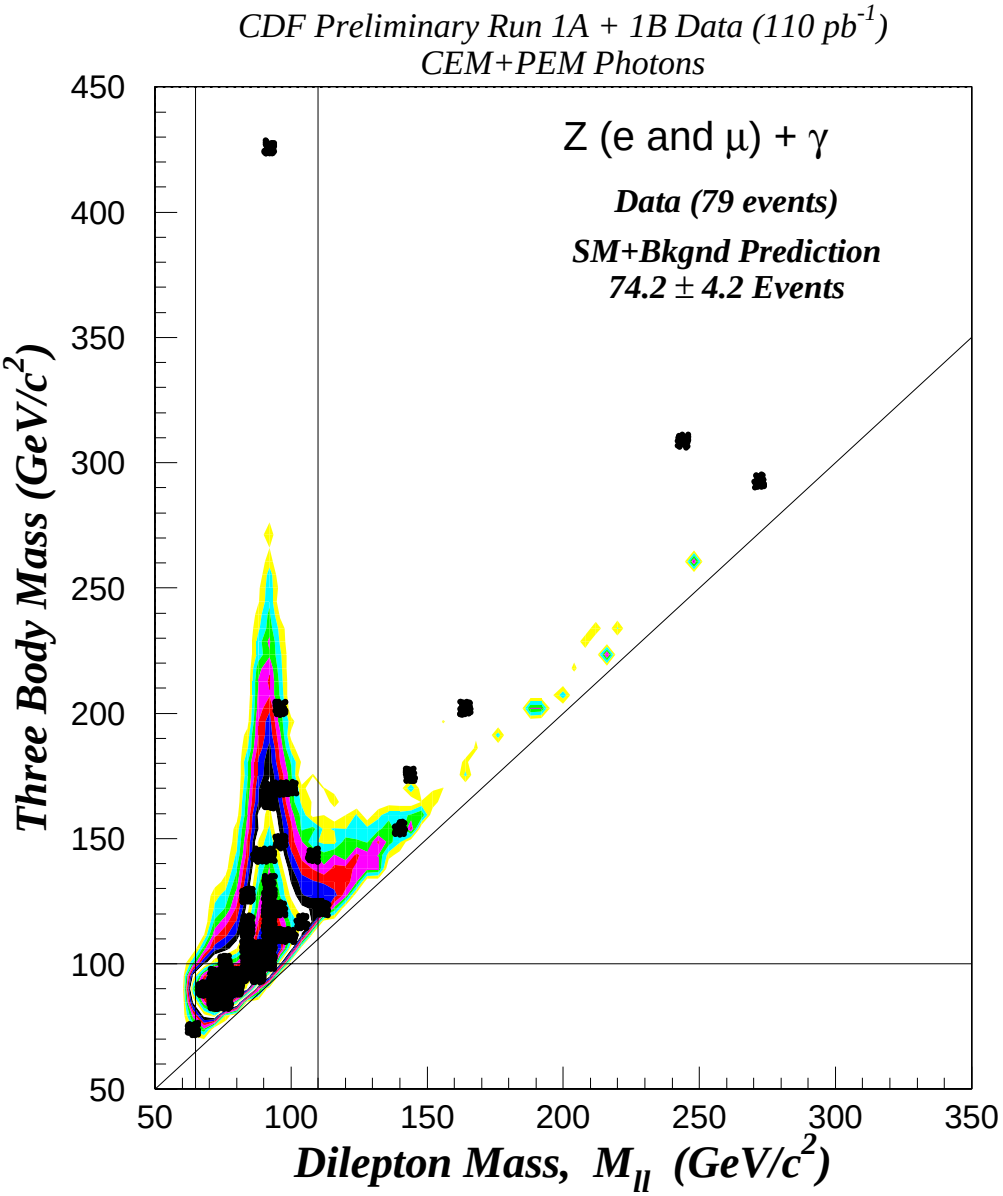

Figure 8.6: $Z/DY + \gamma$ three-body mass versus dilepton pair mass overlaid on the standard model prediction plus background expectation on a logarithmic z scale.

In Figures 8.7- 8.8, the $W\gamma$ photon transverse energy spectrum is plotted on a linear and logarithmic scale, respectively. The data exhibits the steeply falling behavior as expected, but there exists a clear excess of events in the high E_T region by an overall factor of 25%. In Figure 8.9, we plot the lepton-photon angular separation, $\Delta R(\ell - \gamma)$ for $W\gamma$ events. The excess populates the higher region of lepton-photon separation. Note that it is not peaked around 180° (or π), which would be a strong indication of a background process (e.g. one-legged electron Zs or QCD).

The cluster transverse mass or minimum invariant mass, M_{ct}, is displayed in Figure 8.10. The minimum invariant mass of the $W\gamma$ system is defined by [39]

$$M_{ct}^2 = \left[(M_{l\gamma}^2 + \mid \mathbf{P}_T^{\gamma} + \mathbf{P}_T^{l} \mid^2)^{1/2} + \mid \mathbf{P}_T^{\bar{\nu}} \mid\right]^2 - \mid \mathbf{P}_T^{\gamma} + \mathbf{P}_T^{l} + \mathbf{P}_T^{\bar{\nu}_l} \mid^2 \qquad (8.2)$$

This is the three-body mass of the $W\gamma$ system evaluated at the minimum value of the neutrino's longitudinal momentum.

In Figures 8.11- 8.12, we show scatterplots of the minimum invariant mass versus the W transverse mass on a linear and logarithmic z scale, respectively. The vertical lines at $M_W = 40$ GeV/c^2 and 90 GeV/c^2 create a window around the mass of the W boson. The diagonal line with slope equal to one is used to guide the eye and is the dividing line in which all events occur above due to the 7 GeV requirement on the photon. The horizontal line at a minimum mass of 90 GeV/c^2 is used as a lower cut in charged-signed rapidity studies to suppress radiative events which populate the region below it.

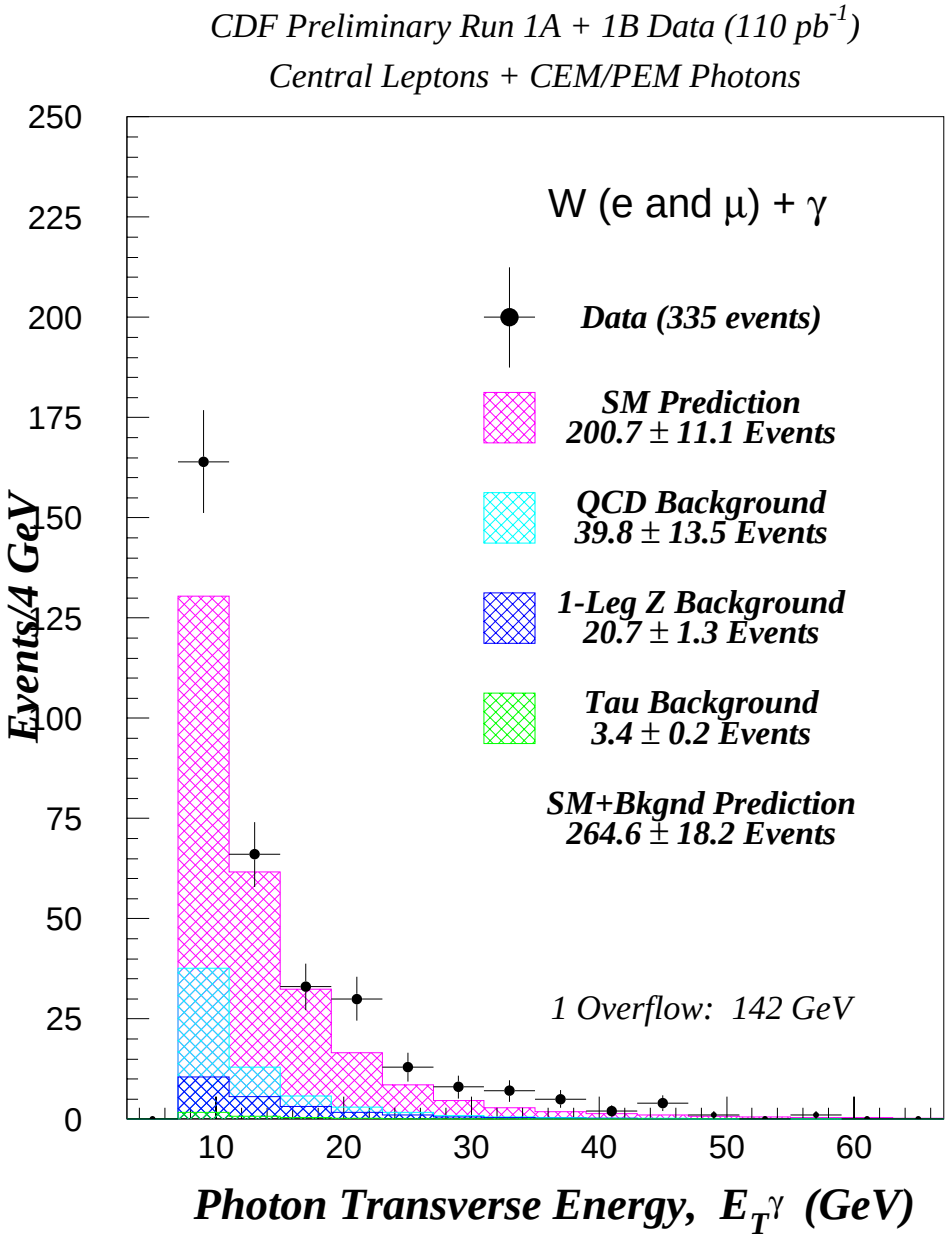

Figure 8.7: $W + \gamma$ transverse E_T^γ overlaid on the standard model prediction plus background expectation on a linear scale.

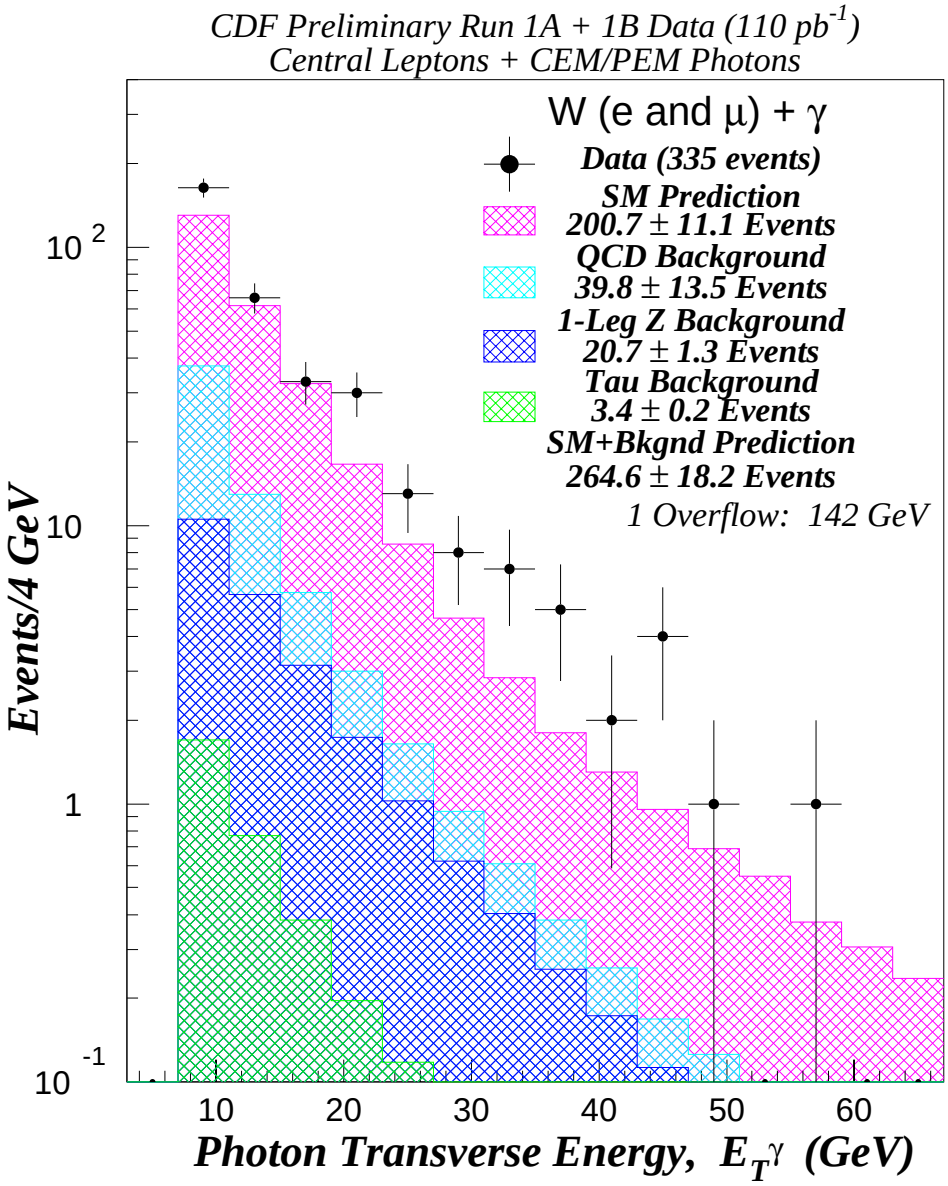

Figure 8.8: $W + \gamma$ transverse E_T^γ overlaid on the standard model prediction plus background expectation on a logarithmic scale.

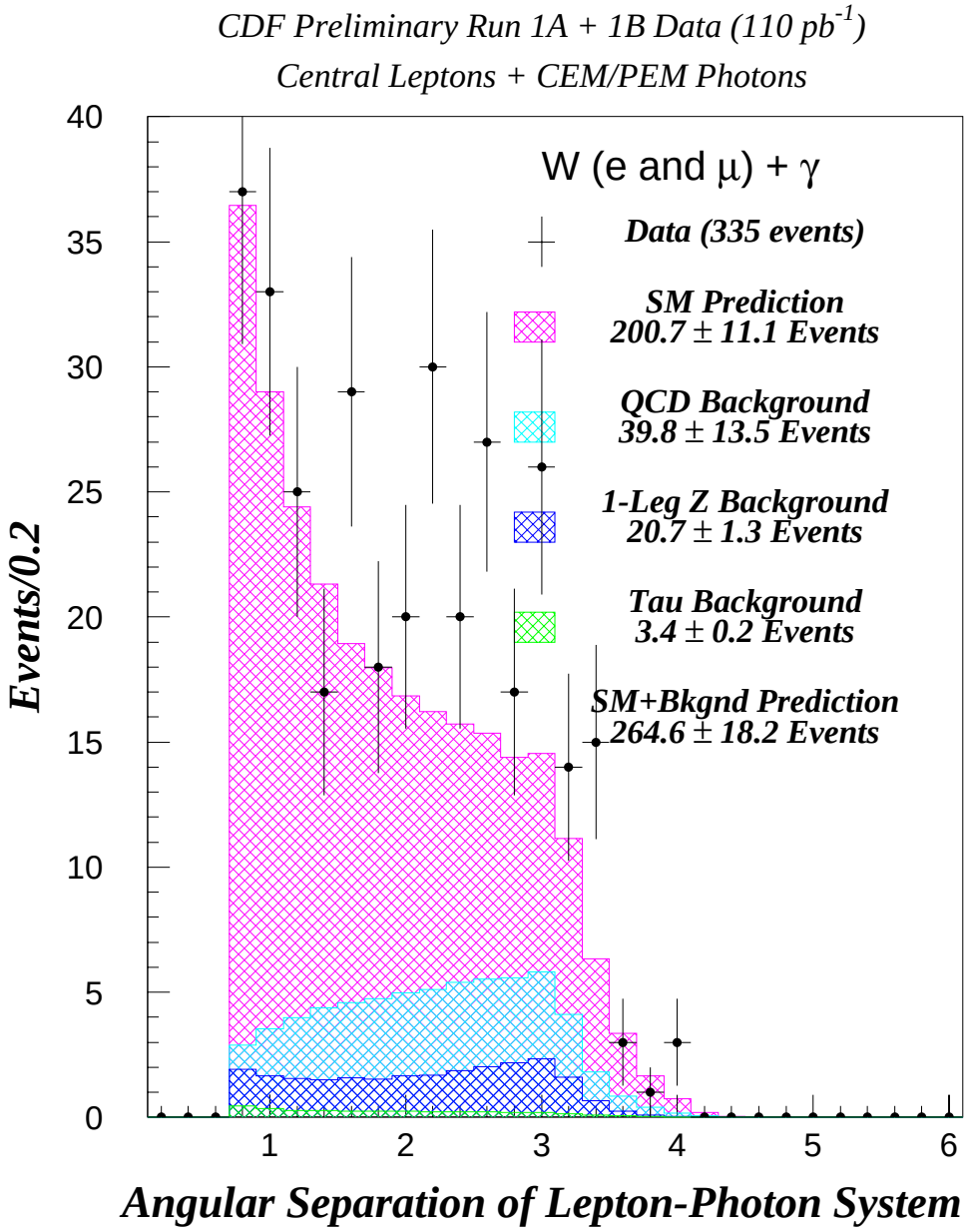

Figure 8.9: The $W+\gamma$ lepton-photon separation, $\Delta R(l-\gamma)$, overlaid on the standard model prediction plus background expectation on a linear scale.

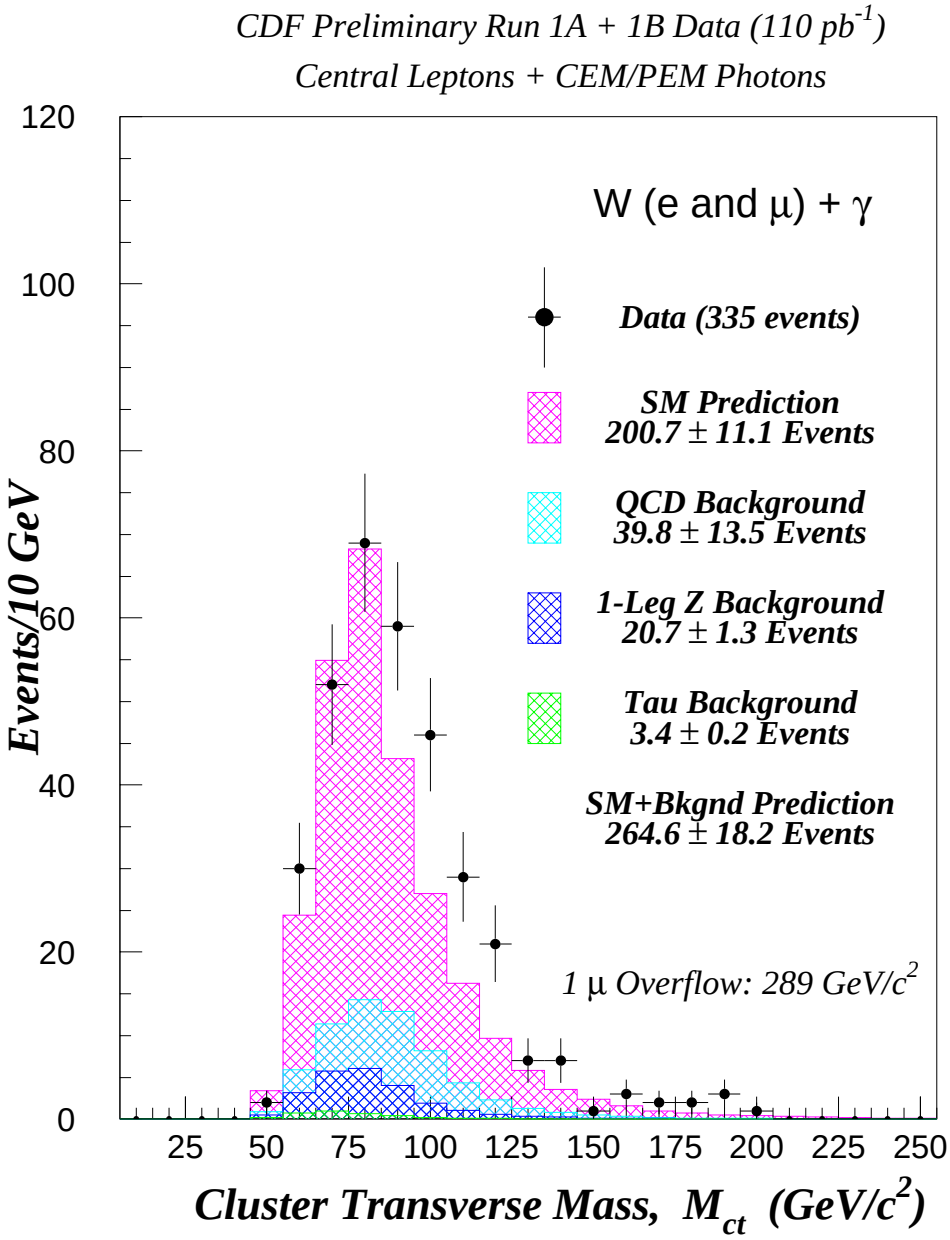

Figure 8.10: $W+\gamma$ cluster transverse mass overlaid on the standard model prediction plus background expectation.

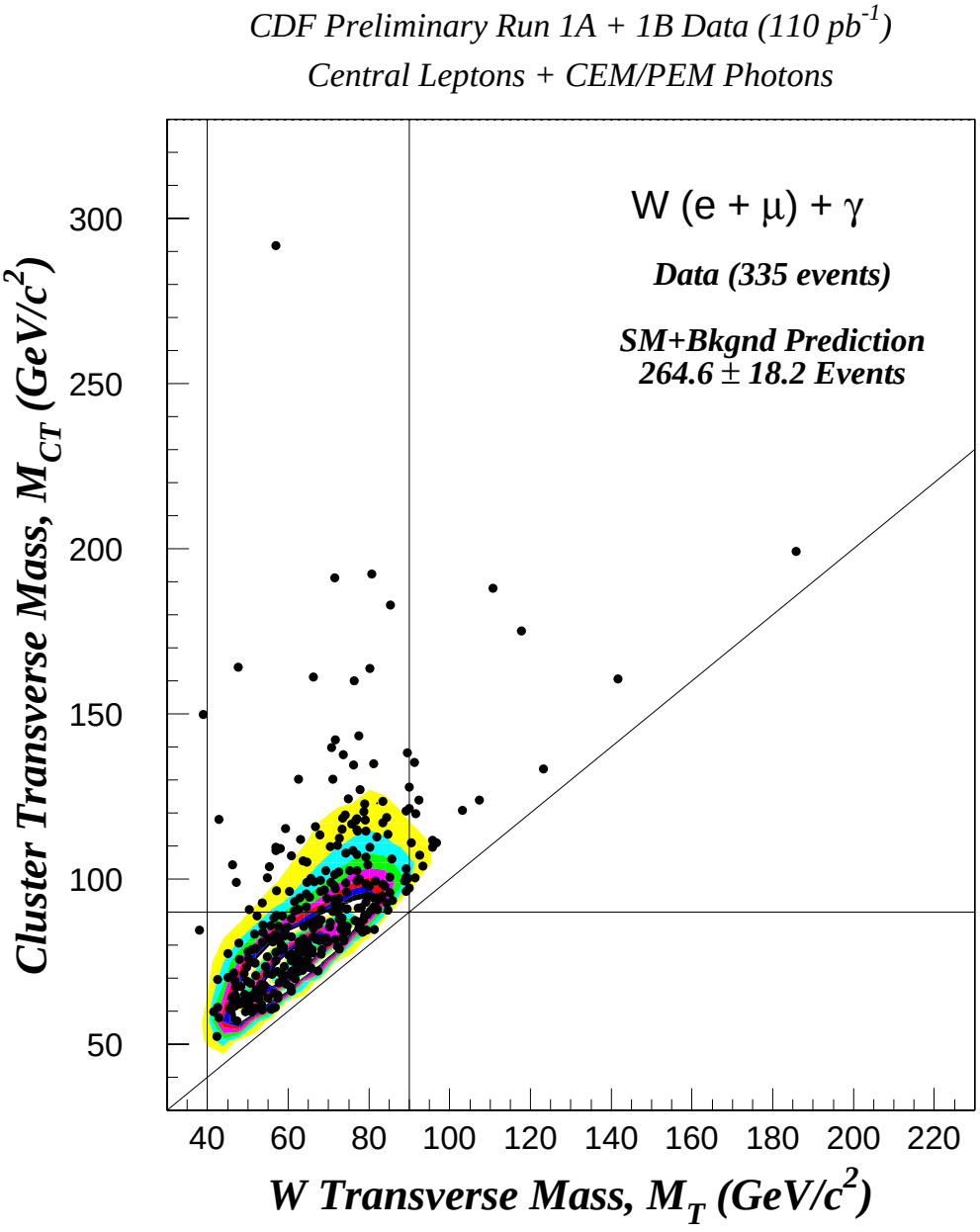

Figure 8.11: $W + \gamma$ cluster transverse mass versus the W transverse mass overlaid on the standard model prediction plus background expectation on a linear z scale.

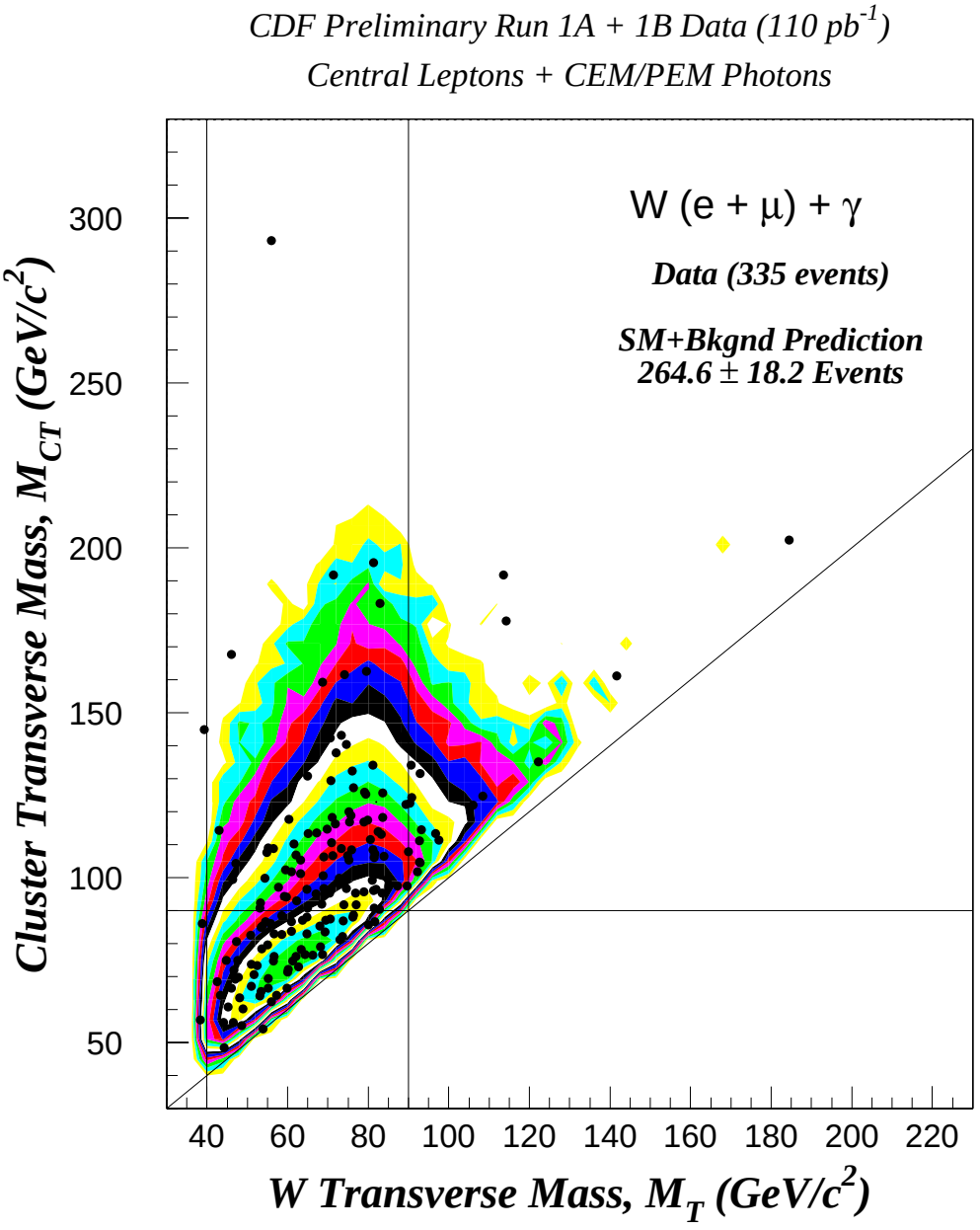

Figure 8.12: $W + \gamma$ cluster transverse mass versus the W transverse mass overlaid on the standard model prediction plus background expectation on a logarithmic z scale.

8.2.2 Radiation Amplitude Zero (RAZ) Studies

The $\Delta R(\ell - \gamma) > 0.7$ requirement dramatically suppresses radiative W/Z decay in the standard (or "default") $W + \gamma$ and $Z + \gamma$ data samples. One can further suppress radiative W and Z decays in these data samples by requiring the three-body mass in the $Z + \gamma$ sample to be greater the 100 GeV/c^2 and by requiring the minimum invariant mass or cluster transverse mass in the $W + \gamma$ sample to be greater than 90 GeV/c^2. We refer to these requirements as RAZ cuts.

The standard model event yield comparison for the $V + \gamma$ RAZ data samples are summarized in Tables 8.11- 8.12 below. A statistically significant excess exists in both the RAZ $Z + \gamma$ and $W + \gamma$ data samples. The statistical significance of these results is discussed in Chapter 9.

In Figure 8.13, we show the photon transverse energy spectrum for $Z\gamma$ events with three-body mass greater the 100 GeV/c^2. Figure 8.14 shows the charged-signed photon-lepton rapidity difference for $Z\gamma$ events using both leptons. The events are required to have a three-body mass greater the 100 GeV/c^2. No dip in this distribution occurs because there are no gauge cancellations in $Z + \gamma$ production.

For $W\gamma$ events, Figure 8.15 shows the photon transverse energy spectrum for $W\gamma$ events with minimum invariant mass greater the 90 GeV/c^2. Also, we show the charged-signed photon-lepton rapidity difference in Figure 8.16. Events are required to have a minimum invariant mass greater than 90 GeV/c^2. A dip in the distribution can be observed as is expected in the standard model, however a clear excess of $W\gamma$ events is present.

The standard model predicts the $W + \gamma$ charged-signed photon-lepton rapidity difference to be strongly asymmetric [9]. Note that the QCD background in $W\gamma$ events is symmetric in the charged-signed photon-lepton rapidity difference.

	Electrons		Muons		
Process	Run 1B	Run 1A	Run 1B	Run 1A	Total
$Z\gamma$	14.55 ± 0.76	3.40 ± 0.18	9.22 ± 0.56	1.54 ± 0.10	28.71 ± 1.60
Jet$\rightarrow \gamma$	1.79 ± 0.61	0.38 ± 0.13	0.89 ± 0.32	0.12 ± 0.04	3.18 ± 1.10
SM Total	16.34 ± 0.97	3.78 ± 0.22	10.11 ± 0.64	1.66 ± 0.11	31.89 ± 1.94
Data	21	5	18	4	48

Table 8.11: Comparison of muon plus electron channel $Z\gamma$ event yields between the standard model plus background expectation and data using the RAZ $V + \gamma$ cuts.

	Electrons		Muons		
Process	Run 1B	Run 1A	Run 1B	Run 1A	Total
$W\gamma$	34.16 ± 1.73	8.04 ± 0.39	19.44 ± 1.23	3.20 ± 0.22	64.84 ± 3.57
Jet$\rightarrow \gamma$	9.85 ± 3.50	2.00 ± 0.73	5.40 ± 1.99	0.76 ± 0.28	18.00 ± 6.50
$OLZ + \gamma$	1.19 ± 0.06	0.23 ± 0.01	3.71 ± 0.24	0.43 ± 0.03	5.56 ± 0.34
$W \rightarrow \tau + \gamma$	0.40 ± 0.02	0.09 ± 0.00	0.24 ± 0.02	0.04 ± 0.00	0.77 ± 0.04
SM Total	45.60 ± 3.94	10.36 ± 0.83	28.79 ± 2.49	4.43 ± 0.38	89.17 ± 7.61
Data	74	17	51	7	149

Table 8.12: Comparison of electron plus muon channel $W\gamma$ event yields between the standard model plus background expectation and data using the RAZ $V + \gamma$ cuts.

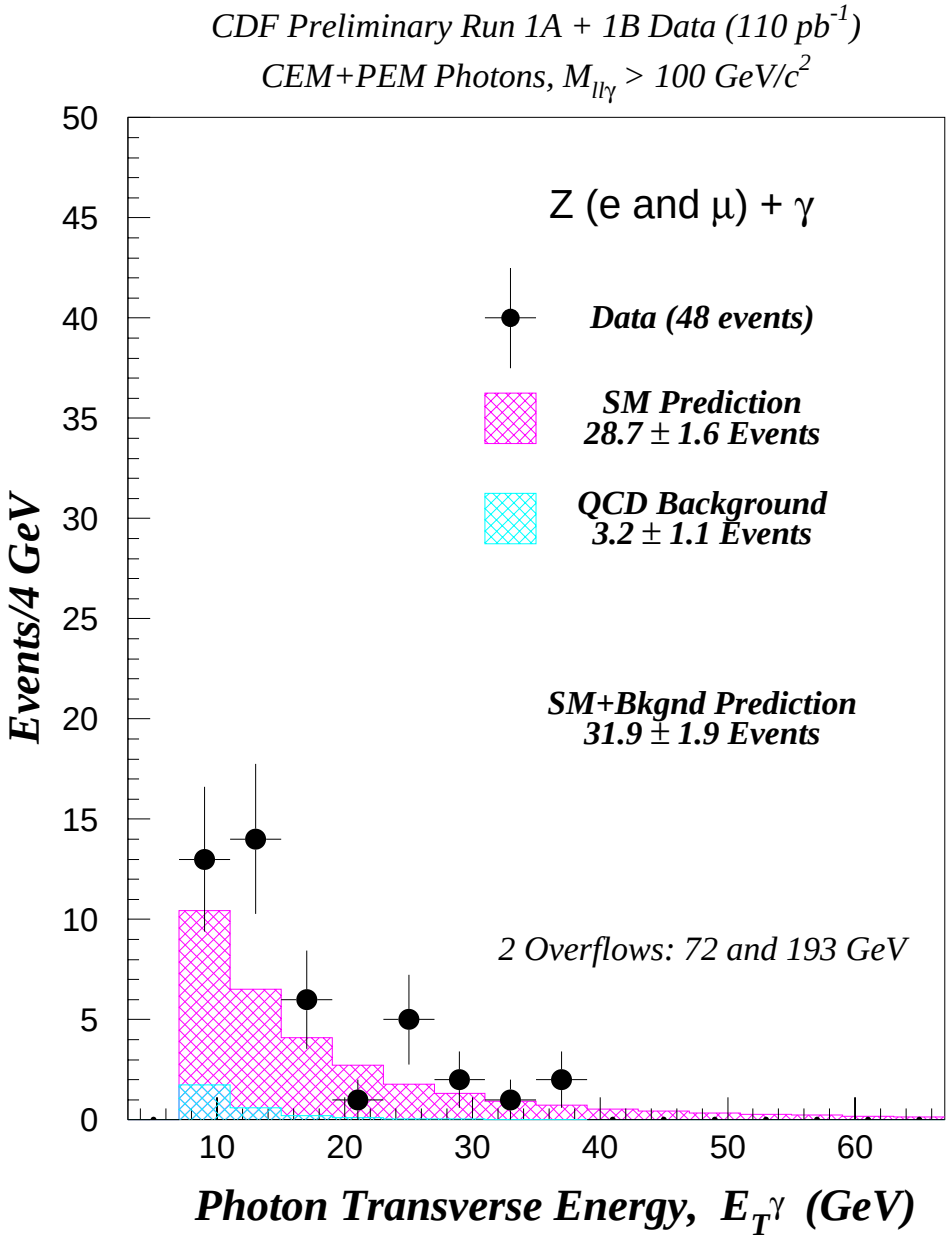

Figure 8.13: The $Z + \gamma$ photon E_T overlaid on the standard model prediction plus background expectation for events with a three-body mass greater than 100 GeV/c^2.

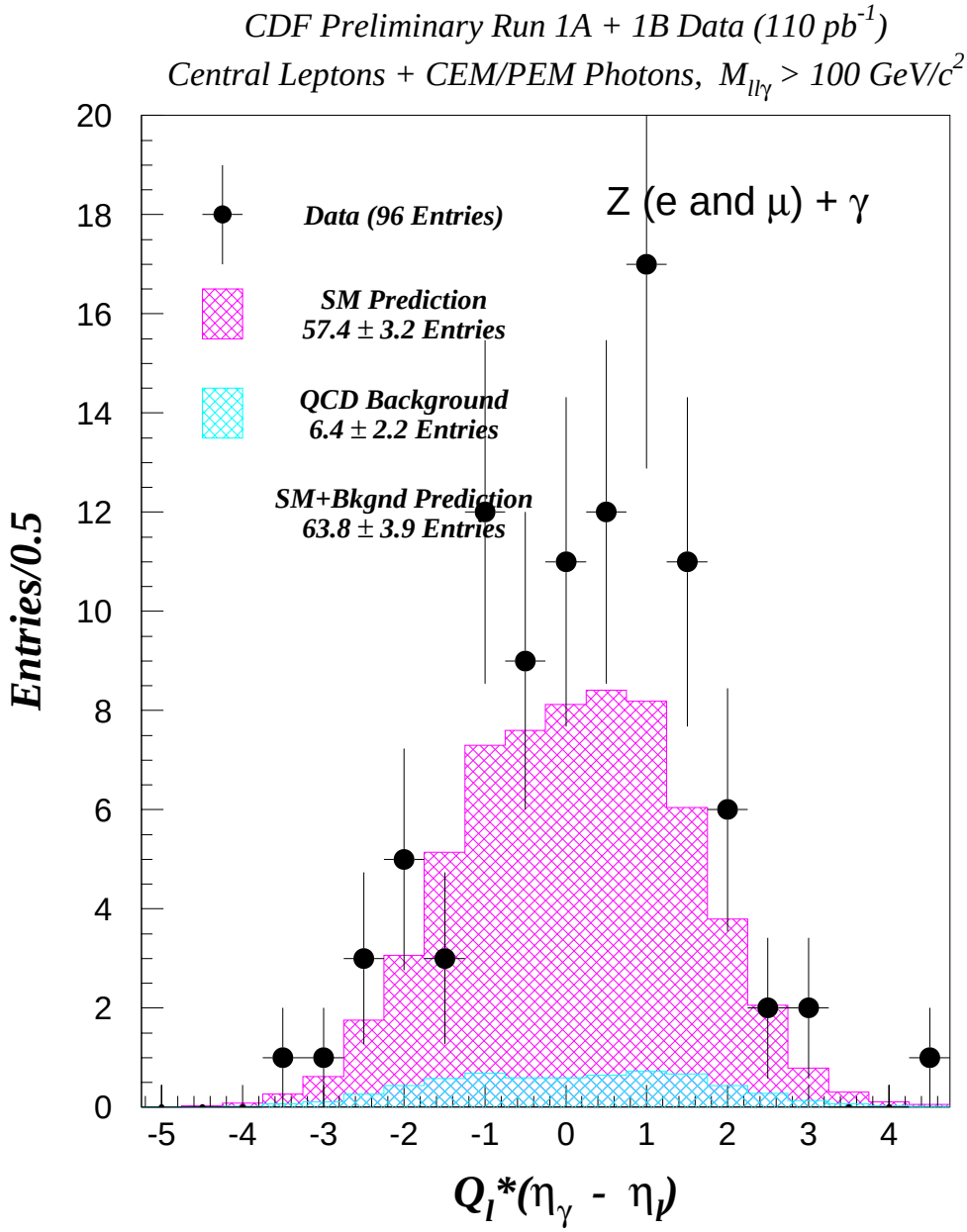

Figure 8.14: The $Z/DY + \gamma$ charged-signed photon-lepton rapidity difference overlaid on the standard model prediction plus background expectation. Note that both legs are plotted.

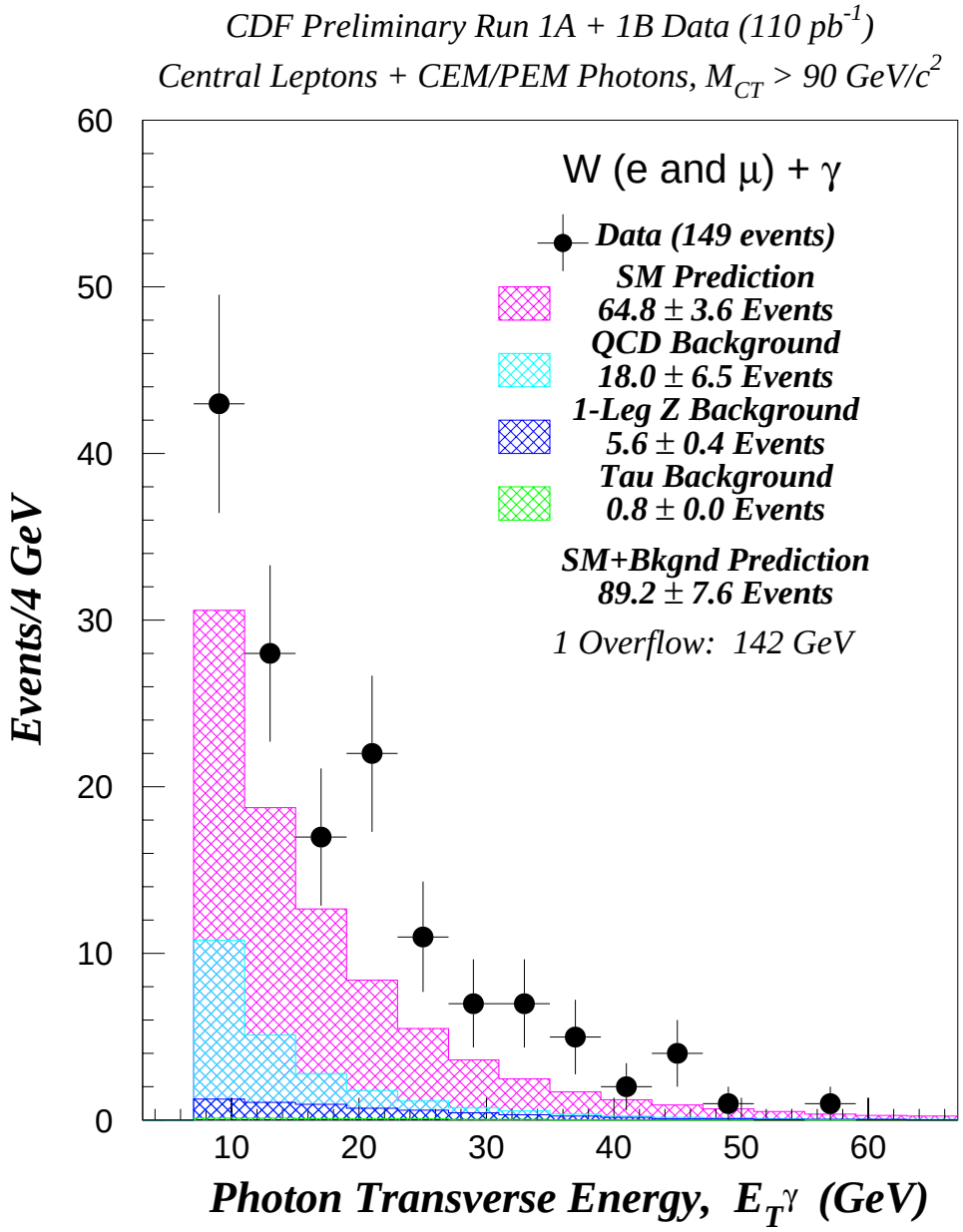

Figure 8.15: The $W + \gamma$ photon E_T overlaid on the standard model prediction plus background expectation for events with a minimum invariant mass greater than 90 GeV/c^2.

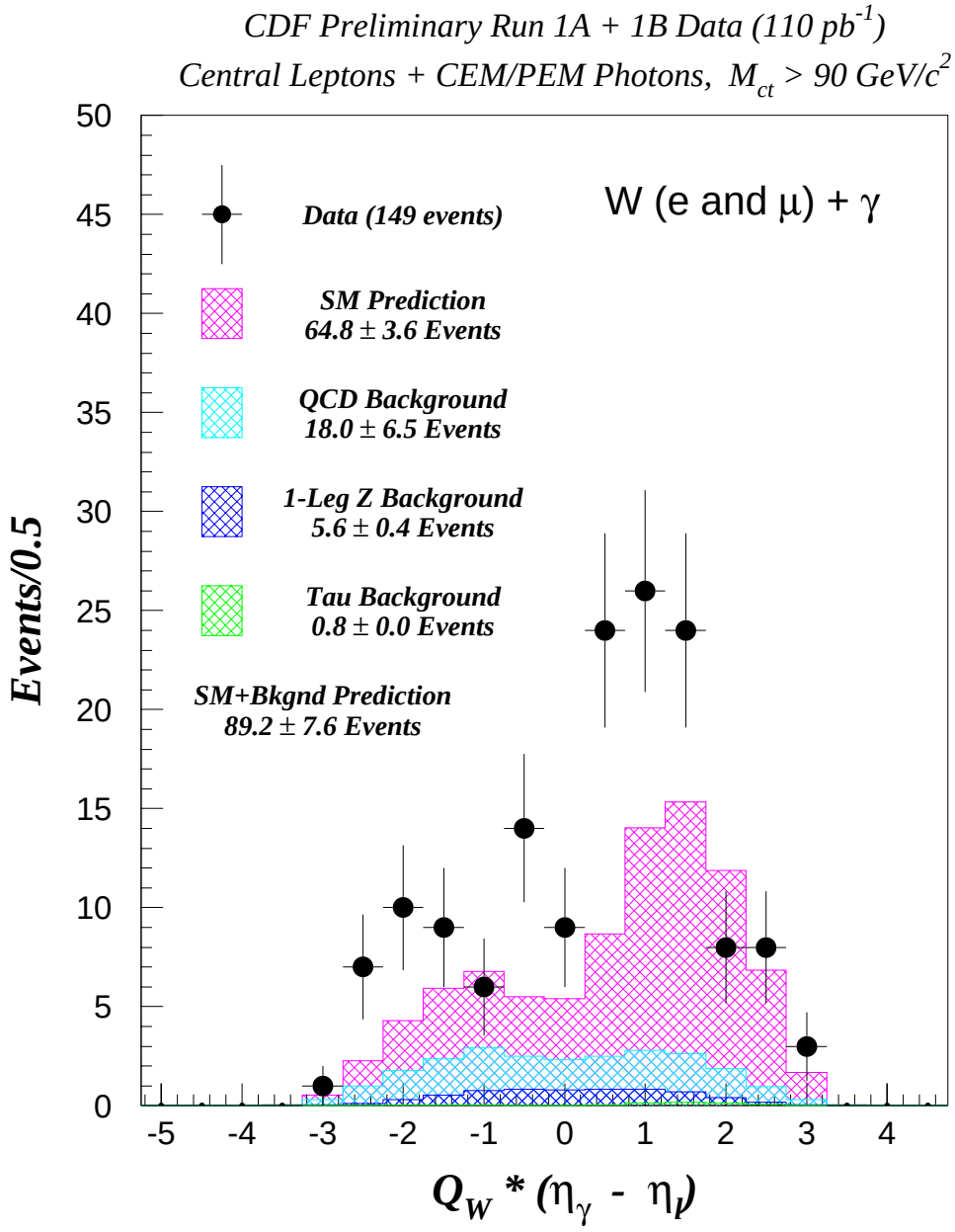

Figure 8.16: The $W + \gamma$ charged-signed photon-lepton rapidity difference overlaid on the standard model prediction plus background expectation.

8.2.3 Additional $V + \gamma$ Standard Model Comparisons

The cross section ratios of $W+\gamma$ to inclusive W and $Z+\gamma$ to inclusive Z as a function of the minimum photon E_T are tools that can be used to study the vector boson self-interactions [40]. These ratios directly reflect the radiation amplitude zero and are sensitive to anomalous couplings. By modifying this analysis slightly, it becomes possible to compare with other CDF experimental results .

Using a minimum photon transverse energy of 25 GeV and raising the lepton P_T and missing transverse energy requirements to 25 GeV, it become possible to compare directly with the University of Chicago's (UC) exotic search analysis [42]. These event selection requirements result in a substantial reduction in the number of $W + \gamma$ and $Z + \gamma$ events. They also suppress radiative W and Z decays along with the QCD to fake photon background. We summarize the event yields of these two analyses in Tables 8.13- 8.14. We also show the photon E_T spectra for these comparisons in Figures 8.17- 8.18. Again, an excess exists in both the raised cuts $Z+\gamma$ and $W+\gamma$ data samples. The statistical significance of these results is discussed in Chapter 9.

	Electrons		Muons		
Process	Run 1B	Run 1A	Run 1B	Run 1A	Total
$Z\gamma$	2.60 ± 0.14	0.62 ± 0.03	2.18 ± 0.13	0.37 ± 0.02	5.77 ± 0.32
Jet$\rightarrow \gamma$	0.05 ± 0.02	0.01 ± 0.00	0.04 ± 0.01	0.01 ± 0.00	0.11 ± 0.03
SM Total	2.65 ± 0.14	0.63 ± 0.03	2.22 ± 0.13	0.38 ± 0.02	5.88 ± 0.32
Data	4	1	4	1	10

Table 8.13: Comparison of muon plus electron channel $Z\gamma$ event yields between the standard model plus background expectation and data using the raised $V + \gamma$ cuts.

	Electrons		Muons		
Process	Run 1B	Run 1A	Run 1B	Run 1A	Total
$W\gamma$	5.50 ± 0.28	1.33 ± 0.06	3.19 ± 0.20	0.55 ± 0.04	10.57 ± 0.58
Jet$\rightarrow \gamma$	0.48 ± 0.16	0.11 ± 0.04	0.31 ± 0.11	0.04 ± 0.01	0.94 ± 0.32
$OLZ + \gamma$	0.30 ± 0.02	0.06 ± 0.00	0.85 ± 0.05	0.11 ± 0.01	1.32 ± 0.08
$W \rightarrow \tau + \gamma$	0.10 ± 0.01	0.02 ± 0.00	0.06 ± 0.00	0.01 ± 0.00	0.19 ± 0.01
SM Total	6.38 ± 0.35	1.52 ± 0.07	4.41 ± 0.27	0.71 ± 0.05	13.02 ± 0.74
Data	9	2	16	0	27

Table 8.14: Comparison of electron plus muon channel $W\gamma$ event yields between the standard model plus background expectation and data using the raised $V + \gamma$ cuts.

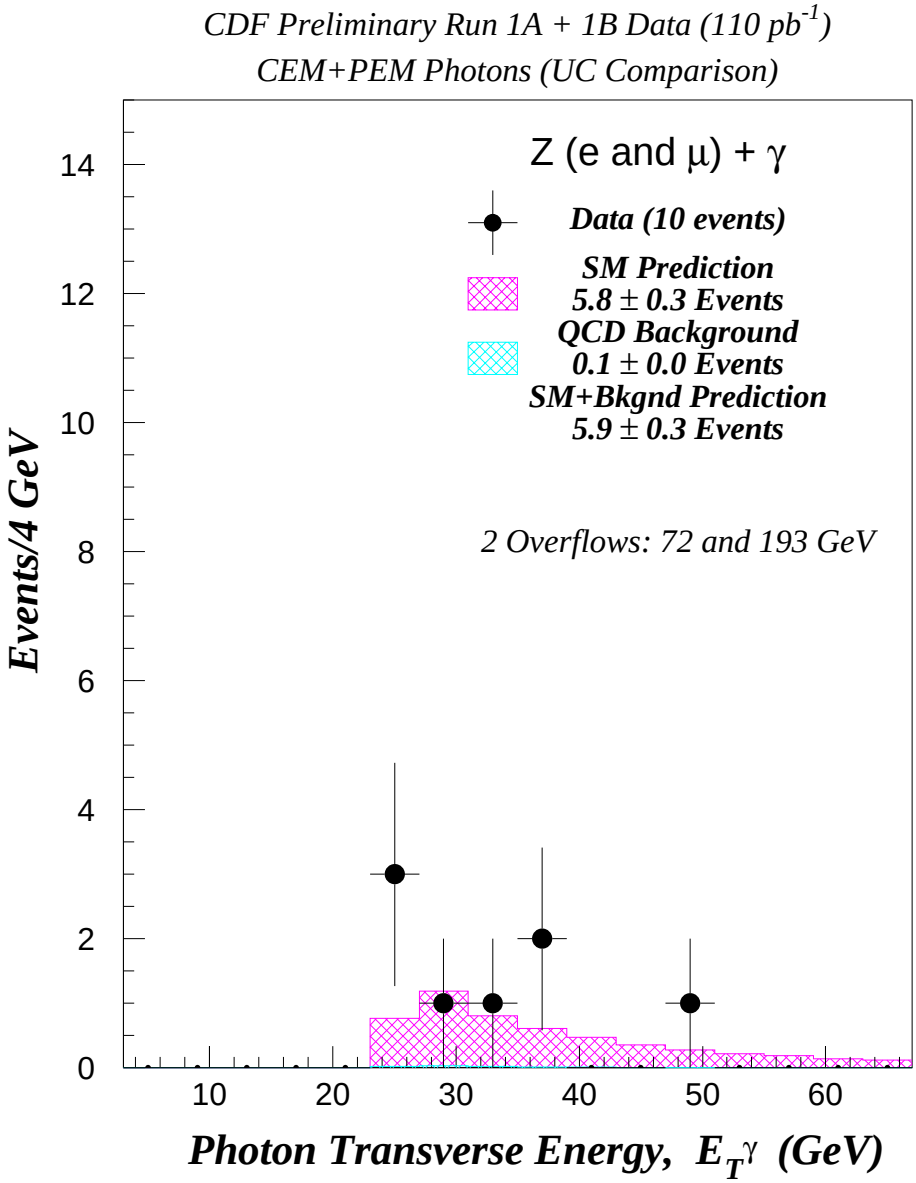

Figure 8.17: Photon transverse energy from $Z/DY + \gamma$ in the combined data sample overlayed on the standard model plus background prediction using the UC requirements.

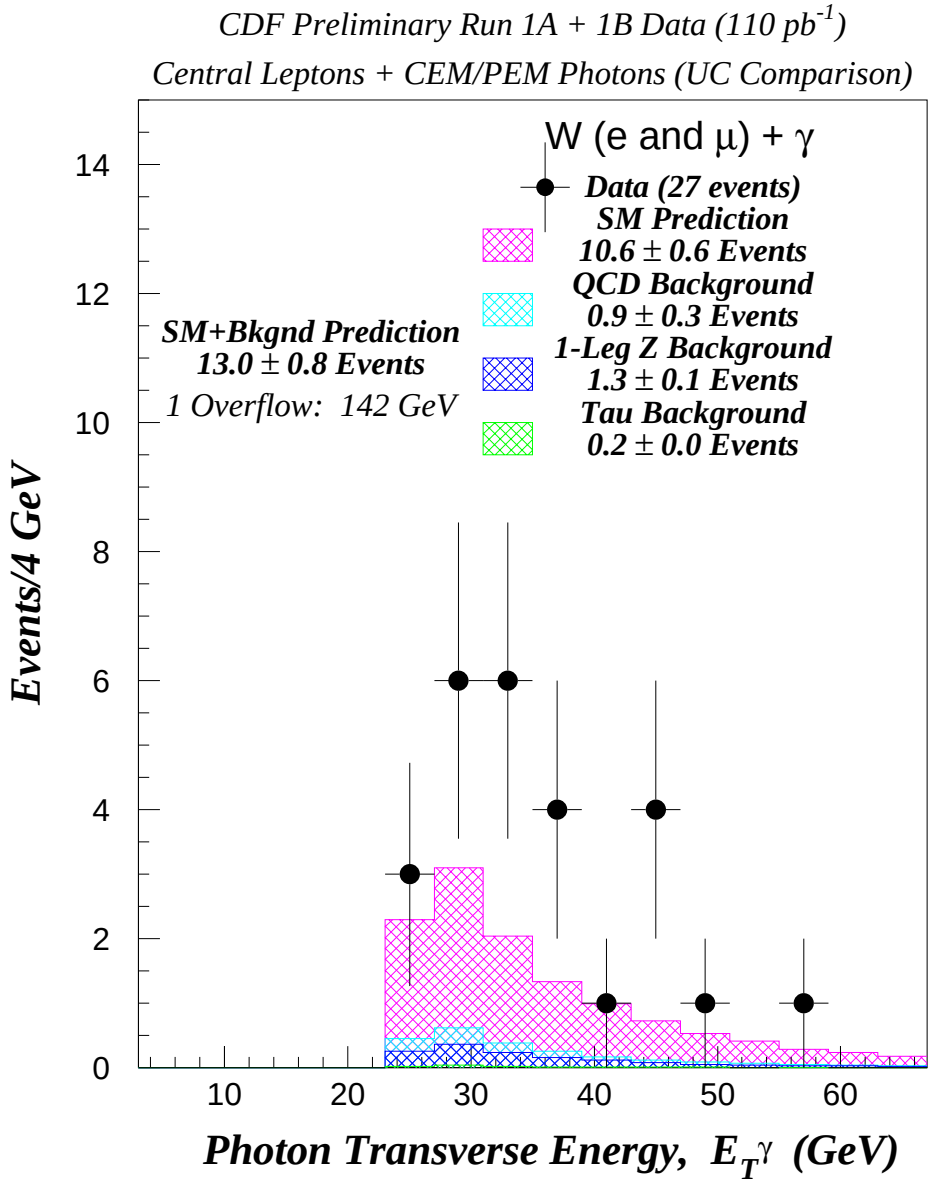

Figure 8.18: Photon transverse energy from $W + \gamma$ in the combined data sample overlayed on the standard model plus background prediction using the UC requirements.

8.3 Cross Sections

We present the experimental results in the muon, electron and combined muon plus electron channel for the cross section times branching ratios for inclusive W and Z production, and for the $W\gamma$ and $Z\gamma$ processes.

For inclusive W and Z production, we have

$$\begin{aligned} \sigma \cdot B(V_l) &= \frac{\mathcal{N}_{sig}(V_l)}{(A_V^l \cdot \epsilon_V^l) \cdot \int \mathcal{L}_l dt} \\ &= \frac{\mathcal{N}_{obs}(V_l) - \Sigma\mathcal{N}_{bkg}(V_l)}{(A_V^l \cdot \epsilon_V^l) \cdot \int \mathcal{L}_l dt} \end{aligned} \tag{8.3}$$

where $\mathcal{N}_{sig}(V_l)$ is the number of true signal events in the W and Z channel, $\mathcal{N}_{obs}(V_l)$ is the number of observed events in the respective channel, $\Sigma\mathcal{N}_{bkg}(V_l)$ is the total number of background events in the respective channel, $(A_V^l \cdot \epsilon_V^l)$ is the total efficiency times acceptance and $\int \mathcal{L}_l dt$ is the integrated luminosity.

Similarly, the cross section times branching ratio, $\sigma \cdot B(V_l + \gamma)$, can be calculated from

$$\begin{aligned} \sigma \cdot B(V_l + \gamma) &= \frac{\mathcal{N}_{sig}(V_l + \gamma)}{(A_{V\gamma}^l \cdot \epsilon_{V\gamma}^l) \cdot \int \mathcal{L}_l dt} \\ &= \frac{\mathcal{N}_{obs}(V_l + \gamma) - \Sigma\mathcal{N}_{bkg}(V_l + \gamma)}{(A_{V\gamma}^l \cdot \epsilon_{V\gamma}^l) \cdot \int \mathcal{L}_l dt} \end{aligned} \tag{8.4}$$

where $\mathcal{N}_{sig}(V_l + \gamma)$ is the number of true signal events in the $W\gamma$ and $Z\gamma$ channel, $\mathcal{N}_{obs}(V_l + \gamma)$ is the number of observed events in the respective channel, $\Sigma\mathcal{N}_{bkg}(V_l + \gamma)$ is the total number of background events in the respective channel, $(A_{V\gamma}^l \cdot \epsilon_{V\gamma}^l)$ is the total efficiency times acceptance and $\int \mathcal{L}_l dt$ is the integrated luminosity.

The cross section times branching ratio results for all channels are summarized in Tables 8.15- 8.16. The standard model predictions for inclusive W/Z production [46]- [48] using MRS R2 structure functions are $\sigma \cdot BR(W) = 2483.6$ pb and $\sigma \cdot BR(Z/DY) = 231.4$ pb. The standard model predictions for $V + \gamma$ production using the Baur $V + \gamma$ Monte Carlo event generators and MRS R2 structure functions are $\sigma \cdot BR(Z/DY + \gamma) = 5.8$ pb and $\sigma \cdot BR(W + \gamma) = 14.8$ pb.

Channel	$\sigma \cdot BR(Z/DY)$	$\sigma \cdot BR(Z/DY + \gamma)$
$\mu\, Z/DY$	178.8 ± 8.4 pb	7.2 ± 1.3 pb
$e\, Z/DY$	234.1 ± 10.2 pb	4.7 ± 0.9 pb
$(e + \mu)\, Z/DY$	206.4 ± 8.7 pb	5.5 ± 0.8 pb
SM Z/DY	231.4 pb	5.8 pb

Table 8.15: Summary of the measured $\sigma \cdot BR(Z/DY)$ and $\sigma \cdot BR(Z/DY + \gamma)$ results for the muon, electron and the combined muon plus electron channel. The uncertainty shown is the combination of the statistical uncertainty and the systematic uncertainty.

Channel	$\sigma \cdot BR(W)$	$\sigma \cdot BR(W + \gamma)$
$\mu\, W$	2405.9 ± 105.4 pb	19.3 ± 2.7 pb
$e\, W$	2483.4 ± 100.9 pb	20.1 ± 2.0 pb
$(e + \mu)\, W$	2462.7 ± 99.1 pb	19.8 ± 1.7 pb
SM W	2483.6 pb	14.8 pb

Table 8.16: Summary of the measured $\sigma \cdot BR(W)$ and $\sigma \cdot BR(W + \gamma)$ results for the muon, electron and the combined muon plus electron channel. The uncertainty shown is the combination of the statistical uncertainty and the systematic uncertainty.

Chapter 9

Conclusions

9.1 Summary of Results

During the course of the CDF Run I $V + \gamma$ analysis, we have carried out several standard model comparisons of inclusive W/Z and $W+\gamma/Z+\gamma$ production in $\sqrt{s} = 1.8$ TeV $\bar{p} - p$ collisions.

Inclusive W and Z production in the muon and electron channel were found to be in good agreement with their standard model predictions as shown below in Table 9.1. This explicit agreement demonstrates that we have a good quantitative understanding of the lepton identification and trigger efficiencies, lepton geometric and kinematic acceptances, detector resolutions, backgrounds and integrated luminosities.

		μ	e	$\mu + e$
Z/DY	SM	4135.4 ± 226.4	7563.8 ± 336.4	11699.2 ± 562.8
	Data	3969	7979	11948
W	SM	39089.3 ± 2244.2	71712.3 ± 2948.0	110801.6 ± 5192.2
	Data	38606	73363	111969

Table 9.1: Comparison of muon and electron channel W/Z event yields with the standard model predictions.

For our standard $V + \gamma$ analysis cuts, the $Z/DY + \gamma$ event yields are in good numerical agreement with their standard model predictions, however the kinematical distributions differ.[1] For our standard $V + \gamma$ analysis cuts, the $W + \gamma$ event yields exhibit a 25% excess which also diverges with increasing photon E_T.

The RAZ standard model comparisons of $Z/DY + \gamma$ data ($M_{\ell\ell\gamma} > 100$ GeV/c^2) and $W + \gamma$ data ($M_{ct} > 90$ GeV/c^2) both exhibit statistically significant excesses. The raised comparison (25/25/25 GeV) of $Z/DY + \gamma$ data and $W + \gamma$ data also show an excess, but with reduced statistical significance. The results are summarized in Table 9.2. The statistical significance of the excesses are discussed in the K-factor studies below.

		Default	RAZ	Raised
$Z/DY + \gamma$	SM	74.24 ± 4.70	31.89 ± 1.94	5.88 ± 0.32
	Data	79	48	10
$W + \gamma$	SM	264.60 ± 18.30	89.17 ± 7.61	13.02 ± 0.74
	Data	335	149	27

Table 9.2: Comparison of muon and electron channel $W + \gamma/Z + \gamma$ event yields with the standard model predictions.

9.1.1 Additional Studies

Hand Scan of $V + \gamma$ Events

All $V + \gamma$ events were hand scanned using the DF event display, and the lepton and CEM/PEM photon properties in each event were carefully scrutinized. We made hardcopies of the event displays and kept them for quick reference for specific events. In the process of developing the quantitative method used for determining the QCD background, large numbers of P23 and JET data events were also hand scanned and their CEM/PEM photon properties carefully scrutinized. Qualitatively, the QCD

[1] The numerical comparison represents an integral comparison, while the kinematic distributions represents a differential comparison.

background in the $W+\gamma$ and $Z+\gamma$ data samples, as determined from hand scanning, was found to be in good agreement with that obtained by our direct QCD background determination method. In other words, we were unable to explain the excess of high E_T photons in our $W+\gamma$ data samples as being entirely due to QCD background.

Also, during the hand scanning we noticed several events with multiple photon candidates. These events were studied further by members of our group [57]. Although no quantitative standard model comparison has yet been explicity carried out, qualitatively there appears to be an excess of $V\gamma\gamma$ events. However, the statistics is extremely limited.

Calorimeter Hot Spots

One possible explanation for the excess in the $W+\gamma$ data samples could be due to possible hot spots in the CEM or PEM calorimeter. Note that the excess in the $W+\gamma$ data samples is comparable in the muon and electron channel and also for CEM versus PEM photons.

We searched for CEM/PEM calorimeter hot spots by plotting the locations of the photons in the CEM/PEM for $V+\gamma$ events. Figure 9.1 shows the scatter plot of the local X position versus the local Z position for CEM photons in a central wedge for $V+\gamma$ events. Figures 9.3- 9.3 show the projections of the local coordinates for $V+\gamma$ events in the CEM calorimeter. Figure 9.4 shows the corresponding plots for plug photons. There is no evidence for photons aggregating in a specific region or hot spots in the CEM/PEM calorimeters.

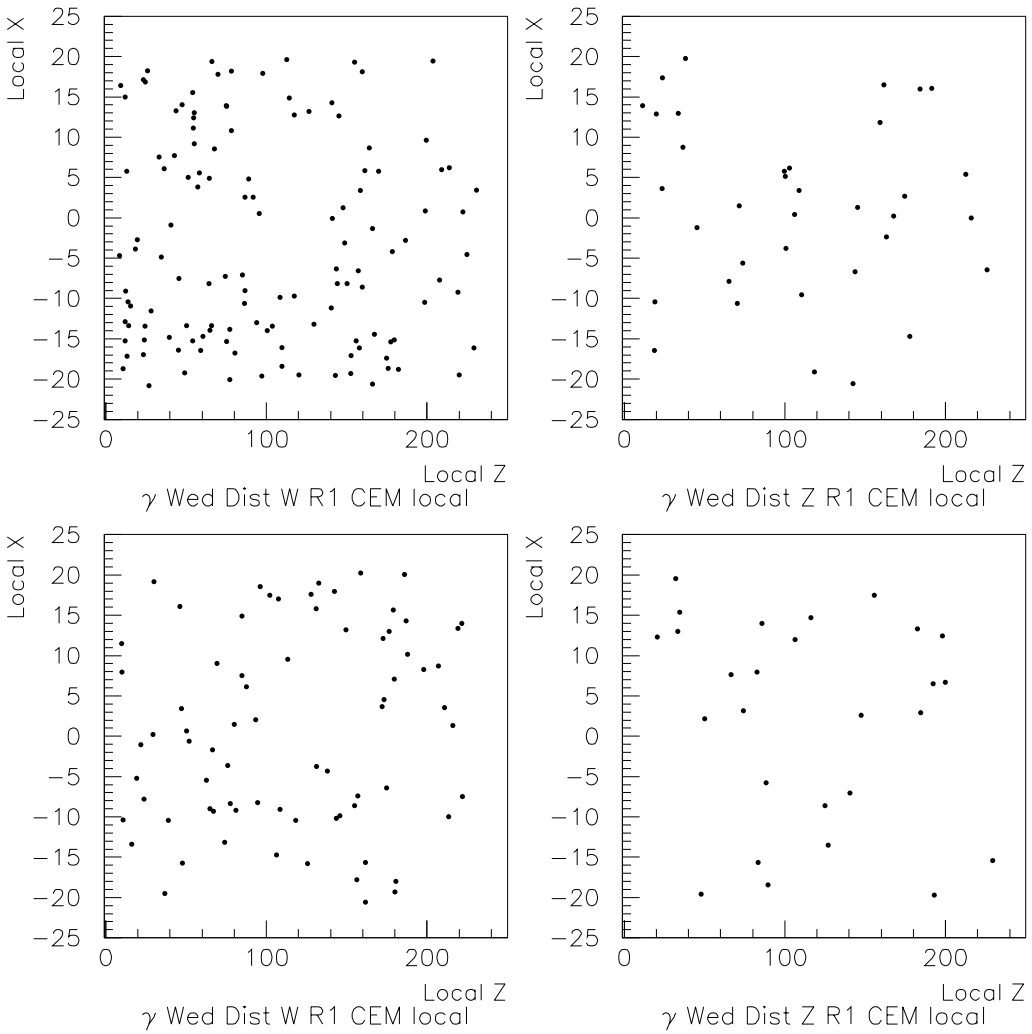

Figure 9.1: The local X position versus the local Z position for CEM photons in the $V + \gamma$ samples. The upper left histogram is for electron channel $W + \gamma$, the upper right histogram is for electron channel $Z + \gamma$, the lower left histogram is for muon channel $W + \gamma$ and the lower right histogram is for muon channel $Z + \gamma$.

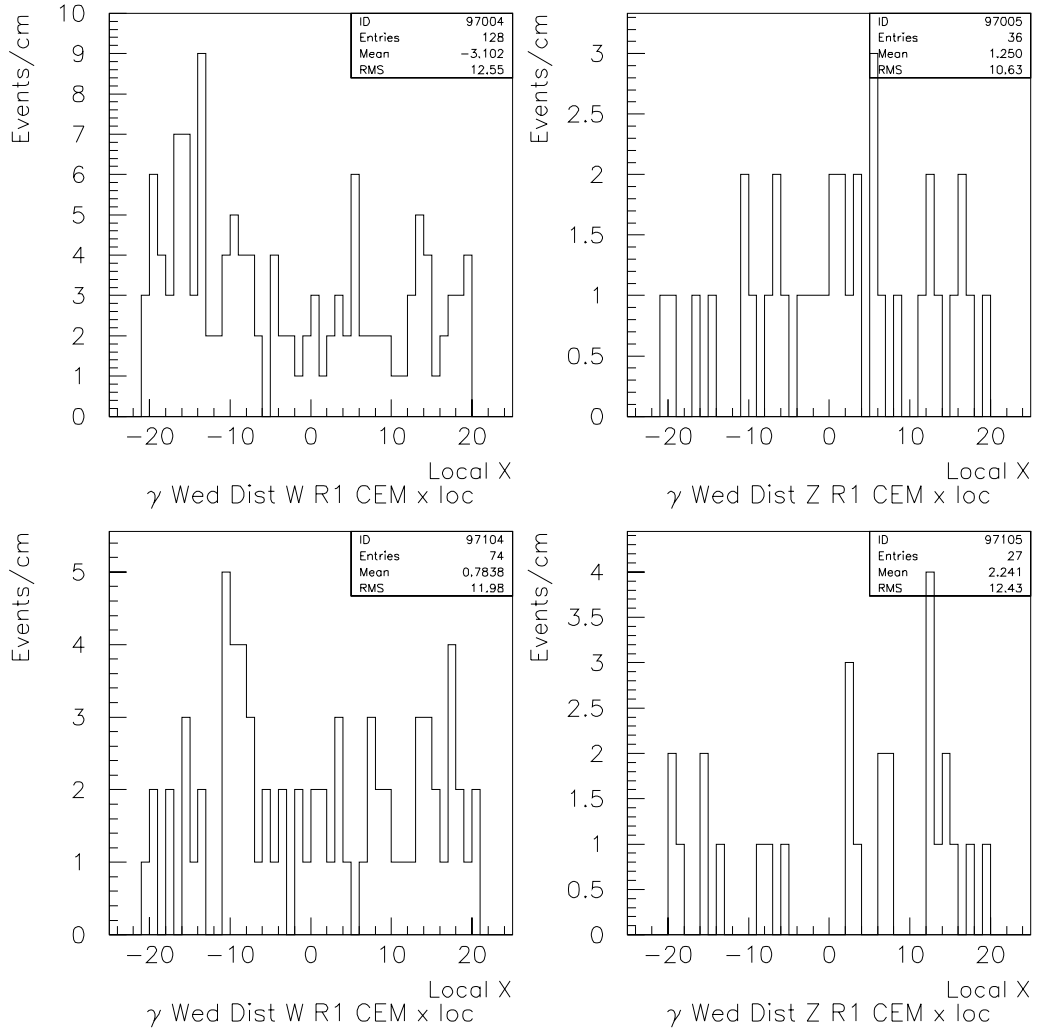

Figure 9.2: The local X position for CEM photons in the $V + \gamma$ samples. The upper left histogram is for electron channel $W + \gamma$, the upper right histogram is for electron channel $Z + \gamma$, the lower left histogram is for muon channel $W + \gamma$ and the lower right histogram is for muon channel $Z + \gamma$.

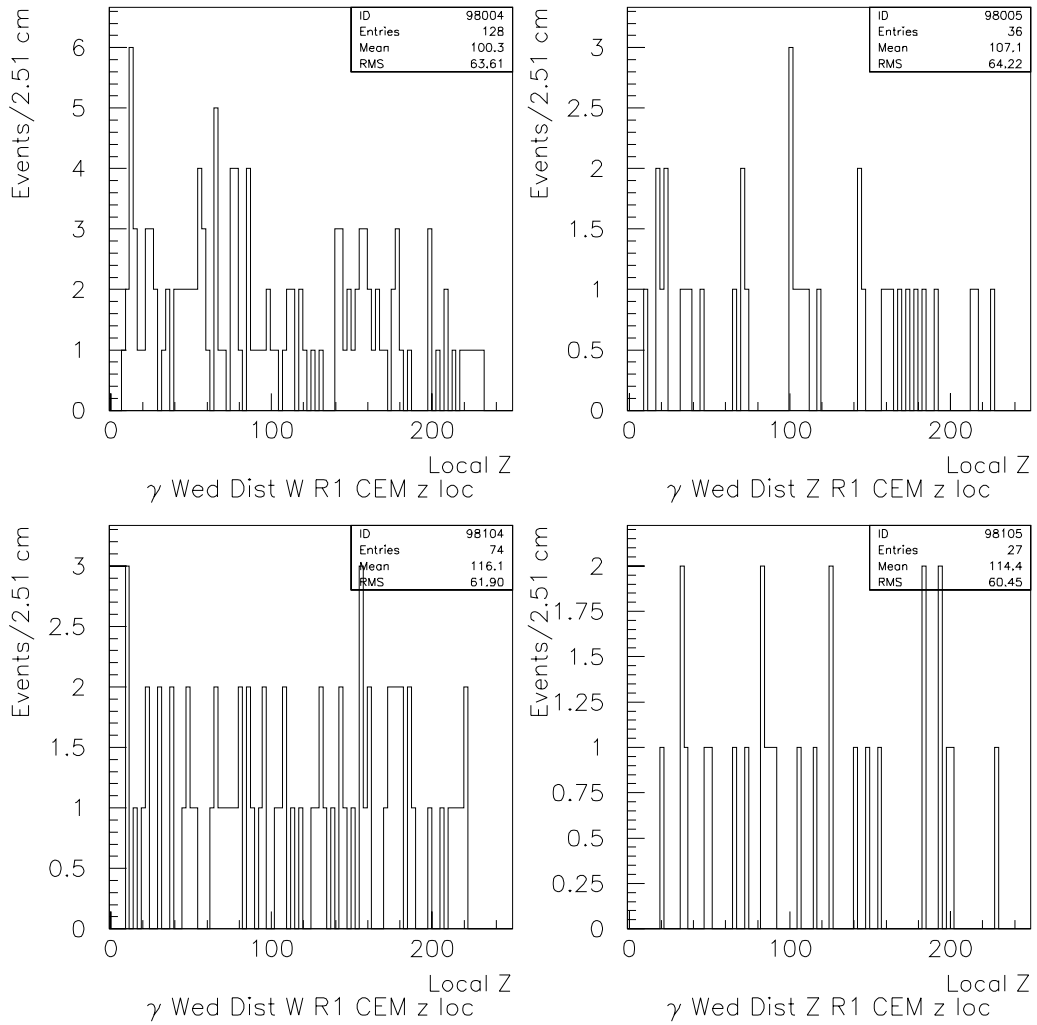

Figure 9.3: The local Z position for CEM photons in the $V + \gamma$ samples. The upper left histogram is for electron channel $W + \gamma$, the upper right histogram is for electron channel $Z + \gamma$, the lower left histogram is for muon channel $W + \gamma$ and the lower right histogram is for muon channel $Z + \gamma$.

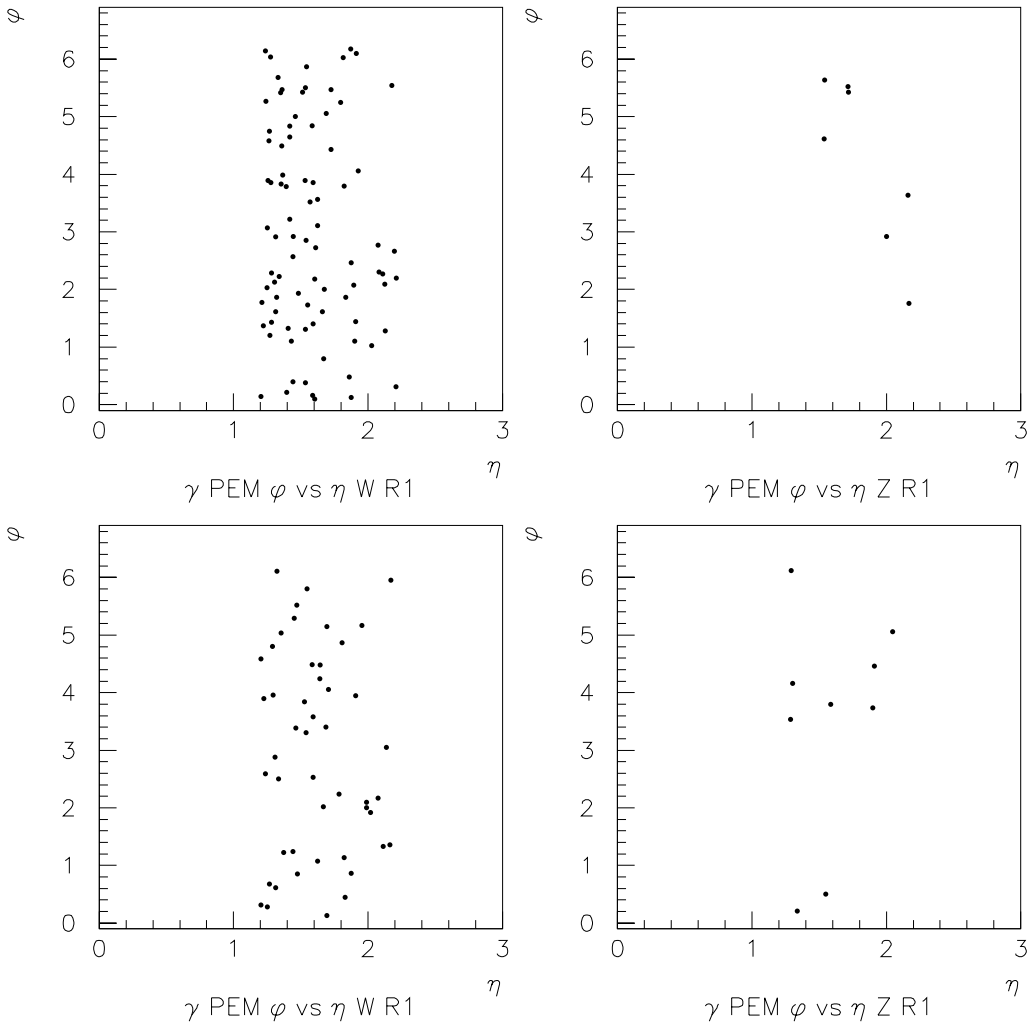

Figure 9.4: Scatter plot of ϕ versus $\mid \eta \mid$ for PEM photons in the $V + \gamma$ samples. The upper left histogram is for electron channel $W + \gamma$, the upper right histogram is for electron channel $Z + \gamma$, the lower left histogram is for muon channel $W + \gamma$ and the lower right histogram is for muon channel $Z + \gamma$.

Jet Multiplicity Studies

Another possible explanation for the excess in the $V + \gamma$ data could be due to a new, hitherto unknown process which produces the same $V + \gamma$ final state as a standard model process, but with additional accompanying jets. We investigated this possibility by studying the jet multiplicity as a function of jet E_T in each of the $V + \gamma$ data samples and compared it to the jet multiplicity distributions in their respective inclusive W/Z data samples. Figure 9.5 shows the normalized jet multiplicity as a function of jet E_T in the inclusive W and $W + \gamma$ samples for the muon and electron channels. Figure 9.6 is the analogous plots for the Z and $Z + \gamma$ data samples. It can be seen from these Figures that the jet activity in $V + \gamma$ data samples is very similiar to that of their parent W/Z data samples. We see no statistically significant evidence for increased jet activity in $V + \gamma$ events.

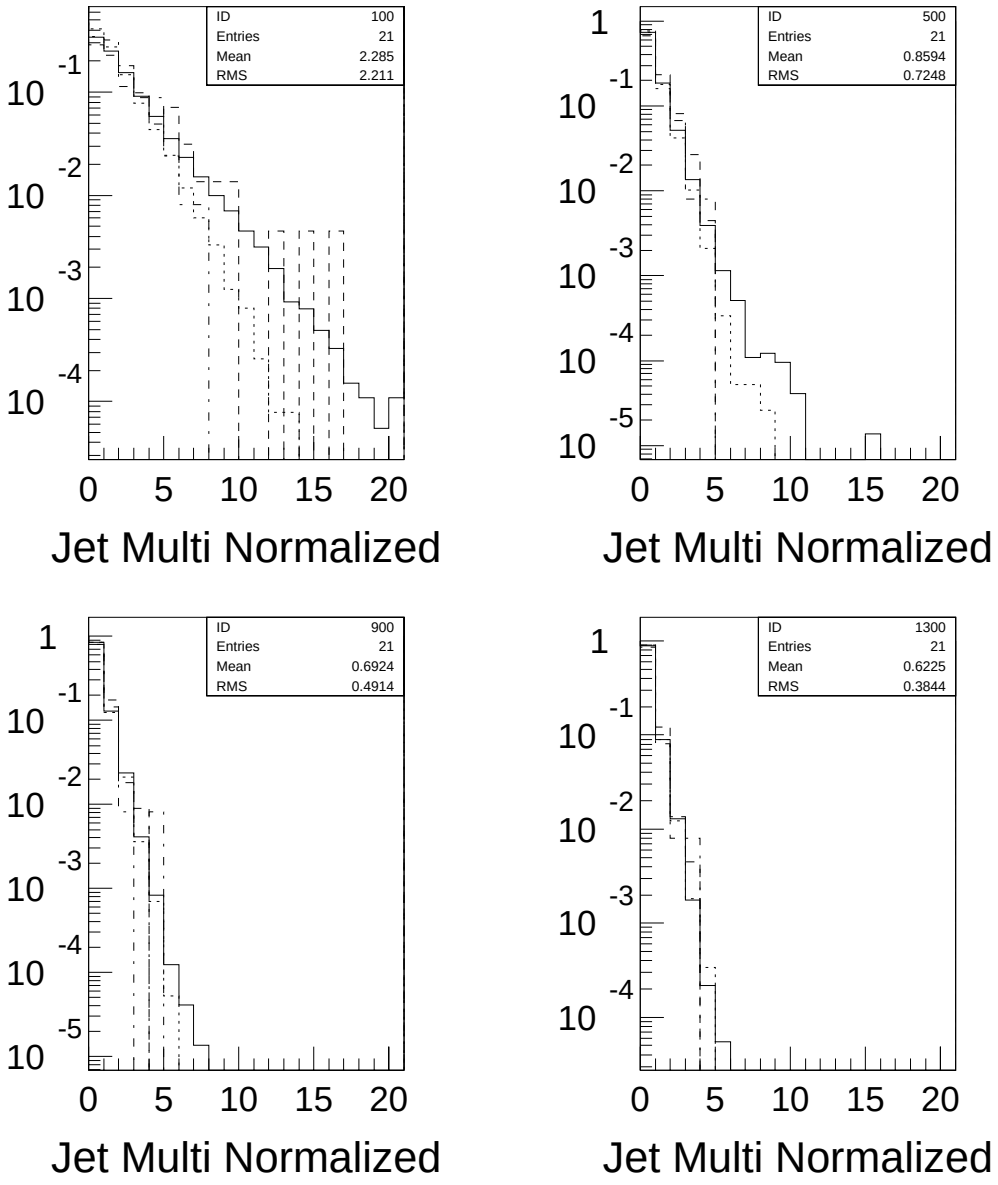

Figure 9.5: The jet multiplicity for W and $W + \gamma$ events in the muon and electron channels. The upper left histogram is with a $E_T^{JET} > 7$ GeV and the upper right histogram is with a $E_T^{JET} > 10$ GeV. The lower left histogram is with a $E_T^{JET} > 15$ GeV and the lower right histogram is with a $E_T^{JET} > 20$ GeV. All jets are required to have $\mid \eta \mid < 2.4$.

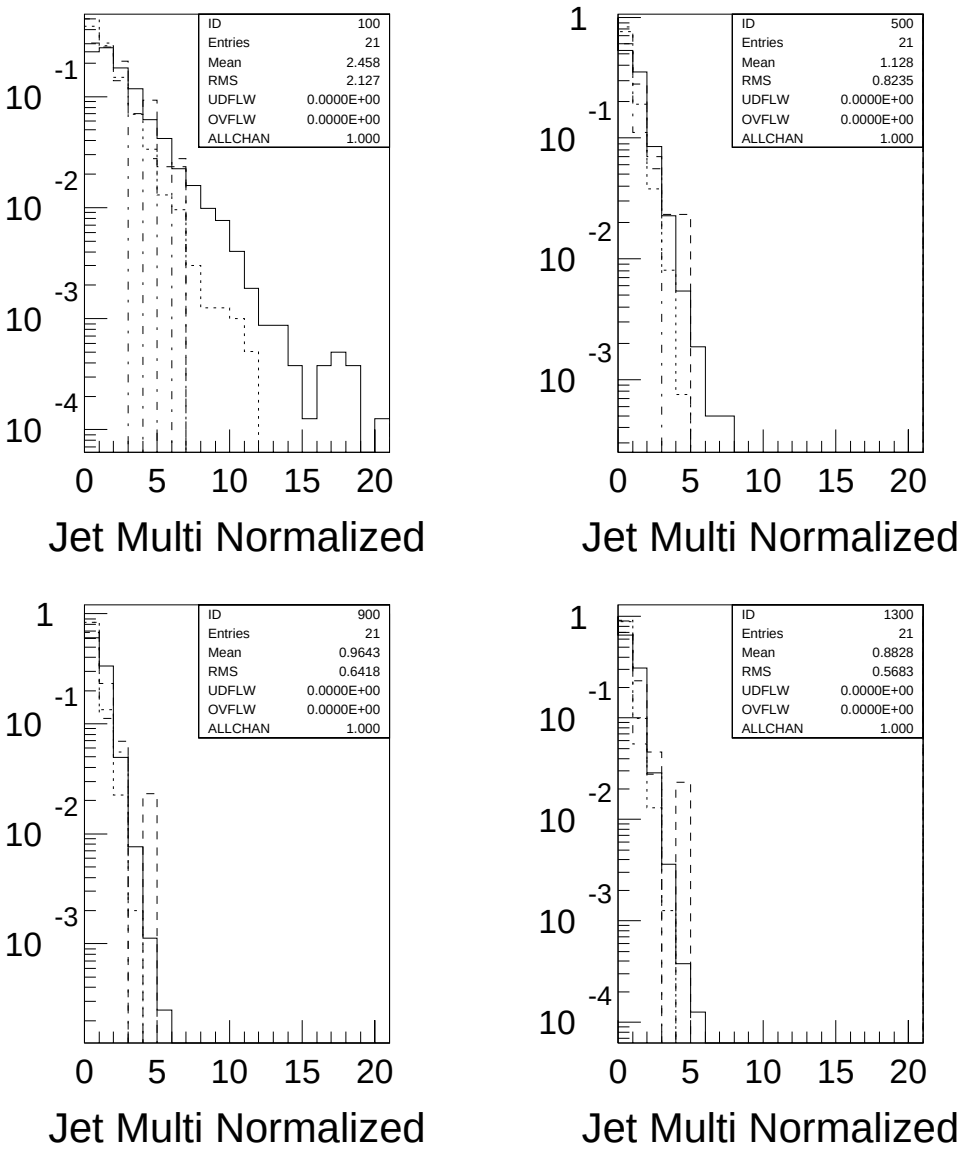

Figure 9.6: The jet multiplicity for Z and $Z + \gamma$ events in the muon and electron channels. The upper left histogram is with a $E_T^{JET} > 7$ GeV. The upper right histogram is with a $E_T^{JET} > 10$ GeV and the lower left histogram is with a $E_T^{JET} > 15$ GeV and the lower right histogram is with a $E_T^{JET} > 20$ GeV. All jets are required to have $\mid \eta \mid < 2.4$.

QCD Jet $\rightarrow$ Fake γ Studies

During the development of the methodology for determining the CEM/PEM QCD jet to fake photon background in the electron and muon Run 1a and 1b $V + \gamma$ data samples from the inclusive W/Z data, a variety of other systematic studies were done. It was found that the CEM P23 QCD jet to fake photon probability was systematically higher by a factor of two - in both the raw and prompt-photon subtracted probabilities - than the corresponding CEM JET QCD jet to fake photon probability. The PEM QCD jet to fake photon probabilities in the P23 and JET data were in reasonable agreement.

The QCD jet to fake photon background used in this analysis was computed using a weighted average of the P23+JET data in both the CEM and PEM regions. We recalculated the background for the CEM region using only the systematically higher P23 data. The overall background increased by 24.9% in the $Z + \gamma$ analysis going from 3.89 ± 1.34 to 4.86 ± 2.23 events and by 24.5% in the $W + \gamma$ analysis going from 39.72 ± 13.48 to 49.47 ± 22.60 events. This increase is not enough to explain the excess of ~ 70 events in the $W + \gamma$ analysis. We also computed the QCD jet to fake photon background in the $V + \gamma$ data sample using just the raw (i.e. prompt photon unsubtracted) probabilities for comparison. It is important to note that the raw jet to fake photon probabilities are unphysical due to the presence of prompt photons in the non-signal data samples used to determine the probability functions. These results are summarized in Tables 9.3- 9.4. Using the raw probability, the $W + \gamma$ data sample has only a $\sim 0.5\sigma$ excess.

	Electrons		Muons		
Version	Run 1B	Run 1A	Run 1B	Run 1A	Total
Default	2.20 ± 0.74	0.44 ± 0.15	1.10 ± 0.39	0.15 ± 0.06	3.89 ± 1.34
P23	2.74 ± 1.25	0.55 ± 0.25	1.38 ± 0.64	0.19 ± 0.09	4.86 ± 2.23
Raw	5.44 ± 2.33	1.14 ± 0.49	2.97 ± 1.27	0.41 ± 0.17	9.96 ± 4.26

Table 9.3: Comparison of the QCD to fake photon background for $Z + \gamma$ events using the weighted average of P23+JET data (default), P23 data (only in the central region) and the raw probability. Note that the raw probability is unphysical and is listed only for comparison.

	Electrons		Muons		
Version	Run 1B	Run 1A	Run 1B	Run 1A	Total
Default	21.72 ± 7.30	4.43 ± 1.52	11.76 ± 4.05	1.81 ± 0.61	39.72 ± 13.48
P23	26.99 ± 12.25	5.53 ± 2.55	14.70 ± 6.77	2.25 ± 1.03	49.47 ± 22.60
Raw	53.93 ± 23.06	11.33 ± 4.85	30.41 ± 12.99	4.57 ± 1.95	100.24 ± 42.85

Table 9.4: Comparison of the QCD to fake photon background for $W + \gamma$ events using the weighted average of P23+JET data (default), P23 data (only in the central region) and the raw probability. Note that the raw probability is unphysical and is listed only for comparison.

K-factor Studies

As discussed in Chapter 7, the QCD corrections to $V + \gamma$ production are estimated by a K-factor. In next-to-leading order, this implies that

$$\sigma \cdot B(W\gamma)_{NLO} = (1 + \frac{8\pi}{9}\alpha_s(< M_{W\gamma} >^2)) \cdot \sigma \cdot B(W\gamma)_{LO} \quad (9.1)$$

$$= K_{NLO} \cdot \sigma \cdot B(W\gamma)_{LO}. \quad (9.2)$$

This corresponds to a value of $K_{NLO} \approx 1.33$. Since $\sigma \cdot B$ and event yields are related, we can determine from data the relative K factor that is needed to bring the theory into agreement with the data from

$$K^{V+\gamma} = \left(\frac{N_{obs} - N_{bkgd}^{TOT}}{N_{Pred}^{SM}}\right) K_{NLO} \quad (9.3)$$

$$= \left(\frac{N_{signal}}{N_{Pred}^{SM}}\right) K_{NLO} \quad (9.4)$$

$$= K_{REL}^{V+\gamma} \cdot K_{NLO} \quad (9.5)$$

Here we are making the assumption that all of the excess in the $V + \gamma$ samples are due to QCD corrections to the cross section. This is equivalent to scaling up the standard model prediction to equal the data.

In effect, we have six separate studies of $V + \gamma$ processes using the default cuts, the radiation amplitude cuts (RAZ: $M_{ll\gamma} > 100$ GeV/c^2 and $M_{CT} > 90$ GeV/c^2) and the raised cuts (25-25-25 GeV). We computed K_{REL} for the six different possibilities as shown in Table 9.5. We also compute the probability of a statistical fluctuation of the standard model prediction up to and above the observed level.

Channel	N_{obs}	N_{BKGD}^{TOT}	N_{Pred}^{SM}	$K_{V+\gamma}$	K_{REL}	$\frac{(K_{REL}-1)}{\sigma_{K_{REL}}}$	Prob
Default $W+\gamma$	335	63.9	200.7	1.79±0.18	1.35±0.14	2.58	0.493%
RAZ $W+\gamma$	149	24.4	64.8	2.55±0.32	1.92±0.24	3.87	0.005%
UC $W+\gamma$	27	2.4	10.6	3.08±0.67	2.32±0.51	2.60	0.469%
Default $Z+\gamma$	79	3.9	70.3	1.42±0.19	1.07±0.14	0.48	31.5%
RAZ $Z+\gamma$	48	3.2	28.7	2.07±0.13	1.56±0.10	5.72	0.000%
UC $Z+\gamma$	10	0.1	5.8	2.26±0.79	1.71±0.60	1.19	11.7%

Table 9.5: The relative K-factors and standard deviations for the six studies in this analysis. The last column is the probability that the standard model expectation fluctuated up to or above the observed level.

9.2 Other Results

9.2.1 D0

The D0 collaboration has also measured the $W\gamma$ and $Z\gamma$ data from their Run I Tevatron data. Analyzing 98.2 pb^{-1} of data, the D0 analysis covered the photon pseudorapidity region $\mid \eta \mid < 2.4$ with the requirement of 10 GeV on the photon transverse energy and lepton-photon separation of $\Delta R_{l\gamma} > 0.7$. They found 57 electron and 70 muon $W\gamma$ events. This is almost a factor of three less than the yields used in this analysis. Their results are consistent with standard model expectations for their experiment. They extracted the following bounds on $W\gamma$ anomalous couplings [58]

$$-3.7 < \Delta\kappa < 3.7$$
$$-1.2 < \lambda < 1.2$$
$$-0.92 < \tilde{\kappa} < 0.92$$
$$-0.31 < \tilde{\lambda} < 0.30.$$

9.2.2 LEP

LEP is the Large Electron Positron collider. Two experiments, OPAL and DELPHI, have extracted limits on CP conserving and CP violating $WW\gamma$ anomalous couplings from W pair production at LEP. OPAL has analyzed 183 pb^{-1} of data at a combined center of mass energy 161-183 GeV and 189 GeV [59, 60]. The limits extracted on CP conserving couplings are

$$\Delta g_1^Z = 0.009^{+0.060}_{-0.057}$$
$$\Delta\kappa_\gamma = 1 - \kappa_\gamma = 0.03^{+0.20}_{-0.16}$$
$$\lambda_\gamma = -0.110^{+0.058}_{-0.055}$$

and the limits on CP nonconserving couplings

$$g_4^Z = -0.02^{+0.32}_{-0.33}$$
$$\tilde{\kappa}_Z = -0.20^{+0.10}_{-0.07}$$
$$\tilde{\lambda}_Z = -0.18^{+0.24}_{-0.16}.$$

DELPHI has analyzed 155 pb^{-1} of data [61] at a combined center of mass energy of 189 GeV and extracted limits on the CP conserving couplings

$$\Delta g_1^Z = -0.02^{+0.07}_{-0.07} \pm 0.01$$
$$\Delta\kappa_\gamma = 0.25^{+0.21}_{-0.20} \pm 0.06$$
$$\lambda_\gamma = 0.05^{+0.09}_{-0.09} \pm 0.01.$$

9.2.3 Brookhaven g-2

The Brookhaven AGS (Alternating Gradient Synchrotron) experiment 821 has conducted an analysis of the positive muon anomalous magnetic moment, $a_\mu(g-2)/2$, using their 1999 data. They report a value of $a_\mu = 11\ 659\ 202(14)(6) \times 10^{-10}$ (1.3 ppm) with a theoretical prediction of $a_\mu(\mathrm{SM}) = 11\ 659\ 159.6(6.7) \times 10^{-10}$ (0.57 ppm) a difference $a_\mu(exp) - a_\mu(SM) = 43(16) \times 10^{-10}$ which gives more than a 2σ deviation from the standard model prediction [62]. If this deviation was due solely to anomalous couplings, it would require a value for $\Delta\kappa \approx 4$ [63].

9.3 Future Prospects

The origin of the discrepancies between the standard model predictions with the observed CDF Run I $V+\gamma$ data samples are not fully understood at this time. We have carried out a long list of in-depth studies in an effort to shed light on the nature of the discrepancies, however we have been unable to find any experimental explanation for them.

The CDF collaboration has been in the process of upgrading the CDF detector in preparation for Run II. The goal of the Tevatron for Run II is the production of 2 fb^{-1} of $\bar{p}-p$ data at $\sqrt{s} = 2.0$ TeV with luminosities up to 2×10^{32} cm^{-2}s^{-1}. The expected Run II event yields for the $W\gamma$ and $Z\gamma$ processes using the criteria discussed in this analysis are ≈ 1500 and ≈ 450 [64], respectively. This five-fold increase in statistics will enable us to further investigate the nature of these discrepancies in a more detailed manner.

Appendix A

Definition of Triggers

The names for triggers represent conditions in the detector that must exist before the trigger is satisified. Triggers ending in _M* and _E* have calorimeter energy cuts applied at the trigger level. The _M* triggers have a minimum ionization requirement in the wedge of $E_T < 3.0$ GeV. The _E* triggers - only for CMX - require non-zero energy in the wedge in front of the muon stub.

- CEM_9_SEED_SH_7_CFT_9_2 - Requires a 9 GeV cluster in the CEM (CEM_9) with a seed tower of at least 7 GeV (SEED_SH_7) and a matching track in the CFT of 9.2 GeV (CFT_9_2),
- CEM_16_ISO - Requires an isolated (ISO) 16 GeV cluster in the CEM (CEM_16) calorimeter,
- CEM_16_ISO_XCES - Requires an isolated (ISO) 16 GeV cluster in the CEM (CEM_16) calorimeter with matching CES hits (XCES),
- CEM_23_ISO_XCES - Requires an isolated (ISO) 23 GeV cluster in the CEM (CEM_16) calorimeter with matching CES hits (XCES),
- CEM_16_CFT_12 - Requires a 16 GeV cluster in the CEM (CEM_16) calorimeter and a matching track in the CFT of 12 GeV/c (CFT_12),
- CEM_8_CFT_7_5 - Requires a 8 GeV cluster in the CEM (CEM_8) calorimeter and a matching track in the CFT of 7.5 GeV/c (CFT_7_5),

- CEM_8_CFT_7_5_XCES - Requires a 8 GeV cluster in the CEM calorimeter (CEM_8) with a matching track in the CFT of 7.5 GeV/c (CFT_7_5) and matching CES hits (XCES),
- CMU_CMP_CFT_9_2* - Requires a stub in the CMU or CMP with a matching CFT 9.2 GeV/c track,
- CMUNP_CFT_9_2* - Requires a stub in the CMU (nonCMP) region with a matching CFT 9.2 GeV/c track,
- CMUP_CFT_9_2* - Requires a stub in the CMU and CMP region with a matching CFT 9.2 GeV/c track,
- CMNP_CFT_12_5DEG_V* - Requires a stub in the CMU (nonCMP) region with a matching CFT 12 GeV/c track in a 5° window (5DEG) (V stands for version),
- CMUP_CFT_12_5DEG_V* - Requires a stub in the CMU and CMP region with a matching CFT 12 GeV/c track in a 5° window (5DEG) (V stands for version),
- CMNP_JET* - Requires a stub in the CMU plus a jet,
- CMUP_JET* - Requires a stub in the CMU and CMP plus a jet,
- CMU_CMP_JET* - Requires a stub in the CMU or CMP plus a jet,
- CMNP_CFT_12_5DEG_M* - Requires a stub in the CMU (nonCMP) region plus a 12 GeV/c CFT in 5° window plus,
- CMUP_CFT_12_5DEG_M* - Requires a stub in the CMU and CMP with a matching CFT 12.5 GeV/c track in a 5° window (5DEG),
- CMX_CFT_12_5DEG_M* - Requires a stub in the CMX and a 12 GeV/c CFT in 5° window,
- CMX_CFT_12_5DEG_E* - Requires a stub in the CMX and a 12 GeV/c CFT in 5° window.

Appendix B

Muon Detector Upgrade

As Run II begins, CDF will be upgrading the current detector to handle the higher luminosity of $10^{32}\text{cm}^{-2}\text{sec}^{-1}$ of the Main Injector and the decreased bunch spacing of 132 ns of the Tevatron. The CMU chambers will use the proportional mode, as opposed to the Run I limited streamer mode. The reduction in gain will be compensated by a chamber mounted amplifier.

We discuss the current work on the CMU upgrades. A test stand has been constructed, as shown in Figure B.1, which consists of one CMU chamber and CMP chambers. The test stand also contains four scintillators which provide a trigger signal for cosmic rays. The scintillators are set up into two pairs. The larger scintillators, which extend the entire length of the CMU chamber, provide higher trigger rates when using cosmic rays. The smaller scintillators extend perpendicular to the CMU chambers across the width of the chamber, and give more localized tracking and position resolution.

The CMU uses charge division to determine the position of a track along the sense wire. This method is derived and discussed below. The CMP chambers are slightly tilted with respect to the longitudinal (z) coordinate and provide a consistency check of z resolution through stereographic projection.

A CMU chamber is composed of 16 drift chambers in one rectangular unit. A schematic representation of the chamber is shown in Figure 3.7. A single drift cell of the CMU is shown in Figure B.2. Three towers placed side by side make a muon

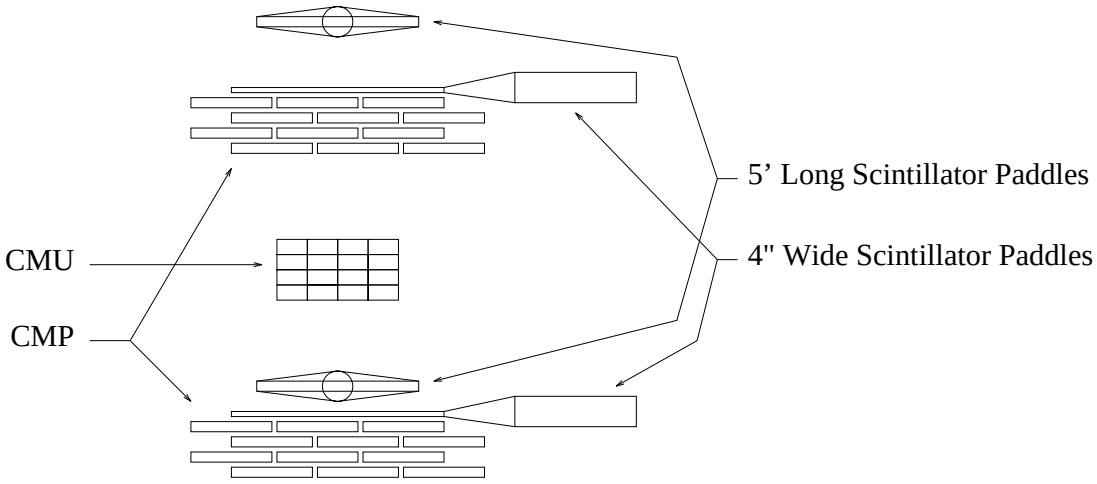

Figure B.1: Diagram of the Cosmic Ray Test Stand.

wedge which is placed outside the hadron calorimeter as shown in Figure 3.6.

B.1 Theory

Suppose a charge particle passes through the chamber such that its z position satifies the equation $0 \leq z \leq 1$. The charge particle creates an amount of charge Q_T at position z. The charge splits according to the amount of resistance it sees existing in each direction. The resistance of the wire per unit length is

$$\rho = \frac{R_{wire}}{2L_{wire}} = \frac{R_{wire}}{2} \tag{B.1}$$

when the length of the wire, L_{wire}, is normalized to unity. The amount of charge that preamp 1 sees, q_1, is given by the formula

$$q_1 = \frac{R_{preamp1}}{R_T} Q_T \tag{B.2}$$

where $R_{preamp1}$ is the resistance between point z and preamp 1 and R_T is the total resistance of the wire with

$$R_{preamp1} = (1 - z)\frac{R_{wire}}{2} + R_{preamp1}. \tag{B.3}$$

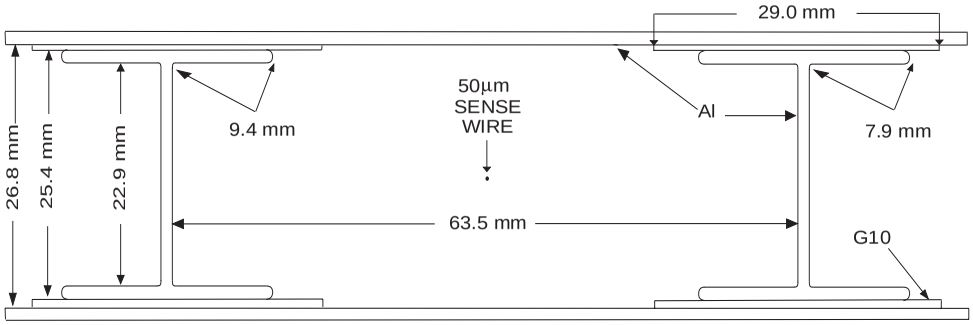

Figure B.2: Diagram of a CMU cell.

The amount of charge arriving at preamp 2, q_2 is given by

$$q_2 = \frac{R_{preamp2}}{R_T} Q_T \tag{B.4}$$

where $R_{preamp2}$ is the resistance between point z and preamp 2 and

$$R_{preamp2} = (1+z)\frac{R_{wire}}{2} + R_{preamp2} + r \tag{B.5}$$

where r is the resistance of the wire at the ganged end.

The gain is a quadratic function of charge given by

$$Q_1 = G_1^{firstorder} f(z, Q_T) + G_1^{secondorder} [f(z, Q_T)]^2 \tag{B.6}$$

where $f(z, Q_T)$ is given by

$$f(z, Q_T) = \frac{(1-z)R_{wire}/2 + R_{preamp1}}{R_T} Q_T \tag{B.7}$$

$$Q_2 = G_2^{firstorder} g(z, Q_T) + G_2^{secondorder} [g(z, Q_T)]^2 \tag{B.8}$$

$$g(z, Q_T) = \frac{(1+z)R_{wire}/2 + R_{preamp2} + r}{R_T} Q_T \tag{B.9}$$

Now assuming that both preamps discharge at the same rate $I_{discharge}$ the time over threshold is given by

$$TOT_1 = Q_1 / I_{discharge} \tag{B.10}$$

and keeping only first order terms

$$TOT_1 = \frac{G_1^{firstorder}[(1-z)R_{wire}/2 + R_{preamp1}]}{I_{discharge} R_T} Q_T \tag{B.11}$$

which can be inverted to find Q_T

$$Q_T = \frac{R_T}{(1-z)R_{wire}/2 + R_{preamp1}} \frac{I_{discharge}}{G_1^{firstorder}}. \tag{B.12}$$

Inserting this formula for Q_T into TOT_2 we get

$$TOT_2 = \frac{G_2^{firstorder}}{G_1^{firstorder}} \frac{(1+z)R_{wire}/2 + r + R_{preamp2}}{(1-z)R_{wire}/2 + R_{preamp1}} TOT_1 \tag{B.13}$$

and denoting the relative gains by R_G and setting $z = 1$ gives

$$TOT_2 = R_G \epsilon TOT_1 \tag{B.14}$$

where

$$\epsilon = \frac{R_{wire} + r + R_{preamp2}}{R_{preamp1}}. \tag{B.15}$$

B.2 Preamplifier and ASD

The Harvard preamplifier shown in Figure B.3 is a charge amplifier with a flat frequency response in our operating region. Using the Ebers-Moll model of the transistor we can calculate the impedance of the preamps

$$Z_{in} = \frac{kT}{qI_c} = \frac{25\text{mV}}{I_c} \tag{B.16}$$

Running with a ± 5 V split power supply the collector current is 100 μamps. This gives a calculated impedance of 250 ohms. The preamp is being used to match the Run I dynamic range.

The ASD is a charge integrating device that integrates the charge dumped on the wire by the muon and discharges the amount of charge at a constant rate giving a interval of time proportional to the amount of charge collected by the preamp. The ASD is shown in Figure B.4. The time difference between the time over threshold (TOT1) for one side of the wire versus the time of threshold (TOT2) for the other side allows a measurement of the z or longitudinal position of the muon.

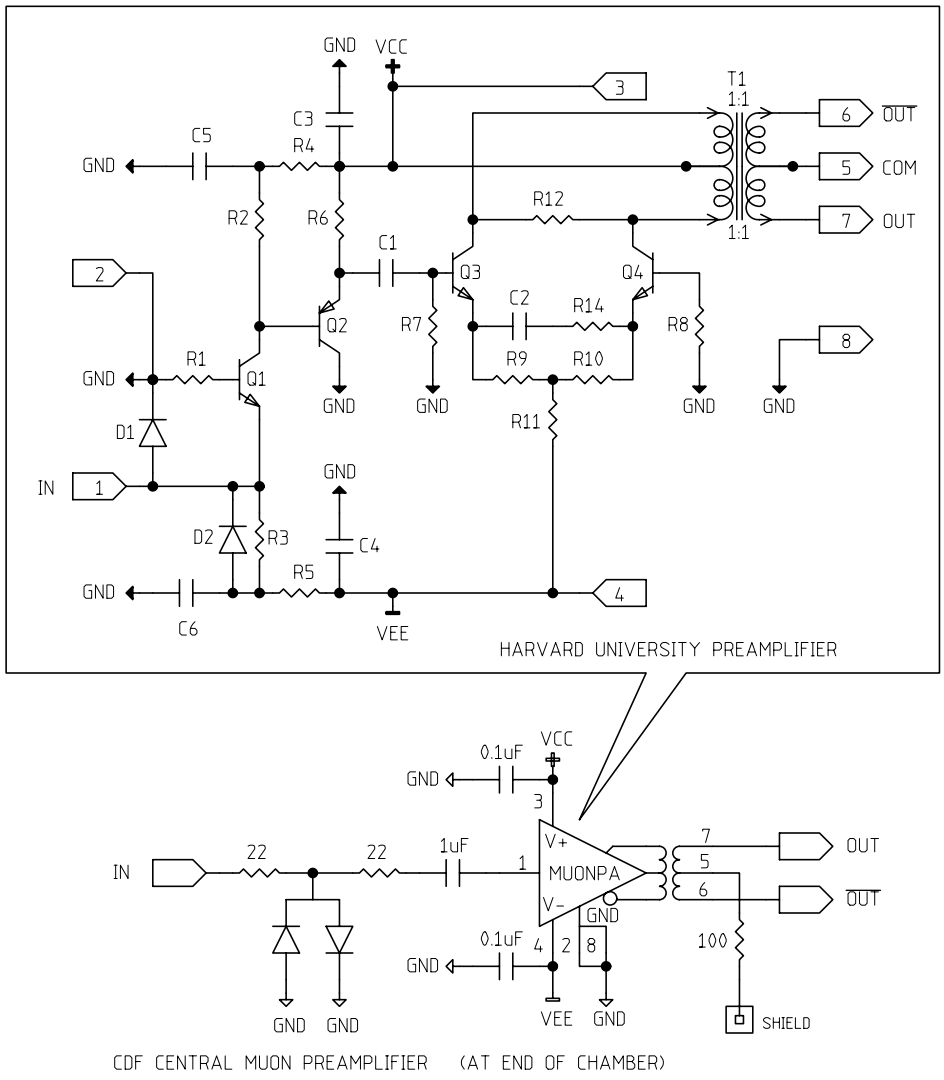

Figure B.3: Schematic of the Harvard preamplifier.

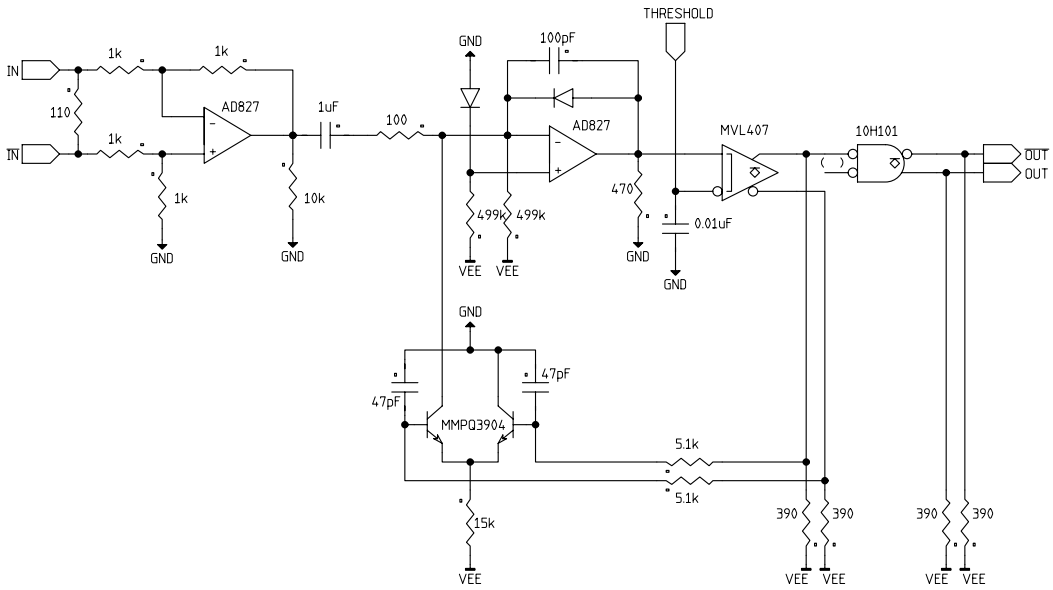

Figure B.4: Schematic of the amplifier-shaper-discriminator.

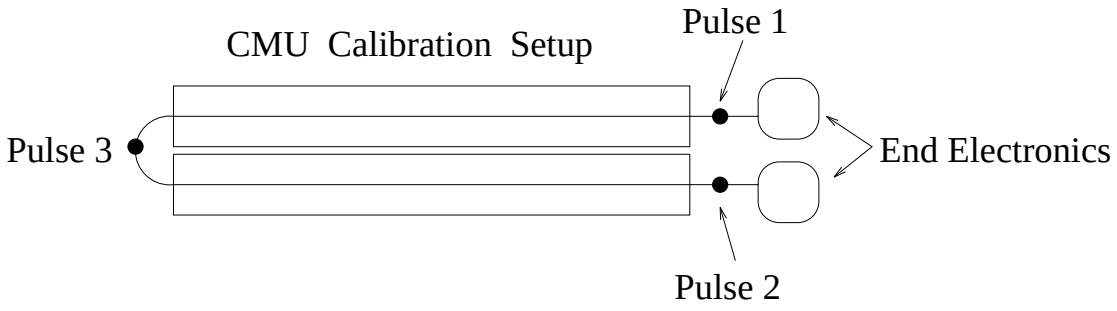

Figure B.5: Diagram of single wire calibration.

B.3 Calibration

The calibration procedure consists of injecting charge into the CMU chamber at three different locations and measuring the time over threshold at the ends of the wire. The three different locations are shown in Figure B.5. The ASD board has 14 built in pulsers which generate a voltage step which creates a test pulse through the 3 pF capacitors connected to the wire. At that voltage, 50 data points are taken. The program then averages the 50 points and calculates a σ. This σ is then used as a consistency check and cut for all data points falling outside 2σ. The average is then recalculated and written to a file. The procedure is repeated for any number of voltage levels choosen and the same procedure used on the other two charge injection points. The results of this procedure are shown in Figure B.6.

The time over threshold of the signal is measured using a Lecroy Fastbus Model 1879 96 Channel Pipeline TDC. The TDC scale is set to 4 ns/tick giving a full scale of 2 μs full scale. The threshold is set by computer through a DAC mounted on the CMU ASD board. Each individual wire can have a seperate threshold. We are using a threshold of 10 mV for each channel for calibrations and cosmic ray runs. A series of noise studies were done by varying the threshold and observing the signal to noise ratio.

The program then uses MINUIT to calculate the slopes of all the arms and the

intersection of the lines in a six parameter fit. These slopes and offsets will be used in calculation of z for cosmic rays. By normalizing the positions of the pulser locations to ± 1 and 0 the slopes are given by the equations

$$m_1 = R_G \frac{R_{p1}}{2R_w + R_G + R_{p2}} \tag{B.17}$$

$$m_2 = \frac{1}{R_G} \frac{R_{p2}}{R_{p1} + R_G + 2R_w} \tag{B.18}$$

$$m_3 = R_G \frac{R_G + 2R_w + 2R_{p1}}{R_G + 2R_w + 2R_{p2}} \tag{B.19}$$

and these can be inverted after a little algebra to give

$$R_{p1} = \frac{-m_1(R_G + 2R_w)(m_2 m_3 - 1)}{m_1(m_2 m_3 - 1) - (m_1 - m_3)} \tag{B.20}$$

$$R_{p2} = \frac{m_2(2R_w + R_G)(m_1 - m_3)}{2m_2 m_3 - m_1 m_2 - 1} \tag{B.21}$$

$$R_G = \frac{(m_1 - m_3) - m_1(m_2 m_3 - 1)}{2m_2 m_3 - m_1 m_2 - 1} \tag{B.22}$$

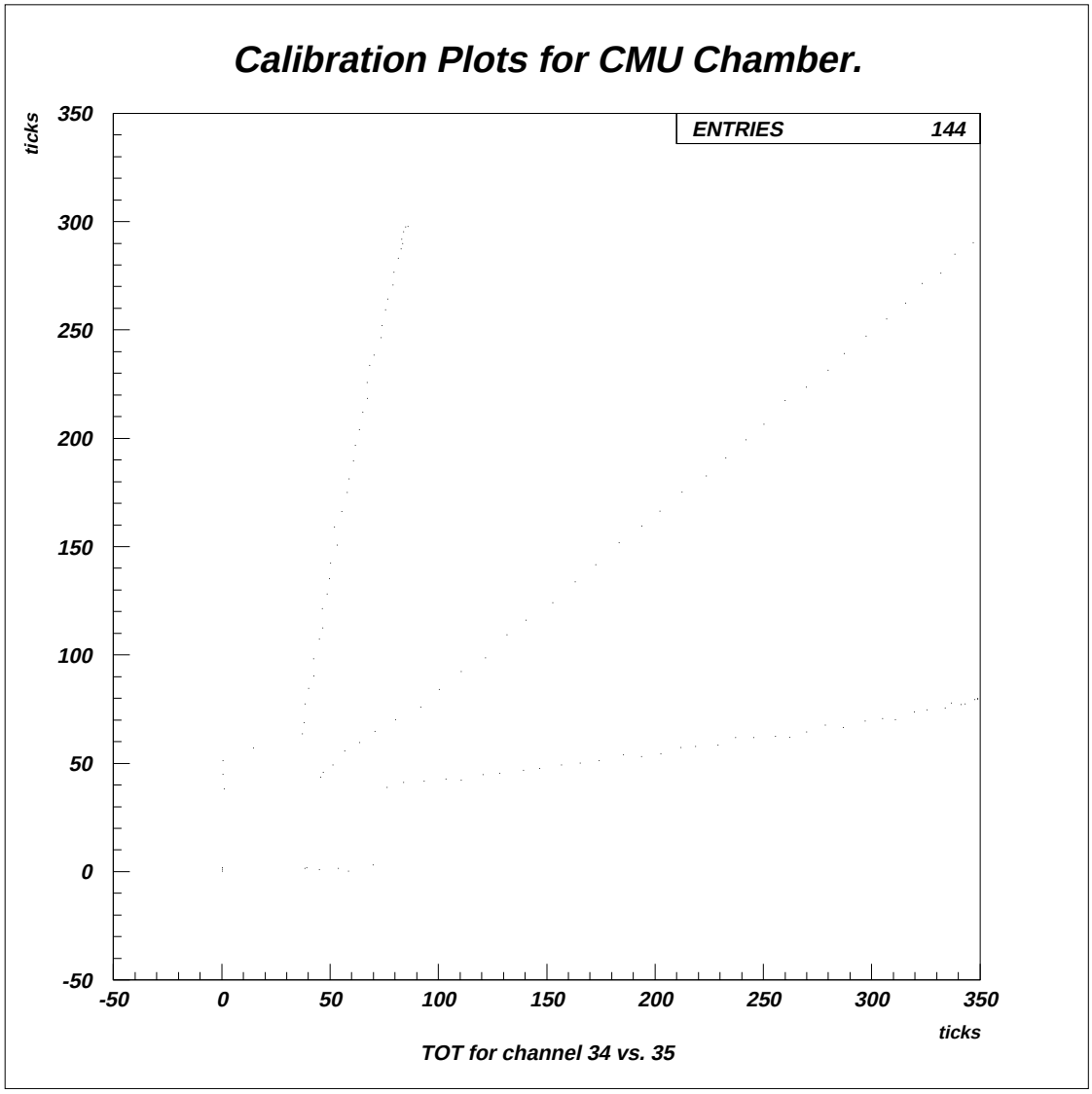

Figure B.6: Calibration Plot of a Single CMU Wire.

References

[1] H. R. Pagels, *Perfect Symmetry*, Simon and Schuster, Pp. 206-228(1985).

[2] J. Bartels, D. Haidt, A. Zichichi, *The European Physical Journal C: Particles and Fields*, Springer, Volume 15, Pp. 1-878(2000).

[3] J. Cortés, K. Hagiwara, F. Herzog, Nucl. Phys. B**278** Pp. 26-60(1986).

[4] U. Baur, D. Zeppenfeld, Phys. Lett. B**201**, Pp. 383-389(1988).

[5] D. Zeppenfeld, *AIP Conference Proceedings 350*, Pp. 46-59(1995).

[6] U. Baur, E.L. Berger, Phys. Rev. D**41**, Pp. 1476-1488(1990).

[7] U. Baur, E.L. Berger, Phys. Rev. D**47**, Pp. 4889-4904(1993).

[8] Durand III, P.C. DeCelles, R.B. Marr, Phys. Rev. **126**, 1882-1898(1962).

[9] U. Baur, S. Errede, G. Landsberg, Phys. Rev. D**50**, Pp.1917-1930(1994).

[10] F. M. Renard, Nucl. Phys. B**196**, Pp. 93-108(1982).

[11] U. Baur, D. Zeppenfeld, Nucl. Phys. B**308**, Pp. 127-148(1988).

[12] J.J. Sakarai, *Modern Quantum Mechanics*, Addison-Wesley Publishing Company, Pp. 399-410(1994).

[13] F. Abe *et al.,* Nucl. Instr. and Meth. A**271**, Pp. 387-403(1988).

[14] D. Amidei *et al.,* Nucl. Instr. and Meth. A**350**, Pp. 73-130(1994).

[15] F. Snider *et al.,* Nucl. Instr. and Meth. A**268**, Pp. 75-91(1988).

[16] F. Bedeschi *et al.,* Nucl. Instr. and Meth. A**268**, Pp. 50-74(1988).

[17] T. Ferbel, *Experimental Techniques in High Energy Physics*, Addison-Wesley Publishing Company, Pp. 257-324(1987).

[18] L. Balka *et al.,* Nucl. Instr. and Meth. A**267**, Pp. 272-279(1988).

[19] Y. Fukui *et al.,* Nucl. Instr. and Meth. A**267**, Pp. 280-300(1988).

[20] G. Brandenburg *et al.,* Nucl. Instr. and Meth. A**267**, Pp. 257-271(1988).

[21] S. Bertolucci *et al.,* Nucl. Instr. and Meth. A**267**, Pp. 301-314(1988).

[22] S. Cihangir *et al.,* Nucl. Instr. and Meth. A**267**, Pp. 249-256(1988).

[23] G. Ascoli *et al.,* Nucl. Instr. and Meth. A**268**, Pp. 33-40(1988).

[24] J.D. Lewis *et al.,* CDF Public Note **2858**(1995).

[25] D. Amidei *et al.,* Nucl. Instr. and Meth. A**269**, Pp. 51-62(1988).

[26] G. Ascoli *et al.,* Nucl. Instr. and Meth. A**269**, Pp. 63-67(1988).

[27] Randy Michael Keup, UIUC Thesis, Pp. 24-36(1995).

[28] C. Grosso-Pilcher, CDF Internal Note **4350**(1997).

[29] D. Cronin-Hennessy, A. Beretvas, S. Segler, CDF Internal Note **4317**(1997).

[30] D. Cronin-Hennessy, Thomas J. Phillips, CDF Internal Note **4085**(1997).

[31] D. Benjamin *et al.,* CDF Internal Note **4193**(1997).

[32] Young-Kee Kim, CDF Internal Note **4067**(1997).

[33] J. Smith *et al.,* Z. Phys. C. : Particles and Fields V44, Pp. 267-290(1989).

[34] J. Ohnenius, Phys. Rev. D**47**, Pp. 940-955(1993).

[35] D. Benjamin *et al.,* CDF Internal Note **3205**(1995).

[36] G. Peter Lepage, J. Comp. Phys. **27**, Pp. 192-202, Academic Press(1978).

[37] PDFLIB, H. Plothow-Besch, Computer Phys. Comm. **75**, Pp. 396-456(1993).

[38] D. Toback *et al.,* CDF Internal Note **4304**(1997).

[39] E.L. Berger, Physics Letters **140B**, Pp. 259-263(1984).

[40] U. Baur, S. Errede, J. Ohnemus, CDF Internal Note **2039**(1993).

[41] D. Benjamin *et al.,* CDF Internal Note **5439**(2000).

[42] J. Berryhill, H. Frisch, CDF Internal Note **5482**(2000).

[43] F. Abe *et al.,* Phys. Lett. **81**, Pp. 5754-5759(1998).

[44] D. Benjamin *et al.,* CDF Internal Note **5446**(2000).

[45] M. Kobayashi, M. Maskawa, Prog. Theor. Phys. **49**, Pp. 652-669(1973).

[46] T. Matsuura, W.L. van Neerven, Z. Phys. **38**C, Pp. 623-642 (1988).

[47] T. Matsuura, S.C. van der Marck, W.L. van Neerven, Phys. Lett. **211**B, Pp. 171-178 (1988).

[48] T. Matsuura *et al.,* Nucl. Phys. **319**B, Pp. 570-622 (1989).

[49] F. Abe *et al.,* Phys. Lett. **66**, Pp. 2951-2970(1991).

[50] Robert M. Harris *et al.,* CDF Internal Note **2318**(1993).

[51] Arthur Maghakian *et al.,* CDF Internal Note **1963**(1992).

[52] D. Benjamin, S. Errede, CDF Internal Note **5440**(2000).

[53] S. Errede, CDF Internal Note **1732**(1992).

[54] F. Abe *et al.,* Phys. Lett. **66**, Pp. 2951-2970(1991).

[55] P.B. Arnold, M.H. Reno, Nucl. Phys. B**349**, Pp. 381-390(1991).

[56] Mark Frank Vondracek, UIUC Thesis, Pp. 24-36(1995).

[57] K. Lannon *et al.,* CDF Internal Note **3798**(1996).

[58] D0 Collaboration, hep-ex/0102017 (1996).

[59] OPAL Collaboration, CERN-EP/2000-114.

[60] OPAL Collaboration, CERN-EP/2000-113.

[61] DELPHI Collaboration, CERN-EP/2001-006.

[62] MUON G-2 Collaboration, hep-ex/0102017 (2001).

[63] Scott Willenbrock, HEP Lunch Seminar (2001).

[64] The CDF II Detector Technical Design Report, Fermilab-Pub-96/390-E, Ch. 2, Pp. 28-32 (1996).

Vita

Leonard Steven Christofek was born in Parma, Ohio on April 23, 1971. At birth, he never left his mother's side. His family moved to West Palm Beach, Florida in 1980. While in elementary school, his father, Richard Christofek Sr., passed away from a rare form of cancer. He graduated from Palm Beach Lakes High School (Twin Lakes).

He attended college in Blacksburg, Virginia at Virginia Tech (Go Hokies!). During the summers, he worked at LAMPF in Los Alamos, New Mexico. He worked on the LSND experiment, which claims to see neutrino oscillations.

Leonard continued his graduate studies at the University of Illinois at Urbana-Champaign. His thesis data was taken at the Fermilab Tevatron in Batavia, Illinois. The results of his thesis data could prove interesting.

Personally, Leonard's interests cover a broad range of topics. He loves to SCUBA dive, drive motorcycles and skydive. He became more graceful after two years of ballroom dancing (the Samba is awesome!). Recently, he started volunteer work at a local church doing home repair for less fortunate families. Most importantly, he loves physics and he loves his work. It is that love that has produced this work.